Molecular Dynamics simulation of polyhedral oligomeric silsesquioxanes (POSS) and their polymeric nanocomposites

Jacob Kristian Earnshaw

A thesis submitted in partial fulfilment of the requirements of

Sheffield Hallam University

for the degree of

Doctor of Philosophy

November 2022

Candidate Declaration

I hereby declare that:

1. I have not been enrolled for another award of the University, or other academic or professional organisation, whilst undertaking my research degree.

2. None of the material contained in the thesis has been used in any other submission for an academic award.

3. I am aware of and understand the University's policy on plagiarism and certify that this thesis is my own work. The use of all published or other sources of material consulted have been properly and fully acknowledged.

4. The work undertaken towards the thesis has been conducted in accordance with the SHU Principles of Integrity in Research and the SHU Research Ethics Policy.

5. The word count of the thesis is 38074.

Name	Jacob Earnshaw
Date	November 2022
Award	PhD
Faculty	Industry and Innovation Research Institute
Director of Studies	Prof. Doug Cleaver

Abstract

Within this thesis, I use atomistic Molecular Dynamics simulation to elucidate the thermo-mechanical properties of polyhedral oligomeric silsesquioxanes (POSS). These molecules have unique and interesting properties due to their nanoscale size and organic-inorganic nature. POSS species comprise a rigid silica core which is functionalised with organic moieties at the vertices. These nanoparticles exhibit a wide range of behaviours and properties due to the scope of viable functionalising groups. I largely focus here on the cubic T_8 conformation, which typically ranges from 1-10 nm in diameter.

For pure POSS systems, I use systematic simulation studies to characterise the sensitivity of the glass transition temperature (T_g), an important macroscopic property, to molecular structure. For POSS species functionalised with eight flexible groups, I identify a key molecular feature, namely, the breathing mode, as the degree of freedom that controls the macroscopic T_g. Due to their high degree of inter-molecular entanglement, these systems exhibit very little molecular mobility. Thus, it is the molecular-level movements within the functionalising groups that underpin the systemic change from a glassy state to rubbery state. The influence of structural morphology in tetra functionalised T_8 systems are also studied. Here, I observe the adoption of richer packing arrangements and shifts in the T_g values due to alternative arrangements of the functionalising groups about the central core. I also examine the spontaneous formation of crystalline structures from amorphous starting configurations by systems of rigid POSS molecules.

Due to the versatility in their structure, POSS are frequently included as a component in nanocomposite materials. Within this work, I have study POSS-polymer hybrids as both blended and grafted nanocomposites. I use hydroxyl-terminated polybutadiene (HTPB) for the polymer matrix and explain the observed changes in T_g as a product of the molecular behaviour and interactions. When grafted, POSS have a local anchoring effect on the dihedral rotational freedom available to the C-C single bonds of the HTPB backbone. Thus, I observe a significant increase in the T_g for these systems. When blended, rigid POSS hybrids exhibit significant phase separation, whereas flexible POSS species are much more dispersed within a HTPB matrix. Both systems impart less specific impact on the dihedral rotation of the HTPB matrix than is observed in the grafted systems. However, increases in T_g are consistently observed with increasing POSS concentration. Through the simulation of POSS blended with a chemically similar but sterically different matrix, I further characterise the mixing behaviours of POSS species as a function of their functionalising group.

These studies provide insight into the structure-property relationship for a variety of POSS species as pure entities and nanocomposite hybrids, thus providing understanding for future programmes of synthesis or nanocomposite design, as well as necessary target properties for candidate coarse-grained models of POSS systems.

Acknowledgement

Contents

Chapter 1

Introduction

The study of polyhedral oligomeric Silsesquioxane (POSS) has become popular within the field of silica (SiO_2) chemistry in recent times. These nanoparticles encompass a diverse range of structures, material properties and molecular behaviours. The molecular formula for this species is $(RSiO_{3/2})_8$ where R represents a given organic group. Within the field, a wide variety of organic moieties have been shown to be viable R groups.[1] As such, numerous hybrid organic-inorganic structures have been curated with specific characteristics, such as the capacity to undergo polymerisation, exhibit particular optical properties or improve mechanical properties.

Within this thesis, the cubic cage conformation of POSS has been studied. The computational technique of Molecular dynamics (MD) has been utilised to investigate the atomic level interactions and behaviours of particular POSS species. In doing so, the molecular level structure to macroscopic level properties relationships have been characterised. The glass transition temperature (T_g) has been the primary macroscale observation for this project. The T_g is an important consideration in the development of new materials.[2] By controlling the T_g of a material, properties such as the processing temperature, service temperature and mechanical properties can be tailored as linked properties, such as viscosity, can be

altered.[3] POSS have been incorporated within a multitude of materials to alter the T_g. For example, Z. Zhiyong *et al* have demonstrated that the physical blending octavinyl POSS within polypropylene can result in an increase in T_g but subsequent decrease in the mechanical modulus. [4] However, when this system undergoes reactive blending to produce a crosslinked system, the T_g decreases and the mechanical modulus increases. The observed dichotomy in material properties has been theorised to result from individual POSS molecules or small cluster being able to diffuse past polymer chains, acting as a plasticiser and enabling polymer segmental dynamics, where as larger clusters reduce the mobility in the polymers.

1.1   Aims and Objectives

Within this work, cubic POSS systems have been studied in a number of different environments, including pure, polymer grafted and polymer blended. The principle motivation behind this work has been to further elucidate the key molecular mechanisms that give rise to the observed T_g and or change to T_g as a result of the addition of a particular POSS species. The aims of the project have been as follows:

- To understand and characterise the molecular level features of POSS systems that give rise to the observed T_g.

- To investigate the sensitivity and tunability of T_g as a product of the POSS molecular structure.

- Characterise and elucidate the impact of POSS species on the occurrence of T_g in nanocomposites featuring a well defined grafted polymeric matrix.

- Understand the POSS-polymer interactions within blended systems to analyse the kinetic and thermodynamic contributions to the observed macroscopic properties.

1.2   Thesis Overview

The chapters within this thesis are outlined here:

Chapter 2 contains a literature review on the study of POSS systems. This covers the experimental study of POSS including the synthesis, characterisation and application of POSS within polymer nanocomposite systems. In addition, the literature surrounding the study of POSS through a variety of computational methods has been discussed.

Chapter 3 describes the methodologies, algorithms and MD approach to atomistic modelling. The force-field used throughout this thesis and associated parameters are described. Also, post processing routines have been provided to describe the methods of characterising the systems.

Chapter 4 is the first results chapter and is dedicated to the modelling of pure POSS system. First, the force-field validation procedure for POSS modelling are outlined. Then, a systematic study of octa-methacrylate functionalised POSS systems is discussed. POSS species functionalised with rigid moieties are examined at higher temperatures. Tetra-functionalised POSS species are then covered to investigate the effect of isomerism. Here, a key molecular level feature has been identified that can be used to predict the T_g of methacrylate functionalised POSS systems.

in Chapter 5, grafted POSS-polymer nanocomposites are studied. Here, Hydroxyl-terminated polybutadiene (HTPB) formulates the polymeric matrix. Within which, POSS species have been physically grafted to the HTPB backbone. The molecular mechanism that dictates the HTPB T_g has been monitored and the impact of POSS on this feature has been studied. A number of different POSS species have been studied at different grafting locations.

in Chapter 6, POSS nanocomposite blended systems are studied. Here, HTPB formulates the polymeric matrix. Within which, POSS species of varying R group have been simulated at different concentrations. To contrast the highly entangled nature of HTPB, studies of the same POSS species have been considered with the chemically similar species of octatetraene.

Phase separation behaviour, molecular packing and mobility and POSS-polymer interaction are discussed.

Finally in chapter 7, conclusions from the project are discussed and recommendations for future work are given.

Chapter 2

Literature review

Within the following section, I discuss the literature enveloping POSS systems in both pure and nanocomposite systems. Section 2.1 introduces and discusses the field of nanocomposite materials to give context for the applications of POSS. I then describe the chemistry of POSS in section 2.2. Here, I discuss the structural properties, experimental properties and synthesis of a selection of POSS species. Several publications on the computational studies of these systems are also discussed in section 2.2.1. Following this, within section 2.3, I review the inclusion of POSS within nanocomposite materials. In the same format as the pure system POSS section, I first describe experimental observations and conclude with the computational study of these systems in section 2.3.1.

2.1 Overview of Nanocomposite Materials

Traditional goods, such as metals and glasses, are now often substituted by highly functional and superior materials in many industrial practices. This is, in part, due to the advancement of polymeric materials and their composites.[5] Such materials are highly processable and can exhibit preferential material characteristics, making plastics an attractive option. Moreover, through the addition of fillers, the material properties of plastics can be further designed to suit a specific need, broadening the array of possible applications.

A variety of additives have been used to improve the properties of polymers. For example, carbon black is often utilised as a reinforcing agent for the rubber in car tires and as a black pigment.[6] Calcium carbonate is also commonly used in composite systems to reduce the cost of production and improve the material processabilty of polyvinyl chloride (PVC), and enhance the mechanical properties of polypropylene (PP).[7] These fillers may be considered components of macroscale composites as the particulates are typically in the range of 1 - 10μm. For nanocomposites, I exclusively consider particles with at least one dimension in the range of 1 - 100nm. Such additives include ZnO nanostructures, gold nanowires and nanotubes. [8–10]

By incorporating nanoparticles into polymeric materials, the mechanical, electronic, thermal or optical properties of the original polymer may be improved without the loss of baseline behaviour. This avoids the common trade-off encountered with macroscale composites.[11–13] For instance, with a macroscale filler, improvement to the flame retardancy can lead to a commensurate loss of toughness.[14] As nanoparticles have a very high surface area to volume ratio, only a small fraction of the mass that would be required for a macro filler is necessary for a nanocomposite. This generally allows the processability and properties of the polymer to be retained in the final material with the additional benefit of the selected nanoparticle functionality.

One prolific example is that of a polymer-clay type nanocomposite system that was developed in 1985 by A. Usuki *et al.* Their nylon 6-clay hybrid system initially consisted of 0.5 - 5%wt clay (montmorillonite) homogeneously dispersed within the nylon matrix, and was shown to improve upon the mechanical and thermal properties of standard nylon.[15] This material was further developed for the electronic, automotive and food industries.[16, 17] Subsequently, full conferences have been dedicated to the subject of polymer clay nanocom-

posites, and hundreds of articles have been published on such materials. In more recent years, nanocomposite hydrogels have been of significant interest. By dispersing hectorite clay homogeneously in poly(N-isopropylacrylamide) gel to form a nanocomposite, K. Haraguchi demonstrated an increase tensile strength with only a slight decrease in tensile modulus, resulting in a more flexible and tougher material.[18] General motors have utilised clay polyolefin nanocomposites as step assistant components in Chevrolet Astro vehicles.[19] Toyota have incorporated N6-Clays into the construction of timing belts for their thermal stability and rigidity.[20] Also, there has been much literature on the application of clay polymer nanocmposites in the biomedical field and in water management.[21, 22] For example, in a recent study, hydrogels enriched with halloysite clay nanotubes have been utilised for the delivery of the anti-microbial, gentamicin sulfate.[23] Nanocomposites are also widely used in the food packaging industry as water vapour and oxygen barriers for transparent thin film wrapping and protection of foodstuff such as fruit juice and processed meat.

The preparation considerations for a conventional polymer composite are fundamentally different from those of a polymer nanocomposite. Properties such as the particle shape, size, size distribution and dispersion are key considerations for a macroscopic filler.[24] Chemically different filler particles, such as $CaCO_3$ and talc, of similar dimensions and distributions often produce similar composite material properties.[6] However, surface interactions between filler and polymer give rise to the change in bulk material properties, which are influenced by the size and distribution etc. As particle size is reduced, the relative impact of the interactions occurring at the molecular level become more influential on the expected properties of the composite. Such considerations include Van der Waals forces, molecular polarity and hydrogen bonding.[25] Features such as the catalytic activity and electrical conductivity may also be altered by manipulating the filler and polymer interactions at their interface. Such changes can be achieved by chemically altering particles that exist on the nanoscale. As nanoparticles have a high surface area to volume ratio, the relative distance between inter-

face domains is much lower, meaning the relative amount of interfacial interaction is higher. This feature is a key characteristic of nanocomposites.[12] Of course, fundamental parameters, such as the molecular shape and volume fraction must also be considered along side the molecular structure and electronic effects.[26]

Within this project, I have undertaken a computational study of a unique 3-dimensional nanoparticle with applications for nanocomposite materials. This nanofiller has a wide diversity of applications and properties due to the nature of its structure. The following section will discuss these systems in the context of current research and their utilisation as nanocomposites.

2.2 Chemistry of Polyhedral Oligomeric Silsesquioxanes (POSS)

Polyhedral Oligomeric Silsesquioxane (POSS) systems are inorganic-organic hybrid molecular structures. Their chemical formula is $R_n(SiO_{1.5})_n$ where n = 8, 10, 12 etc with cages of the corresponding size being labelled T_n. The 'R' group represents organic moieties which are anchored at the vertices of a central inorganic silica core. 3D renderings of the T_8, T_{10} and T_{12} caged POSS structures can be seen in figure 2.2.1. This type of molecular system may also exist as a ladder like structure, i.e. as an unfolded net rather than a caged structure. However, for this study, due to their prevalence and preferential formation during synthesis, I have solely focused on the T_8 cubic conformation. The organic R groups (denoted in blue in figure 2.2.1) can be selected from a variety of available functional groups. Each vertex may be occupied by the same type of moiety, or as is commonly observed, one or more of the eight sites may be occupied by a unique group. These groups can be curated to exhibit specific molecular traits. For example, a POSS system may be introduced into a polymeric matrix as a cross-linking agent. To achieve this, two or more of the organic groups express

polymerisable functional groups, such as acrylate or epoxy. In the same manner, POSS may also be introduced as pendant groups where only a single vertex is functionalised with a reactive group. Conversely, POSS may also be introduced as discrete molecules in a blend. In this situation, the POSS contain nonreactive groups with selected steric or Coulombic properties.[27]
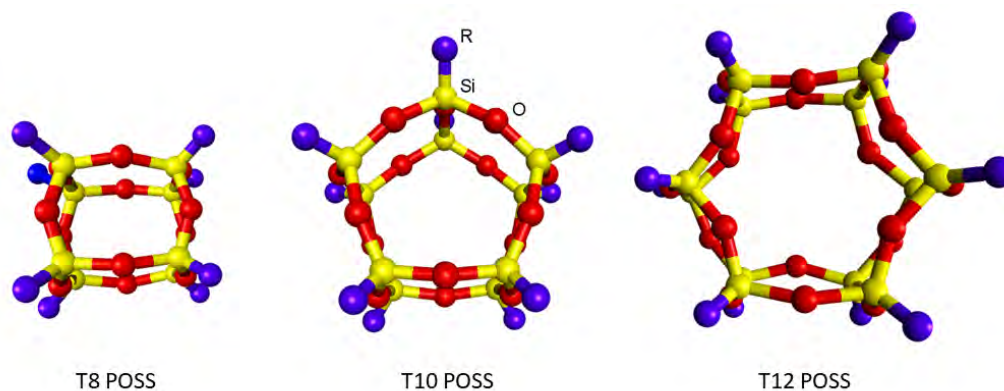
Figure 2.2.1: Three of the possible cage conformations of POSS structures observed in synthesised systems. From left to right, T_8, T_{10} and T_{12} POSS structures where yellow, red and blue atoms correspond with silicon, oxygen and 'R' groups respectively.

Due to the range of available POSS structures, there is great diversity in their observed physical and chemical properties. Experimentally, many T_8 POSS structures have been characterised and analysed. To reduce this field to the scope of this review, I will select a number of POSS structures with differing properties and discuss some of the methods by which they have been characterised, studied and produced. Due to their prevalence in the field of nanocomposites, I will discuss POSS both in the context of pure POSS systems and when integrated into nanocomposite materials. I will focus on the study of pure POSS in this section, and consider nanocomposite implenetation in section 2.3

I first consider T_8H_8 POSS systems, the simplest form of POSS, where each of the eight silicon vertices are functionalised with a single hydrogen atom. T_8H_8 exists as a white solid under standard conditions and was first discovered serendipitously in 1959 by Müller *et*

al.[28] As is common for the confirmation of the successful formation of a chemical compounds, Nuclear Magnetic Resonance (NMR) spectroscopy has been instrumental in the examination of POSS structural integrity, particularly ^{29}Si NMR. For example, Wang Yan Nie *et al* characterised T_8H_8 POSS before and after Silylation and polymerisation with 4,4'-Bis(4-allyloxybenzoyloxy)phenyl diene.[29] For the pure T_8H_8, from the ^{29}Si NMR data there is a single resonant peak at -83.1pmm, corresponding to the Si-H bond. For the nanocomposite material, four separate absorption peaks at -64.85, -83.1 -941 and 108.47 ppm were obtained that correspond to Si-C, Si-H, Si-OH and Si-O-Si respectively. Here, the latter three peaks are due to unreacted POSS vertices. As this reaction changes both the functionalisation of the POSS species and induces the cross-linking of the newly formed T_8(4,4'-Bis(4-allyloxybenzoyloxy)phenyl)$_8$, some of the vertices do not undergo reaction. By calculating the integrated area under the absorption peaks, it was determined that, on average, 6 of the 8 sites reacted successfully. In a similar paper by Qiang Li *et al*, T_8Me_8 was incorporated into a arylacetylene polymer through a Grignard reaction.[30] The precursor T_8Me_8 was characterised by ^{29}Si NMR and demonstrated a single peak at -65.97 ppm. This value is in good agreement for the reported value of -64.85 for the Si-C bond by Wang Yan Nie *et al.*

Crystallography and X-ray diffraction studies have also been utilised for the characterisation of POSS species. Such studies have compared the structural features of different POSS structures. For the T_8H_8 species, a number of crystallography techniques have been applied, including powder and single crystal X-ray diffraction (XRD) and Neutron diffraction.[31] The work carried out by Auf der Heyde *et al* is of particular interest.[32] This study identified, through single crystal XRD, that despite the high symmetry of the T_8H_8 POSS species, the system exhibits tetrahedral T_h symmetry rather than the expected perfect octahedral O_h symmetry. This is due to the observed variance in the distance of separation between adjacent Si atoms. On average, there is a separation of 3.7$\mathring{A}$, and the standard deviation is

determined to be $0.154\overset{\circ}{A}$. Interestingly, this is believed to be due to the nature of the crystal structure. Four intermolecular Si-O bonds preferentially form between molecular pairs, forming an off-axis crystal packing structure. This results in POSS cages with a slightly compressed structure in one of the three dimensions in the plane of the facets. Diffraction studies have also been conducted on amorphous POSS systems.[33] Wide-angle X-ray scattering (WAXD) has been used to identify the existence of amorphous propyl methacrylate functionalised POSS in its pure form and when incorporated into propyl methyl methacrylate matrices.

It is worth noting however, that while in a solution, the T_8H_8 appears to exhibit octahedral (O_h) point symmetry. In a study by Martin Bartsch *et al*, the vibrational structure of T_8H_8 was investigated through IR and Raman Spectroscopy and applied for the production of a force-field for the structure of zeolite A (Sodalite).[34] This work highlights that in solution, ^{1}H NMR, ^{29}Si NMR, IR spectroscopy techniques all indicate that T_8H_8 structure exhibits O_h symmetry. To unite these bodies of work, Derek A. Wann *et al* have conducted Gas-phase Electron diffraction studies on the T_8H_8 structure.[35] This paper concludes that when T_8H_8 is unconstrained by a crystal lattice, the structure is does indeed exhibit O_h symmetry. Further IR-Raman study into the T_8H_8 system has demonstrated that the POSS silica cage exhibits a breathing mode, which is revealed through the inspection of a vibration at 467 cm^{-1}.[34]

Thermal analysis of T_8H_8 has also been under-taken by a number of groups. However, The process of analysing these systems can be complicated. Through thermogravametric analysis (TGA), Wang Yan Nie *et al* demonstrate that T_8H_8 readily sublimes into the gas phase at temperatures over 473 K.[29] The higher order T_8Me_8 POSS species begins to undergo sublimation at 503 K to eventually completely evaporate at 523 K.[36] However, as the percentage of organic character is increased within the molecular structure, using larger

R groups, the thermal behaviour changes drastically. For instance, $T_8(i\text{-Bu})_8$ is reported to melt at 534 K and completely evaporate at 648 K under a Nitrogen atmosphere. This introduction of a soft/fluid phase window for substantial R groups is a general feature. However, when investigated under air, 74% of the overall mass of $T_8(i\text{-Bu})_8$ is evaporated, the remaining 26% being accounted for by a ceramic residue.[37] This remaining material is produced as oxidation has occurred has alongside the sublimation, producing a carbon-containing silica sublimate. This divergent trend from sublimation behaviour continues as the 'R' groups become increasingly complex. As another example of this behaviour, $T_8((CH_2)2\text{-Ph})_8$ has been demonstrated to decompose at 623 K.[38] It should be noted that this trend is quite apparent due to the consideration of high inorganic character POSS systems. As mentioned, POSS systems cover a significant region of chemical space. Their thermal properties are highly dependent on the nature of the incorporated 'R'.

A great deal of interest has been placed into the production of novel POSS structures with unique properties. There are many reported synthetic pathways, each of which is unique to the desired 'R' group and or combination of 'R' groups. These pathways can be separated into two distinct categories; the spontaneous formation of T_8 POSS and the chemical modification of existing T_8 POSS. The first group of syntheses stem from hydrolysis-condensation reaction schemes for chloro or alkoxy silanes.[39] An example reaction scheme of this nature can be seen in figure 2.2.2.[40] This method of synthesis tends to produce a higher proportion of T_8 conformation in varying yields depending on the type of 'R' group. Much research has been carried on the optimisation of this synthetic pathway, however, there are no optimal universal conditions for all 'R' groups. The hydrolysis method and solvent mixture, for example, differ from system to system. This same methodology can be applied to the production of T_8R_7R' type POSS systems through 'corner capping'. Here, the partially condensed POSS $(R_7Si_7O_9(OH_3))$ or conjugate salt react with a silane group of differing 'R' group.[41, 42] This method of producing non-symmetrical POSS molecules, is well estab-

lished and has been applied to many system types where R groups include Ethyl, *i*-octyl or cytosine moieties.
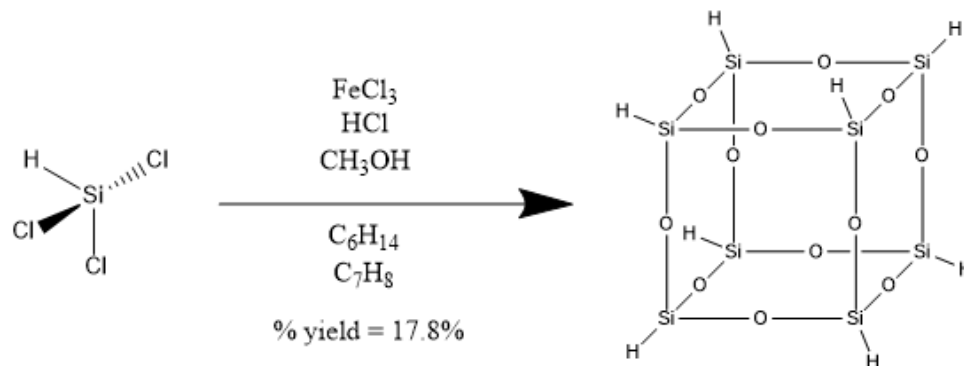
Figure 2.2.2: reaction scheme for the formation of T_8H_8 from the hydrolysis-condensation reaction of trichlorosilane.[40]

The second group of reaction pathways involve the alteration of existing POSS molecules. One of the most common implementations is through the hydrosilylation of the Si-H bond of the T_8H_8 POSS species.[43] A general reaction scheme for this method can be seen in figure 2.2.3. Hydrosilylation is often carried out with a Platinum catalyst and produces good yields of the desired POSS species. However, there are potential draw backs in the production of isomers at the α or β Carbon of the C=C double bond of the reacting species.[40] These methods of T_8 production are far from exhaustive, and a great many system-specific reaction pathways exist that are highly dependent of the nature of the desired R group.
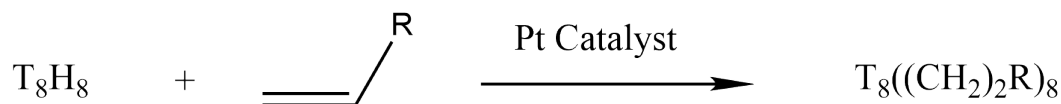
Figure 2.2.3: reaction scheme for the formation of T_8R_8 from the hydrosilylation of T_8H_8

2.2.1 Computational Study of Pure POSS systems

The study of pure POSS systems has also been the subject of several different computational studies, through methods including *ab initio* first principle calculations and classical tech-

niques such as Molecular Dynamics (MD). The advent of computational research into these species was most notable in the 2000s. An early paper by McCabe *et al* in 2004 states that "Although much is known experimentally about the chemical synthesis of POSS derivatives and their characterization, little theoretical understanding exists at the molecular level or beyond.".[44] To begin to develop and inform the production of possible novel POSS compounds, this paper describes some of the early steps in understanding the electronic and atomic level features required to achieve mesoscopic level representation of POSS systems. With this goal in mind, the paper utilises Quantum, atomistic and Coarse-grained Classical techniques. Initially, the electronic properties of T_8H_8 were characterised with first principles density functional theory (DFT). This study notes that the lowest unoccupied molecular orbital (LUMO) is positioned at the center of the POSS cage. From an electronic perspective, this is quite interesting as the cage can readily become ionised and effectively house an electron within itself. This has implications for the luminescence of the POSS species. Restrained Hartree-Fock calculations were also used to inform how the POSS cage structure changes when different R groups are implemented. It is noted that the rigidity of the POSS cage enables its shape to be retained when different alky R groups are included. To investigate the atomistic representation of POSS systems, the UFF, COMPASS and Kieffer force-fields were all implemented through molecular mechanics at a fixed temperature. Each force-field represented a single T_8H_8 molecule in good agreement with the first principle techniques. MD was then utilised to investigate POSS representation in the solid and gas phase, producing good XRD pattern predictions for crystal phases and consistent radial distribution function (G(r)) analysis between force-fields. Course-grained methods are also implemented in an initial investigation of the self-assembly of complex packing regimes in mono and tetra-tethered POSS systems. This important study covers a wide range of computational approaches to POSS systems and very much sets the tone for future work.

The McCabe group have since produced a number of publications in the field of POSS

simulation. In the context of pure POSS systems, they has investigated the implementation of different force-fields for the representation of POSS species and have developed their own set of parameters; the charge-transfer reactive force-field (CTR).[45] Here, the crystal structure of T_8H_8 and $T_8(CH_3)_8$ are simulated with different force-fields and compared to single crystal XRD results. Infra-red specta and crystal melting behaviour are also modelled. All force-fields are able to reproduce experimental crystal data for both systems, however, the CTR force-field outperforms the others for the reproduction of experimental melting behaviour of these POSS systems. A similar study was carried out by Wann *et al.*[35] Here, plane-wave DFT molecular dynamics have also been employed to characterise the T_8H_8 XRD pattern. In another publication, McCabe *et al* utilised MD simulation in conjunction with SAFT methodology to investigate the effect of molecular shape on particular thermodynamic properties.[46] Here, Mono, Di and Tetra functionalised POSS systems were investigated. For mono -tethered POSS, the liquid density was observed to decrease with an increasing linker length and as the number of tethers was increased, the liquid density also decreased.

The Takako *et al* group has studied the formation pathway of $T_8(CH_3)_8$ from the constituent $HSi(OH)_3$ precursor molecules.[47] DFT methods were used to optimise the structure of the reaction intermediates at the B3LYP level with the 6-31G(d) basis set. Overall, it is shown that the production of $T_8(CH_3)_8$ in this method is 48.3 kJmol^{-1} exothermic. Keiffer *et al* have carried out MD simulations of hexyl monofunctionalised POSS.[48] These simulations contained 64 POSS molecules taking the crystal structure conformation from XRD as the starting configuration. The performance of the force-field was characterised by the maintenance of the crystal structure at finite temperature, and replication of IR spectra. Through the implementation of a heating regime, the crystal structure was melted and the liquid density was calculated and compare to that of previous work.[46] The melting temperature is determined to be 430K, from observations where deviation from the lattice sites are first noticed. As the simulation progresses, the single hexyl linkers are able to migrate

and entangle, leading to the strong POSS-POSS interaction being over come, thus enabling the translational migration of the molecules. The melting process has been quantified here through POSS-POSS correlation and torsion angle distribution.

More recently, complex POSS systems have been simulated in their pure form. For example, Neyertz et al have used MD to study three distinct octa-amino functionalised POSS systems.[49] These species consist of propyl linkers extending from the POSS core, followed by an amide group and a terminating cyclic component. POSS 1 is substituted with a C_6H_5OH phenolic ring, POSS 2 features a pure C_6H_6 aromatic ring and POSS 3 has a fully hybridised C_6H_{12} as shown in figure 2.2.4. This study utilised ab $initio$ methods to optimise the molecular structures and used 15,000 atoms during simulation. The simulation cells were annealed at 700 K for 1000 ps. Following this, the systems were cooled at a rate of -1 Kps^{-1} to the target temperature of 298 K. Each production simulation was carried out in the NPT ensemble at 298 K at 1 Bar for a run length of 5000 ps after high temperature annealing. It is reported that the difference in 'R' group has significant effect on the system density and effective interaction potentials. From G(r) and predicted XRD patterns, these systems are surmised to be amorphous. For the aromatic rings, the distance of separation is measured to be as close as $2.9\AA$, where as the cyclohexyl group only get to within 4.9 $\AA$ of one another, suggesting there may be some preferential pi-stacking occurring. Alignment of the aromatic rings is also determined to be preferentially parallel. The separation of the POSS cage and functionalising rings is characteristic of strong 'R' group interlocking. In a later study by the same group, the O_2 transport properties were analysed for the same POSS systems.[50] This was achieved by superimposing an equally dense simulation box of O_2 onto the POSS systems and removing overlaps. The movement of the impregnated O_2 was strongly reminiscent of the behaviour observed for small gas molecules moving through a glassy polymer. This behaviour is denoted by infrequent jumping events into voids that become available through the opening of channels. A recent publication from Hiroshi et al

featured the utilisation of MD for the purpose of understanding the thermal expansion of T_8H_8, T_8i-butyl$_8$ and T_8Cyclopentyl$_8$.[51] The starting crystal structures for these systems were taken from the CCDC and after simulation, the remaining crystal structures were in good agreement with experimental data.
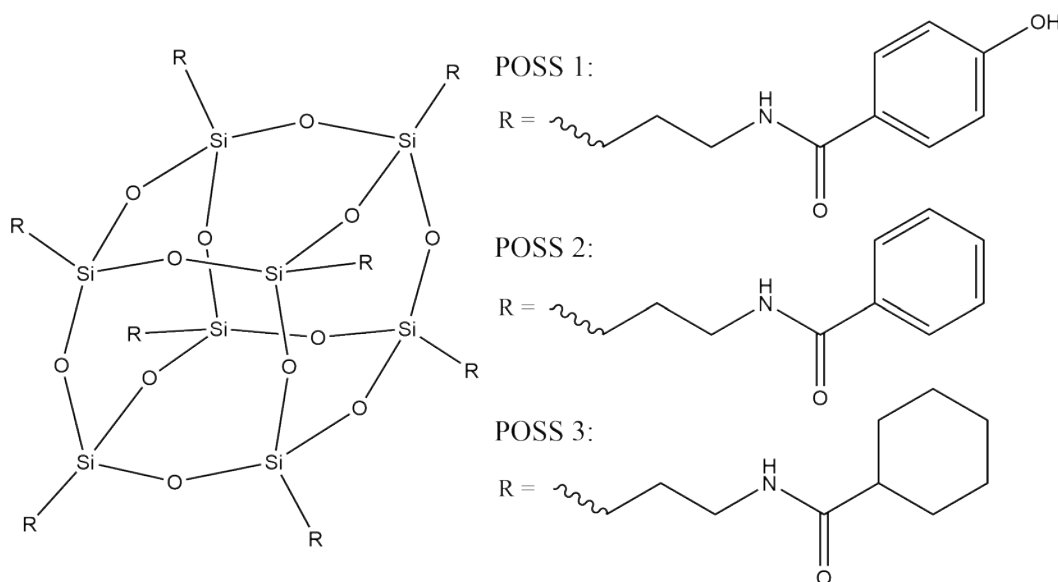
Figure 2.2.4: Chemical structure of the POSS groups studied by the Neyertz group.[49]

The crystal structure of POSS species have featured heavily within the computational study of POSS, particularly the T_8H_8 structure. This has provided an in depth understanding of the T_8 cage behaviour and crystal thermomechanical properties. However, as is evident within the literature, there is a lack of published material with a significant focus on the amorphous phase of condensed POSS. This gap in the literature has been a partial focus for the studies presented in this thesis.

Within this section I have solely focused on the simulation and experimental properties of pure POSS systems. In the following section, I will discuss POSS species in the context of nanocomposites both *in silico* and *ex silico*.

2.3   POSS nanocomposites

In broad terms, POSS provide a means of introducing inorganic character into an organic polymer matrix, fundamentally changing the macroscale properties through molecular level change. The POSS cage is typically 5.5 $\mathring{A}$ between opposite silicon atoms at the largest distance along 3 planes, meaning the POSS structure exists on the same scale as polymer molecules. This allows molecular level interactions to be designed, based on the molecular composition of both the POSS and the polymer. POSS systems may be incorporated into a polymer matrix via a number of different mechanisms: co-polymerisation; pendant grafting; physical blending; POSS-only polymerisation; or as non-reactive bystanders during polymerisation.

The nature of resultant property changes in the baseline material is highly dependant on the method of POSS incorporation. Thermomechanical properties are most affected through the covalent introduction.[39] POSS incorporation has been demonstrated to change the tensile modulus, electrical conductivity and the glass transition temperature (T_g) of polymeric systems among many other material properties.[52–54] The capacity for POSS incorporation to achieve target material properties has also been exhibited for many different polymer matrices, including methacrylates, polyimides and polyurethanes.[55–57]

In particular, methacrylate 'R' group POSS structures have seen significant research. Such systems have been incorporated into triblock coplymeric systems as pendant groups to produce materials with higher glass transition temperatures.[58] Propyl methacrylate functionalised POSS have been physically blended into vinyl ester resins for the development of thermally resistant materials.[59] When compared with a number of different composite materials containing the same vinyl ester matrix, the POSS nanocomposite exhibited the most improved properties. It was reported that the viscosity of the resin was predominantly unchanged, meaning the processability was maintained whilst the flame retardency

was increased. On a molecular level, the degree of cross-linking was increased, lending to an increase in the T_g. Methacrylate functionalised POSS cages have seen a range of potential applications. Their incorporation as crosslinking agents into polyimide has enabled the production of electrically isolating and thermally stable thin films. These materials have potential uses as circuit board substrates or aerospace materials requiring thermal resistance.[60] These systems have also been applied to dental health. Typical dental composites are used to restore teeth by acting as an adhesive or cavity filler. H. Fong *et al* have investigated the effect of incorporating the bisphenol A-glycidyl methacrylate (bis-GMA) of the commonly used -GMA/TEGDMA (triethylene glycol dimethacrylate) two part resin with propyl methacrylate functionalised POSS.[61] At loadings of 10%, the POSS system showed improved flexural strength and Young's modulus after the system had undergone visible light curing. In another study of the same system, at 5% POSS loading, the nanocomposite was reported to have improved scratch resistance and hardness.[62]

The inclusion of non-reactive POSS substituents has also seen significant research. T_8Me_8 often features in research concerned with POSS structures being dispersed in polymer matrices to form a blended nanocomposite material. A study conducted in 2001 by Fu *et al* was the first to investigate a polypropylene matrix with dispersed T_8Me_8 molecules.[63] This study introduced T_8Me_8 into the matrix at 10, 20 and 30%wt loadings and investigated the crystallisation behaviour of the polymer matrix. At lower loadings, the POSS system act as a nucleation site for the polypropylene improving the crystallisation rate. However at higher loadings the crystallisation rate was curtailed due to the physical interruption of the crystal growth mechanism. The same research group has also investigated the effect of blending T_8Me_8 with ethyl-propylene copolymer.[64] Interestingly, it was noted that above melt temperature at 160° C, the addition of T_8Me_8 POSS changed the material state from a melted resin to a solid at 10%wt POSS. The glass transition temperature was also increased upon the addition of the POSS and the formation of POSS crystals within the matrix was also

tracked through XRD. In a broader study, A. Fina *et al* investigated the material properties of polypropylene with T_8Me_8, T_8i-Bu_8 and T_8i-Oct_8 separately.[65] For the polypropylene-T_8Me_8 nanocomposite, the degree of POSS dispersion was comparatively low due to their tendency to flocculate and form microcrystallites of 10-20 μm at 3% and 10% loadings. These structures were identified through Scanning Electon Microscopy (SEM) and XRD analysis. The T_8i-Bu_8 functionalised system appears to involve much more compatible polymer-POSS interactions as no crystallites are evident through SEM. However, Transmission Electron Microscopy (TEM) indicates the presence of nanocrystals on the length scale of 0.5 μm which appear to behave as nucleating agents for the formation of spherulite regions within the polypropylene. The T_8i-Oct_8 crystallites could not be identified in this study, likely due to the liquid nature of T_8i-Oct_8 at the operating temperature, however the polymer spherulites were still observed at 10% loading. Thermal behaviour of these systems was also investigated and the results were quite diverse. For instance, the 10% T_8Me_8 nanocomposite exhibited no change in melting behaviour but the crystallisation temperature was increased slightly from 114° C to 116° C. Conversely, The T_8i-Bu_8 nanocomposite exhibited no difference in the crystallisation temperature but the melting temperature was decreased from 165° C to 159° C. This study was therefore able to conclude that changes in material properties do not simply scale with the length of the alkyl 'R' group. Instead, it indicates that complex mechanisms are at play, relating to the combined effects of each POSS and its host polymer matrix.

2.3.1   Simulation of Nanocomposite POSS systems

POSS-polymer nanocomposites have also been the subject of computational study through MD. These publications aim to elucidate the molecular mechanisms and interactions that occur between POSS and polymer at the molecular level. Amongst the first to publish in this field was Bharadwaj *et al* in 2000.[66] Here, a single polynorborene chain was simulated with randomly distributed POSS pendant groups that were tethered by an ethyl chain at

a concentration of 10%mol. Two different types of POSS structure were investigated. One system was functionalised with 7 cyclopentyl groups and the second group was functionalised with 7 cyclohexyl groups. These simulations were able to capture the experimentally determined T_g for the pure polynorborene of 300 K and the POSS grafted systems of 370 and 350 K respectively. The packing and mobility of the POSS for each system was analysed and determined to be different in each case. The cyclohexyl system was less efficiently packed due to greater steric hinderance whilst the cyclopentyl system exhibited greater mobility. Through the addition of either POSS, the movement of the polymer chain was inhibited and the elastic properties were enhanced. In a joint computational and experimental study conducted by Choi et al, the mechanism by which tethered POSS cages interact with epoxy resin was investigated.[67] The computational component formed a comparatively small section of this study, however, the nature of the tether being directly linked to the material properties. Rigid POSS tethers produced a higher T_g and elastic modulus, whereas flexible tethers produced a lower T_g and elastic modulus with a higher fracture toughness. The degree of molecular mobility was determined to be a contributing factor to the material property change.

Patel et al have used MD simulation to characterise the behaviour of polystyrene and poly methacrylate chains that have cyclopently, cyclohexyl, iso-butyl and phenyl substituted POSS cages at 1, 4, 5 and 10% as pendant groups.[68] Smaller concentrations of POSS raised the predicted T_g values for the styrene nanocomposite and lowered the T_g for polymethacrylate nanocomposite. The phenyl substituted styrene systems exhibited the greatest increase to T_g. This behaviour was attributed to the efficient packing of the polymer around the POSS cube due to the favourable interaction between the phenyl groups of the POSS and the styrene backbone, effectively reducing the mobility of the backbone and reducing the degrees of freedom available for dispersion of energy. In doing so, the molecular motion and rubbery behaviour of the polymer matrix was restricted at higher temperatures; resulting in

a higher T_g. Polymethacrylate is a significantly more polar molecule, so the degree of the interaction with the non-polar 'R' groups resulted in a smaller effect on the T_g.

McCabe *et al* have also used MD to investigate POSS nanocomposites. These studies were focused on the simulation of dispersed T_8Me_8 in polydimethyl siloxane and *n*-hexadecane.[69, 70] The diffusion coefficient of each POSS system was found to be dependent on the nature of the POSS functionalisation. Further, the effective POSS-POSS interaction was investigated as a function of the temperature and functionalisation type. In a similar study, Capaldi *et al* have studied the addition of octa-cyclopentyl functionalised POSS dispersed in polyethylene.[71] Three different systems were studied of concentration 5%, 15% and 25% POSS by weight. For the 15% and 25% systems, through radial distribution analysis, a strong tendency for the POSS to aggregate was observed at 500 K. It is postulated that these structures represent initial stages of microcrystallites, however the time scale of the simulation prevented the formation of full crystal structure, as the aggregates exhibited amorphous structuring. The polymer molecules in these systems were noted as diffusing at a rate 33% faster than the POSS molecules and aligning at the surface of the POSS aggregates tangentially. Yani *et al* have used MD to study polyimide doped with 5%wt T_8H_8 or 6, 11 or 20%wt T_8amino-phenyl$_8$ POSS systems.[72] Here, the inclusion of T_8H_8 showed a decrease in T_g whereas the T_8amino-phenyl$_8$ systems showed an increase in T_g. These systems achieved crystalline packing and amorphous packing of POSS flocks respectively.

In more recent publications, Zhu *et al* have used MD to analyse the applicability of POSS in solid polymer electrolytes.[73] Currently, polyethylene oxide has applications in this field. When used in conjunction with a metal oxide, the -O- ether component of the polymer enables the Li^+ to migrate through continuous coupling-decoupling. In turn, this produces movement in the polymer matrix, driving the polymer to a crystalline state, resulting in a loss of conductivity. The addition of POSS to these matrices has been demonstrated to

improve the longevity of these materials by generating free volume within the nanocomposite to encourage continuous ion exchange.[74] The exact types of POSS used in this simulation work are highly complex and for clarification I encourage the reader to check the source for reference. This work was able to predict that the grafted POSS species increased the T_g and inhibited the polymer crystallisation process. The resultant increase in polymer chain mobility also enabled greater migration of Li^+ ions, producing a predicted higher conductivity. Simulations of POSS in dental composites have also been conducted by Xie *et al.*[75] Here, T_8Me_8 and $T_8Phenyl_8$ POSS were introduced as pendant groups within a DGEBA/OSC double-crosslinked epoxy resin at 6, 11, 16 and 20%wt. Interestingly, this was achieved by first equilibriating the reactant molecules and conducting another simulation to break and reform covalent bonds to form a cross-linked model.[76] For both POSS systems, the T_g was increased at all concentrations and 11%wt showed the greatest increase. The degree of epoxide mobility was most decreased for the 11%wt systems in both POSS species as calculated by the mean-squared displacement. This study has identified that these chemically distinct POSS systems are able to produce very similar differences in the material properties of the studied epoxide system.

Kopesky *et al* published a rigorous publication regarding polymethyl metacrylate matrices with separate tethered and un-tethered POSS species.[77] Within this study, the POSS species were non-reactive and relatively small, such as T_8iso-butyl$_8$. Here, the thermorheological properties were explained through the description of the polymer entanglement and POSS packing behaviour. The grafted systems exhibited reduced entanglement due to the presence of POSS pendant groups, generating softer materials. The non-grafted systems exhibited POSS crystallisation at concentrations as low as 1% Vol. Below, 5% Vol, the non-tethered POSS molecules acted as a plasticizer. Beyond this concentration, the POSS cubes acted as hard-sphere fillers. Kopesky *et al* have since followed up with publications on polypropyl methacrylate of differing size with $T_8propyl$-methacrylate$_8$ POSS cubes.[78,

79] From these works, it was observed that for both systems, the addition of T_8propyl-methacrylate$_8$ reduced the glass transition temperature until a critical concentration was reached and the T_g-concentration curve plateaued off. Within the short and long chain polymethyl methacrylate studies, T_8propyl-methacrylate$_8$ was able to be well dispersed as individual molecules until 10% loading where significant phase separation was observed. The presence of POSS within these blends resulted in a higher proportion of free-space within the structure, producing a lower T_g. Through the agglomeration of POSS cages, the transition temperature decreased due to the liberation of free-space within the blend. In more recent years, a number of further publications have been released on the topic of blended POSS systems, investigating the interplay of phase separation and inter-molecular interactions on composite material properties. [80–83]

A. Striolo *et al* have published a number of articles on the atomistic simulation study of blended POSS with hexadecane, hexane and poly(dimethylsiloxane) matricies.[69, 84, 85] These works have primarily focused on small POSS species and their aggregation and transportation behaviour. Effective potentials between POSS molecules have been determined over a range of temperatures and POSS atomic site radial distributions have been calculated with a view to developing coarse-grained models.

Q. Zhang *et al* have published an article on T_8*iso*-butyl$_8$ polymethyl methacrylate (PMMA) blended systems.[86] This work sought to understand the transport properties of diatomic molecules (O_2 and N_2) through the blend. At lower concentrations, the well distributed POSS molecules acted as a plasticizer, producing a lower density system than the pure PMMA. Interestingly, the mobility of PMMA increased with concentration of POSS. This behaviour was due to an increase in amorphous PMMA regions, enabling a higher degree of molecular mobility. The diatomic molecules also exhibited a higher degree of diffusivity with T_8*iso*-butyl$_8$ concentration up to 14.85%. In a very recent paper by Young *et al*, exper-

imental, all-atom and coarse-grained simulation methods have been utilised to investigate the glass transition temperature as a function of POSS structure. This study considered a poly(2-vinylpyridine) matrix and variably functionalised aminophenyl POSS. The calculated degree of hydrogen bonding between polymer and POSS was then hypothesised to be related to the observed enhancement of the T_g.

Within this chapter, I have reviewed many aspects of the published literature surrounding POSS. This has included the chemical and physical properties, synthesis and the computational study of pure POSS systems. I have also covered POSS in nanocomposite materials and the effect these systems have on polymer matrices. In the following results chapters, I have studied a variety of POSS systems, in pure and nanocomposite environments. In doing so, the POSS-POSS interaction and behaviour, as well as the POSS-polymer interaction, have been analysed. By studying pure POSS systems, the molecular mechanisms that contribute to the observed macroscopic properties can be defined. This is important as agglomeration and phase separation of POSS species has proved to be a common observation in nanocomposite systems. As such, studying pure POSS systems has a direct link to their presence within nanocomposite systems in tandem with the successfully blended and grafted nanocomposite systems. As discussed within this chapter, the computational study of POSS species containing flexible R groups has been limited. Indeed, the computational study of amorphous POSS is scarcely reported. This gap in the literature has motivated the focus of this project on methacrylate functionalised POSS species. This variant of POSS is readily available and has been the subject of many articles featuring POSS nanocomposites.[87–89] To compliment the study of these systems, different conformations of tetra methacrylate functionalised POSS have also been studied to characterise the contribution from the organisation of R groups can affect the molecular and macroscopic behaviour. The use of methacrylate functionalised POSS has facilitated the study of blended and grafted nanocomposite systems, thus enabling a diverse range of systems and properties to be charac-

terised. This has resulted in the generation of novel insights into POSS systems and selected nanocomposites.

In the following chapter, I present the simulation methodology I have used to conduct my study into POSS systems. Then I move onto the results chapters for this thesis in which comprise simulation studies of POSS systems and polymer-POSS nanocomposites.

Chapter 3

Computer Simulation Methodology

Within this chapter, I describe the method of Molecular Dynamics (MD) simulation and the key principles that are associated with this technique. I also discuss some of the analysis routines I have generated for the characterisation of POSS systems.

3.1 Molecular Dynamics Simulation

MD is a computational technique that allows me to describe and analyse the motion of particles, atoms and molecules through time. The progression of such simulations is commonly referred to as the time evolution. MD Simulations are able to progress the behaviour of many body systems in time by numerically and computationally solving integrals of the Classical equations of motion shown in equation 3.1 and 3.2 where $\mathbf{F}_i$ is the force acting on particle i, $-\nabla_{ri}U$ is the negative change in the potential energy, m_i is the mass and $\mathbf{a}_i$ is the acceleration of particle i.

$$\mathbf{F}_i = -\nabla_{ri}U \tag{3.1}$$

$$\mathbf{F}_i = m_i\mathbf{a}_i \tag{3.2}$$

Through this, 3-dimensional trajectories for each particle may be stored and analysed in, for example, a time averaged manner. It should be noted that for very large systems or time

scales, individual hypothetical particles may be used to represent many atoms or molecules through a process called coarse-graining. In this work though, I focus solely on atomistic simulations. The generic work flow for the production of a successful simulation is quite ubiquitous and is shown in figure 3.1.1.
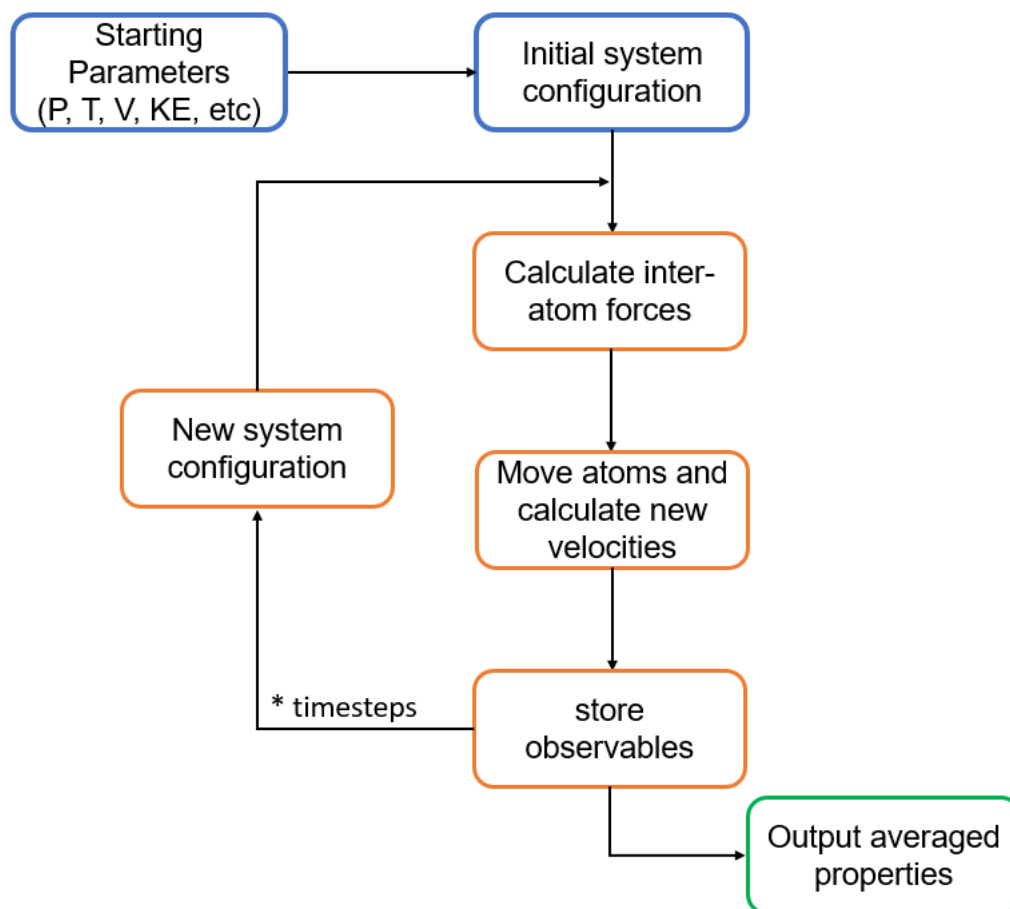
Figure 3.1.1: A flow diagram to represent the general procedure undertaken during an MD simulation where P, T, V and KE represent pressure, temperature, volume and kinetic energy respectively

3.2   System Initialisation

Prior to an MD simulation taking place, a starting configuration of the system must be constructed with initial velocities assigned to each atom. Starting positions are generally systematically distributed in a 3D cubic lattice at a low density to ensure that overlaps do

not occur, therby preventing the occurrence of unrealistic and potentially simulation break-
ing forces. Such starting configurations have become straightforward to generate through
Software such as Packmol and the solvation functionality of DL_FIELD.[90, 91] Initial ve-
locities can then be assigned. Typically, this is achieved by random allocation according to
a Maxwell-Boltzmann distribution (equation 3.3) with velocity scaling in accordance with
the user-requested temperature. Within this equation, $f_{MB}(T)$ is the fraction of particles at
velocity v, m is the atomic mass, T is the temperature and k_B is the Boltzmann constant.

$$f_{MB}(T) = \left(\frac{m}{2\pi k_B T} \right)^{\frac{3}{2}} e^{-\frac{mv^2}{k_b}} \tag{3.3}$$

3.2.1   Force-Fields

With the starting configuration in place, it is necessary to identify a set of parameters for the
interactions occurring between atoms; this collection of parameters is known as a force-field
which enables the calculation of the overall potential energy. Due to the nature of atomistic
simulation, explicit molecules are common place, meaning multiple types of inter- and intra-
molecular interactions must be described. Within generic atomic force-fields, bonding, bond
angle, dihedral angle, Van Der Waals and Coulombic interactions are typically incorporated.
More complex and specialised force-fields may contain additional parameters, such as the
CHARMM force-field that contains a term to constrain out of plane bending.[92]

To model molecules with atomistic MD, covalent bonding must be represented. for every
bonded pair, there is an average bond length that depends on the nature of the chemical envi-
ronment. Considerations such as the types of atoms within the bond, their hybridisation and
their direct neighbours are taken into account when characterising the bond behaviour. To
model this type of intra-molecular interaction, two functional forms are commonly utilised,
the harmonic potential or the Morse potential. The harmonic function is the simplest (equa-
tion 3.4) where r_{ij} is the distance of separation between atom i and j, r_0 is the equilibrium

bond length and k_b is the force constant. Figure 3.2.1, presents the a shape of a harmonic potential and illustrates the variables where the equilibrium bond length is 1.34 $\mathring{A}$. Alternatively, the Morse potential may be used, as shown in equation 3.5. Here, α describes the bond stiffness and D_e describes set the bond energy. In many cases, the Morse potential is considered overly complex and an unnecessary use of computational resource.

$$V^{bond}(r_{ij}) = k_b(r_{ij} - r_0)^2 \tag{3.4}$$

$$V^{bond}(r_{ij}) = D_e(1 - e^{-\alpha(r_{ij}-r_0)})^2 \tag{3.5}$$

(a)   (b)
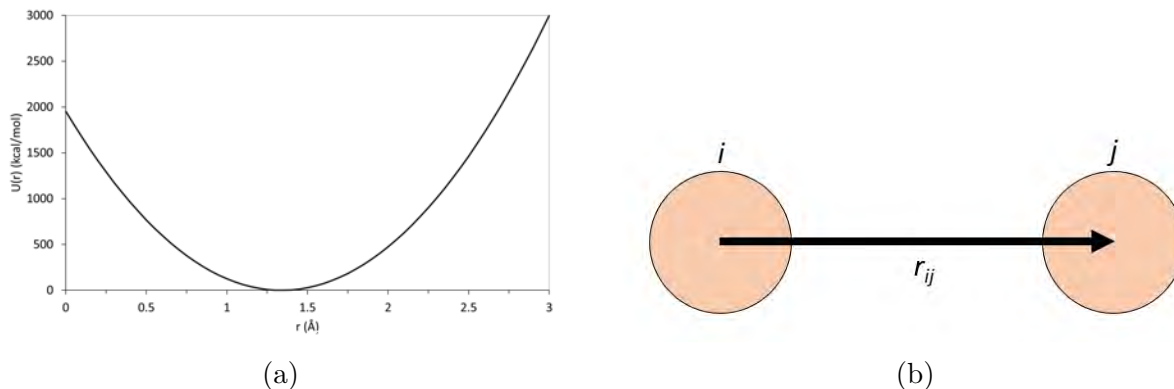
Figure 3.2.1: The form of the harmonic potential for a single bond (a). Illustration to depict bonding interaction between two atoms.

In addition to covalent bonds, bond angles must be represented. This type of potential effectively accounts for the arrangement of electron orbitals about the contributing atoms to model the observed angle between these atoms. An equilibrium angle exists for any given group. In simulation, fluctuation about this angle is determined by a potential. These bond angles can be modelled using the same approach as bond lengths; through the harmonic or Morse potential. Equation 3.6 describes the harmonic potential for bond angle where θ is the measured bond angle, θ_0 is the equilibrium bond angle and k_a is the force constant.

Figure 3.2.2 illustrates the harmonic angle potential where θ_0 is 112.3^o.

$$V^{angle} = k_a(\theta - \theta_0)^2 \tag{3.6}$$

(a)

(b)
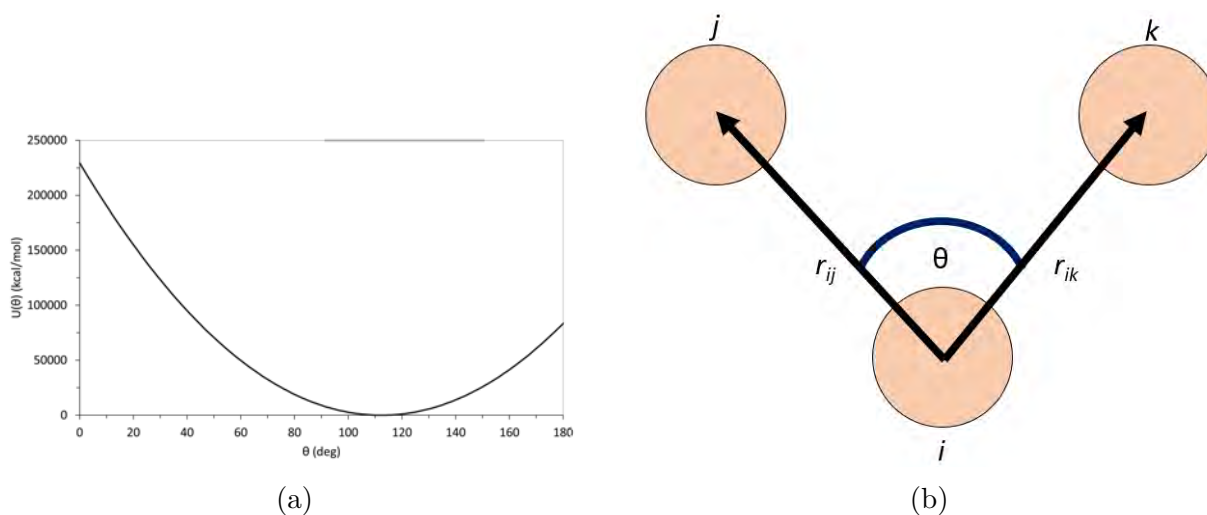
Figure 3.2.2: The form of the harmonic potential for a bond angle (a). Illustration to depict bond angle between three atoms and the associated terms.

A function to describe dihedral torsion, or twisting about a bond, is generally included as a means to model molecular structure. In nature, a bond may be double or triple bonded, thereby preventing dihedral rotation. Equally, the nature of the neighbouring groups may influence the dihedral behaviour of a single bond. Typically, to model dihedral torsion, an expanded Fourier series is used (equation 3.7) where ϕ is the dihedral angle and k_n^d is the dihedral force constant. Figure 3.2.3 illustrates equation 3.7 and the terms included within the equation.

$$V^{dihedral} = \sum_{n=1}^{3} k_n^d(1 - cos(n\phi)) \tag{3.7}$$

(a)   (b)
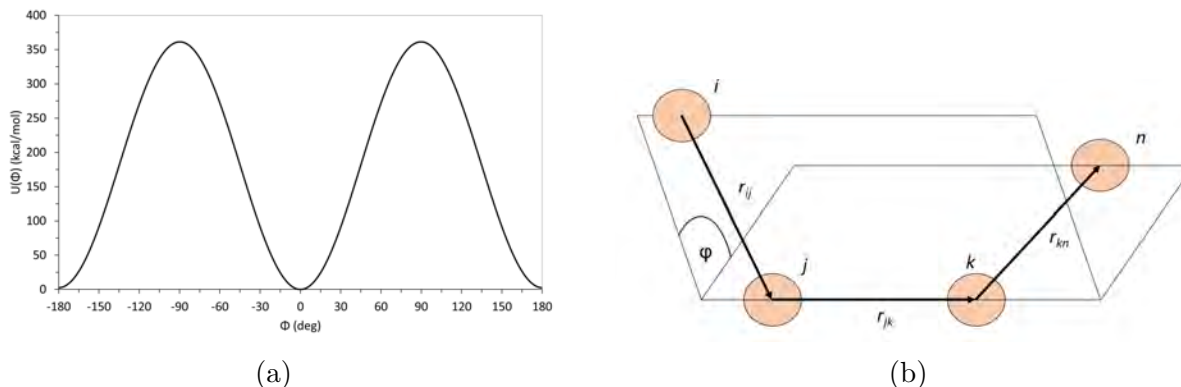
Figure 3.2.3: The form of the quartic potential for a dihedral angle about a single bond (a). Illustration to depict dihedral structure between four atoms and the associated terms.

Inter-molecular and non-bonded interactions must also be considered. In an atomistic molecular system, these include Van der Waals and Coulombic contributions. Van der Waals forces account for three types of mid-range interaction, including induction (Debye) forces, orientation (Keesom) forces and dispersion forces. Collectively, these forces act attractively over a range of distances for any atomic pair. Debye forces arise in atomic pairs with a permanent electron dipole inducing a dipole within another atomic pair, creating a mutual attraction. Keesom forces arise due to the rotation and change in orientation of permanent dipoles about one another. These forces are distinct from those acting between two orientationally locked dipoles, which varies with $\frac{-1}{r^3}$ where r is distance. Finally, and perhaps most importantly, dispersion forces, or London forces, form a part of the Van der Waals forces. This type of force is exhibited in non-polar and polar pairs of atoms. The moment to moment change in electron density within the atomic electron shells generates a change in the electic field, which has a polarizing effect on the distribution of electrons of other atoms. The consequent generation of instantaneous dipole pairs across space leads to a net attractive force.

All three of the VDW terms vary with $\frac{-1}{r^6}$ where r is distance.[93, 94] To model this type of interaction, it is convenient to use the Lennard-Jones Type equation, as shown in equation

3.8 and Figure 3.2.4, which incorporates the attractive $\frac{-1}{r^6}$ van der Waals forces in conjunction with a short-range repulsive $\frac{1}{r^{12}}$ contribution where ϵ is the depth of potential well and σ is the distance of separation at which the inter-particle potential is 0. This repulsion effectively represents the overlap of occupied electron orbitals between atoms in close proximity, as described in the Pauli exclusion principle. The use of a $\frac{1}{r^{12}}$ repulsive term is principally pragmatic, due to the computational efficiency of calculation as the square of the $\frac{1}{r^6}$ term.

$$V_{LJ} = 4\epsilon_{i,j} \left[\left(\frac{\sigma_{ij}}{r_{ij}} \right)^{12} - \left(\frac{\sigma_{ij}}{r_{ij}} \right)^6 \right] \tag{3.8}$$
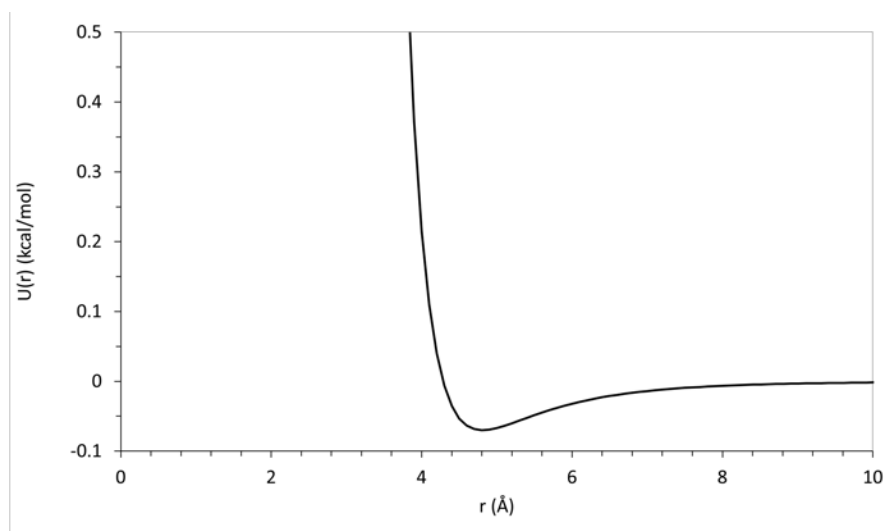
Figure 3.2.4: 12-6 Van der Waals potential

Electrostatic forces are also typically considered for atomistic MD. electrostatic interactions between charged particles can achieved through a standard Coulombic potential, as illustrated in equation 3.9 and figure 3.9, where q_i and q_j represent the point charges of atom i and j respectively. The form of this potential is shown in figure 3.2.5.

$$V_{Coul} = \frac{q_i q_j}{r_{ij}} \tag{3.9}$$
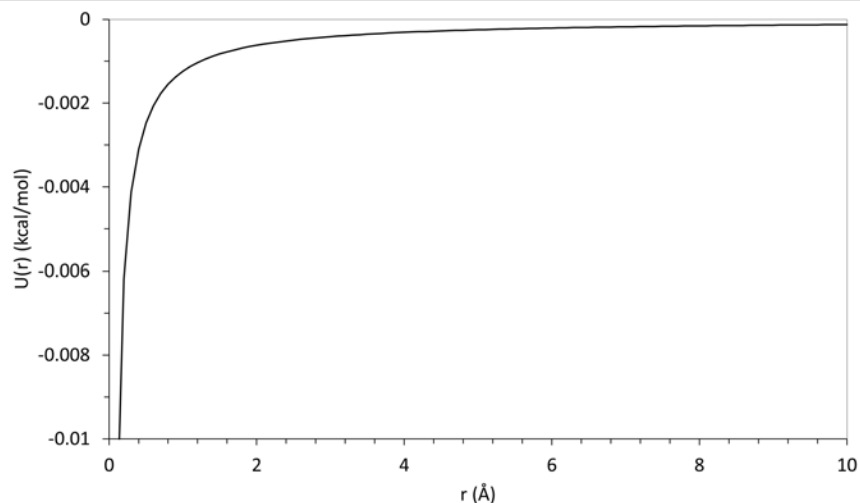
Figure 3.2.5: Form of Coulombic potential between atoms of opposite charge.

Within molecular systems, it is common for the atoms of a covalent bonds to be non mirror images of one another, that is to say that the distribution of electrons within a bond is likely to be polarized due to the difference in electronegativity. This generates regions of higher electron density and lower electron density across a bond. This principle can be expressed in MD through allocating partial charges to atoms to represent the dispersion of electron density as electrons are not explicitly considered.

Throughout this thesis, I have principally used the polymer consistent force-field (PCFF) developed by H. Sun *et al* for the purpose of simulating polycarbonates. The energetic and electrostatic properties for this force-field were derived from *ab initio* HF/6-13G* calculations that have been scaled to fit experimental data for a number of organic compounds.[95]

Equation 3.10 shows the functional form of the PCFF force-field.

$$
\begin{aligned}
V(r) = &\sum_{bonds} [k_2^b(r-r_0)^2 + k_3^b(r-r_0)^3 + k_4^b(r-r_0)^4] + \\
&\sum_{angles} [k_2^a(\theta-\theta_0)^2 + k_3^a(\theta-\theta_0)^3 + k_4^a(\theta-\theta_0)^4] + \\
&\sum_{dihedrals} [k_1^d(1-cos\phi) + k_2^d(1-cos2\phi) + k_3^d(1-cos3\phi)] + \\
&\sum_{inversions} [k^i(\omega-\omega_0)^2] + \\
&\sum_{\substack{(i,j) \\ vdw}} \epsilon_{i,j} \left[2\left(\frac{\sigma_{ij}}{r_{ik}}\right)^9 - 3\left(\frac{\sigma_{ij}}{r_{ij}}\right)^6 \right] + \sum_{\substack{(ij) \\ Coul}} \frac{q_i q_j}{r_{ij}}
\end{aligned}
\tag{3.10}
$$

As shown, the bonding and bond angle potentials use a quartic Fourier expansion of the harmonic function. The dihedral potential also uses an expanded Fourier series potential. In addition, PCFF incorporates an inversion potential. This type of potential are required for functional groups that contain three atoms surrounding a central atom in a particular arrangement. For example, in a trigonal planar arrangement, if the central atom is permitted to pass through the trigonal plane, a new arrangement has formed. This potential imparts a restriction on this type of transformation. Figure 3.2.6 illustrates the inversion harmonic potential and origin of the ω term within the equation. Van der Waals interactions have been represented through the 9-6 Lennard Jones potential and Coulombic interactions through the Coulombic potential.
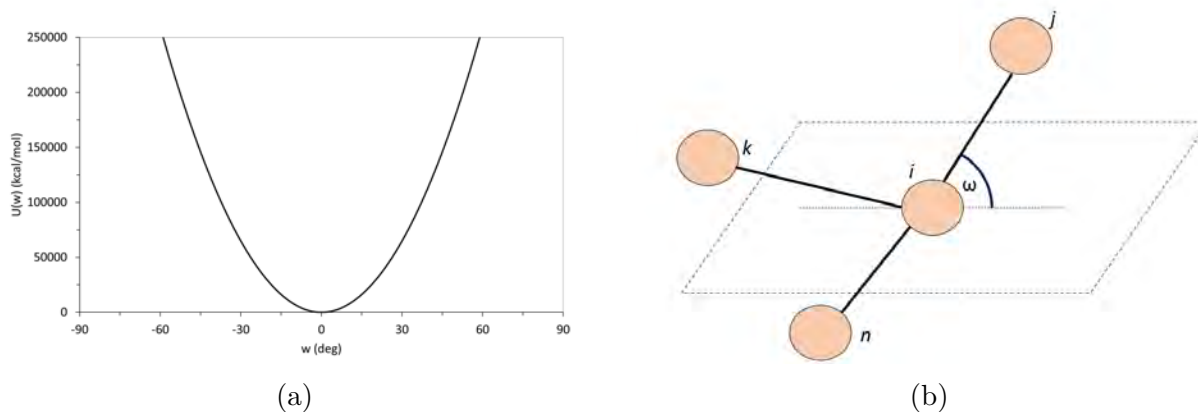
Figure 3.2.6: The form of the harmonic potential for out-of-plane bending interaction (a). Illustration to depict out-of-plane bending (b).

Within this work, the cross-terms from the original PCFF publication have been omitted. This has been carried out as the parameterisation of these terms would have required significant effort and time as they are not supplied in the default implementation of DL_POLY. For this project, the use of a force-field that was transferable enough to represent POSS species in pure and nanocomposite context has been required. This has necessitated the use of a general force-field capable of representing a variety of systems. In addition, the ligands of POSS species are typically quite short and the POSS cage is very rigid. As such, there is little variation in the bond lengths and bond angles. Thus, the necessity for cross-terms is redundant.

In the series of tables given in appendix A, the force constants and equilibrium values used for each potential in PCFF are provided. A key to understand the atom types has been included in appendix A.1. Within the following section, the methods of progressing a simulation through time is discussed.

3.3 Integration Algorithm

MD simulation is founded on the ability to progress the system through time. This principally involves the numerical integration of the Classical equations of motion. Through this, the velocities, accelerations, positions etc at time t are updated in the context of a discrete forward step to time $(t+\Delta t)$. This resultant updated configuration then becomes aligned with a new time t and the process to update to $t + \Delta t$ is repeated iteratively over a given number of timesteps. To do this efficiently and computationally, there are 3 common methods; the Verlet, Leap-frog and velocity-Verlet algorithms. The Verlet method for progressing the atomic positions in time is summarized in equation 3.11 where $\mathbf{a}$ is the acceleration, $\mathbf{r}$ is the vector of the atomic position, t is the time and Δt is the timestep.[96]

$$\mathbf{r}(t + \Delta t) = 2\mathbf{r}(t) - \mathbf{r}(t + \Delta t) + \Delta t^2 \mathbf{a}(t) \tag{3.11}$$

This method has been shown to achieve energy conservation, be time-reversible and numerically stable. However, the algorithm omits the determination of velocities from the calculation of the positions due to the nature of its derivation from a second-order differential equation. This presents a problem when calculating the Kinetic and Total energy, as an extra equation is required, so reducing efficiency. To address this deficit, the Leap-frog method was proposed (equations 3.12, 3.13 and 3.14).[97]

$$\mathbf{v}(t + \frac{1}{2}\Delta t) = \mathbf{v}(t - \frac{1}{2}\Delta t) + \Delta t^2 \mathbf{a}(t) \tag{3.12}$$

$$\mathbf{r}(t + \Delta t) = \mathbf{r}(t) + \Delta t \mathbf{v}(t + \frac{1}{2}\Delta t) \tag{3.13}$$

$$\mathbf{v}(t) = \frac{1}{2}\mathbf{v}(t + \Delta t) + \mathbf{v}(t - \Delta t) \tag{3.14}$$

With this method, the vector of atomic positions ($\mathbf{r}$), accelerations ($\mathbf{a}$), mid step velocities $\mathbf{v}(t - \frac{1}{2}\Delta t)$ and full step velocities ($\mathbf{v}$) are stored. The first step of this method is equation 3.12

which generates the new mid step velocities to allow equation 3.14 to generate the current velocities while equation 3.13 generates the next positions. The inclusion of the velocities within the integration algorithm has practical benefits in simulation as they are often scaled with temperature and the associated Kinetic energy.

The Velocity-Verlet algorithm, the most recent of these procedures, has demonstrated good energy conservation and numerical stability.[98] Again it is an adaptation of the Verlet algorithm that generates positions, accelerations and current velocities. In contrast to the Leap-frog method, the updated positions ($\mathbf{r}(t + \Delta t)$) are calculated (equation 3.16) before the mid-point velocities (equation 3.15). Between these steps, the forces and accelerations ($\mathbf{a}$) are calculated and, finally, the new velocites ($\mathbf{v}(t + \Delta t)$), as shown in equation 3.17. The Kinetic energy and Total energy can then be calculated.[99] As I am concerned with atomic systems, I am solely concerned with translational motion, although the Velocity-Verlet algorithm has been extended to account for the rotational motion of rigid bodies.

$$\mathbf{v}(t + \frac{1}{2}\Delta t) = \mathbf{v}(t) + \frac{1}{2}\Delta t^2 \mathbf{a}(t) \tag{3.15}$$

$$\mathbf{r}(t + \Delta t) = \mathbf{r}(t) + \Delta t \mathbf{v}(t + \frac{1}{2}\Delta t) \tag{3.16}$$

$$\mathbf{v}(t + \Delta t) = \mathbf{v}(t + \frac{1}{2}\Delta t) + \frac{1}{2}\Delta t \mathbf{a}(t + \Delta t) \tag{3.17}$$

For these simulations, I have primarily used the Velocity Verlet algorithm as implemented within the MD software DL_POLY_4.[100] This general purpose MD package has been developed at the Daresbury Lab as part of the UK's Collaborative Computational Project on Molecular Simulation (CCP5) by W. Smith and I. T. Todorov and is free for academic use. The package contains many features for MD simulation including a capacity to simulate many different systems, such as metals, zeolites and organics and a variety of force-fields and boundary conditions. To describe the interactions for these system, Dl_POLY_4 does

not have its own force-field but is, instead, designed to allow the user to define their own potentials. This may take the form of, for example, the GROMOS or Dreiding force-field, however the user is able to impose additional parameters, such as rigid units.[101, 102]

DL_POLY_4 is written in FORTRAN and is fully modularised into subroutines. The program is designed to be executed on a multi-core processor with distributed memory. This particular version of DL_POLY utilises the Domain decomposition method for paralellisation of the executed code. DL_POLY_4 is the successor to the MD package DL_POLY_Classic which utilises a different method to exploit parallel programming. This form of DL_POLY is still available as the method is more efficient for smaller system sizes.[103]

3.4   Partial Charge Calculation

To generate the partial charges for all of the atoms for each molecule, I have employed a number of different computational techniques, including density functional theory (DFT) and the calculation of restrained electrostatic potential (RESP) charges. Within this work, the DFT methodology has been utilised to generate files that contain information regarding the molecular orbitals, vibrational frequencies and cartesian eigen-vectors, known as .molden files. To achieve this, I first start with a molecular structure that has been optimised with PCFF. The Cartesian coordinates for the optimised structure are then passed to the *ab initio* quantum chemistry program Orca where single point calculations are performed at the PBE0 level of theory with the D3BJ dispersion correction and def2-sVP basis set.[104] Of course, ideally, a full geometry optimisation from DFT methodology would be undertaken. However, some of the smallest molecular systems I have considered through this project are quite large at the size of 104 atoms, and because DFT is generally recognised to scale with $O(N^3)$ where N is the number of atoms or electrons, the method of pre-optimising with PCFF has been used, essentially as a compromise to account for the available computational resources. The

.molden file is then passed to the wavefunction analysis software Multiwfn to produce the RESP charges.[105] This method of fitting RESP charges is quite appropriate in this case as the flexible nature of the organic functional groups of the POSS system means there will be degrees of chemical equivalency, for instance, the hydrogen atoms of a methyl group. The RESP charges are calculated by considering many ESP fit conformations such as those from the CHELPG scheme.[106, 107]

3.5   System observables

In order to quantify and measure the behaviour of a molecular system in the context of a macroscale material, it is important for me to take measurements of both local behaviours and multi-molecule thermomechanical properties. Also, from a practical point of view, it is quite useful to monitor properties such as the Kinetic and Potential energy, pressure, temperature etc to understand whether the simulation is progressing as intended.

The total kinetic energy is defined as the sum of the kinetic energy of each particle (equation 3.18) where N is the number of particles, $\mathbf{v}_i$ is the vector describing the velocities in the x, y and z directions and m is the atomic mass. As I am only concerned with an atomistic system, I do not consider the rotation of any particle. This allows me to define the total kinetic energy as it is in classical mechanics.

$$E_{Kinetic} = \sum_{i=1}^{N} \frac{m\mathbf{v}_i^2}{2} \tag{3.18}$$

The total potential energy describes the sum of all pair wise potentials within the system, including all inter and intra-molecular potentials described in the force-field section. By summing the total Kinetic and Potential Energy, I can calculate the Hamiltonian for the whole system, which must be maintained when simulations are carried out in the NVE ensemble. The equipartition function allows me to characterise the system temperature

from the time average total Kinetic Energy (equation 3.19) where K_b is the Boltzmann constant, T is the temperature and N is the number of particles.

$$< E_{Kinetic} >= \frac{3}{2} N K_B T$$

(3.19)

This measurement is crucial when simulating in the NVT ensemble as temperature must be maintained. In this ensemble the pressure is free to fluctuate and can be calculated through the Virial theorem,

$$P = \frac{1}{3V} \left(N K_B T + \sum_{i=1}^{N} \sum_{j<i}^{N} \mathbf{F}_i \cdot \mathbf{r}_i \right)$$

(3.20)

where P is the pressure, V is the system volume, N is the number of particles, K_B is the Boltzmann constant, T is the temperature, $\mathbf{F_i}$ is the force vector for particle i and $\mathbf{r_i}$ is the position vector for particle i. In many simulations, the Canonical ensemble (NVT) is used where the number of particles (N), the volume (V) and temperature (T) remain constant.

3.6   Simulation procedure

MD has been the principle means of study for the thermomechanical properties of POSS species. The MD simulation suite DL_POLY has been used throughout these studies. DL_POLY is a parallel package that provides efficient implementation of MD methods within a high performance computing (HPC) cluster. Production phase cooling sequences and annealing procedures have been carried out in the Nose-Hoover isothermal-isobaric *NPT* ensemble. Here, the number of particles (N), pressure (P) and temperature (T) are kept constant, enabling the system volume to self-adjust. Periodic boundary conditions have also been implemented.

As discussed in section 3.2.1, PCFF has primarily been used to describe the inter- and intra-molecular interactions during simulation. Here, quartic harmonic functions are used to

describe the bond and bond angle behaviour. Dihedral torsion is described through a quartic harmonic cosine function. Van Der Waals interactions are represented through a Lennard-Jones 9-6 potential. Coulombic interactions have been considered through the use of partial charges and the Ewald summation method. Equation 3.10 provides the full functional form of PCFF.

Simulation cells consist of a given number of molecules. This number changes depending on the system being studied. The starting molecular structures have been designed in the Biovia software Discovery Studios and optimised with the PCFF Force-field.[102] Packmol has been used to populate the simulation cell with the given number of optimised structures. Initially, low density systems are generated. In doing so, Packmol prevents molecules from overlapping, which can potentially lead to non-physical, and simulation breaking, interactions. Simulation cells are firstly annealed at high temperature. This has been carried out at a starting temperature of 700 K, with 100 K decrements until 500 K. From here, the system is cooled to 450 K and decremented by 10 K until the production phase begins at 400 K. For each temperature, the simulation has been carried out for 500,000 timesteps, with a step interval of 0.001 ps. The first 250,000 time steps have been used for structural equilibriation in the canonical (NVT) ensemble. Long range interaction cutoff distance has been set to 12 $\mathring{A}$ and Ewald precision set to $1x10^{-6}$.

3.7   Practical Aspects

3.7.1   Periodic Boundary Condition

In real world experiments, the number of particles is usually of the order 10^{23}, which would describe 12.01g of carbon. In MD studies, a simulation with a number of particles on this scale would be far too computationally expensive to be viable - typical simulations are considered large when of the scale 10^6. If the simulation boundaries were to be hard and

repulsive, then the particles near to the boundary would experience a significantly different environment to those in the centre of the simulation box. To over come both of these problems, periodic boundary conditions are often employed. Where a particle trajectory leads it to travel across the boundary, its image would instead appear on the opposite side of the simulation box; as if a replica of the simulation box had been adjacent to itself. This boundary type gives the impression of repeated simulation cells in x, y and z positive and negative axes. Figure 3.7.1 depicts a visual representation a system of T_8 POSS subject to periodic boundary condition.
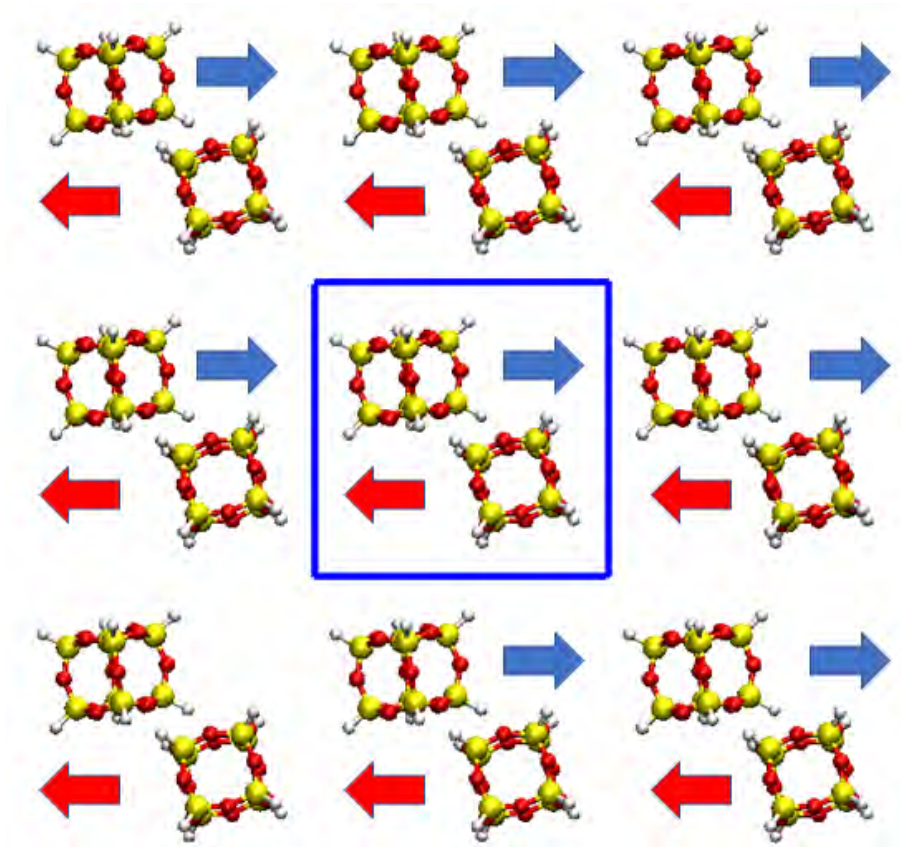
Figure 3.7.1: Depiction of two T_8 POSS cubes within a blue cubic simulation cell exhibiting the effects of the periodic boundary condition.

However, the use of periodic boundary conditions introduces new problems in that, when calculating interaction potentials, one must restrict the calculations to particles that are in range for the determination of non-bonded interactions. Without this restriction, a particle

would interact with a repeat image of itself or multiple images of other particles. The minimum image convention accounts for this problem by ensuring that particles only interact with the closest image of the particles within the simulation box. This is achieved through the introduction of a cut-off radius (r_c) for the Van der Waals potentials. In this, after a distance of typically 10Å the cut off is introduced to prevent statistically insignificant forces being calculated, and computational resource being wasted. This distance is calculated to be where the potential reaches about 1% of the well-depth. To implement a the cutoff distance, one must execute a check to determine if two particles are within the cutoff range. This process saves computational resource in that the required number of potential and force calculations is reduced, however, it still involves iteratively checking the distance for all particle pairs within the system. This is another unnecessary computational cost which can be circumvented through use of the Verlet Neighbour list. This involves generation of a list of neighbouring particles at a distance of marginally larger than the cutoff radius. Particles that reside at the limit of the cutoff are then still considered. After the force-loop has been executed and the simulation has progressed for several hundred timesteps, the list can be updated with the new particles that have moved into the proximity of the cutoff, and those that have moved away can be replaced, so as to maintain efficiency.

3.7.2   Thermo and Barostats

Depending on the desired statistical ensemble that is being employed, different parameters may need to be controlled. For instance, to model a Canonical Ensemble (NVT), the temperature must be maintained by controlling the Kinetic energy of the system. Alternatively, if the isothermal-isobaric ensemble (NPT) is desired then both the temperaure and the pressure must be maintained, the latter being controlled by changes in the volume of the simulation cell. The Berendsen thermostat is a simple implementation for temperature control (equation 3.21) that can be implemented within the Verlet algorithm. [108] This

requires calculation of

$$\chi(t) = \left[1 + \frac{\Delta t}{\tau_T} \left(\frac{T_0}{T(t)} - 1 \right) \right]^{\frac{1}{2}} \tag{3.21}$$

Where Δt is the time step, $T(t)$ is the instantaneous temperature, T_0 is the target temperature and τ_T is a user variable which controls the magnitude of temperature readjustment. The value of $\chi(t)$ can be used within the velocity Verlet algorithm to scale the velocities (as shown in equation 3.22) of the particles within the system to those more aligned to the target temperature.

$$v_i(t + \Delta t) = \chi v_i(t + \Delta t) \tag{3.22}$$

The Berendsen Barostat method works by rescaling the simulation box x, y and z axes in a analogous way to the thermostat, using the vairable M(t) calculated as

$$M(t) = \left[1 - \frac{\Delta t}{\tau_P} (P_0 - P(t)) \right]^{\frac{1}{3}}. \tag{3.23}$$

Here, the instantaneous pressure is $P(t)$, the target pressure is P_0 and the user control parameter is τ_P. The Nosẽ-Hoover thermo-barostat has been developed with the equipartition function in mind (equation 3.24).[109]

$$\dot{\zeta} = \frac{1}{Q} \left[\sum_{i=1}^{N} \frac{p_i^2}{2m_i} - \frac{3N+1}{2} k_B T \right] \tag{3.24}$$

$$\frac{\partial \vec{p_i}}{\partial t} = \vec{f_i} - \zeta \vec{p_i} \tag{3.25}$$

In this equation 3.24, the first term in the sum describes the total Kinetic energy for the particles in the system where f_i, p_i and m_i are the ith particle force, momentum and mass respectively. The second term is a constant that describes the target total Kinetic energy for a system of given size and temperature where N is the number of particles, k_B is the Boltzmann constant and T is the target temperature. The second term is then subtracted

from the first and the result scaled by $\frac{1}{Q}$ where Q is a user-controlled parameter.

3.8   Post Run Processing

Within this section, I highlight some of the key analysis methods and subroutines used to characterise this molecular systems. For the purposes of this section, I describe this analysis in context of Hydroxy-terminated polybutadiene (HTPB) polymer. Butadiene is the polymerising monomer that produces HTPB. During the polymerisation process, each joining butadiene unit can connect in one of three conformations, *trans*, *cis* or *vinyl*. The molecular structure of butadiene and a common variant of HTPB, can be seen in figure 3.8.1. In this image I highlight the *trans* conformation in green, *cis* in pink and *vinyl* in purple. This conformation is known as HTPB 311 as the unit cell has 3 trans, 1 cis and 1 vinyl. I have utilised this polymer as part of the current project as an extension to a previous project relating to understanding the molecular mechanisms that lead to the low glass transition temperature in HTPB.[110]
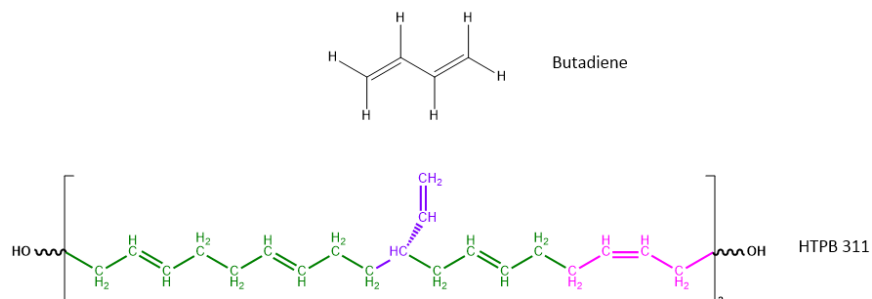
Figure 3.8.1: Molecular structure of butadiene (top) and HTPB 311 (bottom).

To start with, I need to describe a typical simulation, the data I am handling and its layout. For a given temperature, simulations undergo 500 000 timesteps, the first half of which are dedicated to equilibration in the NPT ensemble, while the second half yield data for production in the NPT ensemble. Each time step is 1fs. Once a successful simulation has been completed, DL_POLY provides a number of different output files with information

relating to the system.

The STATIS (statistics) file is accumulated sequentially over the course of the simulation according to a specified drop rate, for example every 200 timesteps. This file provides formatted data describing the instantaneous values for pressure, volume, temperature, total bond energy, enthalpy etc. For isobaric-isothermal simulations, this file is used to calculate the time-averaged volume for a system. From this, I can measure the specific volumes (cm^3/g) of a system. This then offers a route to identification of the glass transition (T_g) temperature.

The T_g of a material describes the temperature at which an amorphous liquid or viscous rubbery material changes to form an amorphous glassy solid.[111] The process of producing a glass typically involves cooling a liquid rapidly to reduce the molecular mobility. With a sufficient cooling rate, the time required for structural relaxation is not met, resulting in a non-equilibrated solid structure.[112] Within this work, I am able to use the specific volume vs temperature relationship to predict T_g as, during a cooling sequence, the specific volume decreases due to thermal contraction. However, as the T_g is reached, the rate of thermal contraction decreases as the system becomes glassy. This produces two distinct regions with different gradients, being a glassy range of temperatures and liquid/rubber range of temperatures. On a specific volume vs temperature graph, I am able to identify the T_g as the temperature at which these regions intersect. Figure 3.8.2 shows an example of a specific volume vs temperature graph and a fit of these data to a bi-linear form. The intersect of the blue and red trend lines then identifies the temperature at which there is a change in phase within the bulk material from plastic to glassy.

This method of T_g prediction is ubiquitous within the field of molecular dynamics.[113, 114] However, there are associated uncertainties with this method. As shown in figure 3.8.2, the T_g is predicted to be a specific value. However, the glass transition can be a process,

rather than a sudden change at a given temperature. As the temperature must be inter-preted, this can lead to differences in the experimental and modelled T_g values. In addition, the gradient change observed for a given system may be quite small, meaning identification of the intersect can be difficult. Also, fluctuation in the determined specific volume can potentially lead to an inaccurate identification of T_g. These uncertainties manifest in the bi-linear plots for T_g prediction. However, agreement in the region of glass transition provides confidence in the model representation.

The T_g is unique to each material and depends on a number of molecular level proper-ties. For polymers, the dependence of T_g on molecular mass has been well studied. In general, the T_g for polymers increases with molecular mass. This is due to the increase in the proportion of chain components over end point components.[115] End point compo-nents have a higher degree of translational and rotational freedom available, meaning that more structural conformations can be taken. This is due to end point components having less physical restraint compared to components within the polymer chain. This degree of restraint is often described as free volume. During the cooling of a polymeric system, free volume decreases until a critical temperature is met. At this temperature, all segmental mobility is lost, resulting in the complete restriction of molecular conformation. This critical temperature is the T_g in polymeric systems. The relationship between T_g and molecular mass has been characterised by the Flory-Fox equation as,

$$T_g = T_{g,\infty} - \frac{K}{M_N},$$ (3.26)

where $T_{g,\infty}$ is the T_g for a polymer of infinitely large molecular weight, M_N is the molecular weight and K is a parameter that relates to the free volume.[116, 117] This equation has been applied sufficiently to a number of different polymers, however it fails for polymers with smaller M_N values.[118] Several alternative equations have been developed for specific

polymer structures.[119]
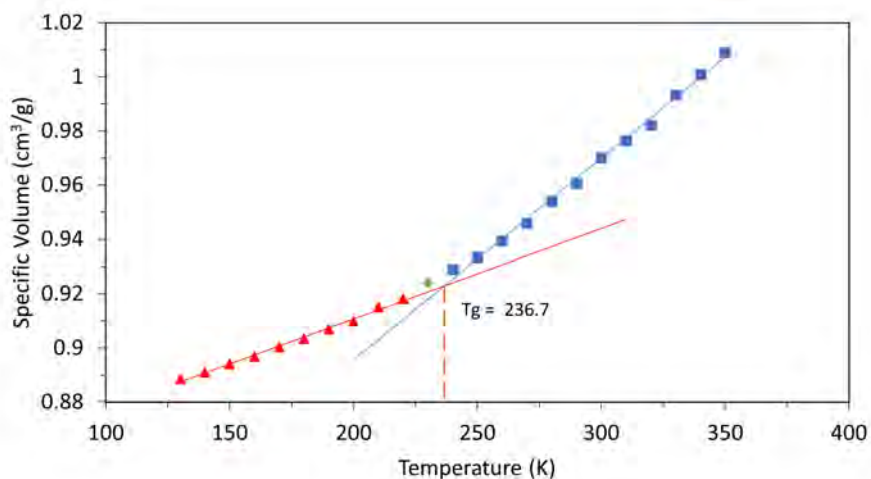
Figure 3.8.2: A typical specific volume vs temperature graph. In this case, I show data from the HTPB 311 system with PCFF description.

In Figure 3.8.2, I observe a linear increment of 10K between each data point. This is due to the typical implementation of a cooling sequence to produce data for a range of temperatures. By sequentially passing the final configuration of each completed simulation to the following temperature, I qualitatively imitate the cooling conditions present in differential scanning calorimetry (DSC) instruments. Quantitatively, cooling rates are much faster in simulation than in experiment, but this is compensated for by the smaller sample size and idealised approach to thermalisation. This method maintains consistency between temperatures and ensures that each starting configuration is near to the target specific density; for which the thermalisation period will adjust for. Prior to the production of this data, the system also goes through an annealing phase where high temperature simulations are conducted which do not yield data. This approach is beneficial for the setup of representative simulations as the systemic memory of the starting configuration is lost; so as not to have any effect on the output data. This is very important for POSS systems in which molecular mobility is very low, even above T_g.

The application of the specific volume vs temperature relationship depends on the prin-

ciple that a material contracts when cooled and expands when heated. This is measured
with the equation,

$$\frac{V}{V_0} = \alpha \Delta T \tag{3.27}$$

where V is the present volume, V_0 is the starting volume, α is the thermal expansion coef-
ficient and ΔT is the change in temperature. In addition to predicting the T_g for a given
system, one may also calculate the thermal expansion coefficient from simulation and ex-
perimental data, thus providing a method to assess the accuracy of a model. However,
unfortunately, it has not been feasible to use this method during the force-field assessment
phase of this project. Primarily, this has been due to the fact that "there is no experimental
value of the thermal expansion coefficient of POSS materials in the open literature".[120]
Within the majority of POSS literature, they are used as nanofillers in blended systems,
rather than as pure systems. In addition, during the synthesis of POSS T_8H_8, it is typical
for the product to comprise a mixture cage structures (e.g. T_8H_8, T_8H_8, T_8H_{10} etc) and
ladder structures. As such, even if thermal expansion coefficient data was readily available,
it may not be applicable to the 100% POSS systems used within this thesis.

The HISTORY file contains the trajectory or time evolution of the system for the given
temperature. In the simplest form, this file contains stacks of indexed elements and the
associated Cartesian coordinates. Figure 3.8.3 shows the first 18 lines of a HISTORY file
for context. These files enable me to visualise the simulations and investigate, by post-
processing, molecular level properties and behaviours based on atomic positions. These files
are crucial for understanding how characteristic bulk level properties manifest from molecular
level details such as structure variance.

```
CoMS from polar transform - HISTORY - by Jacob
0       2       258     126     7542362
timestep   250000     258 0 2              0.001000           250.000000
68.0648846236                  0.0                    0.0
0.0                    68.0648846236                  0.0
0.0                    0.0                    68.0648846236
Cd      1       1       1       1
        -6.447779829568739      15.167235821720627      7.091393379822038
Cd      2       1       1       1
        9.61291677169879        -1.2080388809154503     -30.384323904877437
Cd      3       1       1       1
        26.087793875912215      28.074097179282543      -20.27280330348792
Cd      4       1       1       1
        8.137009053046997       -26.21139216184405      -1.7182503785686367
Cd      5       1       1       1
        16.796756160390853      -1.8641706740312713     10.560130762117033
Cd      6       1       1       1
        -28.51296396676751      -19.061117754916417     -11.004359461579137
```

Figure 3.8.3: The header section from a sample HISTORY file. The first line is a comment for reference. from line 4-6 I see the cubic simulation cell dimensions and for each 'Cd' element, I have an associated index, and directly below each index has Cartesian coordinates

3.8.1   Radial Distribution function G(r)

The radial distribution function is a critical measure for understanding the packing and order within a molecular system. In short, it reports the probability of an atom appearing at a distance of separation from the subject atom. This is achieved by first selecting an atom or atom type and constructing a sphere of radius 'r'. A second sphere is then constructed of radius r+Δr. All atoms of interest within the interstitial region between the two spheres are then counted. This process is then iterated over a range of values to sample the surrounding area of an atom. In conjunction with this, the determined values are normalised by shell volume and averaged over every configuration that forms part of the history file. The radial distribution function can be represented with the following equation:

$$G(r) = \frac{1}{\rho 4\pi r^2 \delta r} \sum_{r_0=1}^{N-1} \sum_{i=2}^{N} \delta(r = |r_0 - r_i|) \tag{3.28}$$

where ρ is the density for the system at a shell radius of r with a shell thickness of dr. Figure 3.8.4 (left) shows a simple 2D array of atoms with the sampling section of the G(r) analysis being carried out on the orange atom with the plotted G(r) values (right).

(a)   (b)
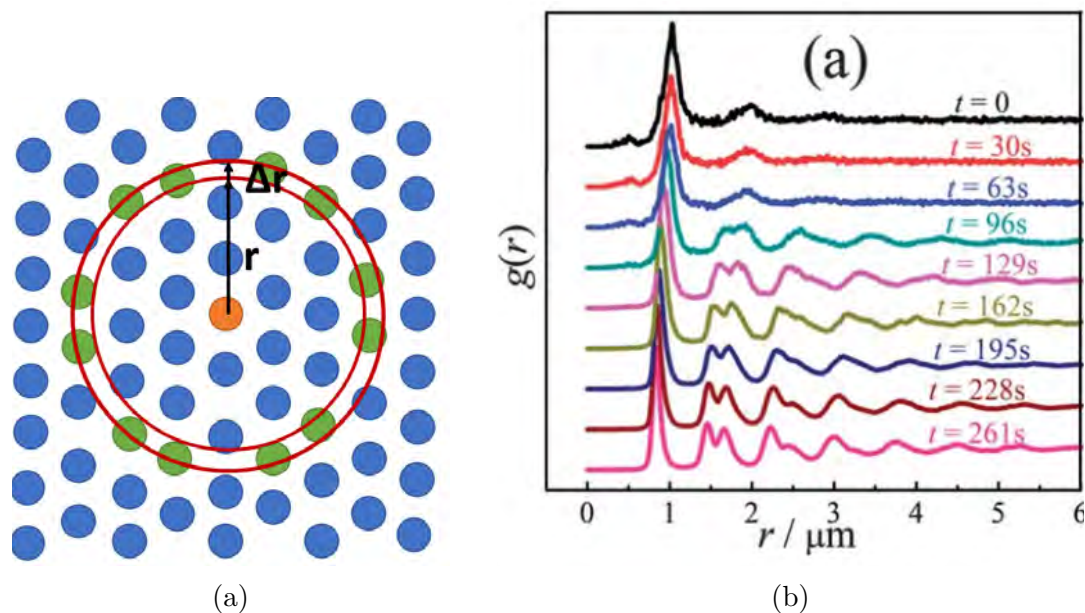
Figure 3.8.4: Left: A simple idealised crystal 2D arrangement of atoms to depict how the sampling of space about the orange atom is carried out during the calculation of the radial distribution function. Right: Radial distribution analysis for idealised hexagonal crystal lattice at t=261s.[121]

The G(r) data is derived from the analysis of the centre of mass for each molecule in this simulation cell. HTPB 311 molecules are linear and flexible, and exhibit movement in the same way a chain might. Each chain link is rigid individually; this is due to the double bond sections through the backbone of HTPB where rotational freedom is restricted. However, the connection between links allows for the chain to be flexible on the macro-scale, as the sp^3 hybridised sections between double bonds allow the HTPB molecule to flex. This behaviour is seen during simulation and shown in figure 3.8.5. Here I show 8 of the 288 total molecules within the simulation cell with hydrogen atoms omitted. I can see that the molecules are heavily entangled with one another in a disordered manner. To add context to the G(r) graph shown in figure 3.8.4, the centres of mass for the given molecules are also shown. Because of this disorder, I do not observe characteristic peaks of ordered packing within the G(r) (not shown). In this case, G(r) analysis does not provide a great deal of information other than to confirm the observed disorder, however, in different systems I can use this analysis to identify long-range and short-range packing features.
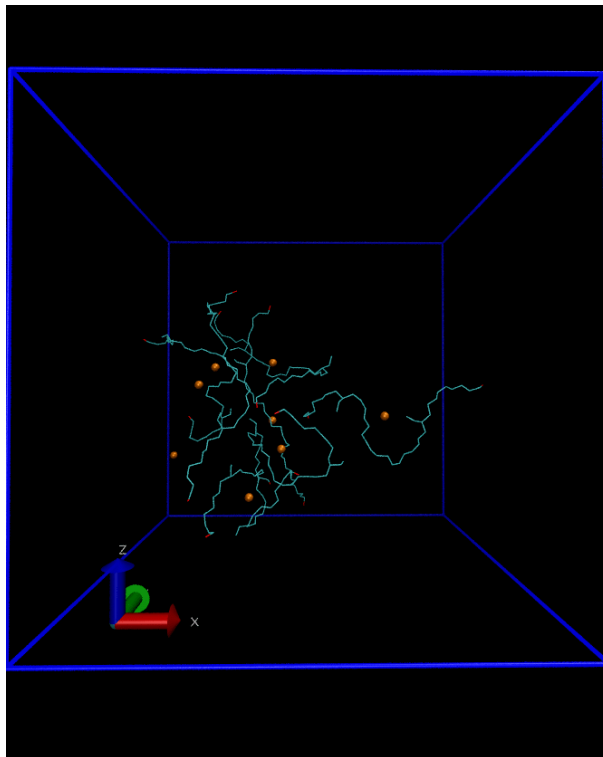
Figure 3.8.5: A visualisation of 8 HTPB 311 molecules in a simulation containing 288 molecules. Carbon and Oxygen atoms are represented by blue and red lines respectively. For clarity, the hydrogen atoms have been omitted. The orange spheres represent the calculated centres of mass for the shown molecules.

3.8.2   Mean squared displacement

Mean squared displacement is a means to study the average displacement of a particle from a given starting position over a range of time. This measure enables me to understand the molecular mobility within a system and make observations on the nature of the system. For example, if the MSD curve undergoes gradual flattening, I can attribute this to the particle existing in a constrained environment. The MSD is calculated according to the following equation:

$$MSD(\tau) = \frac{1}{N_{conf}N_{POSS}} \sum_{t=0}^{N_{conf}} \sum_{i=1}^{N_{POSS}} |x_i(t+\tau) - x_i(t)|^2 \qquad (3.29)$$

where N_{conf} and N_{POSS} describe the number of saved configurations and number of POSS molecules respectively, x is the position of particle i, t is the time and τ is a time interval for

each measurement. Each value of τ is iterated over for all viable timestamped configurations of the simulation.

3.8.3 Voronoi Analysis

As an additional form of structural analysis, I have used 3-dimensional Voronoi investigation. This mathematical method is well studied and provides a number of useful insights such as the number of near neighbours, directionality and molecular volume.[122] In a sample box of molecules, I first determine their centres of mass (CoM) and describe these coordinates as pseudo particles. A cell for each of these pseudo particles is then constructed which contains all of the volume closest to that particle in respect to all other pseudo particles. A simple 2D representation of this can be seen in figure 3.8.6. Here, a straight line is drawn between particles 'G' and 'F' and a hashed bisecting line is passed through it, dividing the area between these two particles equally. This process is then carried out for all near neighbours and where two bisecting lines meet is the location of a vertex for the Voronoi polygon. In 3-dimensions, a straight line is still drawn between near neighbours, however instead of a bisecting line, I form a bisecting area. Intersecting faces then form the 3D cell for each particle.
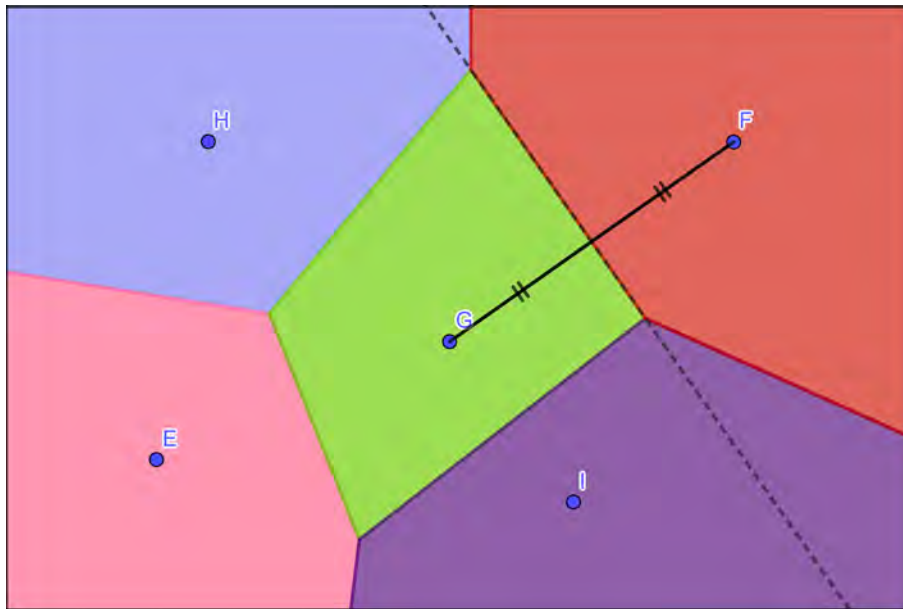
Figure 3.8.6: A simple 2D voronoi diagram where particles 'G' and 'F' have a connecting and bisecting line

The aforementioned methodology is quite rudimentary as it fails to consider the shape of a molecule if I focus solely on the CoM. Molecules may exist in a variety of conformations and shapes; this is particularly true in polymeric systems. Instead, therefore, it may be more appropriate to consider the backbone sites of each molecule and count near neighbours to these as near molecules. This method generates a more accurate description for the molecular volume, though, the development of this type of analysis is quite demanding. Fortunately, the Voronoi diangram software 'Pomelo' is able to conduct this exact analysis. I have employed this software to determine Voronoi properties of the systems as a function of molecular structure.[123]

3.8.4   Moment of Inertia Tensor (MOI)

The moment of inertia can be used to describe molecular shape and, thus, rotation. This property is calculated as the sum of the of the mass of each atom and the square distance of the atom to the centre of mass. For this purpose I consider all molecular atoms to describe how the mass of a molecule is distributed about the centre of mass to achieve an

effective description of the molecule shape. The following equations describe the necessary calculations to determine this symmetrical 3x3 matrix for the MOI.

$$I = \begin{bmatrix} I_{xx} & I_{xy} & I_{xz} \\ I_{yx} & I_{yy} & I_{yz} \\ I_{zx} & I_{zy} & I_{zz} \end{bmatrix} \tag{3.30}$$

where,

$$I_{ij} = \sum_{k=1}^{N} m_k(||r_k||^2 \delta_{ij} - x_i^k x_j^k) \tag{3.31}$$

and N = Number of atoms, k = index of atom, m_k = the mass of atom k, $r_k = (x_1, x_2, x_3)$ the vector of atom k to the centre of mass and δ_{ij} is the Kronecker delta. From this matrix, 3 eigen-values can then be calculated. These values are characteristic of the shape of the molecule and the distribution of its mass. I can calculate these values for each molecule in each configuration and track them over the course of the simulation, effectively generating a history file for the MOI tensor. Figure 3.8.7 shows a plot of these eigen-values over the course of an HTPB simulation at 200K.
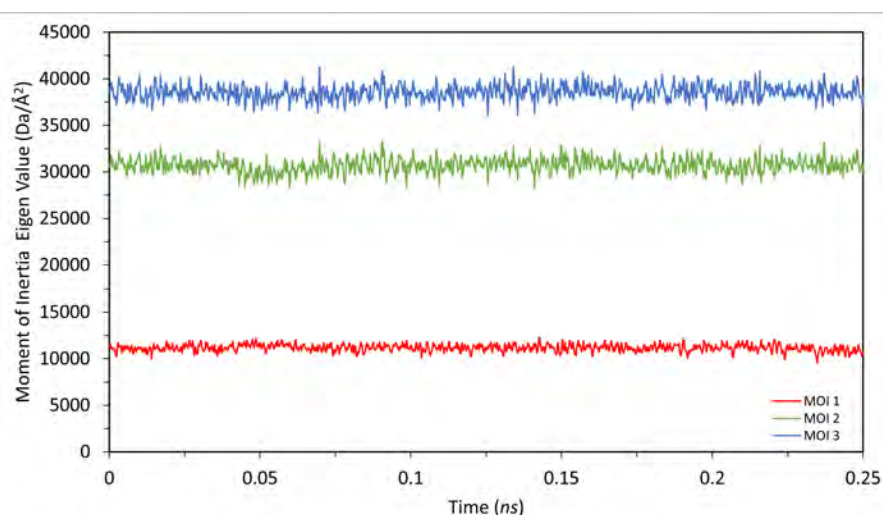
Figure 3.8.7: The moment of inertia eigenvalues for an individual HTPB molecule in during simulation at 200 K.

3.8.5   Dihedral bond Rotation Analysis

This analysis routine was originally developed to investigate the molecular level behaviour of HTPB molecules. HTPB 311 has a low T_g compared to differing conformations of HTPB, and the reason for this was under investigation. As mentioned above, HTPB molecules are highly entangled, even at room temperature, so energy cannot be dissipated through molecular translation; that therefore, is not the mechanism that gives rise to the unusually low T_g. Free dihedral rotation about single bonds is maintained at low temperature, however, allowing the molecules to remain flexible and the bulk material to remain in a plastic phase at lower temperatures. To quantify this information, all dihedral angles within the molecules were monitored and recorded over the course of the cooling sequence of simulation. Between configurations, if the dihedral angle changed above a set threshold ($60°$) a 'rotation' event was noted for that bond. Whilst alternative threshold values could be employed, to achieve qualitative equivalent information, I have utilised 60° throughout since it coincides with a maximum in the dihedral potential and so any rotation beyond that value can be viewed as a switch away from the local dihedral minimum. From this, molecular regions of high rotation activity could be identified as shown in Figure 3.8.8. Here, the average number of rotations per molecule of each single bond are plotted along the backbone of the HTPB 311 molecule. Of course, the recorded frequency of rotations for a bond depends on the threshold angle chosen. From a previous study focused on the analysis of the dihedral rotation of bonds within HTPB molecules, I noted that the frequency of rotations scaled linearly for all bond types across a range of threshold angles (from $0°$ to $180°$ at $10°$ increments).[110]
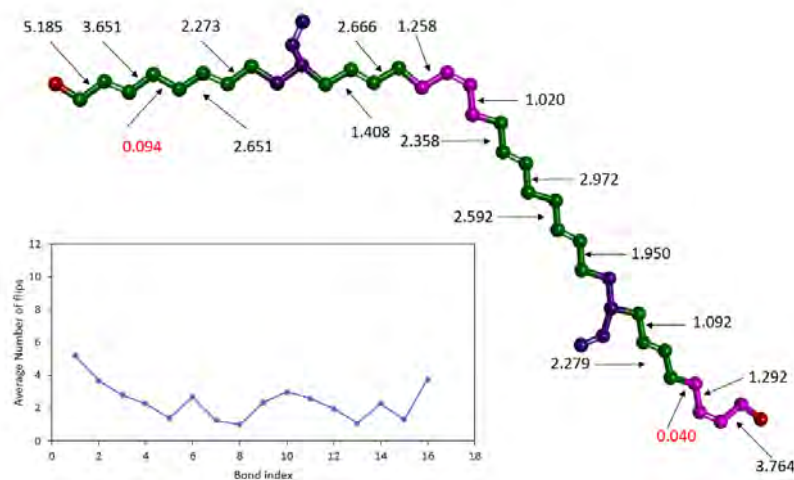
Figure 3.8.8: A depiction of the HTPB 311 molecular back bone with the key rotation 'hotspots' identified for a run at T=310 K. These values represent the average number of rotations per molecule over the course of the simulation. These same data are depicted graphically for all but the non-rotating single bonds.

Further-more, this type of analysis can also be applied to the prediction of the macroscale property of the glass transition temperature in the same fashion as I have previously implemented for synthetic volume. As shown in figure 3.8.9, by summing all dihedral rotations for each temperature over the course of each simulation, bi-linear graphs can be achieved. For HTPB, the intercepts of these lines prove to be an effective molecular-based measure of T_g. [110]
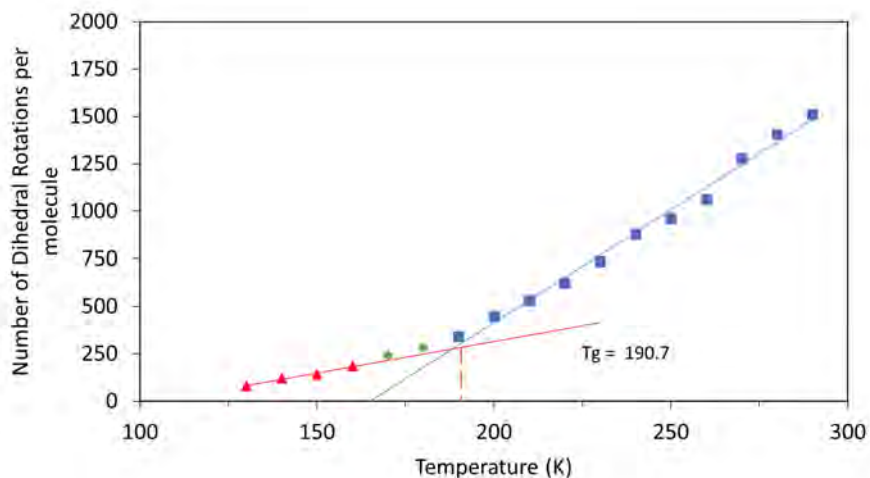
Figure 3.8.9: By using the total number of rotations during simulation, the glass transition temperature was predicted in good agreement with experimental results.

3.8.6   Molecular Rotation Autocorrelation

To characterise the molecular rotation during simulation, I have developed an analysis routine to track the degree of molecular rotation as a time series. To do so, I first determine three independent unit vectors that pass from the Centre of mass of each POSS through three orthogonal faces as shown in figure 3.8.10. These unit vectors are selected by summing the the position vectors of two opposite silicon atoms for the same POSS facet then dividing by the magnitude of the vector. Following this, the dot product is then calculated for each interval of the time series for each vector to produce a complete time autocorrelation function. This data is then averaged for all molecules, as shown within the following equation:

$$A(\delta t) = \frac{1}{N_{conf} N_{POSS}} \sum_{t=0}^{N_{conf}} \sum_{i=1}^{N_{POSS}} \hat{\underline{u}}_i(t).\hat{\underline{u}}_i(t + \delta t) \tag{3.32}$$

where N_{conf} and N_{POSS} describe the number of saved configurations and number of POSS molecules respectively and $\hat{\underline{u}}_i$ describes the unit vector for particle i. To compare the degree of molecular rotation as a function of temperature, I then take the natural log of this data and calculate the gradient of this now linear relationship.
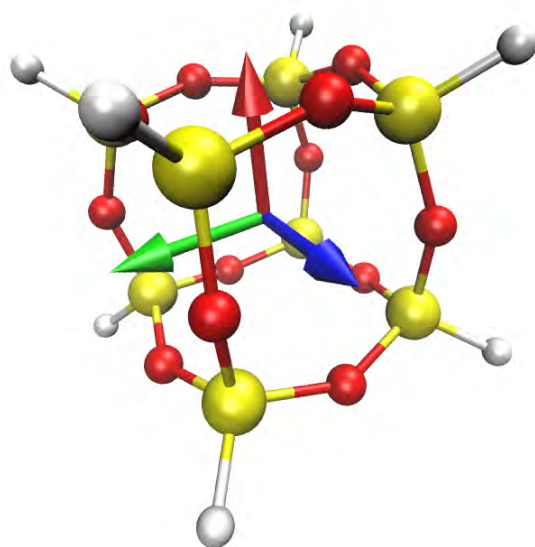
Figure 3.8.10: A rendering of T8 POSS with Hydrogen functionalising groups. The red, green and blue axes within the POSS molecule represent the vectors chosen for the rotation autocorrelation analysis.

Chapter 4

Pure POSS

In chapters 2 and 3, I have discussed key articles from the field of POSS systems and described the methodologies I have implemented throughout this work. Within this chapter, I present results from the simulation of pure POSS systems. Firstly, in section 4.1, I present the results from the validation steps required for the selection of an appropriate force-field for the study of POSS. Following this, in section 4.2, I present results from the systematic study of octa-functionalised POSS species with different but related morphologies. Here, I describe and characterise the structure-property relationship for these species. In the same fashion, I have also systematically investigated tetra-functionalised POSS in section 4.4 and 4.4.2. In contrast to the flexible groups discussed in these sections, I have also simulated in-flexible POSS groups in section 4.3 to diversify my understanding of these systems.

Through the work carried out in this chapter, I aim to elucidate the important molecular features for the prediction of macro-scale properties. Firstly, I consider the capacity to simulate POSS systems through the molecular dynamics method. I analyse the required system size for the accurate representation of bulk behaviour through the methodical studies of different POSS systems. I also characterise the sensitivity of my simulations to molecular detail using systematic analyses of different POSS structures, and the reproducibility of the

simulation results using multiple repeat runs of some systems. Through the inspection of molecular level observations and behaviour, I aim to understand the macro-scale properties from molecular level features.

4.1 Force-field Validation

Force-fields describe a set of parameters and equations to define the potential energy surface for a given molecular system. Chemical diversity is represented through a series of atomic classifications as a product of their environment within the simulation. For example, sp^2 hybridised C=C carbon atoms may be categorised as C_2, and sp^3 hybridised C-C carbon categorised as C_3. Each classification describes distinct parameters, allowing the interactions between different groups to be modelled. Many different force-fields are available for MD simulation, with each targeted to a different region of chemical space through unique equations and parameters. For example, the AMBER force-field is prevalent in the simulation of peptides and DNA as this force-field was parameterised on such systems.[124–126]

Within this project, I have worked to ensure that my simulation models are as representative as possible. To do so, I have selected the most suitable force-field from a number of options. As stated in section 2.2.1, previous MD based studies of POSS have largely used the Compass force-field.[127] However, Compass is a propriety feature within the Materials studios simulation suite of Biovia. I have investigated the efficacy of two different force-fields available to the DL_POLY MD suite for the simulation of POSS, the Polymer Consistent Force-field (PCFF) and the Consistent Valence Force-field (CVFF). PCFF was developed by H. Sun *et al* in 1996 and is the predecessor to the Compass force-field which was later released by the same group in 1998.[127, 128] PCFF and Compass utilise the same functional form and are both second generation force-fields. PCFF was parameterised from the energy surface of a range of molecular functional groups from HF/6-31G* level *ab initio* calcula-

tions. These data were scaled to experimental values from the solid phase. Compass was parameterised from the same *ab initio* data as PCFF with the addition of some functional groups. However, non-bonding Van Der Waals parameters and dihedral terms were scaled to experimental results from the condensed phase. CVFF was first developed in 1988 by Dauber-Osguthorpe *et al* for general use with small molecules including peptides.[129] Of the available force-fields, these were identified as the most suitable due to the inorganic-organic nature of POSS.

To examine these force-fields, I have simulated two chemically distinct POSS systems; the T_8vinyl_8 (OVP) and $T_8phen-ethyl_8$ POSS (OPEP) (Figure 4.1.1). These structures have been selected due to the stark difference in their molecular and macroscale properties. From the literature, the OVP system has a glass transition temperature (T_g) of 411.1 K and OPEP has a T_g of 260.1 K.[130–132] This difference in T_g provides a good target for investigating the capabilities of each force-field. Both POSS species have been described with CVFF and PCFF independently and simulated separately as pure entities. To investigate the importance of charge considerations, separate simulations have also been carried out with implicit partial charges omitted. I now discuss the results from this investigation, beginning with the OVP system.
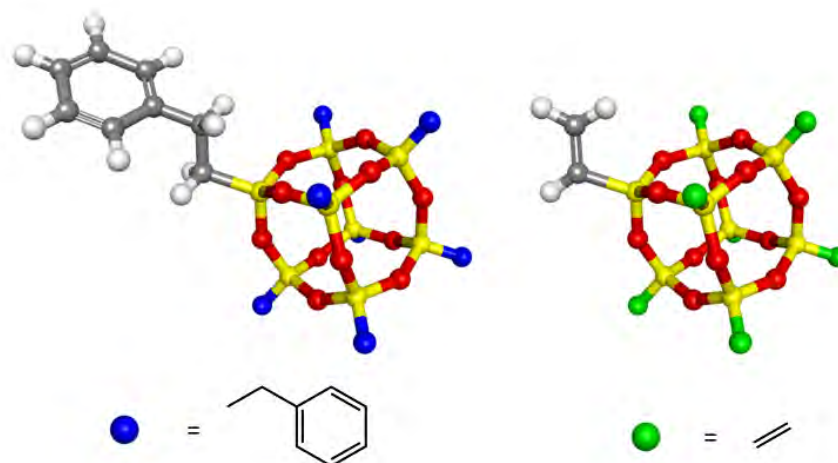
Figure 4.1.1: The molecular structure of T$_8$phen-ethyl$_8$ (OPEP) and Octa T$_8$vinyl$_8$ (OVP) from left to right respectively. Seven of the eight functionalising groups have been omitted for clarity. Red, white, grey and red spheres represent silicon, hydrogen, carbon and oxygen atoms respectively.

4.1.1 Octa vinyl POSS (OVP) Simulation

As OVP and OPEP have very different T$_g$ values, I have used a broad cooling sequence that ranges from 500 to 200 K for both systems (see section 3.7 for more information regarding cooling sequences). All simulations have been carried out in the NPT ensemble with the run lengths at each temperature step being 0.5 ns. Initial simulations were performed with 120 molecules of OVP, equal to 7200 atoms. This relatively small number of atoms was chosen to permit short run times and rapid learning of MD practicalities. The simulations were subsequently scaled up to assess reproducibility and system-size dependence.

In Figure 4.1.2, I present the calculated specific volume (cm^3/g) for each temperature during the cooling sequence with charge considerations included. Data from the PCFF simulations are in blue and the CVFF data are in orange. Here, I plot bi-linear relationships for each force-field where a change in gradient is observed. In doing so I identify the phase change from a rubbery state (higher temperature) to a glassy state (lower temperature). For PCFF, I predict a T$_g$ of 400.3 K, in good agreement with the experimental value of 411 K. CVFF

also predicts the T_g well with a value of 399.1 K.
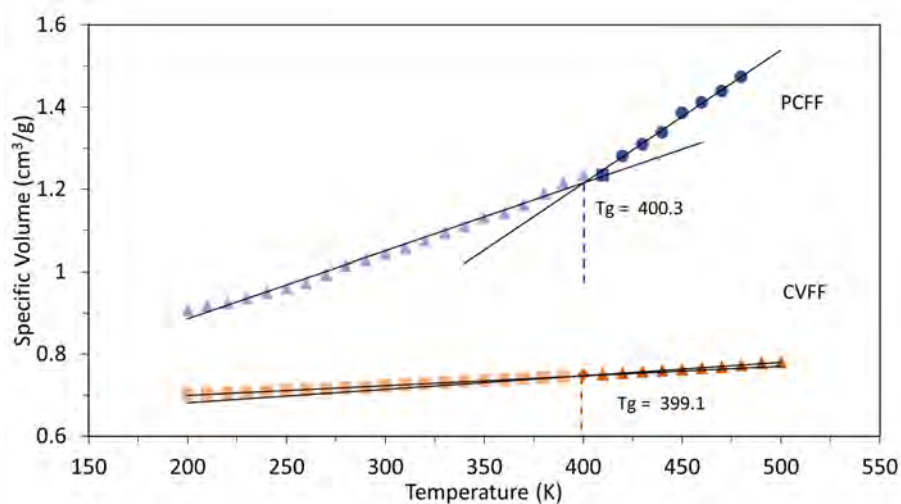
Figure 4.1.2: Change in specific volume (cm^3/g) Vs Temperature (K) for 120 OVP molecules. Green data points are derived from simulations featuring PCFF and blue feature CVFF. Both groups have partial charge considerations included

However, the position and shape of these data are not in agreement. The PCFF data describe a more easily identifiable bi-linear relationship, with the angle between the two trend lines being much greater than that of the CVFF data set. This results in a lower margin of error for T_g prediction. A tighter fitting of the CVFF data is given in figure 4.1.3 to clearly demonstrate the identified intersect. Each force-field also predicts different densities. According to literature, OVP has a density of 0.93 g/cm^3.[133] At close to standard conditions (270 K), I see an under prediction of 0.47 g/cm^3 for CVFF and a small over prediction of 0.08 g/cm^3 for PCFF.
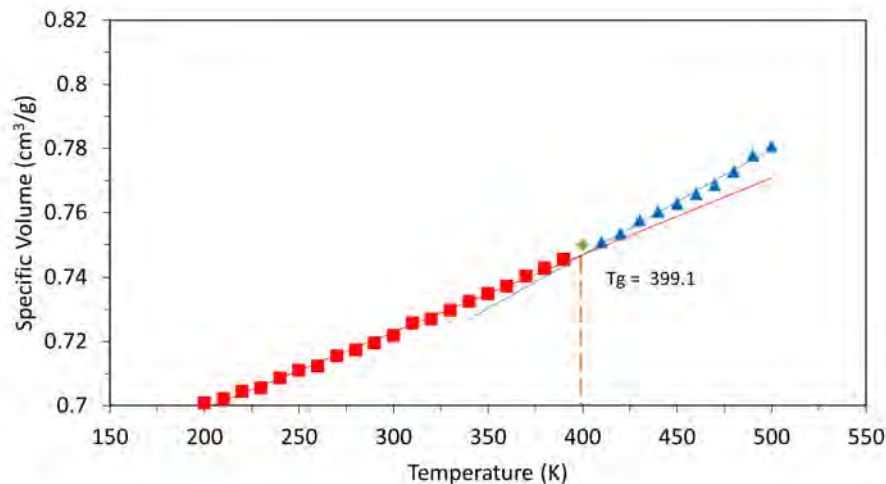
Figure 4.1.3: Specific volume vs Temperature relationships for 120 OVP molecules described by CVFF with partial charges included.

I also consider the behaviour of equivalent systems where partial charges are not included. Specific volume behaviour for these are shown in figure 4.1.4. Here, the PCFF representation out-performs the CVFF, as I predict T_g values of 387.5 and 299.1 K respectively. Again, the PCFF data present a clear change in gradient and predict a T_g in better agreement with the experimental value. Comparing to the previously presented systems, density is consistently higher in systems where charges are included. The average difference in density between the systems with and without charges is 0.064 and 0.054 g/cm^3 for PCFF and CVFF respectively. Thus, the molecules are more closely packed when charges are considered. The vinyl ligands and silicon atoms are highly polarised due to the electronegativity of the oxygen atoms. In the calculation of partial charge, it was not uncommon to see silicon atoms with charges greater than + 1. Thus, it is not unexpected that inclusion of partial charges is necessary for the accurate representation of these systems.
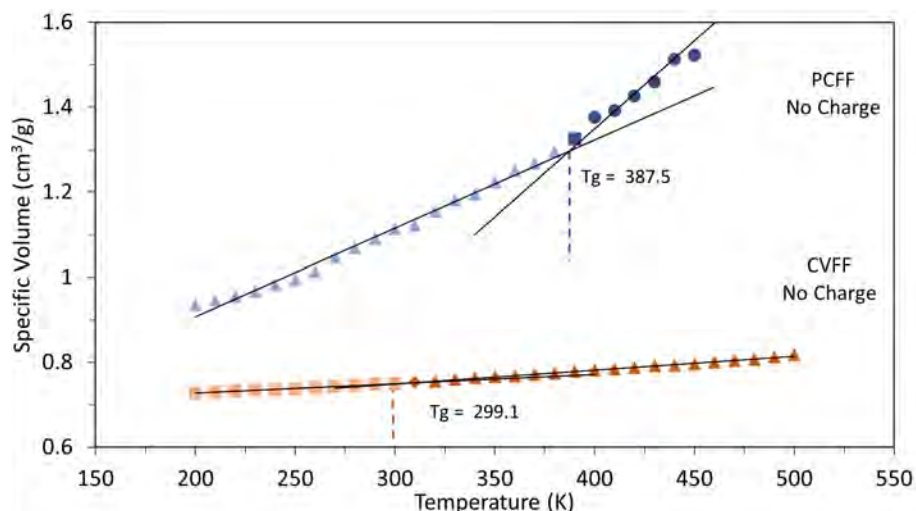
Figure 4.1.4: Specific volume vs Temperature relationships for 120 OVP molecules described by PCFF (blue) and CVFF (orange) where charges have not been included.

Further simulations of OVP with a system size of 160 molecules have also been carried out. In figure 4.1.5 I present the predicted T_g for from the PCFF and CVFF force-fields with partial charges included. Again, both methods predict T_gs in good agreement with the experimental value, being 389.5 K and 392.7 K respectively. Both data present similar behaviour to that of the smaller systems in that the PCFF data intersect is much clearer and consistently less dense that the CVFF data.
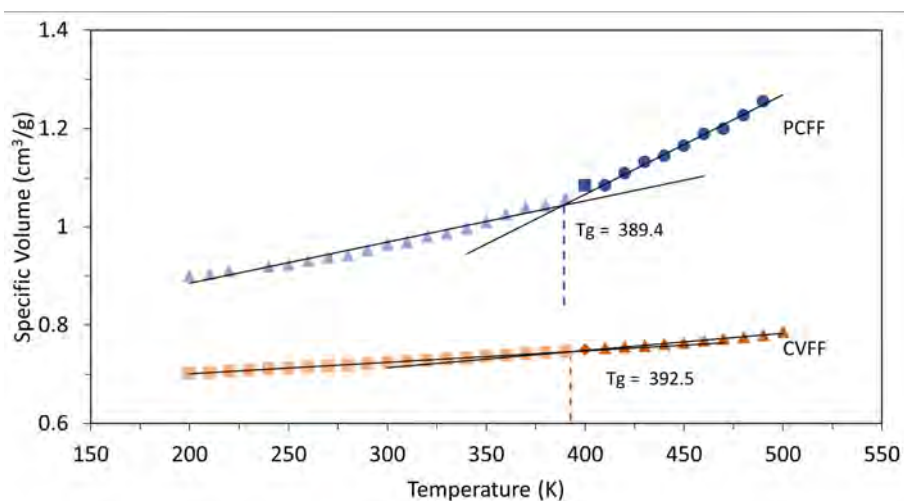
Figure 4.1.5: The specific volume vs temperature relationship and predicted T_g value for 160 OVP molecules from PCFF (blue) and CVFF (orange) data. Partial charges have been included.

4.1.2   Octa phen-Ethyl POSS (OPEP) Simulation

Exploratory simulations of T_8phen-ethyl$_8$ POSS (OPEP) have also been carried out. From the literature, the experimental T_g for OPEP is 260.1 K.[131, 132] For this larger molecule, I first consider my smallest system size of 60 molecules (7200 atoms). In figure 4.1.6a I present the predicted T_g from PCFF and CVFF where partial charges have been included. PCFF predicts a value of 297.3 K, which is a closer match to the experimental T_g. CVFF-over predicts with a value of 365.0 K. For these systems, the calculated densities are in better agreement than was seen for the OVP systems. This suggests that PCFF has a higher sensitivity to molecular structure as there is a differentiation between OVP and OPEP. As shown in figure 4.1.6b, where partial charges have been omitted, PCFF and CVFF over predict the T_g by $+54.1$ K and $+80.3$ K respectively. For both force-fields, then, significantly closer alignment with experiment is achieved when charges are included.
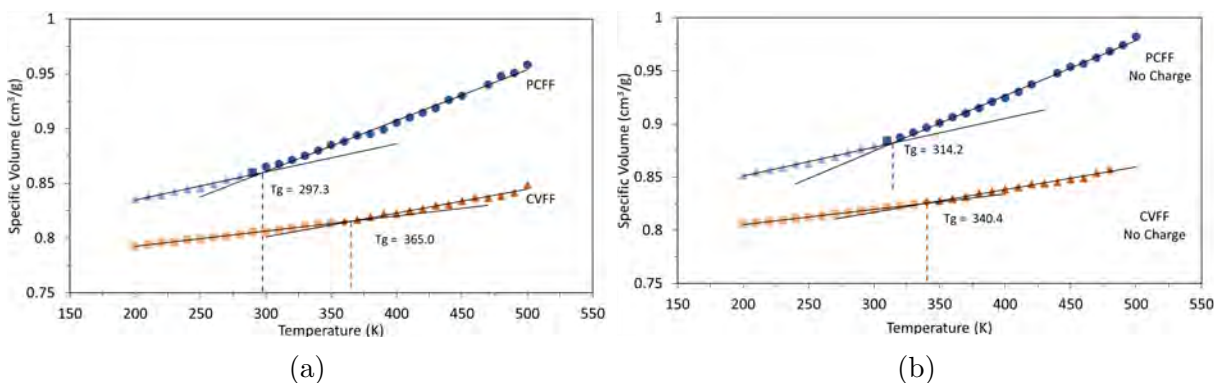
Figure 4.1.6: The specific volume vs temperature relationship and predicted T_g value for 60 OPEP molecules from PCFF (blue) and CVFF (orange) data. Graph (a) is from data simulations with charges and graph (b) has charges omitted.

70 molecules (8400 atoms) of OPEP have been simulated in the same fashion. The specific volume vs Temperature relationship for both force-fields can be seen in figure 4.1.7 with partial charges included (left) and excluded (right). Where partial charges are included, PCFF predicts a T_g of 303.7 K and CVFF of 350.0 K. Again, both force-fields over-predict the T_g, with PCFF performing somewhat better. This over-prediction of T_g is also observed where charges are excluded. Here, as shown in figure 4.1.7b, PCFF predicts a value of 311.9K

and CVFF 350.5 K.

From these initial exploratory simulations, I conclude the inclusion of charges is required for the representative simulation of POSS. All simulations discussed for the remainder of this section therefore will include partial charges. Due to its consistently better agreement with experimental T_g in both OPEP and OVP systems, and the less ambiguous temperatures at which the bi-linear plots intersect, I have identified that, of those available, PCFF is the force-field of choice for POSS simulation.
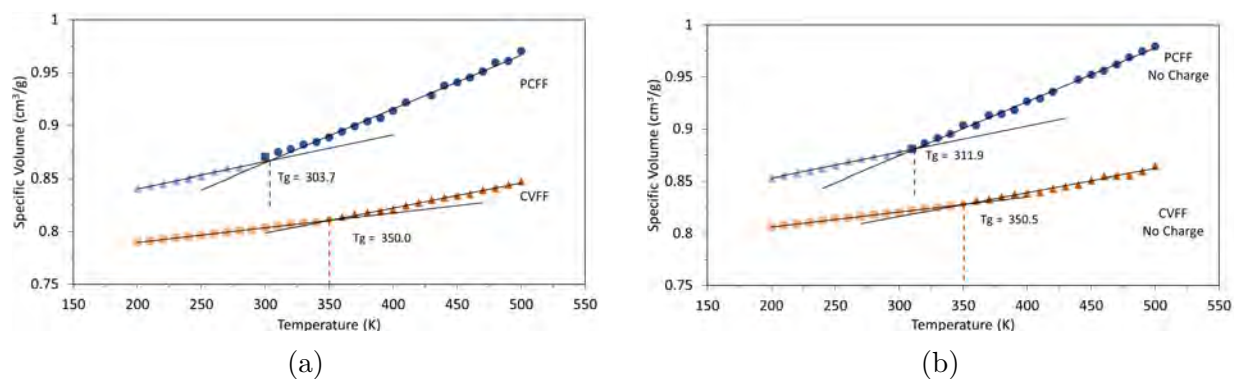
Figure 4.1.7: The specific volume vs temperature relationship and predicted T_g value for 70 OPEP molecules from PCFF (blue) and CVFF (orange) data. Graph (a) is from data simulations with charges and graph (b) has charges omitted.

4.2 Study of POSS Systems with Eight Flexible Functional Groups

Having identified the PCFF force-field with partial charges as appropriate for modelling POSS systems, I now employ this in the context of single component, octa-functionalised POSS systems. In this, I initially assess the sensitivity of simulation results to molecular details, before going on to probe a range of system variables and, so, go beyond the specific volume-temperature based characterisation listed to date. In this, I directly address my aim of relating molecular level features to bulk properties.

To assess the sensitivity of my simulations to subtle molecular difference, I have simulated T_8phen-propyl$_8$ POSS (OPPP) and compared the outputs with those of my OPEP simulations. The molecular structure of OPPP can be seen in figure 4.2.1. To the best of my knowledge, this structure does not appear in the experimental literature. For both OPEP and OPPP, I have simulated 15,000 and 25,000 atom systems. Here, the cooling sequences have been altered to the range of 160 - 370 K to reflect the experimental T_g value of 260.1 K for OPEP.
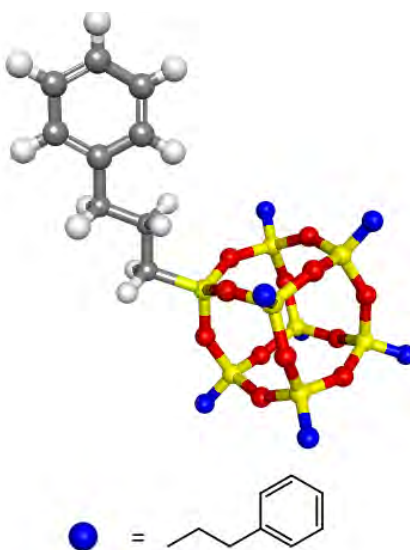
Figure 4.2.1: The chemical structure of the T_8phen-propyl$_8$ POSS (OPPP). Seven of the Eight functionalising groups have been omitted for clarity. Yellow, White, grey and red spheres represent silicon, hydrogen, carbon and oxygen atoms respectively.

In figure 4.2.2, I present specific volume data cooling sequence performed with 96 and 156 molecules of OPEP. As shown, these predict values of 253.0 and 279.9 K respectively. Both results are in better agreement with the experimental value of 260.1 K than the 60 molecule OPEP system which gave 303.7 K. However, the larger system over-predicts the T_g by 19.8 K, and the densities of these systems are not in perfect agreement. In table 4.1, I present the predicted T_g values for all OVP and OPEP systems covered in this chapter.
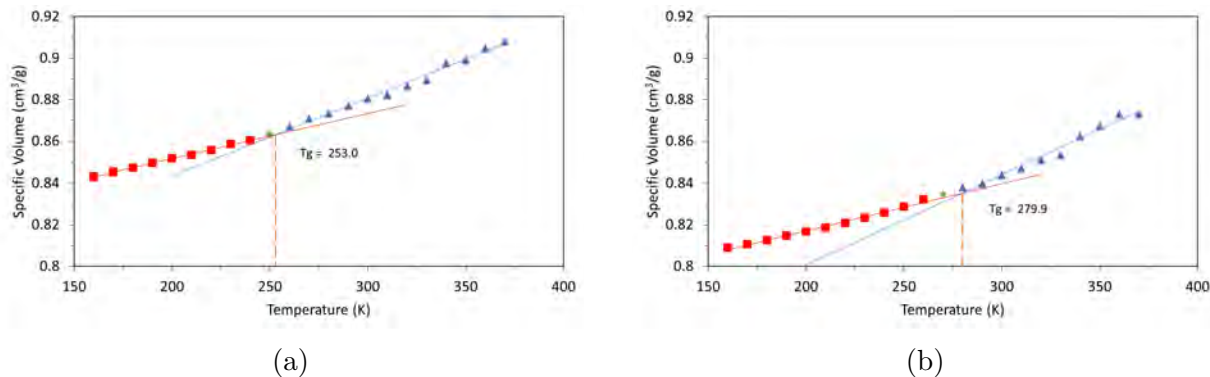
Figure 4.2.2: The specific volume vs temperature relationship for OPEP at 96 (left) 156 (right) molecules.

Molecular structure	Number of Molecules	Specific Volume T_g (K)
OVP	120	400.3
	160	389.4
Molecular structure	Number of Molecules	Specific Volume T_g (K)
	60	297.3
OPEP	70	303.7
	96	253
	156	279.9

Table 4.1: The predicted T_g for all OVP and OPEP systems from the specific volume method.

For the OPPP structure, I have simulated 83 and 138 molecule systems. Here, fits to specific volume data predict T_g values of 272.8 and 273.1 K respectively (figure 4.2.3). These results are in excellent agreement with one another in terms of T_g and system density. These predictions demonstrate that PCFF is sensitive to slight differences in molecular structure for POSS systems. The OPPP molecular structure has a higher proportion of organic character compared to OPEP, which would intuitively result in a lower T_g.
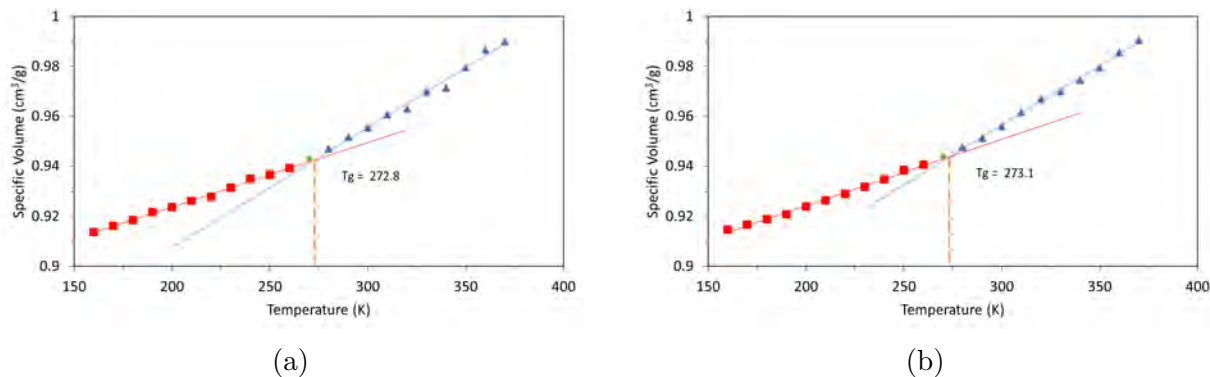
Figure 4.2.3: The specific volume vs temperature relationship for OPPP at 83 (left) and 138 (right) molecules.

The increase in T_g with organic character lead me to consider the molecular level behaviour. By monitoring the molecular trajectory data, I identified that these systems were conformationally locked at all temperatures.[134] That is to say that the there was no movement en masse or significant molecular slippage between these POSS molecules. To quantify this, Mean Square displacement (MSD) analysis has been carried out on molecualar centers of mass for temperatures above and below T_g. In figure 4.2.4, I present the MSD analysis for the 156 and 138 molecule systems of OPEP and OPPP, respectively. For both systems, MSD increases on average with temperature. However, for all temperatures, I see very little mobility with CoM displacements below 1 Å over 0.25 ns. From this, I determined that the glass transition observed in these systems is not related to molecular translational degrees of freedom. This suggests that a different molecular mechanism must be attributed to the arrival of T_g.

(a)   (b)
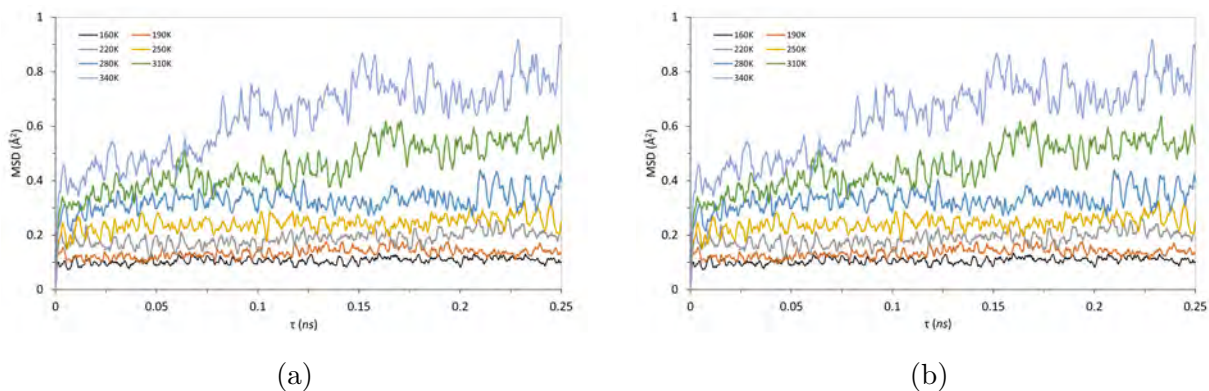
Figure 4.2.4: MSD analysis for 156 OPEP molecules (left) and 138 OPPP molecules (right).

To examine this further, I have considered the change in molecular shape as a function of temperature. For this, shown in figure 4.2.5, I have calculated the moment of inertia (MOI) tensor to describe the overall shape of each molecule. This procedure is covered in section 3.8.4. Here, as an example, I present the eigen-values from the MOI tensor for one particular OPEP molecule at 200, 260 and 320 K from the cooling sequence. From this data, below (200 K) and at T_g (260 K), the overall shape of the molecule does not change as the averages of each of the eigen-values remain fixed. Above Tg, however, the MOI data shows that the molecule is able to change shape much more, with some significant long lived changed. Since these molecules are immobile, such changes represent configurational changes within the organic functional groups.

Whilst these configurational changes can be detected at the molecular level, they only lead to a small adjustment to average MOI eigenvalues. Indeed, distribution of all eigenvalues show no significant or consistent temperature variation. Thus, despite their ability to reproducibly exhibit a glass transition which appears to be sensitive to molecular detail, the POSS molecule in these systems are severely constrained - each one has its position and shape impaired by a cage which is established at much higher temperatures than T_g.

(a) 200 K

(b) 260 K

(c) 320 K
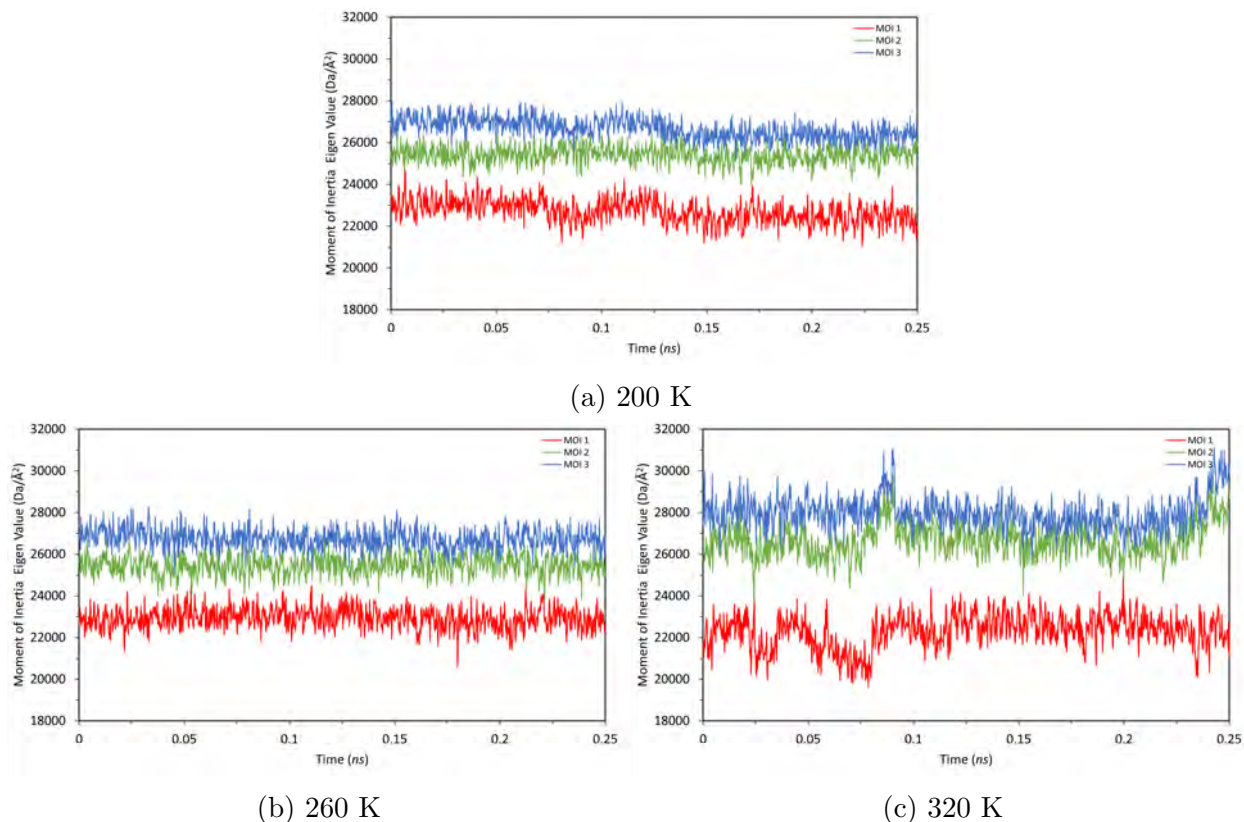
Figure 4.2.5: eigen-values from the calculation of the moment of inertia for the same OPEP molecule at 200, 260, 320 K.

While the mean eigen-values remain fixed, and different for each molecule, I have identified that the degree of fluctuation about the mean increases with temperature. To quantify this, I have calculated the standard deviation for each MOI eigenvalue and averaged over all molecules. For example, the average MOI standard deviation for all OPEP molecules at 200, 260 and 320 K is 476.8, 589.4 and 824.4 Da/Å^2 respectively. In figure 4.2.6, I present the MOI timeline for one of the 138 OPPP molecules. Again, particularly between 200 and 260 K, the overall structure of the molecule is maintained, but fluctuation about that structure increases. Here at 200, 260 and 320 K, the average standard deviation in the MOI eigen-values are 619.0, 798.6 and 1165.1 Da/Å^2 respectively.

This upward trend in MOI fluctuation with temperature is a feature which I have observed in simulations of OPEP, OPPP, T_8propyl-methacrylate$_8$ and T_8propyl-methacrylate$_4$methyl$_4$

etc. I therefore assert that it is a generic property of flexible POSS species, which is sensitive
to detail of functional group chemistry

(a) 200 K

(b) 260 K

(c) 320 K
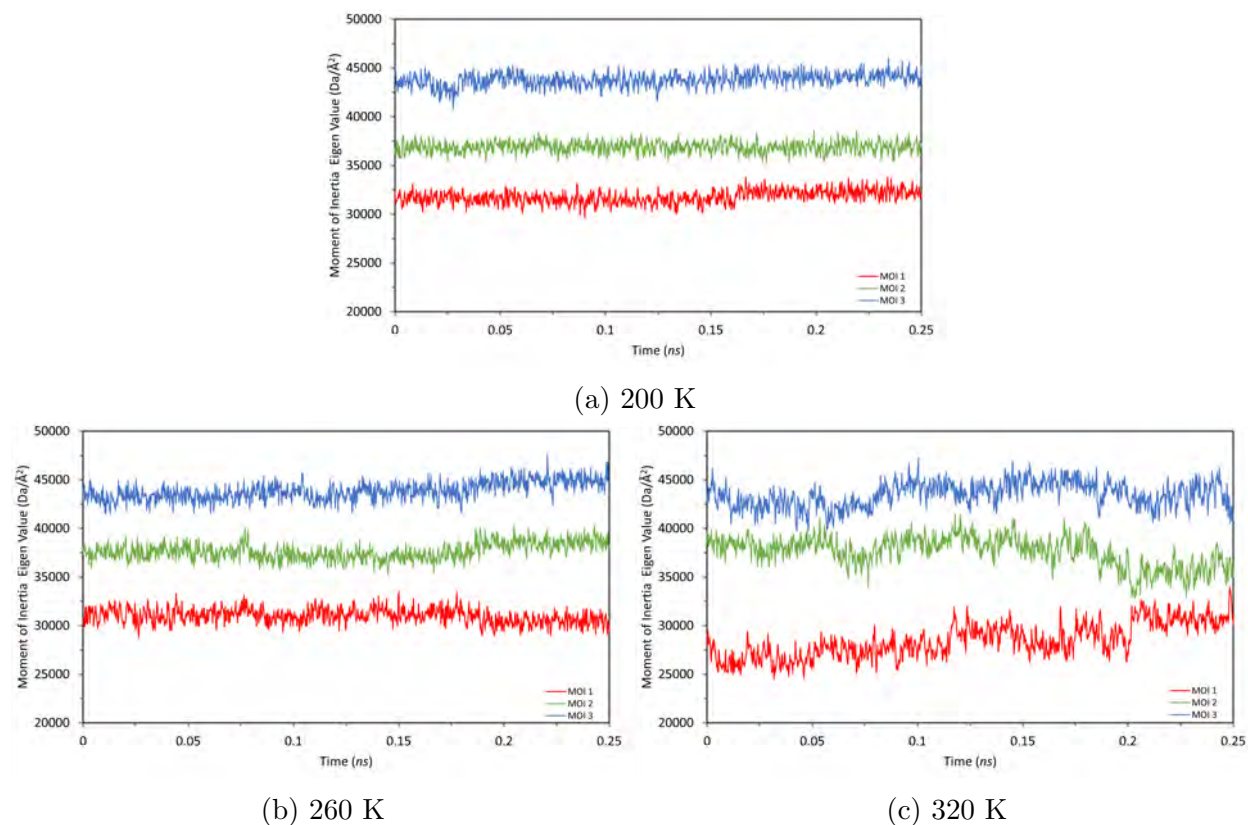
Figure 4.2.6: eigen-values from the calculation of the moment of inertia for the same OPPP
molecule at 200, 260, 320 K.

To describe these fluctuations in the moment of inertia, I now introduce the term "breath-
ing mode" to characterise the associated molecular behaviour. Within this, the overall struc-
ture and shape of each POSS is upheld, however, the local movement of bonded atoms within
the functionalising groups manifest in the the observed breathing mode. As these systems
are so conformationally constrained,I am able to utilise the breathing mode as a quantifiable
molecular feature, and to relate it to macroscale properties. To this end, in figure 4.2.7, I
present the average standard deviation in the MOI eigen-values as a function of temperature
for the OPEP and OPPP systems. For both systems, clear bilinear plots result. From which
a single temperature is identifiable at which the linear gradient of breathing mode fluctua-
tions changes discontinuously. Further, these temperatures map very closely to the T_g value

previously reported for these systems. For 156 molecules of OPEP, the discontinuity is at 277.2 K, in agreement with the experimental T_g value of 260.1 K. Similarly, in Figure 4.2.7b, for 138 molecules of OPPP, I obtain 273.1 K, which is in agreement with T_g results from the specific volume method shown in figure 4.2.3.
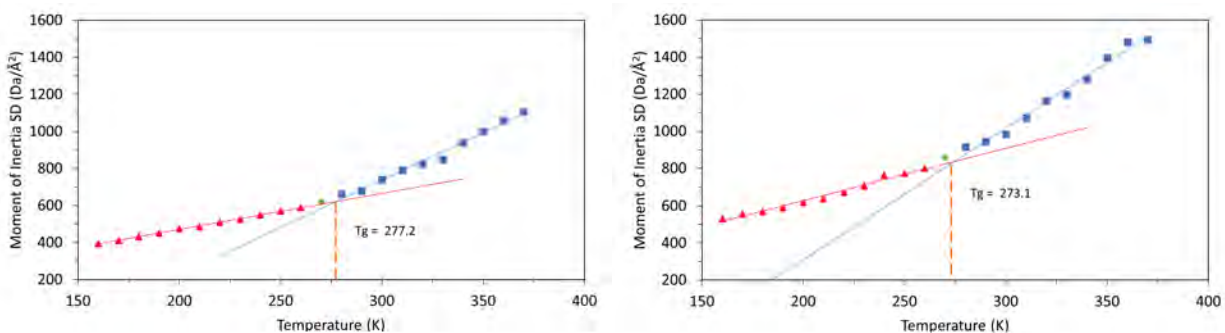
(a) MOI data from 156 OPEP molecules.   (b) MOI data from 138 OPPP molecules.

Figure 4.2.7: The predicted T_g for 156 molecules of OPEP (left) and 138 molecules of OPPP (right) from the average standard deviation in the moment of inertia as a function of temperature.

To investigate the structural properties of the systems, I also have conducted radial distribution analysis (G(r)). The G(r) methodology is covered in section 3.8.1. Through the MOI standard deviation analysis, I consider the behaviour of each molecule without reference. Through G(r) analysis, I consider the packing and arrangement of molecules in reference to one another. In figure 4.2.8, I present the G(r) data for the OPEP (left) and OPPP (right) at 220 and 280 K. For both systems, the shapes of the G(r) curves are very similar at both temperatures. The main features, such as peak and trough locations are independent of temperature, but do vary between OPEP and OPPP. The main temperature effect observed in figure 4.2.8 is that the G(r) curves are less smooth at lower temperatures. This is due to the fluctuation type movement of the centers of mass within the mobility-free structures. Not withstanding their lack of mobility, both systems have G(r) plots of the dampened oscillatory form associated with spherical bodies in amorphous arrangement. Both have central void regions of 9 Å, indicative of steric repulsion between the functionalised silica cages. The OPPP system exhibits a clear first peak, corresponding to a nearest neighbour

shell, centered on 13 Å but spread over several Angstroms. For OPEP, the first peak is less well defined, however, and the G(r) data becomes amorphous beyond 17 Å. I return to the significance and reproducibility of G(r) curves in flexible POSS systems in a following section.

(a) G(r) OPEP at 220 K.

(b) G(r) OPPP at 220 K.

(c) G(r) OPEP at 280 K

(d) OPPP at 280 K
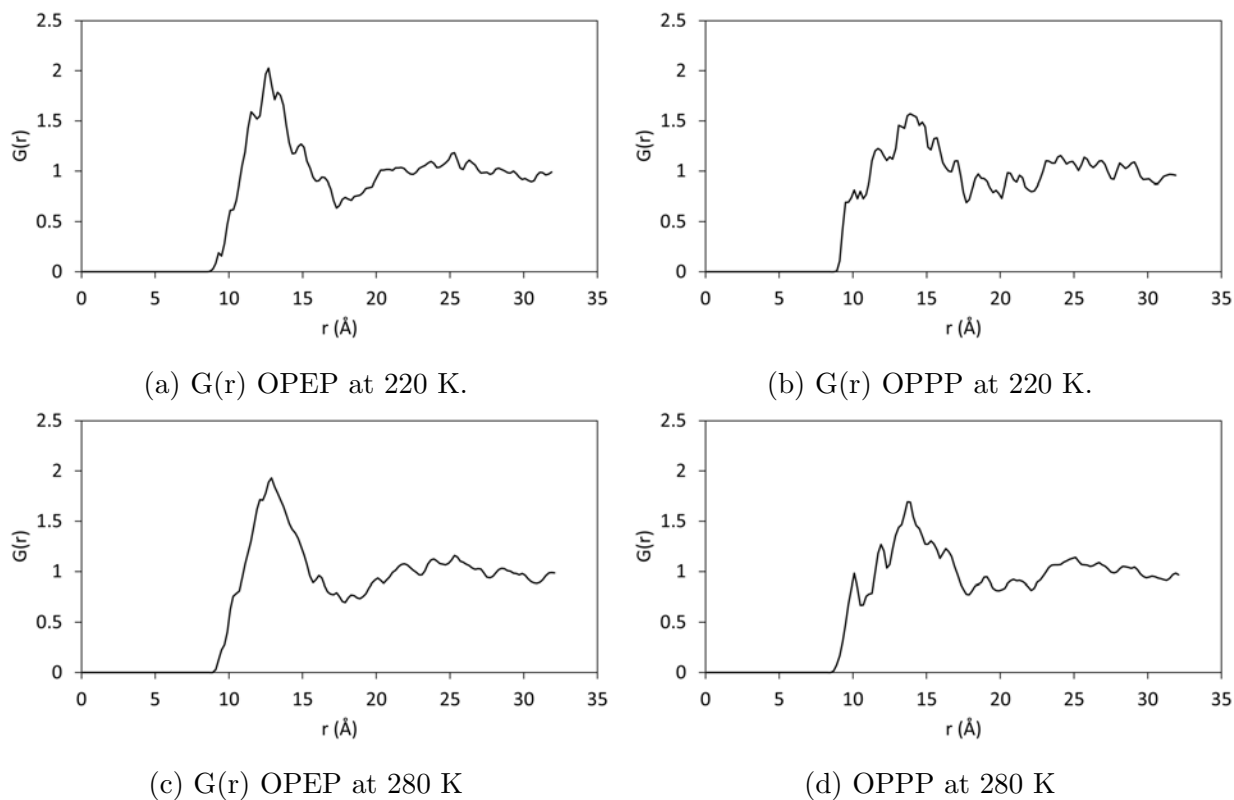
Figure 4.2.8: G(r) analysis for 156 OPEP (left) and 188 OPPP (right) systems at 220 and 280 K. These analyses are based on the centre of mass.

Throughout this work, I have worked to ensure that our systems are equilibrated. In figure 4.2.9, I present the G(r) analysis for OPEP and OPPP at 390 K. As shown, the G(r) shape for each system is maintained throughout the cooling sequence indicating that the system has reached a steady state in a higher temperature and the inter-molecular arrangement does not change throughout the cooling sequence. In addition, in figure 4.2.9, the G(r) curves are smooth, suggesting that the molecules are able to fluctuate in position about a mean position over the course of the simulation.

(a) OPEP at 390 K

(b) OPPP at 390 K
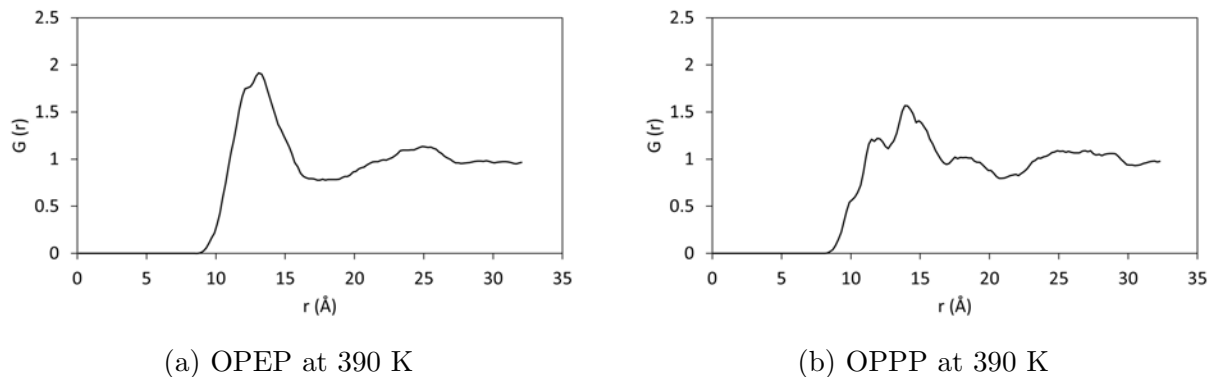
Figure 4.2.9: G(r) analysis for 156 OPEP (left) and 188 OPPP (right) systems at 390 K. These analyses are based on the centre of mass.

In this section, octa phen-linker POSS structures have been used to elucidate of a key molecular feature of POSS species, namely the breathing mode. To further investigate this feature, I have conducted a systematic analysis of octa functionalised methacrylate based POSS systems, as discussed in the following section.

4.2.1 Methacrylate Functionalised POSS Systematic Analysis

Within the previous section, all functionalising groups have been non-polar. Here, I investigate the behaviour of methacrylate functionalised POSS to diversify my understanding to include systems with polar functionalising groups. From the literature, the experimental T_g value of T_8propyl-methacrylate$_8$ has been reported as 218.2 and 231.2 K from different studies.[33, 135] In-house DSC analysis of T_8propyl-methacrylate$_8$ has been performed by Dr. Ronak Jananai and results have been discussed in private communication. I determine the T_g for this system to be 220 K. However, I note that change in the cooling rate can affect the observed T_g in experiment. The molecular structure and DSC plot can be seen in figure 4.2.10 where the plateau between 223.2 and 213.2 K marks a change in the material property.
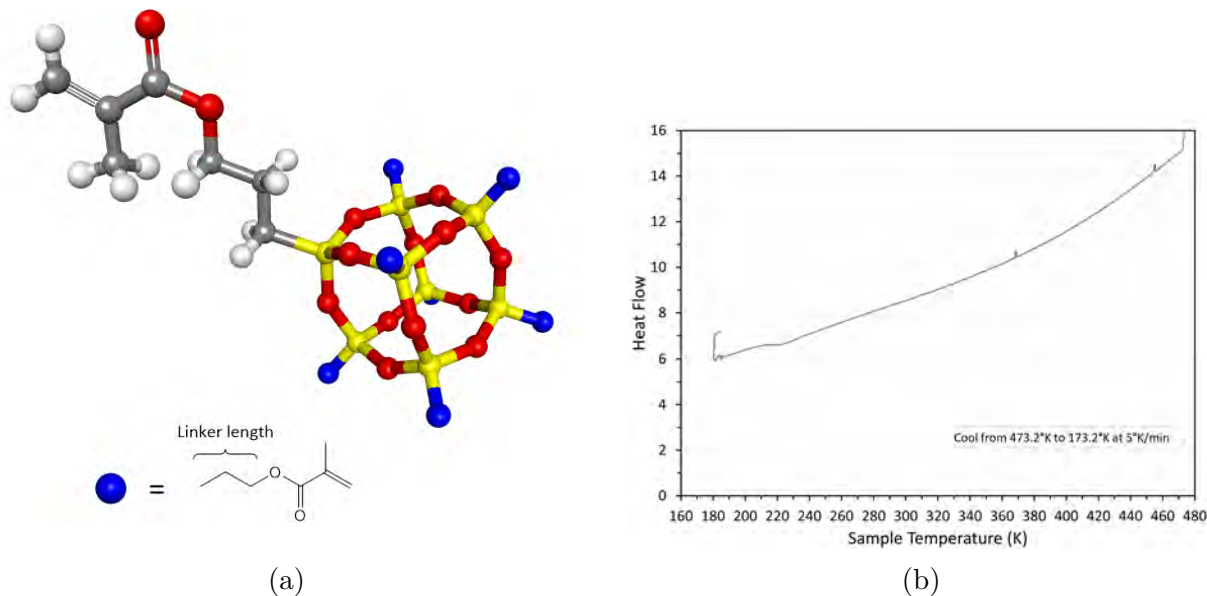
Figure 4.2.10: (a) The molecular structure and (b) DSC results for T_8propyl-methacrylate$_8$ obtained by a colleague Dr. Ronak Janani

In figure 4.2.10a, I have illustrated the propyl linker length version of methacrylate fuctionalised POSS. Within this section, I conduct a systematic analysis of methacrylate functionalised POSS through the use of different linker length $(CH_2)_n$ where n = 2, 3, 4, 5 and 6. Throughout this work I describe each linker length with the aliphatic naming convention, where ethyl is C_2H_4 and propyl is C_3H_6 etc. Also, for all systems, just as before, two groups of simulations have been carried out, one with 15,000 atoms and the other with 25,000 atoms.

In figure 4.2.11, I present the predicted T_g obtained with the specific volume vs temperature relationship and the standard deviation in the MOI method for both 83 and 138 molecule system sizes of T_8propyl-methacrylate$_8$. For the specific volume method, I predict T_g values of 258.2 and 259.1 K, respectively. While these T_g are in good agreement with one another, they are significantly higher than the experimental value of 218.2 K. This disagreement is also present for the predicted T_g through the standard deviation in the MOI method. Here, I predict a T_g of 274.3 and 268.1 K for the 83 and 138 molecule systems, respectively (figures 4.2.11c and 4.2.11d). Again I see little variation between the predicted T_g values obtained

with different system sizes. Based on this evidence, it may be the case that PCFF is unable to generate the same degree of representivity as I have observed for the previous non-polar systems.

Within this work, I have used static partial charges to model Coulombic interactions. As POSS systems have diverse structures and distributions of charge, it is possible, therefore, that this loss in representivity is due to the absence of charge dynamics in the model. The use of dynamic charges is computationally more expensive as charges are calculated at each timestep based on the local environment during simulation. This represents intramolecular polarizability within POSS species, which may be an influential factor for some systems. Further, as POSS molecular weight is increased by use of longer (and more flexible) R groups, the degree of this reduced representivity will diminish.

(a) 83 molecules

(b) 138 molecules

(c) 83 molecules
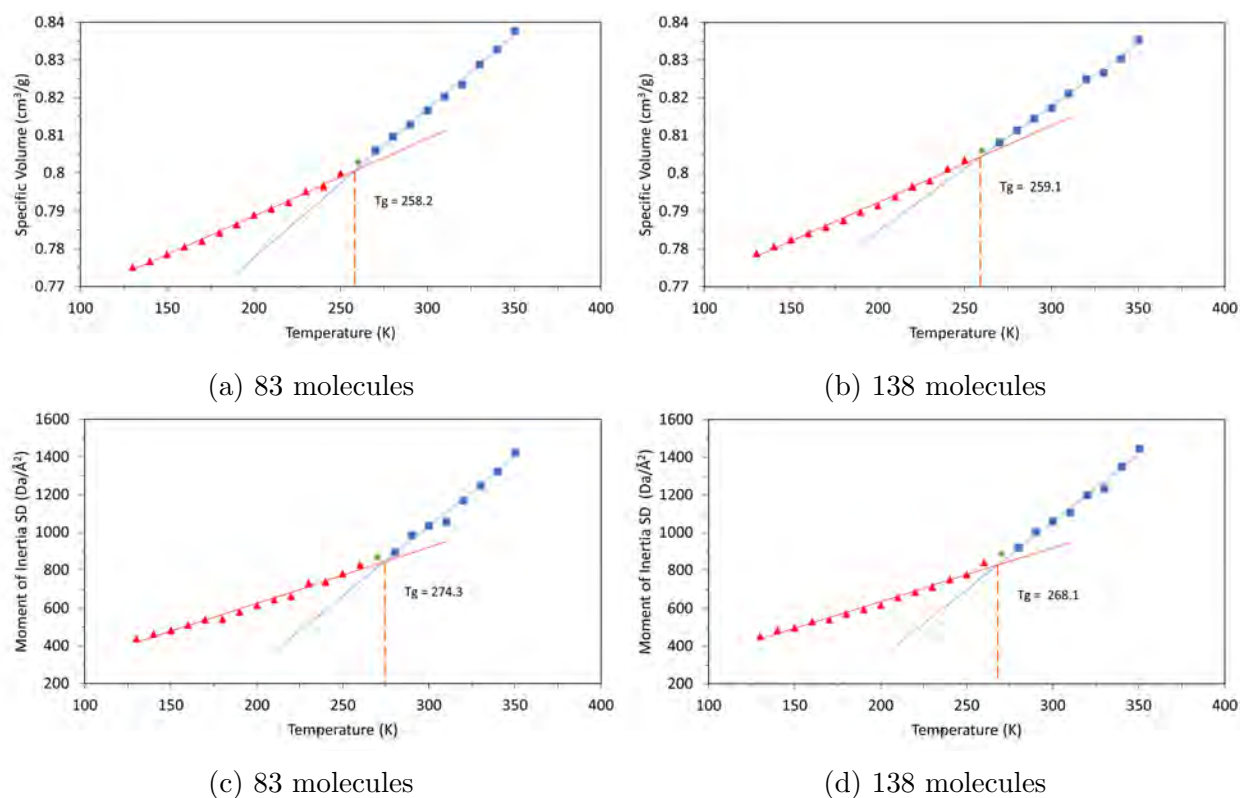
(d) 138 molecules

Figure 4.2.11: The predicted T_g for 83 (left) and 138 (right) molecules of T_8propyl-methacrylate$_8$ from the specific volume vs temperature relationship and SD in the MOI method.

In Figure 4.2.12 I present the predicted T_g values obtained over a range of linker lengths from the specific volume and MOI method. The error bars given here have been determined from intercepts of the +1 and -1 standard deviation fit lines obtained from each of the two phases. The observed trtend of T_g with linker length is consistent with the calculated error estimates. Figure 4.2.12a and figure 4.2.12b present the predicted T_g from 15,000 and 25,000 atom systems, respectively. Here, I maintained the system size in terms of atoms by changing the number of molecules present.

(a) 15,000 atoms   (b) 25,000 atoms
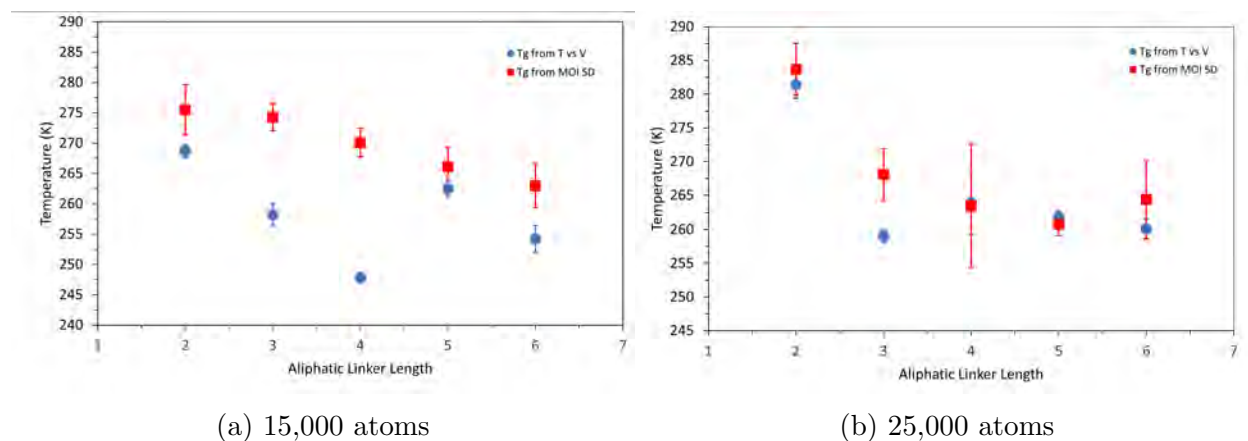
Figure 4.2.12: The predicted T_g for methacrylate functionalised POSS systems with different linker lengths from the specific volume method (blue) from 15,000 (left) and 25,000 (right) atom simulations.

For the 15,000 atom systems, from the standard deviation of MOI method, the predicted T_g decreases with increasing linker length. This downward trend is very distinct from 275 to 265 K from ethyl to hexyl linker length. This trend is also observed for the specific volume method, however I see a higher degree of deviation in the trend line. For all linker lengths, the MOI method predicts a higher T_g than the specific volume method.

For the 25,000 atom systems, I also observe a decrease in T_g with increasing linker length. Here, I see good agreement between the two methods for predicted T_g value. From the standard deviation in the MOI method, the trend resembles an asymptotic curve. The addition of aliphatic character produces a softer material, however, this trend may form a plateau

with greater linker lengths beyond hexyl.

In figure 4.2.13, I summarise the MSD measurements for each methacrylate functionalised system at 160, 250 and 350 K. As shown, for all temperatures, there is very little mobility within each system as the molecules are positionally locked.

(a) 160 K

(b) 250 K

(c) 350 K
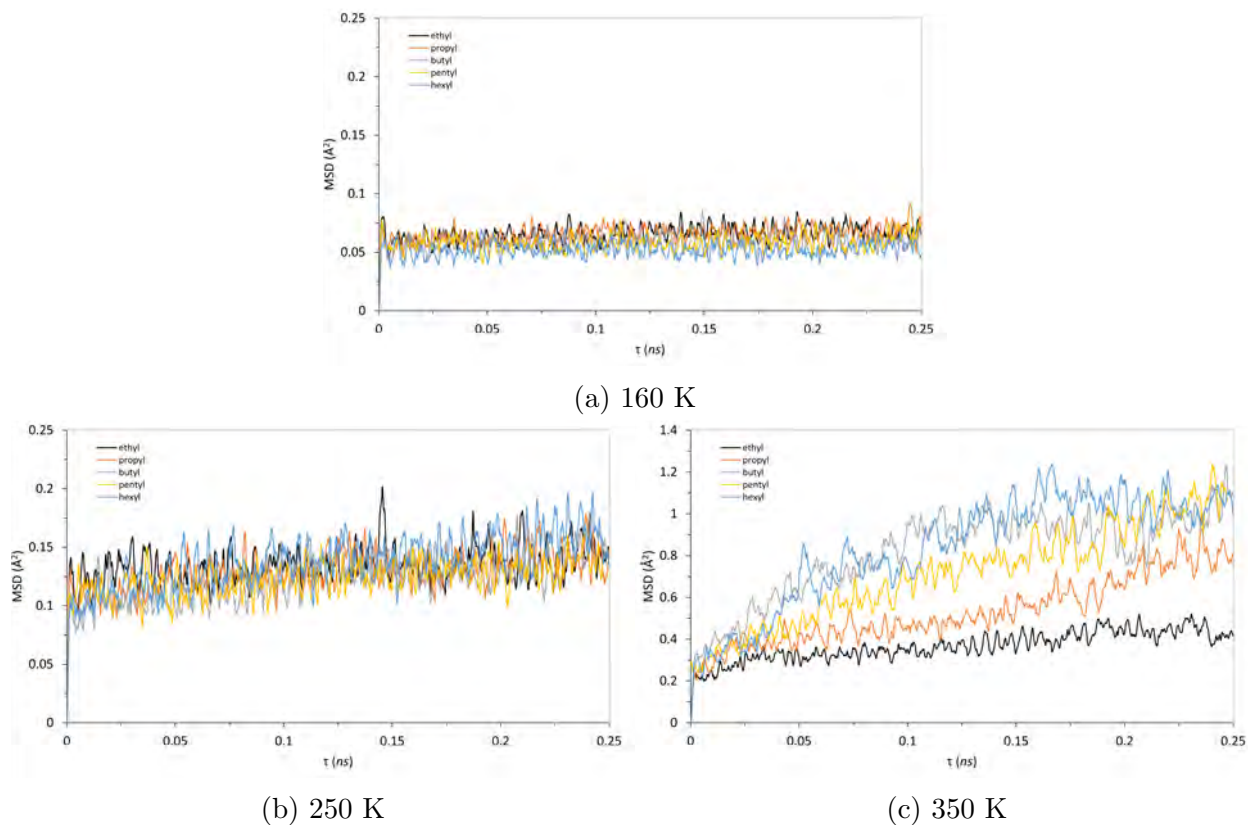
Figure 4.2.13: The MSD for each methacrylate funtionalised POSS system at 160, 250 and 350 K.

(a) T$_8$ethyl-methacrylate$_8$

(b) T$_8$propyl-methacrylate$_8$

(c) T$_8$butyl-methacrylate$_8$

(d) T$_8$pentyl-methacrylate$_8$

(e) T$_8$hexyl-methacrylate$_8$
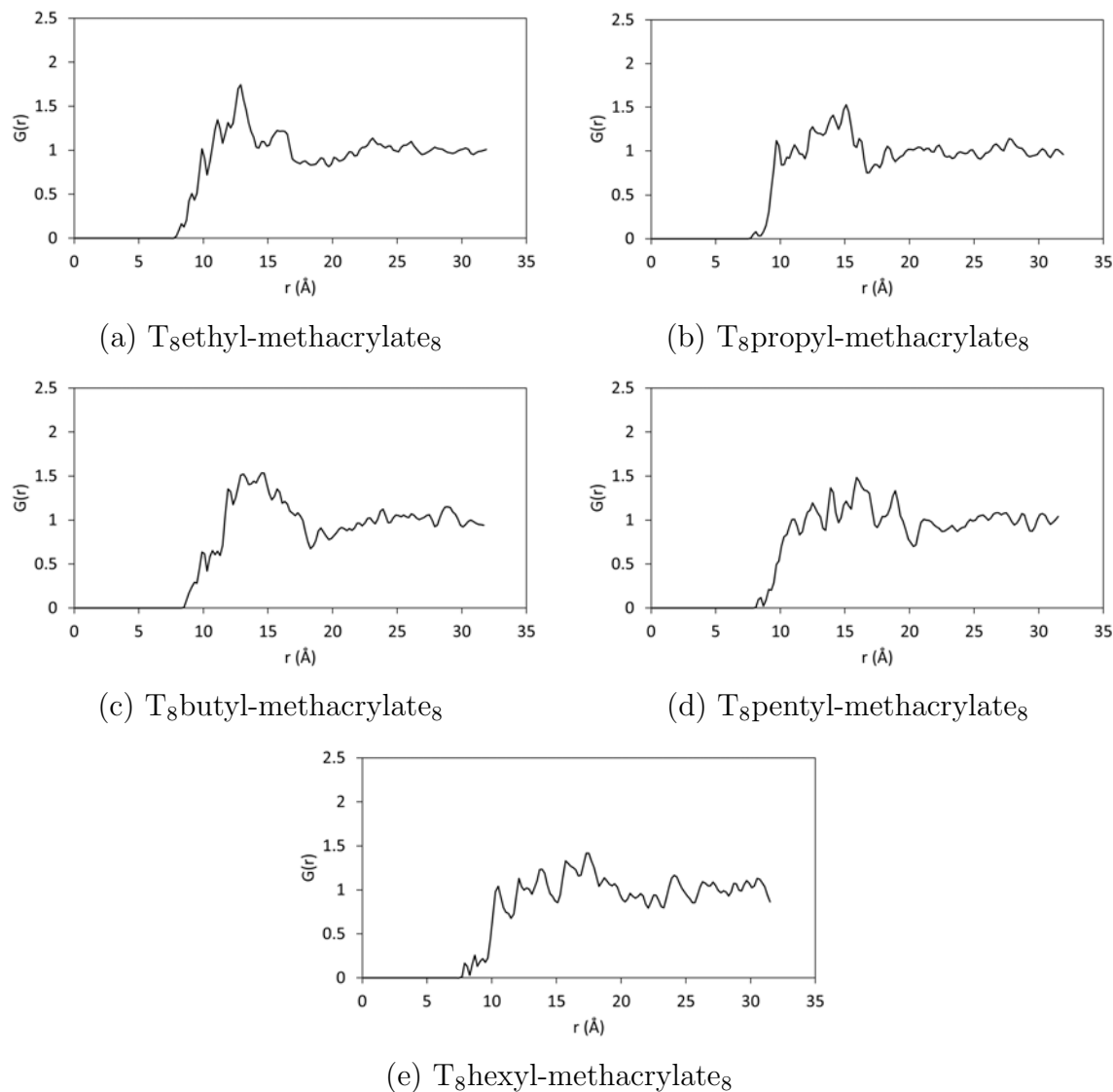
Figure 4.2.14: The G(r) analysis of methacrylate functionalised POSS systems at 280 K at a system size of 25,000 atoms.

To ensure that the systems are equilibrated, in figure 4.2.15, I present the G(r) analysis for all methacrylate functionalised systems at 390 K, which is well above the predicted T$_g$ value for these systems. Similarly to the results shown in figure 4.2.9, these graphs demonstrate similar curve structures to their lower temperature counter parts (figure 4.2.14). This indicates that the molecular arrangement is not changing over the course of the cooling sequence. In addition, the smoother curves indicate greater fluctuation of POSS centers of mass about a mean equilibrium position. This observation of smoother G(r) curves at higher

temperatures has been observed for all flexible POSS systems.

(a) T_8ethyl-methacrylate$_8$ G(r) at 390 K

(b) T_8propyl-methacrylate$_8$ G(r) at 390 K

(c) T_8butyl-methacrylate$_8$ G(r) at 390 K

(d) T_8pentyl-methacrylate$_8$ G(r) at 390 K

(e) T_8hexyl-methacrylate$_8$ G(r) at 390 K
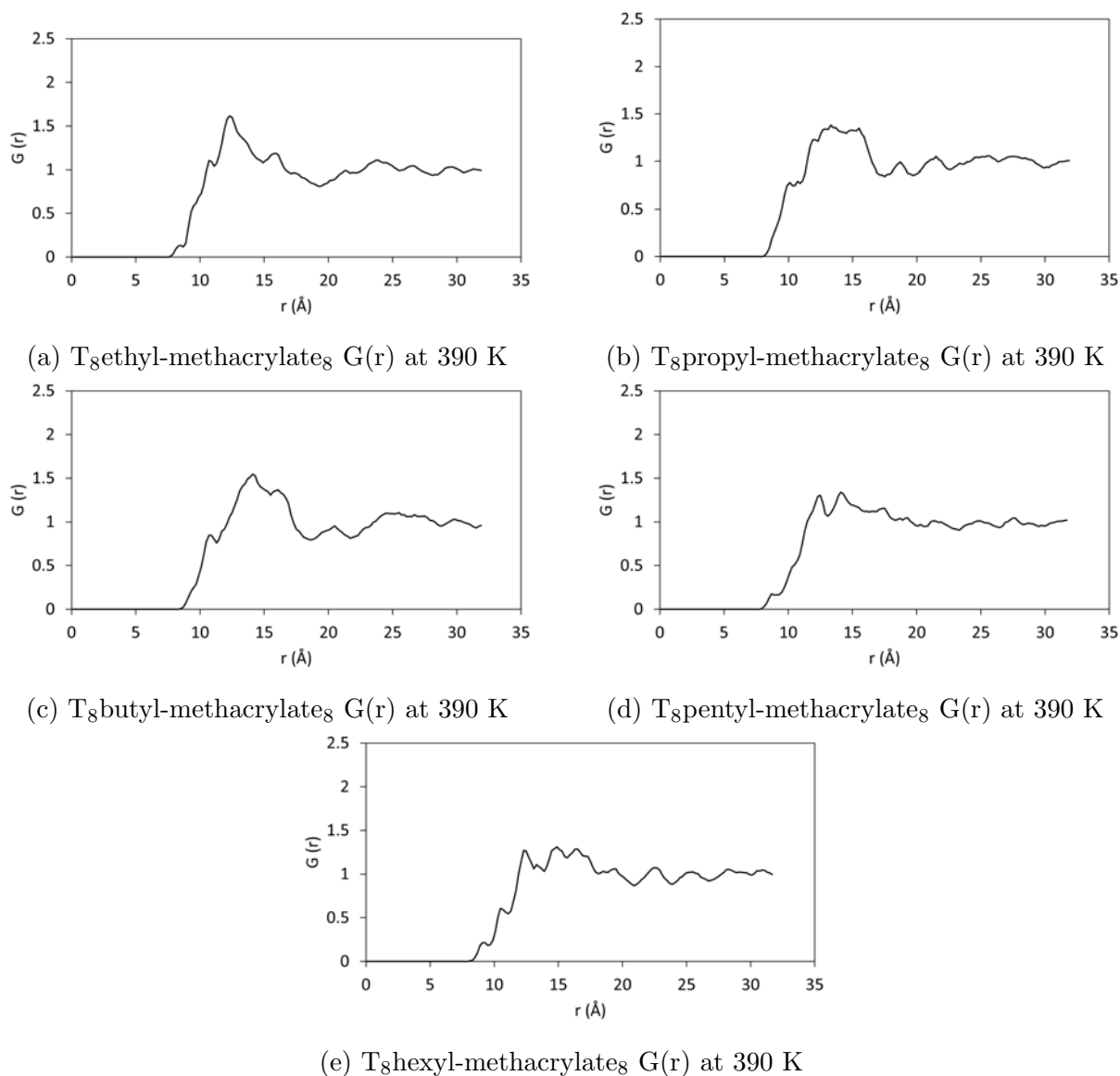
Figure 4.2.15: The G(r) analysis of methacrylate functionalised POSS systems at 390 K at a system size of 25,000 atoms.

In figure 4.2.14, I present the G(r) data for the five octa-methacrylate functionalised POSS systems at T = 280 K. For all systems, I see the characteristic initial rise from 8 Å due to the steric hindrance of the silica core. While a first peak is identifiable for short linker systems, these graphs demonstrate an incremental flattening in the G(r) with increasing linker length. This progressive flattening is indicative of a trend in the molecular shape

adopted. I propose that the available permutations of structural conformations available to the longer linker lengths enables shape polydispersity to arise. That is to say that a longer linker may be more curled up or extended out. In combination with entanglement between functionalising groups from neighbouring POSS molecules, this leads to the possibility of more and less closely packed POSS. Some POSS molecules may maintain coiled ligands close to the POSS cube where-as other molecules may have more penetrating, extended ligands.

I have therefore used more sophisticated Voronoi analysis to determine the number of near neighbours within each system. The Voronoi methodology is covered in section 3.8.3. In figure 4.2.16, I present the average number of near neighbours for the largest T_8propyl-methacrylate$_8$ system. Here, I have constructed Voronoi tessellation diagrams for each molecule at all temperatures. For each tessellation, I have then averaged the number of facets to determine the number of near neighbours. I present Voronoi near neighbour data obtained using two different methods. The red circles represent data from tessellations constructed from the hydrogen atom stripped skeletal structure of each molecule. These provide a more complex and fine grain representation of each molecule since they capture entanglement behaviours. The blue squares are from tessellations derived from the center of mass of each molecule, thereby providing a simpler representation. Figure 4.2.16 shows that, for all temperatures considered, the average number of neighbours, calculated from molecular centers of mass is 15. This is higher than both the rhombic dodecahedron value of 12, and the value of 14 seen in simulations of hard spheres.[136] Thus, the soft halo of the POSS molecules leads to them having more neighbours. As shown in figure 4.2.16, the H-stripped representations consistently have a higher number of near neighbours. This is due to the more complex topology of the tessellation and inter-digitation of the functionalising groups. As the functionalising groups are permitted to be extended from the silica core, the tessellation is able to identify a higher number of facets with more distant molecules. The lack of thermal dependence in these data is entirely consistent with my previous observations

of very low molecular mobility. A basic analysis of G(r) profiles allows the number of near neighbours to be estimated from the area under the first peak.[136] For the ethyl and butyl data presented in figure 4.2.14, this yields values of 10.4 and 10.0. However, such calculations are not feasible for the very flat G(r) profiles obtained for the larger linker lengths.
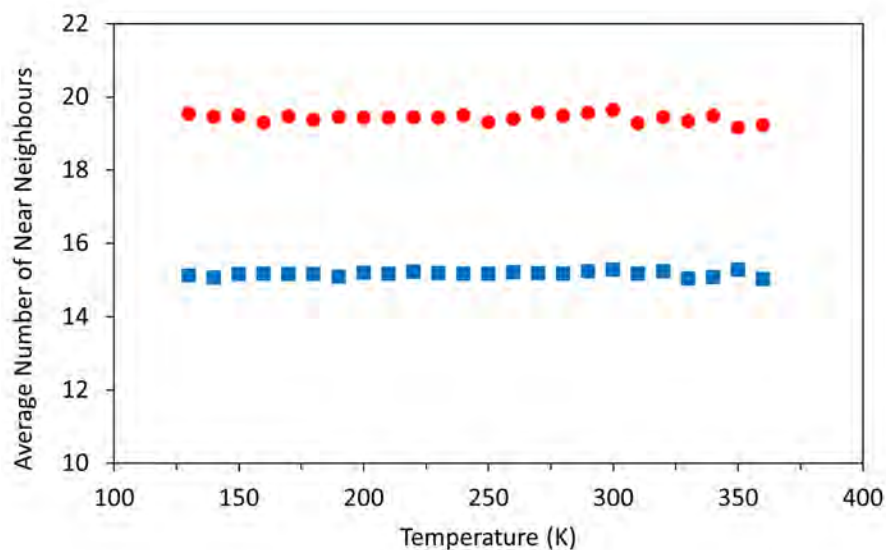
Figure 4.2.16: The average number of molecular near neighbours for the pure T_8propyl-methacrylate$_8$ system. molecular skeletal (H-stripped) voronoi tessellations are shown in red and the center of Mass tessellations are shown in blue.

In figure 4.2.17, I present the average number of near neighbours for each linker length from the center of mass and H-stripped Voronoi tessellations. The standard deviation and average values have been determined over all temperatures. From the center of mass data points, I see that the mean value of near neighbours is between 15 and 15.25, consistently above the value for rigid sphere models. The standard deviation for all linker lengths is also very low. For the H-stripped tessellations the average number of near neighbours increases from 18.6 to 21.8 for ethyl to hexyl respectively. This increase demonstrates the greater capacity for inter-digitation within larger POSS systems as more separated molecules become recognised by the Voronoi analysis. In addition, the standard deviation is greater for the larger systems, meaning that there is increased variance with temperature.
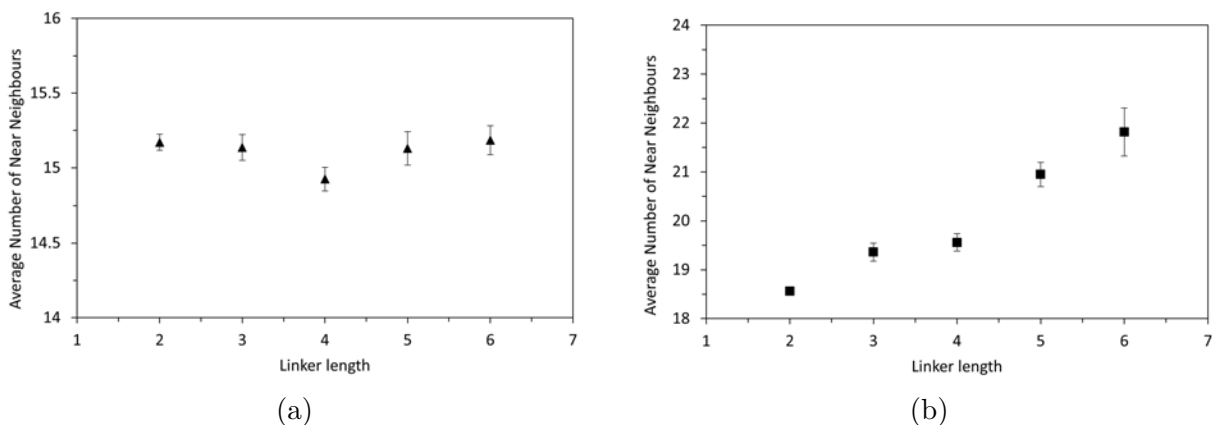
Figure 4.2.17: The number of near neighbours for T_8alkyl-methacrylate$_8$ molecules from the center of mass (left) and H-stripped skeletal structure (right) of each molecule. The alkyl linker lengths are denoted in the abscissa

In addition, I have investigated how the functionalising groups are organised around the core of the molecule. To do this, I have measured the distance between the center of mass calculated for the whole molecule and that of the silica core only. In so doing, I have compared the observed molecular morphology to that of the perfectly symmetrical version of the molecule. Figure 4.2.18a presents the mean distance of separation between the silica core and whole molecule center of mass for every molecule at 160, 250 and 360 K. As linker length is increased, the average distance of separation increases linearly from 0.6 to 1.3 from ethyl to hexyl respectively. There is very little variation of their mean value with temperature. The spread of these values is shown in figure 4.2.18b. At higher temperatures there is a higher value in the standard deviation of the mean distance of separation. This is particularly true of longer linker lengths which present more variance than the shorter lengths above T_g (350 K). There is a slight upward trend in the spread of these values with linker length below T_g (160 and 250 K). However there is a clear capacity for the longer groups to exhibit greater variance in molecular morphology.

(a)   (b)
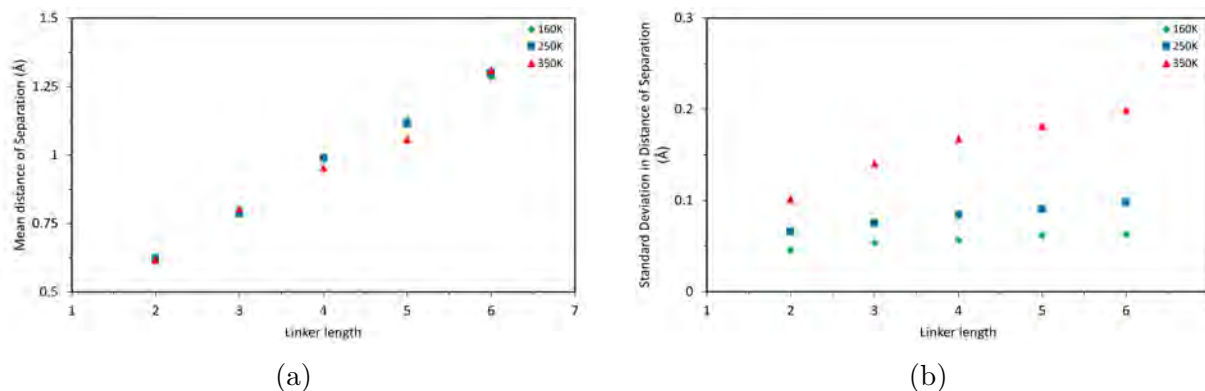
Figure 4.2.18: The average distance of separation (left) and standard deviation (right) between the center of mass for the whole molecule and the Silica core only for methacrylate functionalised POSS species of different linker lengths.

Given the very low molecular mobilities observed in the flexible POSS systems presented in sections 4.1 and 4.2, it is necessary to question how representative the simulations are, and whether their finding are reproducible. To this end, I have performed repeats of the sample preparation process using T_8propyl-methacrylate$_8$. These replicated systems have the same number of molecules as the original T_8propyl-methacrylate$_8$ simulation, however the starting conformation is unique in each case. To determine whether my results are reproducible, I have used G(r) analysis comparatively between the replicated systems and original data. These data are given in figure 4.2.19. As shown, these values follow a very similar shape in the G(r) analysis. All systems exhibit an initial rise at 8 Å to a maximum between 12 and 16 Å, followed by a plateau with some fluctuation. Thus the spread between these 7 repeat runs is less than the variation between systems observable from figure 4.2.14
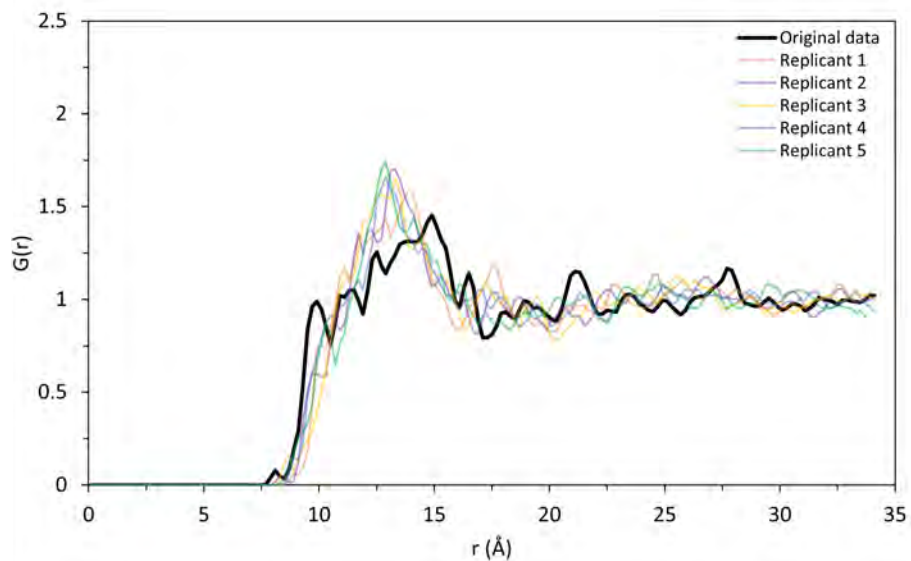
Figure 4.2.19: The G(r) analysis for the original T_8propyl-methacrylate$_8$ system and repli-cated T_8propyl-methacrylate$_8$ systems at 310 K.

In addition, I have used MSD analysis comparatively for the original and replicated systems. Thus, in figure 4.2.20 I present the MSD for the replicated systems alongside the MSD of the original T_8propyl-methacrylate$_8$ system. As shown, the values are in good agreement with one another.
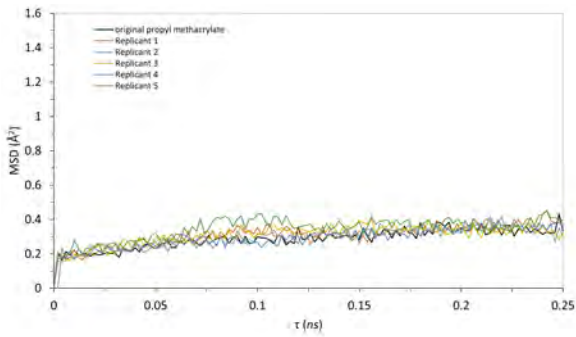
(a) 310 K
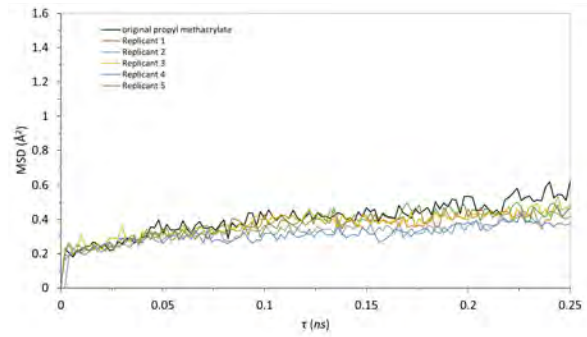
(b) 320 K
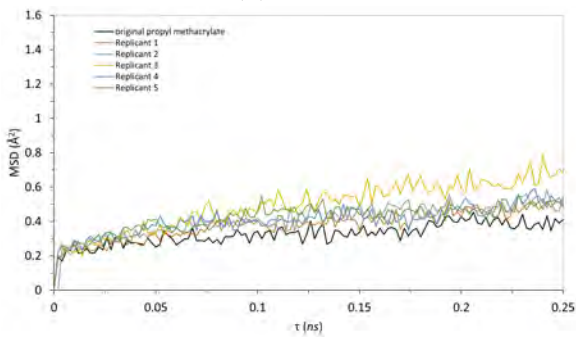
(c) 330 K
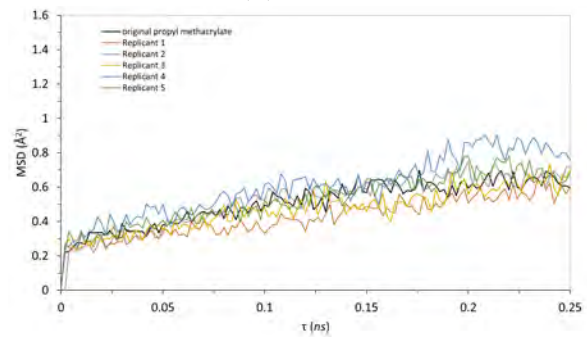
(d) 340 K
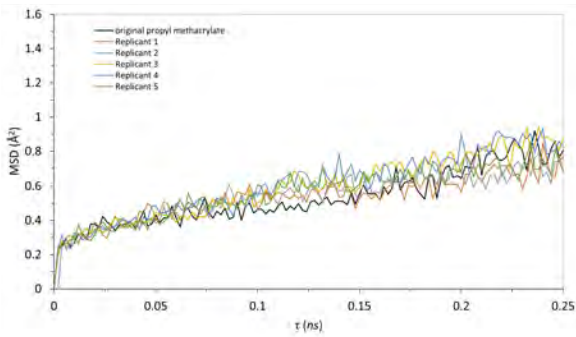
(e) 350 K
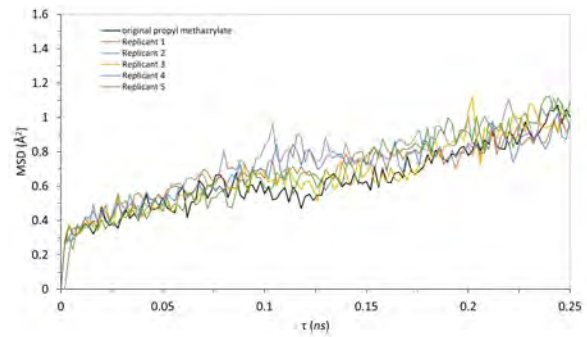
(f) 350 K
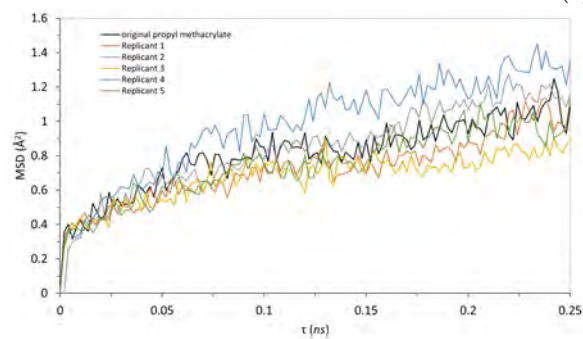
(g) 370 K

Figure 4.2.20: The MSD for the original T_8propyl-methacrylate$_8$ data and replicant T_8propyl-methacrylate$_8$ data at 310, 320, 330, 340, 350, 360 and 370 K.

4.3 Study of POSS Systems with Fixed Molecular Shape

To complement the just presented study of POSS functionalised with flexible organic moieties, I have also examined more rigid POSS species, including T_8H_8 and T_8*tert*-butyl$_8$. The molecular structure of these systems are shown in figure 4.3.1. Due to their much reduced tendency to entangle and have interdigitating halo regions, these systems provide a useful comparison to further elucidate the relationship between functionalising group and macroscopic properties.

(a) T_8H_8　　　　(b) T_8*tert*-butyl$_8$
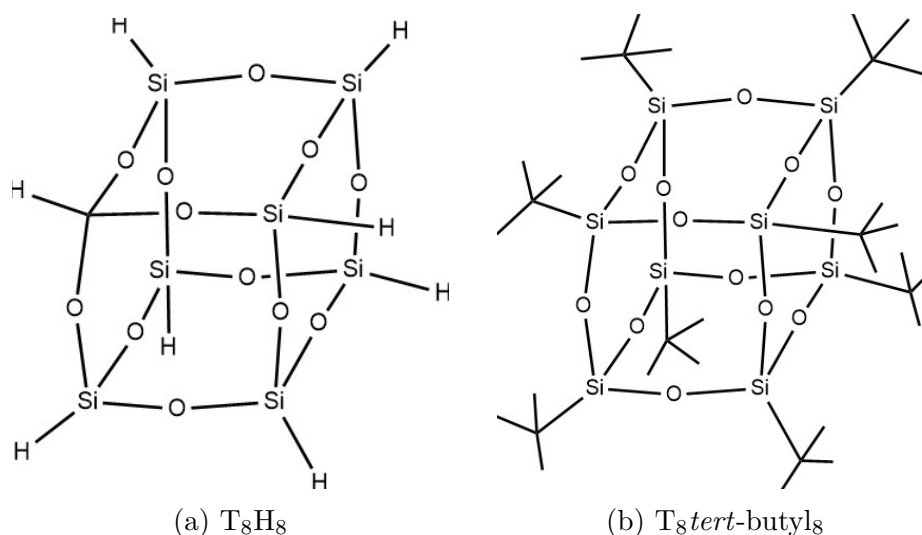
Figure 4.3.1: Molecular structure of T_8H_8 (a) and T_8*tert*-butyl$_8$ (b).

As discussed in Section 4.1 and 4.2, flexible octa-functionalised POSS species exhibit very little molecular mobility above and below the T_g. For the T_8H_8 and T_8*tert*-butyl$_8$ systems, as demonstrated in figure 4.3.2, there is also very little molecular mobility within the temperature range that was the focus of the previous section (160-360 K).

(a) T_8H_8 (b) T_8*tert*-butyl$_8$
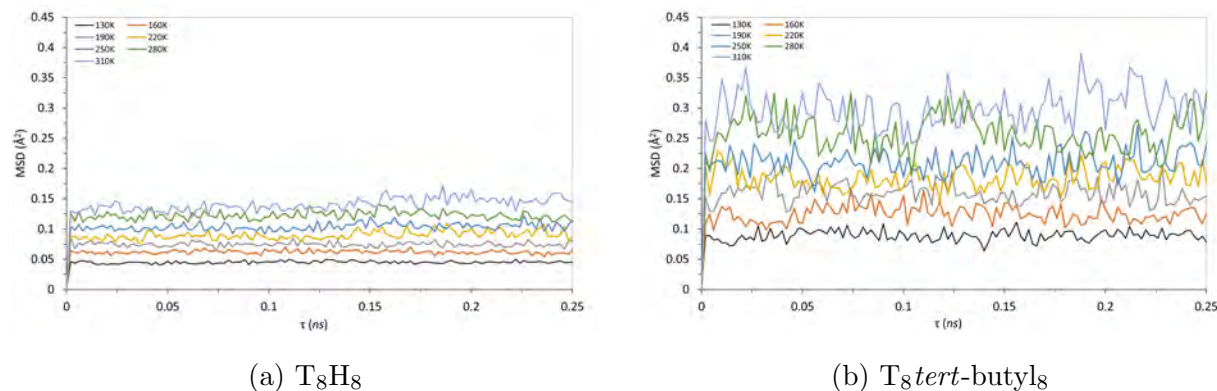
Figure 4.3.2: The mean squared displacement for T_8H_8 and T_8*tert*-butyl$_8$ over a range of temperatures.

However, these systems do not exhibit bi-linear relationships in either their specific volume vs temperature method and the moment of inertia eigen-value standard deviation data. Indeed, due to to their rigidity and symmetrical nature these POSS consistently have three very close MOI eigenvalues, rather than the spread of values seen in figure 4.2.5. To highlight the difference in molecular shape between flexible and rigid POSS species, In table 4.3.3 I present the average normalised eigenvalues for T_8*tert*-butyl$_8$ and T_8H_8 from simulations at 200, 260 and 320 K. This table shows that at all three temperatures, the spread between the eigenvalues is very small, indicating consistently near spherical shape. The larger T_8*tert*-butyl$_8$ system has slightly greater spread, suggesting slightly more diversity of molecular shape. Further, in contrast to the large functionalised POSS systems, the G(r) analysis for these systems is very distinct as shown in figure 4.3.3. These graphs present systems with strong, long range ordering. Indeed, visualisations confirm that these systems show near crystalline packing when prepared using exactly the same annealing sequence as was used for the flexible POSS species, as shown in figure 4.3.4.

$T_8 t\text{-butyl}_8$			
normalised eigen-values $(Da/\text{Å}^2)$	200 K	260 K	320 K
eigenvalue 1	0.3119	0.3123	0.3139
eigenvalue 2	0.3374	0.3367	0.3345
eigenvalue 3	0.3506	0.3510	0.3517
spread	0.0386	0.0387	0.0378
$T_8 H_8$			
normalised eigen-values $(Da/\text{Å}^2)$	200 K	260 K	320 K
eigenvalue 1	0.327251	0.326432	0.325702
eigenvalue 2	0.33334	0.333337	0.333337
eigenvalue 3	0.339409	0.340231	0.340961
spread	0.012157	0.013798	0.015259

Table 4.2: The normalised eigenvalues from the average moment of inertia values for the $T_8 tert\text{-butyl}_8$ and $T_8 H_8$ systems at a range of temperatures.

(a)

(b)
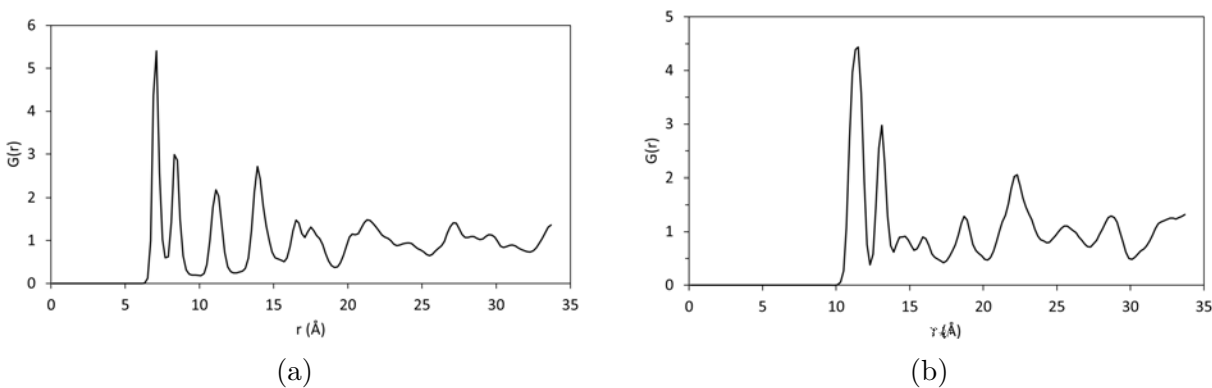
Figure 4.3.3: The G(r) analysis for $T_8 H_8$ (left) and $T_8 tert\text{-butyl}_8$ (right) at 310 K

(a) T_8H_8 (b) T_8*tert*-butyl$_8$
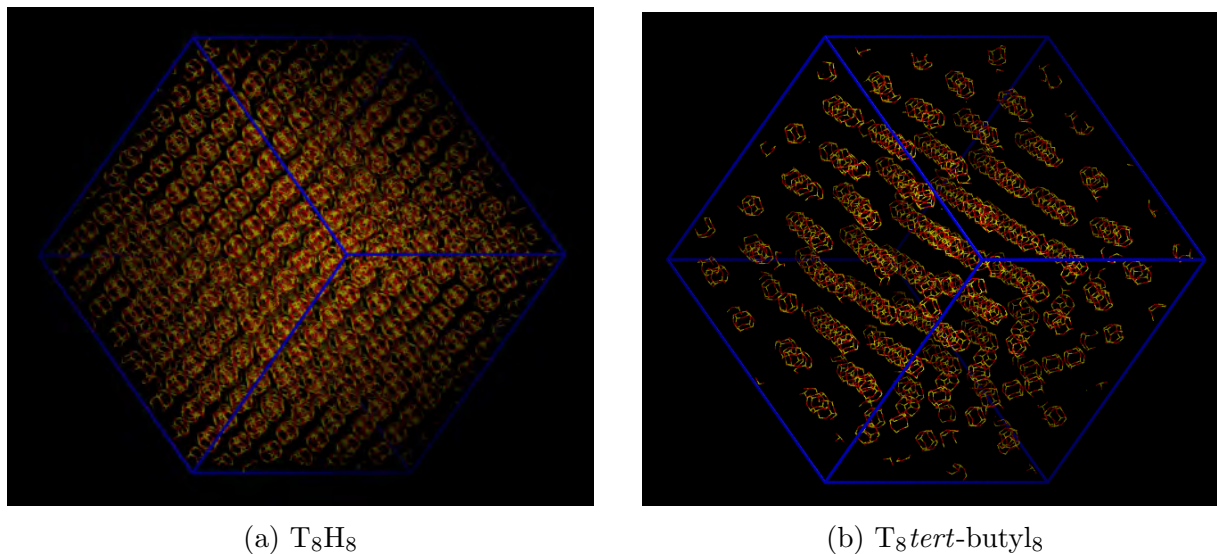
Figure 4.3.4: Configuartion visualisations from the simulation of T_8H_8 (left) and T_8*tert*-butyl$_8$ at 310 K

This spontaneous formation of highly ordered systems from initially disordered configurations prompted us to investigate into these systems at significantly higher temperature. As mentioned in 2.2, experimentally, T_8H_8 begins to undergo sublimation at 473 K. Thus I have investigated T_8methyl$_8$, T_8*tert*-butyl$_8$ and T_8*iso*-butyl$_8$ in the temperature range 600 - 800 K. The molecular structure of these systems is given in figure 4.3.5. For this, I have used a cooling sequence across this range, with a temperature decrement of 20 K. Initial annealing runs were conducted at 900 and 850 K for 0.5 ns each before each cooling sequence. The system size was set at 30,000 atoms. In figure 4.3.6, the mobility of T_8methyl$_8$ molecules over the course of the cooling sequence is presented. As shown, at 680 K and above, there is a great deal of molecular mobility. Below this temperature, however, the mobility is reduced to the level observed at the lower temperature cooling sequence range.

(a) T$_8$methyl$_8$

(b) T$_8$*tert*-butyl$_8$

(c) T$_8$*iso*-butyl$_8$
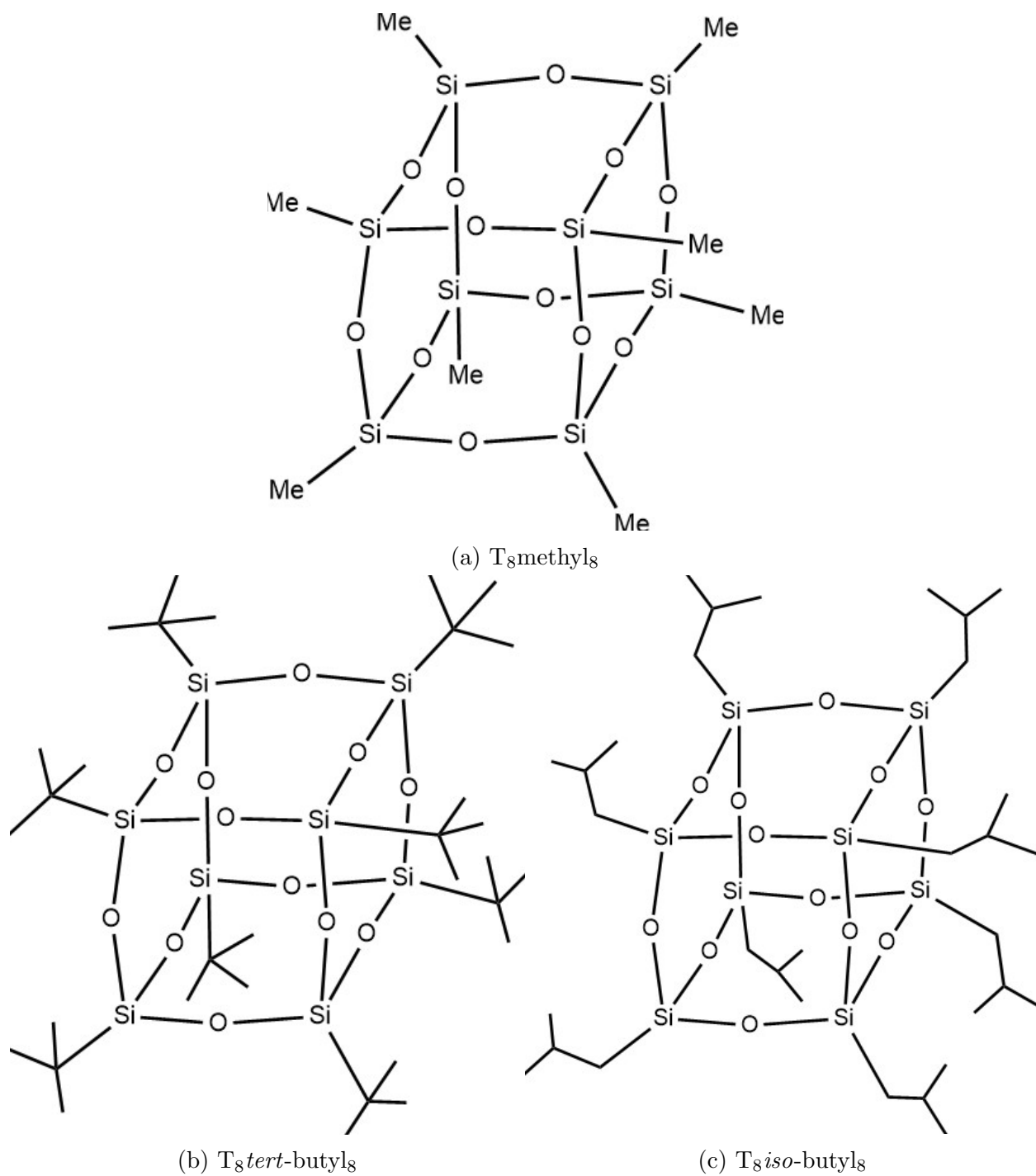
Figure 4.3.5: The molecular structure of in-flexible POSS structures
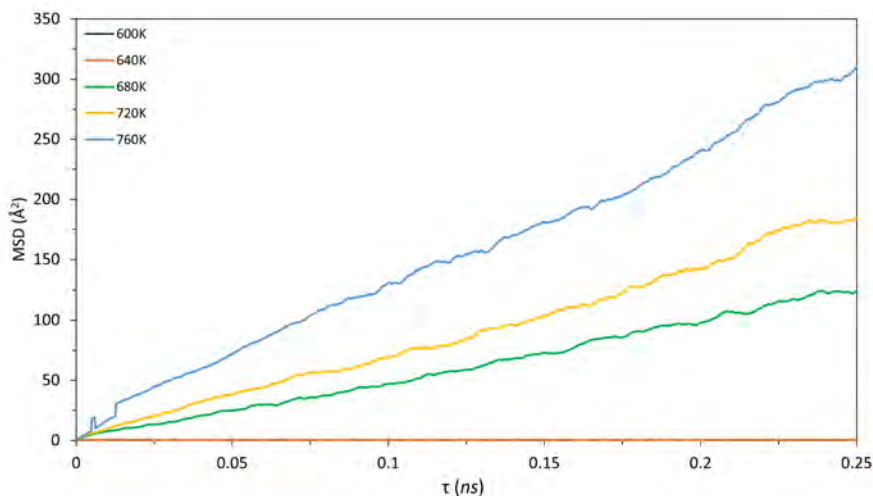
Figure 4.3.6: The MSD analysis for T_8methyl$_8$ at high temperature

Interestingly, through the use of G(r) analysis, I have again identified the formation of a near-perfect crystalline phase from liquid. Figure 4.3.7 presents these results. As shown, at 740 K, these molecules behave similarly to a liquid of spherical species with diffusive mobility. At 640 K, the system has organised to a crystalline phase. Thus, these systems exhibit a crystallisation temperature (T_c) rather than a glass-transition temperature.

(a)

(b)
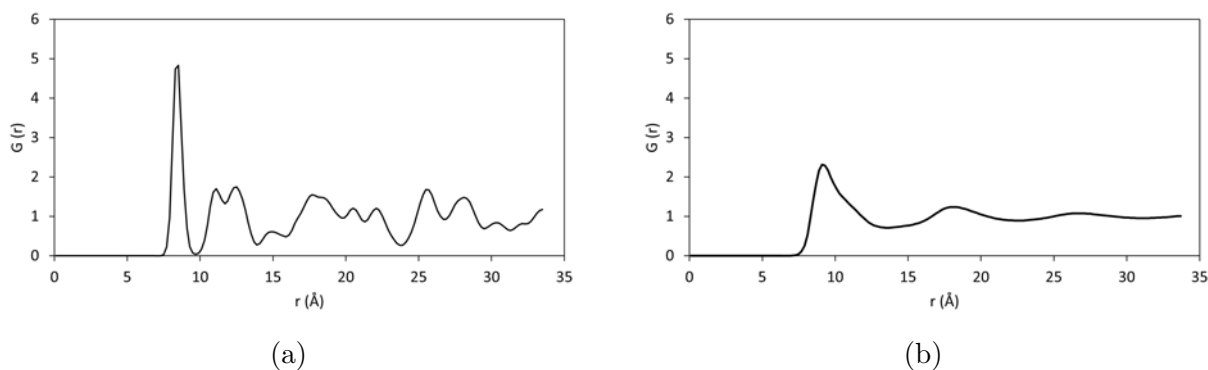
Figure 4.3.7: The G(r) analysis of T_8methyl$_8$ at 640 K (left) and 740 K (right)

To characterise the T_c for this system I have studied the rotational freedom of each molecule over the course of each simulation. Here, I have used the rotation autocorellation function covered in section 3.8.6. The gradient of the natural log for the rotation autocorellation is shown in figure 4.3.8. Here, the capacity for T_8methyl$_8$ molecules to rotate begins

at 660 K, where there is a slight displacement from 0 in the natural log gradient. These data also strongly correlate with the G(r) analysis for crystal formation.
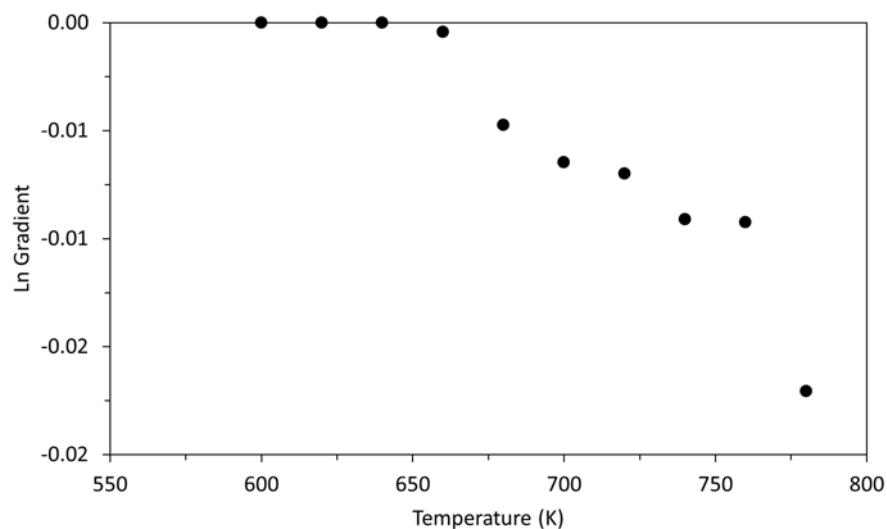
Figure 4.3.8: The calculated gradient for the natural log of the rotation autocorellation for each molecule of T_8methyl$_8$ at a high temperature

In addition, I have studied the higher order T_8*tert*-butyl$_8$ structure at high temperature. Interestingly, despite the higher proportion of organic character, the T_c for this system appears at a much higher temperature. In figure 4.3.9, I present the MSD analysis for the T_8*tert*-butyl$_8$ system at high temperature. Here, all temperatures below 800 K exhibit very little mobility.
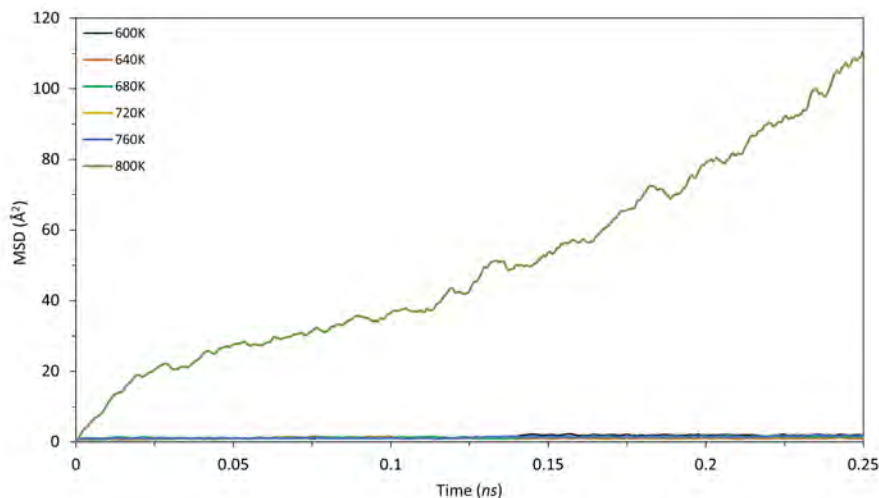
Figure 4.3.9: The MSD analysis for T_8*tert*-butyl$_8$ at high temperature

For this system, the crystal phase is observable at much higher temperature than T_8methyl$_8$ POSS. In figure 4.3.10, the G(r) analysis for this system is presented at 740 and 780 K. Again, the system passes from a freely diffusive fluid state, exhibiting spherical fluid type packing, to a highly ordered crystal phase over the course of the cooling sequence.

(a)   (b)
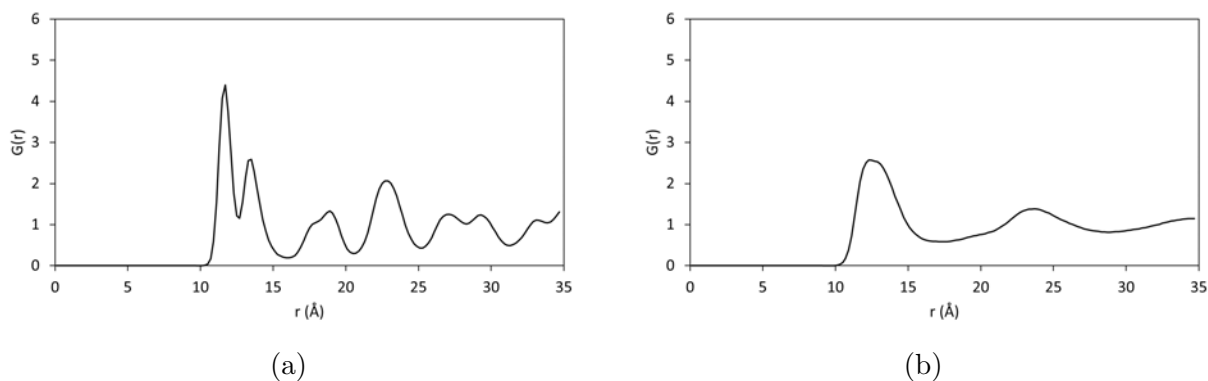
Figure 4.3.10: The G(r) analysis of T_8*tert*-butyl$_8$ at 740 K (left) and 780 K (right)

Again, I am able to characterise this transition from the molecular rotation as I did for the T_8methyl$_8$ system. These results are shown in figure 4.3.11. Below 760 K, these molecules do not rotate, presumably due to their confinement within the crystal structure. At 760 K, the system enters a fluid state, permitting the molecules to translate and rotate.
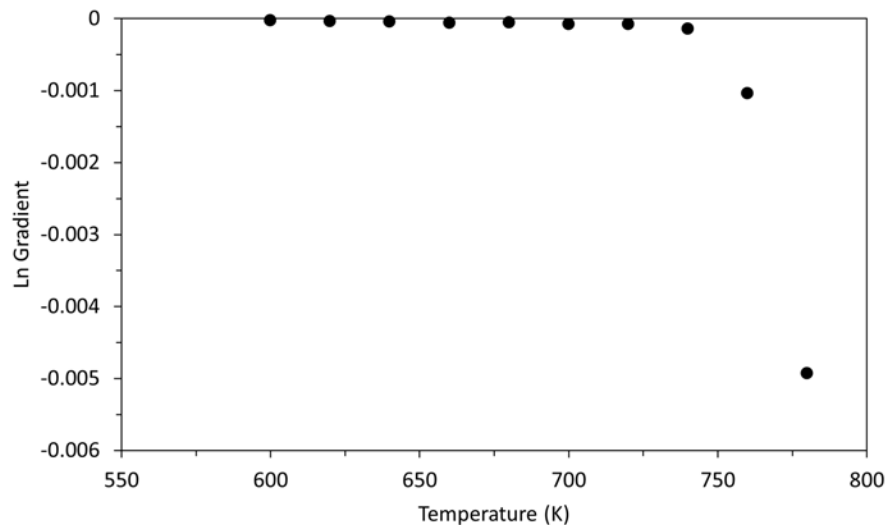
Figure 4.3.11: The calculated gradient for the natural log of the rotation autocorellation for each molecule of $T_8 tert$-butyl$_8$ at a high temperature

As a final demonstration of the importance in functionalising group selection, I have investigated the behaviour of $T_8 iso$-butyl$_8$ POSS at high temperature. Despite the molecular formula being identical to the $T_8 tert$-butyl$_8$ system, these systems have very different behaviour. In figure 4.3.12, I present the MSD analysis for this system at high temperature. As shown, the mobility of this system is well maintained throughout this cooling sequence.
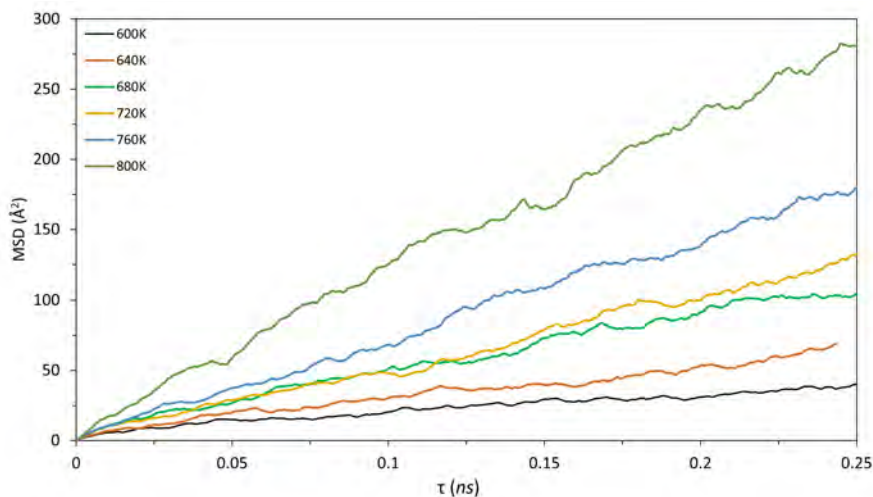
Figure 4.3.12: The MSD analysis for $T_8 iso$-butyl$_8$ at high temperature

The rotation autocorrelation analysis for this system is also indicative of a fluid system

where the natural log gradient follows a negative linear relationship with temperature as shown in figure 4.3.13.
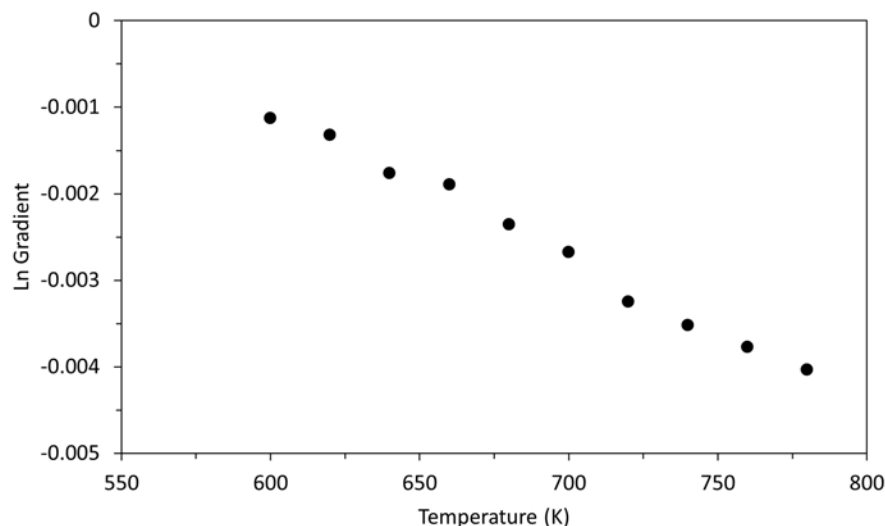
Figure 4.3.13: The calculated gradient for the natural log of the rotation autocorellation for each molecule of $T_8 iso$-butyl$_8$ at a high temperature

Finally, for this system I have utilised G(r) analysis for this system as shown in figure 4.3.14. Here, I present the G(r) analysis for $T_8 iso$-butyl$_8$ at 600 and 740 K. At both temperatures, I observe that the G(r) is very similar, indicating that the state of matter has not changed. Partnered with the observed mobility and rotational freedom, I can conclude that this system maintains a liquid state throughout this cooling sequence.

(a)   (b)
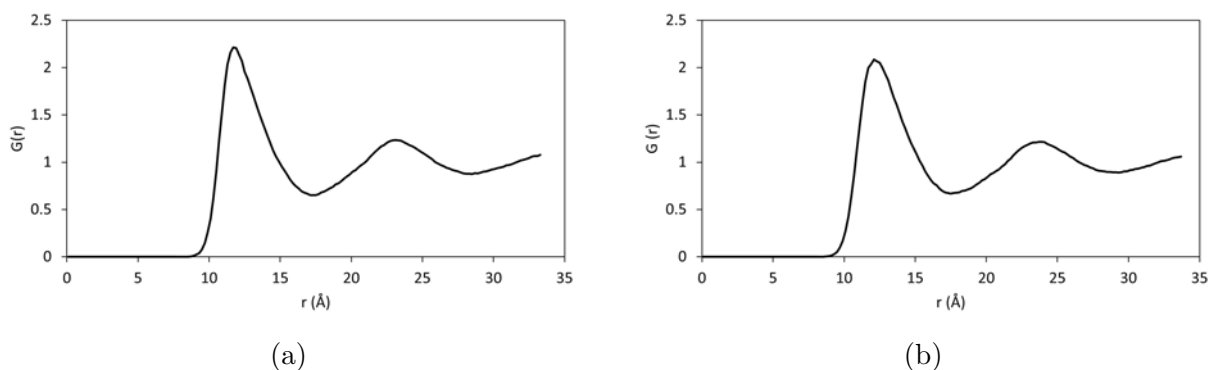
Figure 4.3.14: The G(r) analysis for $T_8 iso$-butyl$_8$ at 600 K (right) and 740 K (left)

4.4 Heterogeneously Functionalised POSS Systems

4.4.1 Systematic study of Heterogeneous POSS

Within the previous section of this Chapter, we have focused on fully functionalised POSS systems with a singular functionalising moiety. From this, we have demonstrated a link between molecular shape and glass transition through the characterisation of molecular packing and mobility. We now investigate how chemical variation within the molecular structure can change the macroscale properties and molecular level behaviour of POSS systems.

For this, we have constructed a range of POSS variants featuring different functionalising groups. The chosen moieties reflect those discussed in the previous section. Here, we construct arrangements in which four of the eight vertices have been functionalised with different organic groups. We have organised the morphologies for these molecules into two categories, the Shuttlecock (SC) and Tetra (Tet) conformations as shown in figure 4.4.1. The remaining structures have been functionalised with hydrogen or a short aliphatic group. Collectively, we shall refer to these POSS systems as heterogeneously functionalised POSS.
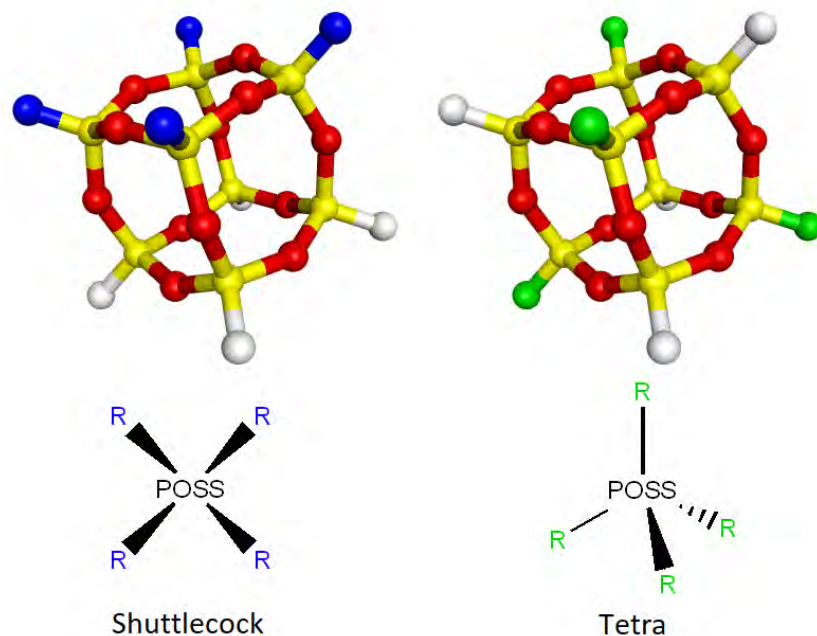
Figure 4.4.1: The molecular structures of the SC (Left) and Tet (Right) Heterogeneous POSS configurations.

We have conducted a systematic study of these species to investigate the change in macroscopic properties with molecular level changes. We use the alkyl methacrylate functional group with different linker lengths as the repeating motif. Initially, the remaining vertices have been functionalised with methyl groups. In both the SC and TET conformation, we have simulated these POSS systems with linker lengths from propyl to hexyl at a system size of 30,000 atoms.

We will first discuss results from the simulation of heterogeneous T_8propyl-methacrylate$_4$methyl$_4$ systems in the SC and TET conformation. These molecular structures are given in figure 4.4.2.
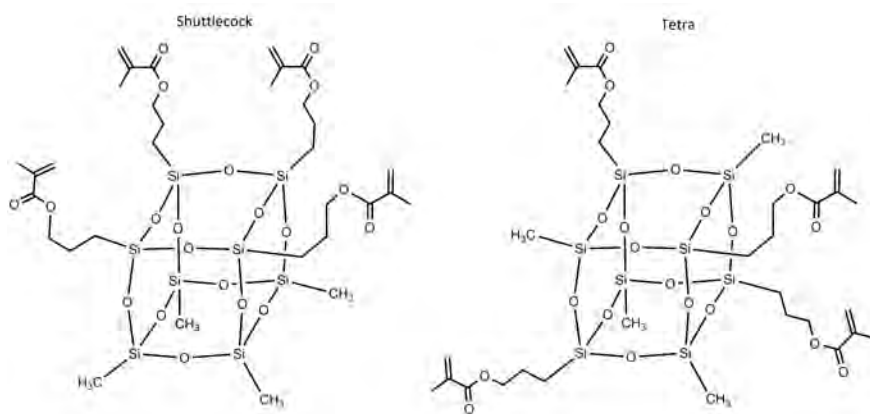
Figure 4.4.2: The molecular structures of heterogeneous T_8propyl-methacrylate$_4$methyl$_4$. Both the SC (Left) and TET (Right) configurations are displayed.

Similarly to the octa-functionalised POSS demonstrated in section 4.2.1, the SC and TET morphologies exhibit very little molecular mobility. In figure 4.4.3, we present the MSD analysis for the SC and TET T_8propyl-methacrylate$_4$methyl$_4$ over a range of temperatures. As shown, throughout this cooling sequence, these systems exhibit very little movement. This behaviour has been observed for all heterogeneously functionalised POSS systems.

(a)   (b)
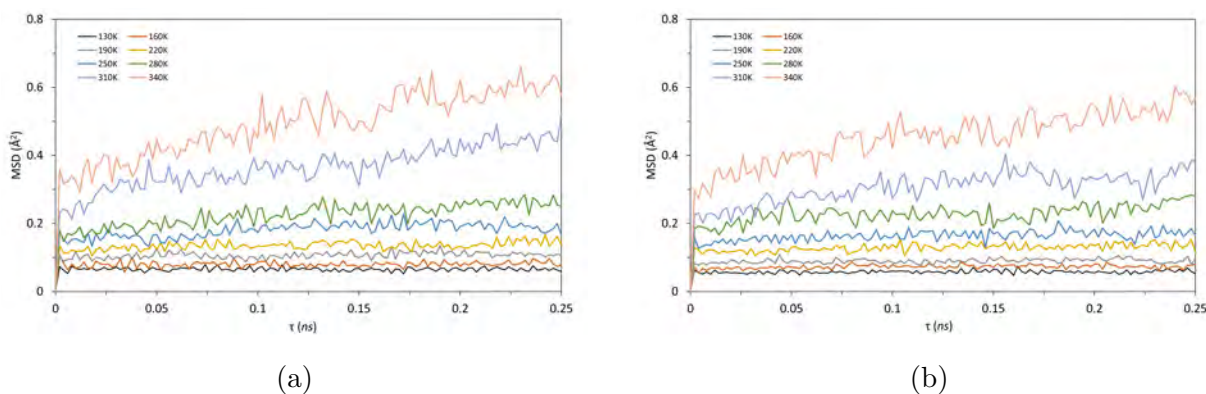
Figure 4.4.3: The MSD analysis for T_8propyl-methacrylate$_4$methyl$_4$ in the SC (left) and TET (right) morphologies at a range of temperatures.

As shown in figures 4.4.4a and 4.4.4b, from the specific volume temperature method, we predict Tgs of 258.3 K and 271.7 K for the SC and Tet conformations respectively. This difference indicates the relevance of structural parameters on the macroscale properties of these systems. In figures 4.4.4c and 4.4.4d, we also provide the data for the standard

deviation in the MOI(T) relationships for the same systems. From this method, we predict T_g values of 267.6 and 269.6 K for the SC and Tet systems. These values are in good agreement with those data using the former method as both fall within a 10 K range of the V(T) calculated values.

(a) T_8propyl-methacrylate$_4$methyl$_4$ SC

(b) T_8propyl-methacrylate$_4$methyl$_4$ TET

(c) T_8propyl-methacrylate$_4$methyl$_4$ SC

(d) T_8propyl-methacrylate$_4$methyl$_4$ Tet
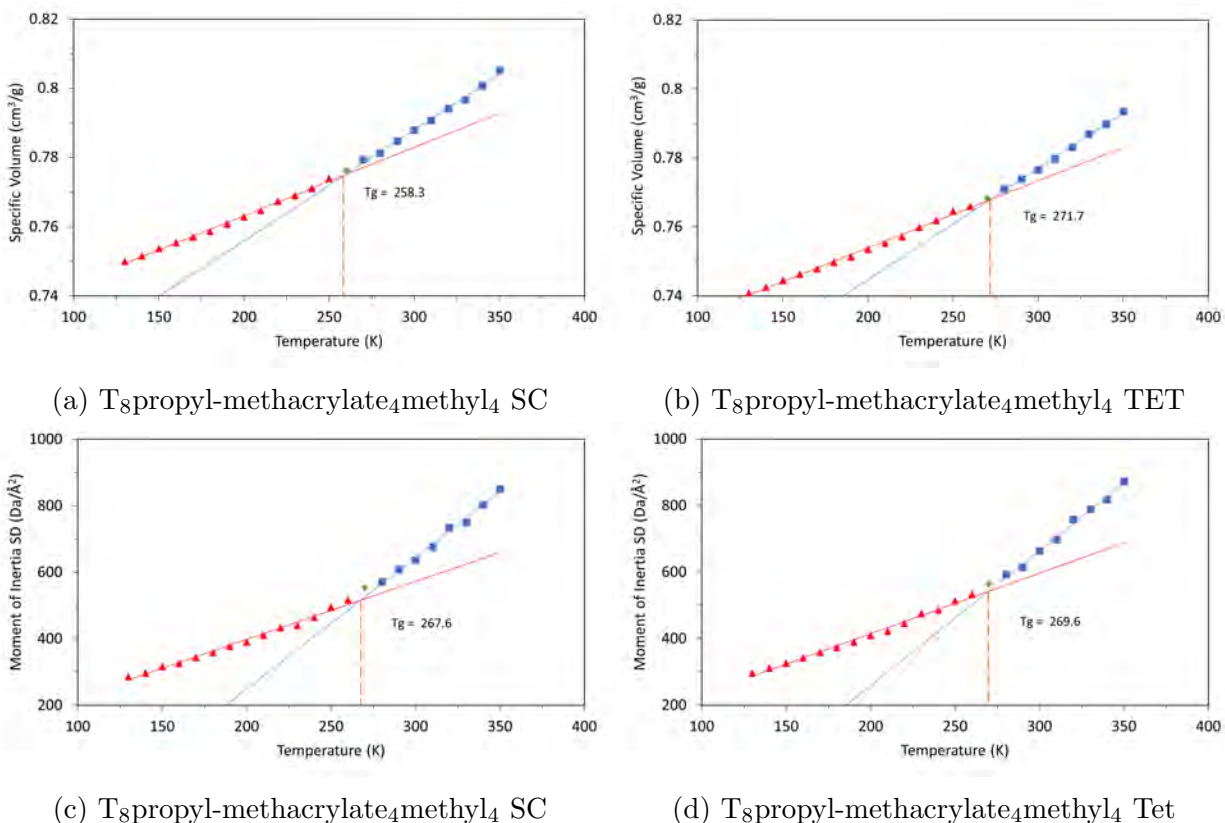
Figure 4.4.4: The specific volume temperature, and MOI SD temperature relationships for the SC (left) and TET (right) conformations of T_8propyl-methacrylate$_4$methyl$_4$ hetero functionalised POSS

In Figures 4.4.5a and 4.4.5b, we present the predicted T_g for hetero SC and TET functionalised POSS as a function of linker length. For the SC systems, The V(T) and MOI(T) predicted T_g values are in good agreement. However, unlike the octa-functionalised system, we do not observe a linear trend with linker length. From Propyl to Butyl linker, we identify an increase of 30 K for the V(T) method and 25 K for the MOI(T) method. The T_g then trends downward with increasing linker length until the hexyl length which has similar predicted T_g values to the propyl length. This sudden rise and fall in predicted T_g is not

observed for the Tet systems. Again, the predicted T_g for the V(T) and standard deviation in MOI(T) methods are in agreement. The predicted T_g values decrease from 269.9 to 259.1 K from propyl to hexyl linker length from the standard deviation in MOI method. A downward trend is also observed from the standard deviation in the MOI(T) method, however there is an increase in the T_g from Butyl to Pentyl.

(a) SC Hetero POSS   (b) TET Hetero POSS
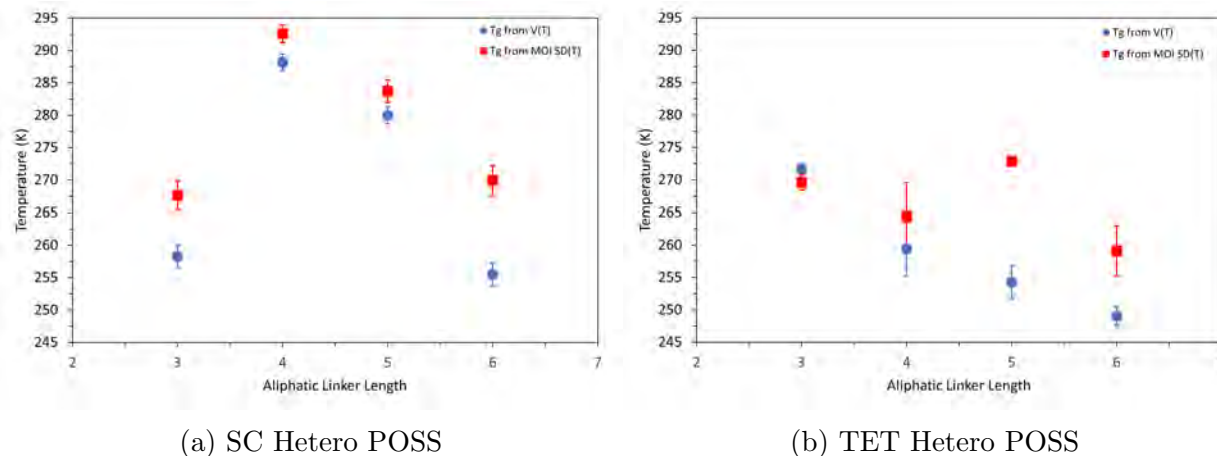
Figure 4.4.5: The predicted T_g for SC (left) and TET (right) T_8linker-methacrylate$_4$methyl$_4$ POSS with different linker lengths. Tgs are predicted using the specific volume temperature relationship (blue) and standard deviation in the MOI method (red).

These results demonstrate that divergence in molecular configuration has an acute effect on macroscale properties. To investigate the nature of this difference, we have carried out two different methods for calculating the G(r). Typically, for an atomistic molecular system, the G(r) is taken from the centre of mass which, in an octa functionalised POSS molecule, is at the centre of the the POSS cube. However, intrinsically for the SC system, the mass is distributed asymmetrically. This results in the centre of mass residing closer to the methacrylate functionalised facet on average. This provides an opportunity to investigate how the position of the POSS cages relate to one another, as well as the overall molecules. In figure 4.4.6, we present the G(r) analyses for the the center of mass of the whole molecule (blue) and the Silica core independently (orange) for T_8propyl-methacrylate$_4$methyl$_4$ and T_8butyl-methacrylate$_4$methyl$_4$ SC and TET systems at 310 K. For both SC systems (figures 4.4.6a and 4.4.6c), the G(r) plot is sensitive to the point of reference. Where the silicon

atoms have been considered only (orange), the first peak is a sudden sharp rise to a G(r) value of 2 at 9 $\mathring{A}$ followed by a comparatively flat amorphous behaviour. This suggests the formation of dimeric couplings within the first coordination sphere. As this peak occurs at a small distance, we can infer that the methyl functionalised facet of the molecule are preferentially stacking face to face. For the TET conformation, the 'all atom' and 'Si only' plots agree far more closely. This slight difference is due to the mobility within the methacrylate functional groups producing micro-differences in the positioning of the centers of mass. Figures 4.4.6c and 4.4.6d display the same G(r) plot but for the T_8butyl-methacrylate$_4$methyl$_4$ hetero functionalised POSS. For both the SC and Tet conformations, we see the same data trend as those seen for the hetero T_8propyl-methacrylate$_4$methyl$_4$ POSS.

(a) T_8Propyl-methacrylate$_4$Methyl$_4$ SC (b) T_8Propyl-methacrylate$_4$Methyl$_4$ TET

(c) T_8Butyl-methacrylate$_4$Methyl$_4$ SC (d) T_8Butyl-methacrylate$_4$Methyl$_4$ TET
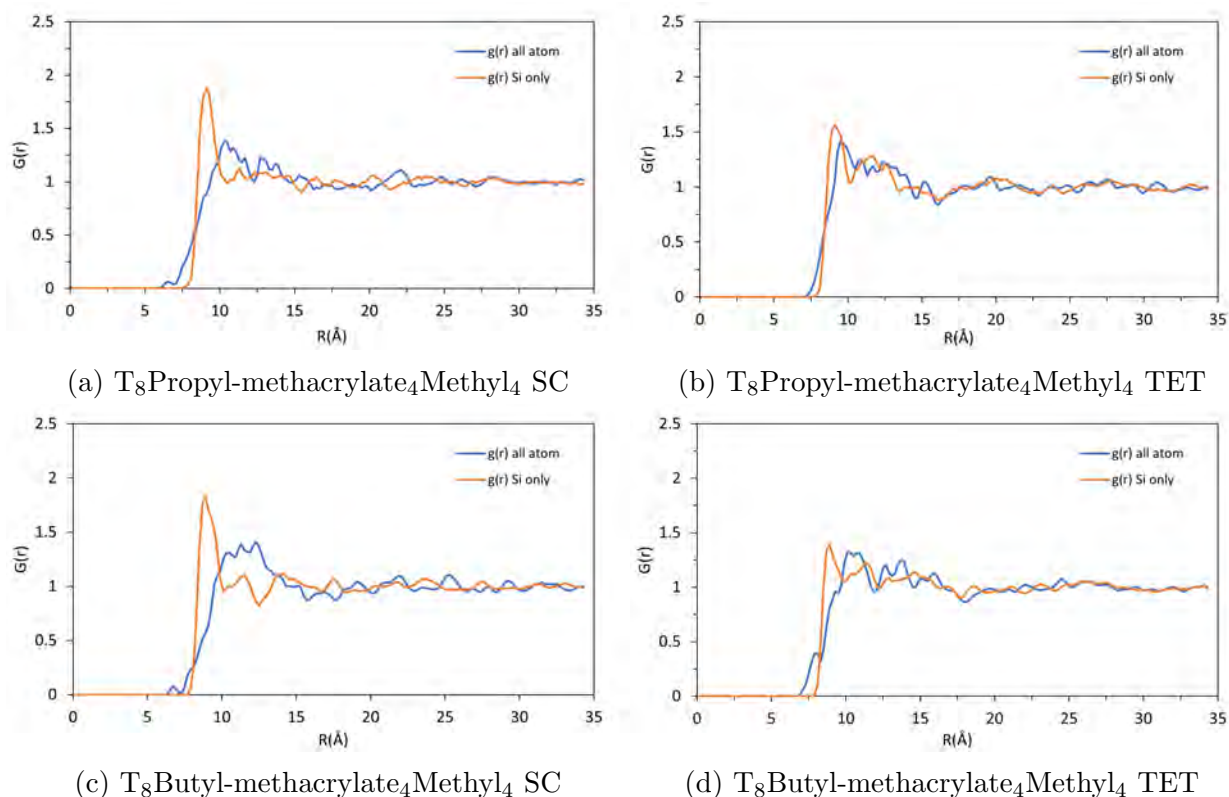
Figure 4.4.6: The G(r) analysis for T_8propyl-methacrylate$_4$methyl$_4$ and T_8butyl-methacrylate$_4$methyl$_4$ in the SC (left) and Tet (right) morphologies at 310 K. The blue G(r) is from the center of mass of every atom, and the red line is from the center of mass from the Si atoms only.

To assess reproducibility, we have again carried out G(r) analyses on two additional

replica systems for the $T_8Propyl-methacrylate_4Methyl_4$ and $T_8butyl-methacrylate_4Methyl_4$ SC and TET systems. Each replica system has the same number of molecules and force-field descriptions with the starting configurations randomly seeded. Annealing of the system under went the same routine as previously described, but the cooling sequence was restricted to a final temperature of 260 K. This range has been used as we know from visualisations, MSD data and G(r) analysis that these molecules do not undergo translational movement en masse. In figure 4.4.7, I can see that for both the all atom and Si only G(r) calculation, the replica data is in good agreement with the original G(r) for plots for the SC and Tet system.
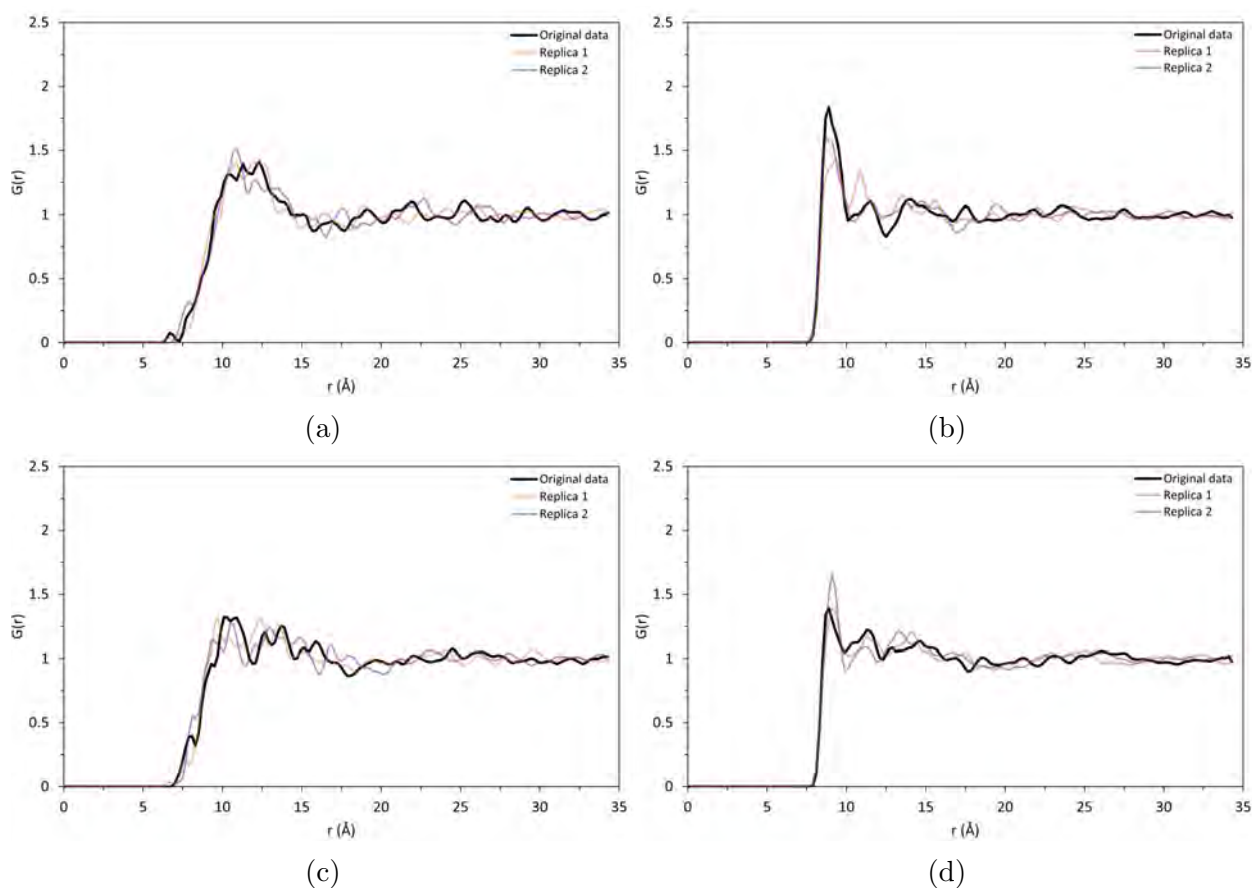
Figure 4.4.7: The G(r) analysis of $T_8butyl-methacrylate_4methyl_4$ and replicas at 310 K in the SC (top) and TET (bottom). These G(r) analyses are taken from all atoms (left) and the silicon atoms only (right).

In figure 4.4.8, We have used G(r) analysis to analyse six replica $T_8propyl-methacrylate_4methyl_4$

systems in addition to the original G(r) data presented in figure 4.4.6. Here, for the SC morphology, the replica data are in good agreement with the original G(r) data. Also, the trend seen in the T_8butyl-methacrylate$_4$methyl$_4$ Si atom only G(r) that these molecules preferentially form dimeric clusters at short range is also present in the T_8propyl-methacrylate$_4$methyl$_4$ SC morphology. Conversely, the T_8propyl-methacrylate$_4$methyl$_4$ TET morphology show similar behaviour when only Si atoms are considered. However, when all atoms are considered, the T_8propyl-methacrylate$_4$methyl$_4$ systems produce a flat G(r) relationship.
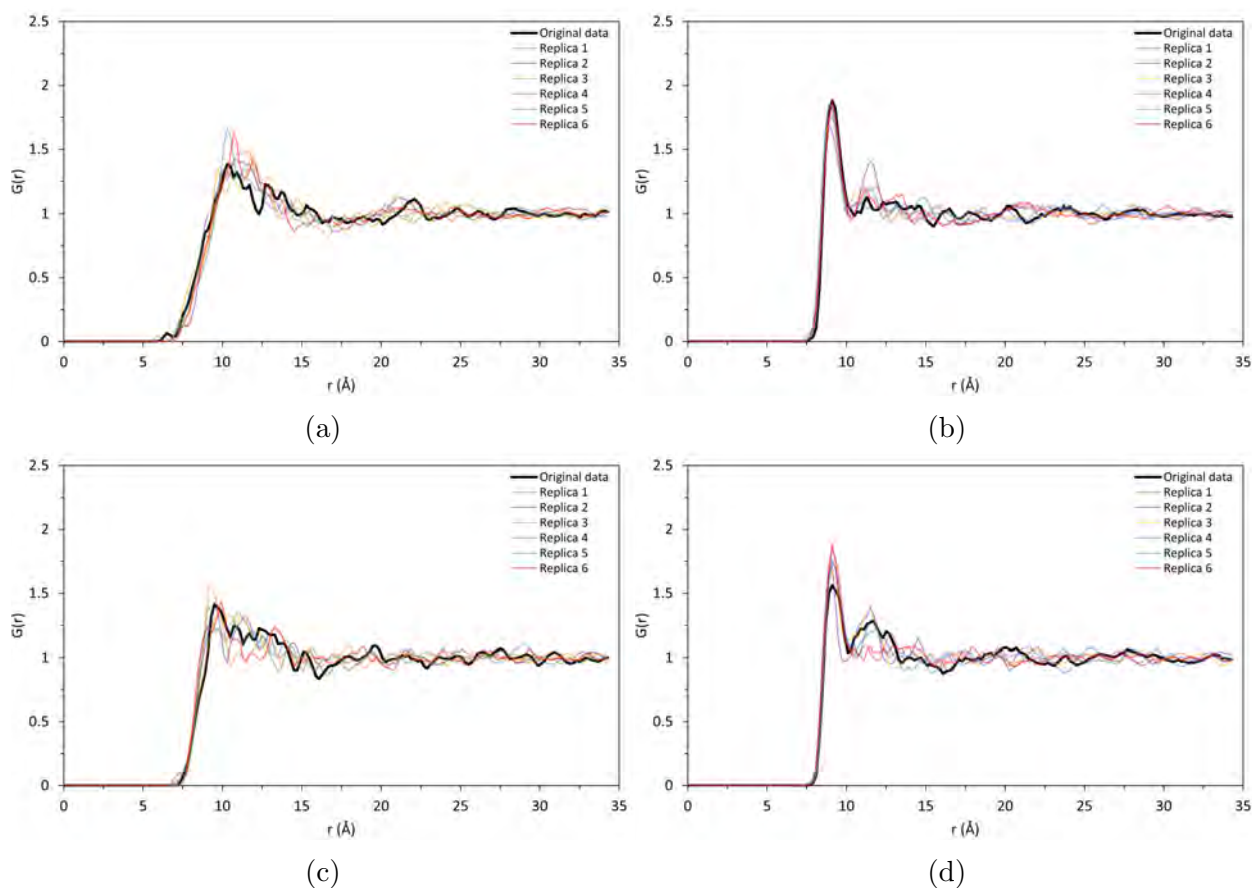
Figure 4.4.8: The G(r) analysis of T_8propyl-methacrylate$_4$methyl$_4$ and replicas at 310 K in the SC (top) and TET (bottom). These G(r) analyses are taken from all atoms (left) and the silicon atom cubes only (right).

4.4.2 Heterogeneous POSS with Alternative Counter Groups

To further investigate the nature of heterogeneously functionalised POSS, we have simulated heterogeneous butyl-methacrylate functionalised POSS with alternative counter groups in the SC morphology. That is to say that we have used different groups to the methyl group discussed in the previous section. Specifically, We have studied the use of hydrogen and *tert*-butyl as counter functionalisng groups, as shown in figure 4.4.9. These groups have been selected due to their different steric properties. From hydrogen to *tert*-butyl, we are systematically increasing the degree of shielding for the silica core of the POSS cube. These systems have been simulated at the same size (30,000 atoms) and with the same cooling sequence as the previous heterogeneous POSS system.
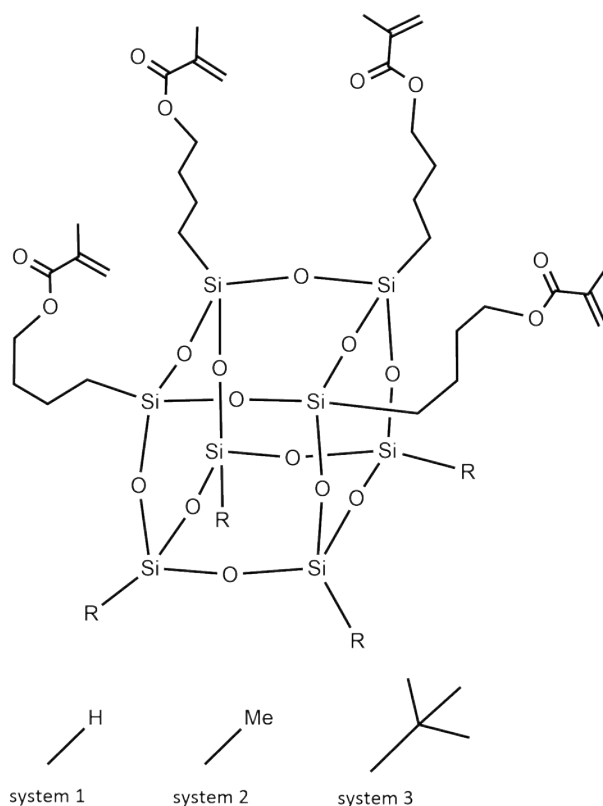
Figure 4.4.9: The molecular structure for hetero SC butyl-methacrylate functionalised POSS where 'R' represents H, Methyl or *tert*-butyl as counter functionalising groups.

In figure 4.4.10, we present the predicted Tgs for these systems from the specific volume temperature method and standard deviation in the MOI method. For all systems, the pre-

dicted Tgs from these methodologies are in good agreement. For the hydrogen, methyl and *tert*-butyl systems, from the specific volume temperature method, we predict Tgs of 275.7, 288.2 and 276.1 K respectively. The standard deviation in the MOI methodology follows a similar pattern with 271.3, 293.5 and 286.1 K being predicted respectively. As methyl is the intermediate steric structure, it is interesting to observe this system has the highest predicted Tg. This trend in predicted Tgs suggests different molecular level behaviours between systems. For both the methyl and *tert* butyl systems, the degree of fluctuation in the MOI is much greater than the hydrogen functionalised system. As discussed in section 4.3, T_8H_8 systems demonstrate very little compressiblity and variance in the moment of inertia. This phenomenon is exhibited here despite the inclusion of butyl-methacrylate functional groups as demonstrated in figures 4.4.10a and 4.4.10b.
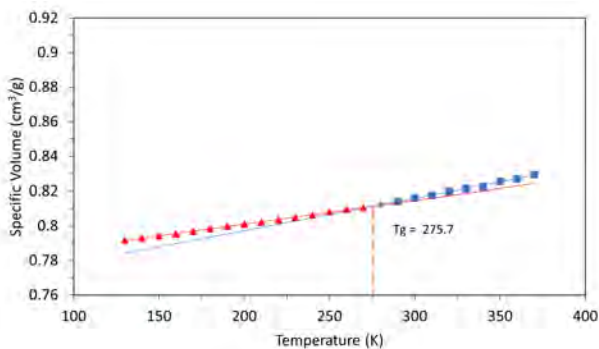
(a) T_8butyl-methacrylate$_4$H$_4$
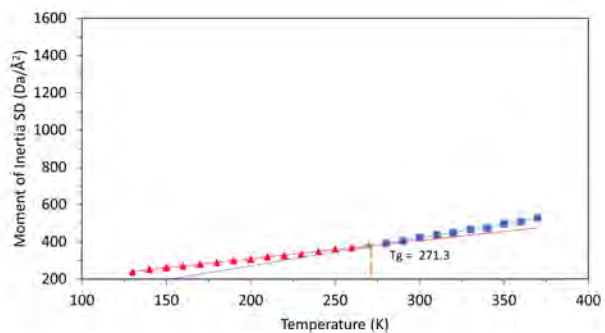
(b) T_8butyl-methacrylate$_4$H$_4$
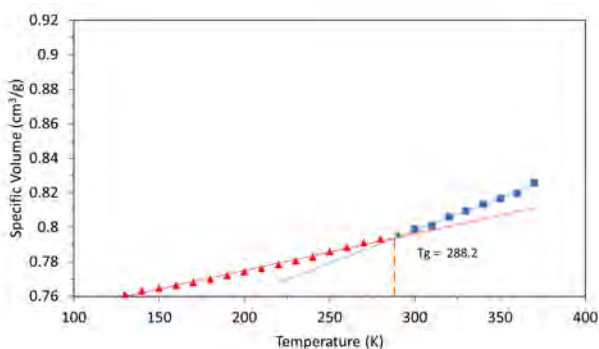
(c) T_8butyl-methacrylate$_4$Methyl$_4$
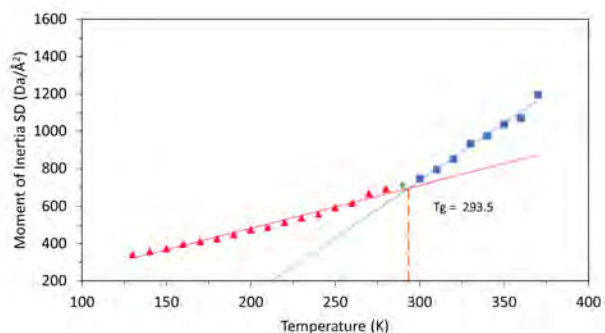
(d) T_8butyl-methacrylate$_4$Methyl$_4$
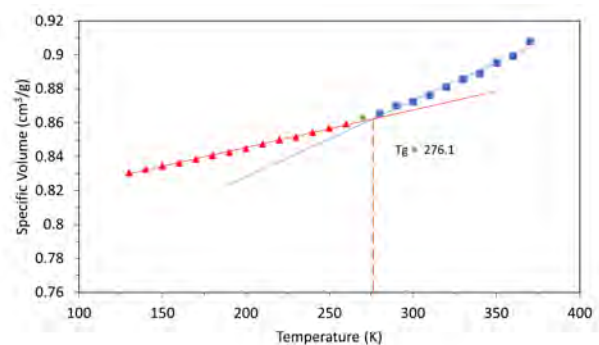
(e) T_8butyl-methacrylate$_4$t-butyl$_4$
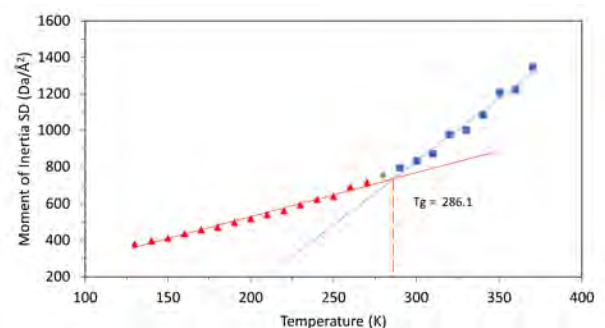
(f) T_8butyl-methacrylate$_4$t-butyl$_4$

Figure 4.4.10: The predicted Tgs for hetero SC butyl-methacrylate functionalised POSS with hydrogen, methyl and *tert* butyl counter functionalising groups. The left column contains results from the specific volume Temperature relationship and the right column contains the standard deviation in MOI Temperature relationship results.

The G(r) analyses for these systems are equally interesting and varied, as shown in figure 4.4.11. For the T_8Butyl-methacrylate$_4$H$_4$ system shown in figure 4.4.11a, for the all atom data (blue), the G(r) data depicts a well dispersed system. However, for the silicon atoms only data (orange), the G(r) is very different. Here, there is a strong shoulder peak at 8 $\overset{\circ}{A}$

prior to the larger peak at   11 $\mathring{A}$. This is due to POSS cubes preferentially packing at the hydrogen functionalised facet, similarly to the T_8propyl-methacrylate$_4$methyl$_4$ G(r) shown in figure 4.4.6a. As mentioned, the T_8butyl-methacrylate$_4$Methyl$_4$ system (figure 4.4.11b) exhibits the same packing behaviour as described for the T_8propyl-methacrylate$_4$methyl$_4$ system. By changing the methyl group to a hydrogen, we observe a much more significant change in the organisation of these molecules than if we were to alter the linker length.

The T_8Butyl-methacrylate$_4$*t*-butyl$_4$ system Si only G(r) greatly resembles the all atom G(r). *tert*-butyl and butyl-methacrylate functional groups are fundamentally different in nature, both chemically and in terms of mobility. However, this observation implies that the centre of mass of these POSS molecules is much closer to the middle of the POSS core. We may infer from this that the butyl-methacrylate functional groups are well distributed on the butyl-methacrylate fuctionalised side of the molecule.

(a) T_8Butyl-methacrylate$_4H_4$

(b) T_8Butyl-methacrylate$_4$Methyl$_4$

(c) T_8Butyl-methacrylate$_4t$-butyl$_4$
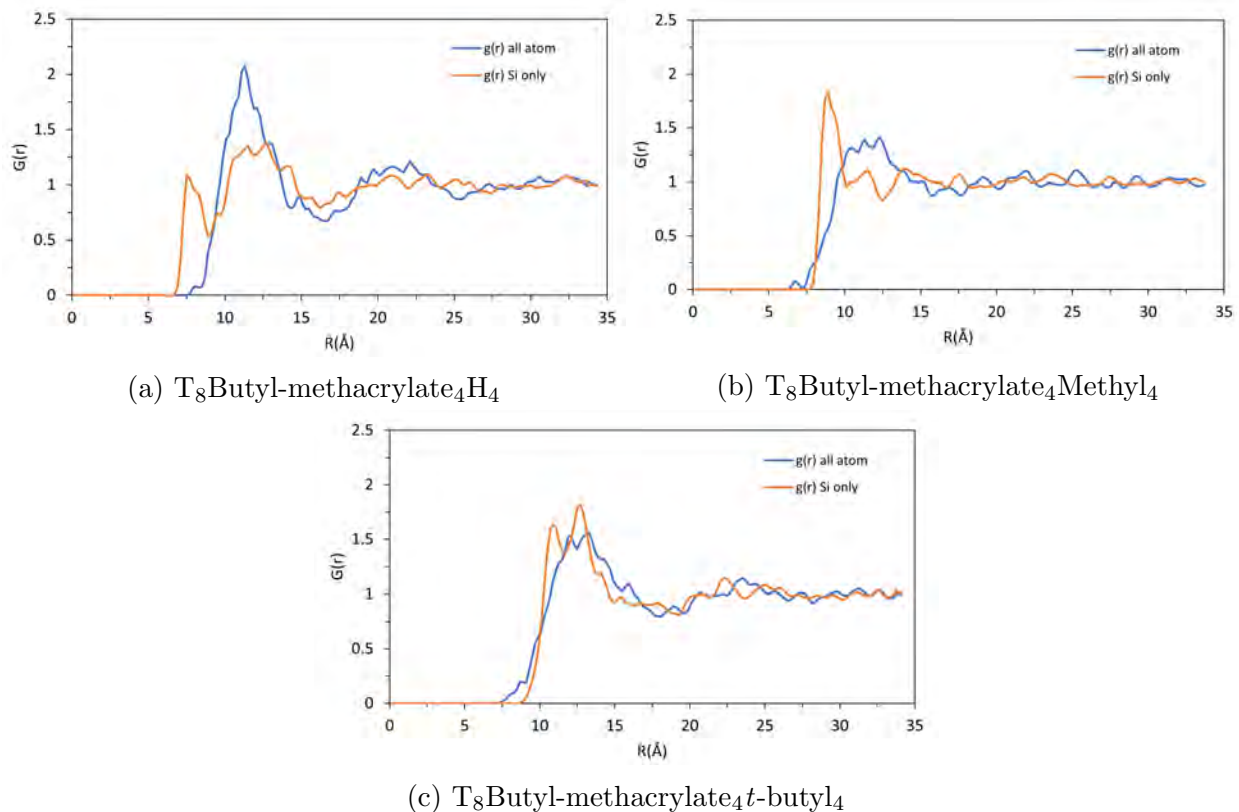
Figure 4.4.11: G(r) analysis for the hetero SC butyl-methacrylate functionalised POSS with hydrogen, methyl and *tert* butyl counter functionalising groups. The blue line displays the data where all atoms have been considered for the determination of the center of mass, and the orange line is solely from Si atoms.

We have also conducted Voronoi analysis for each of these systems. As mentioned in the previous section, through this analysis we are able to calculate average number of near neighbours, the area and volume of the 3D voronoi tessellation images. In figure 4.4.12, we provide these data for the H-stripped T_8Butyl-methacrylate$_4H_4$ SC system. As expected, for these condensed systems, the area and volume increase linearly as a function of temperature. The same trends are also observed for the methyl and *tert*-butyl systems. Due to the the entangled nature of these systems, the number of near neighbours for this system remains relatively constant at approximately 16.5 molecules on average with a standard deviation of 0.042 for all temperatures considered.

(a)   (b)

(c)
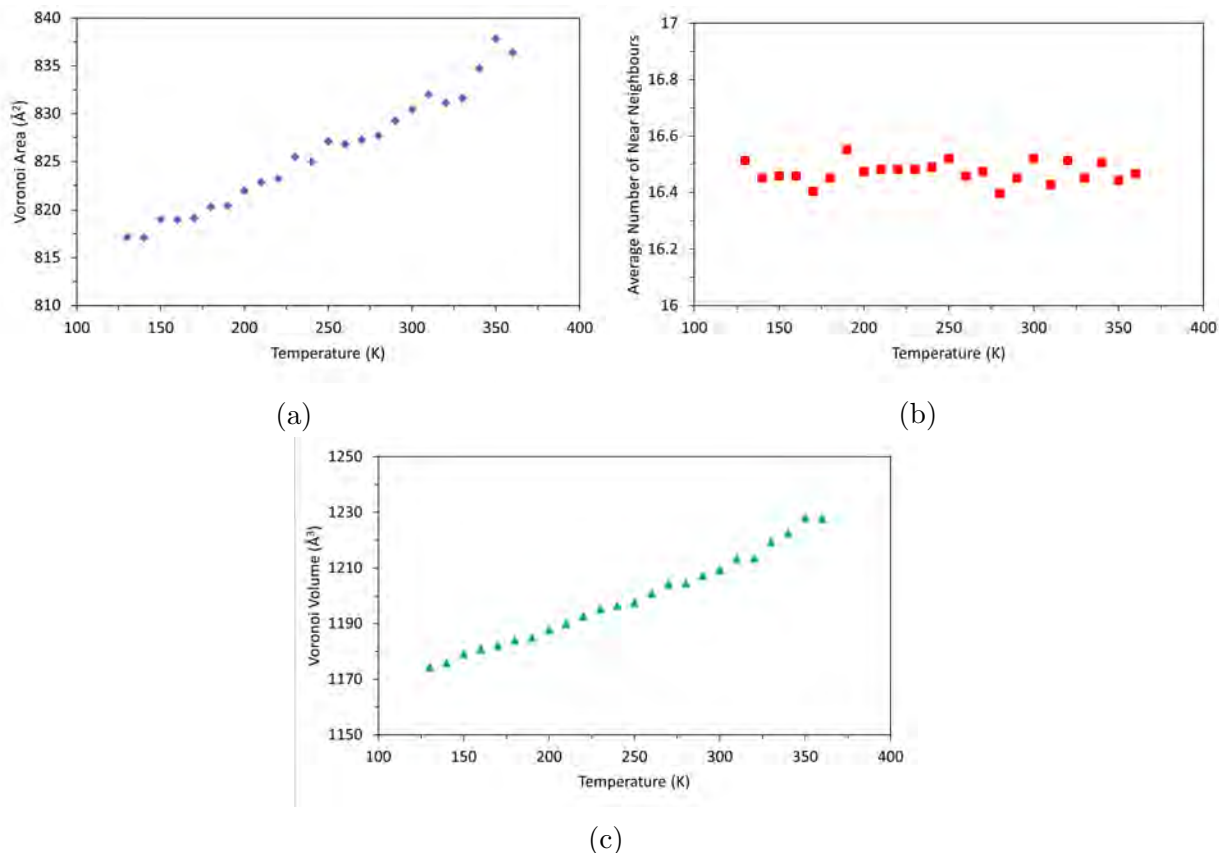
Figure 4.4.12: The area, number of near neighbours and volume for T_8Butyl-methacrylate$_4$H$_4$ SC system determined for a H-stripped atomic system.

These data become quite interesting when we consider the the number of near neighbours for all three systems, as shown in figure 4.4.13. for the hydrogen, methyl and *tert* butyl systems, there are 16.5 ± 0.042, 18.9 ± 0.14 and 17.5 ± 0.082 near neighbours on average respectively. Once again, we observe the peculiar trend in these species that the methyl functionalised system does not follow an obvious trend, as the highest number of near neighbours is exhibited by the methyl functionalised system. This data suggests that the methyl system is able to inter-digitate with the surrounding molecules to a higher degree than the other systems.
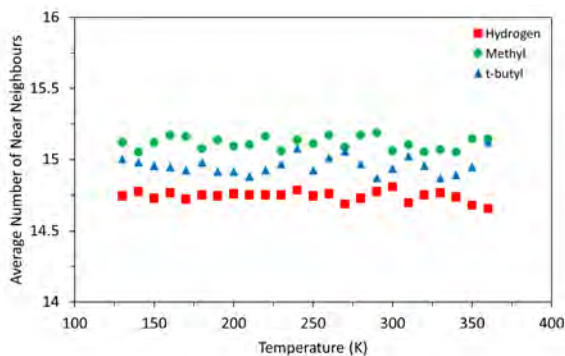
(a) All atom center of mass   (b) Si only center of mass
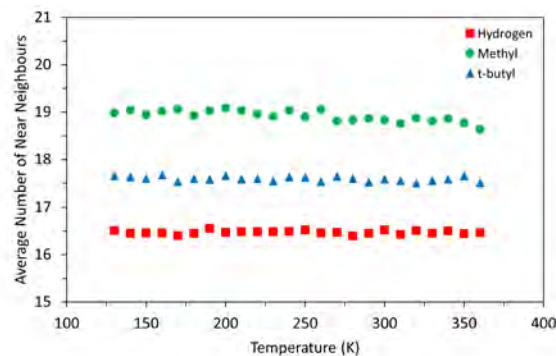
Figure 4.4.13: The average number of near neighbours for hetero butyl-methacrylate func-tionalised systems with hydrogen (red), Methyl (green) and t-butyl (blue) as measured from the center of mass (left) and hydrogen stripped skeletal structure.

We have also carried out this analysis for the T_8Butyl-methacrylate$_4$Methyl$_4$ TET hetero morphology. From this, we see another significant difference in behaviour. In figure 4.4.14, we show the Voronoi area and volume which follow the same trend as the previous systems. However, the average number of near neighbours is 20.5 with a standard deviation value of 0.08 across the range of temperatures. This is the highest value observed for the hetero functionalised systems. These divergences in the number of near neighbours demonstrate the importance of structural morphology when considering the capacity for inter-molecule penetration.

(a)

(b)

(c)
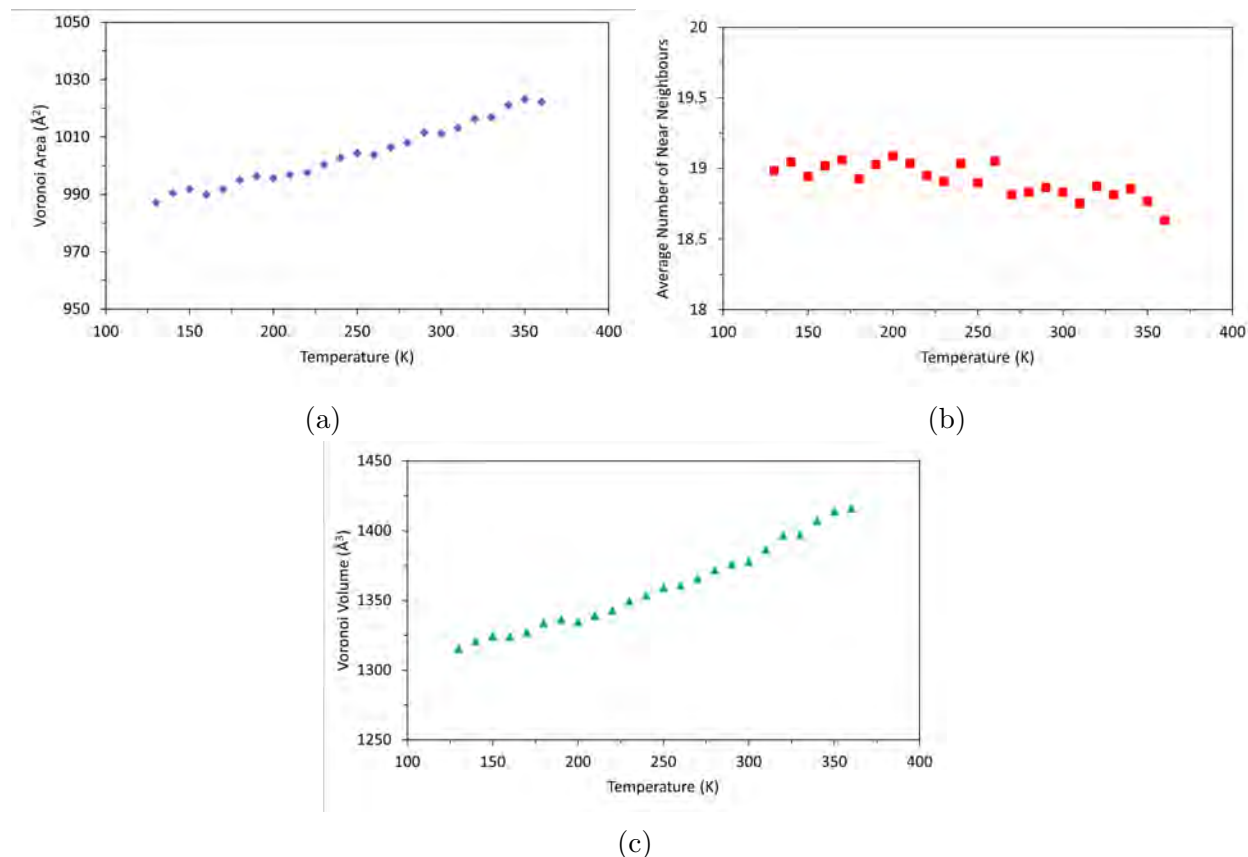
Figure 4.4.14:   The area, number of near neighbours and volume for the T_8Butyl-methacrylate$_4$counter-group$_4$ TET POSS system determined for a H-stripped atomic system.

To further demonstrate this, in figure 4.4.15 we present renderings of the T_8Butyl-methacrylate$_4t$-butyl$_4$ Voronoi tessellation images from the H-stripped structures of selected individual molecules. These images reinforce the notion that the TET morphology is able to more easily interdigitate with the surrounding molecules. As shown, the TET conformations are typically splayed outward from the silica core, thus enabling contact with further afield molecules. The SC conformations, conversely, demonstrate tighter clustering of their functional groups on an individual molecule basis.

(a) T_8Butyl-methacrylate$_4$$t$-butyl$_4$ SC (b) T_8Butyl-methacrylate$_4$Methyl$_4$ TET
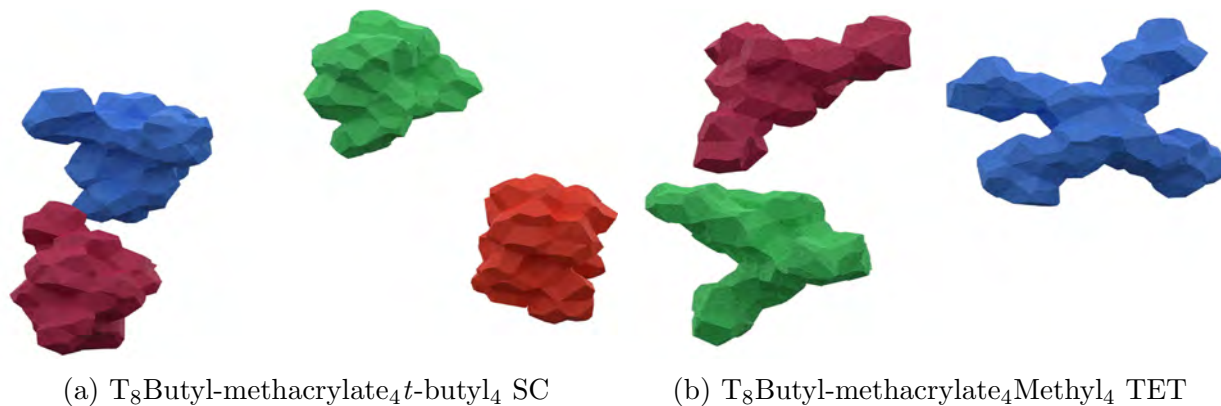
Figure 4.4.15: Renderings from a selection of voronoi tessellations for T_8Butyl-methacrylate$_4$Methyl$_4$ in the SC (left) and TET (right) morphology at 310 K.

4.5 Discussion

Within this chapter, I have presented results from the simulation of several pure POSS systems. These have included different system sizes, molecular morphologies and cooling regimes. I now discuss these results in context of the literature surrounding pure POSS systems.

Some of the earliest simulation work on pure POSS has been carried out by McCabe *et al.* These studies have investigated the molecular level features of POSS, including the internal bond lengths and bond angles of the POSS cage.[44] In addition, the crystal structures of small POSS structures such as T_8H_8 and T_8methyl$_8$ have been studied.[45] Here, starting configurations were taken from XRD data at a system size of 2,688 atoms. These structures were equilibrated at 100 and 300 K respectively, and then passed through a warming sequence of 100 K intervals for 0.1ns per temperature step until melting was observed. The capacity for each of the tested force-fields to replicate the melting behaviour for each system has been measured. In a separate study, Keiffer *et al* have investigated a mono-hexyl functionalised POSS structure..[48] This study starts with a crystalline structure and passes it through a warming and cooling sequence to produce a molten state Here, the melting transition is

identified through the specific volume temperature relationship and quantitative analysis of molecular level behaviour including MSD. In a similar study Abe *et al* have investigated the thermal expansion behaviour of several POSS structures including T_8methyl$_8$, T_8i-butyl$_8$ and T_8cyclopentyl$_8$.[51] For this study, crystal structures of each system at a system size of 4,992 atoms were subjected to a warming sequence to very high temperatures. The volume expansion as a product of temperature was determined to be unique for each structure.

These studies form the majority within the literature that are concerned with pure POSS systems. Each study is principally examining crystal structures of POSS. The derivation of melting properties and crystal integrity have been overarching themes across these papers. Within this Chapter, I have also considered crystal structures of POSS. However, rather than starting with crystal structures, I have observed their spontaneous formation for a number of small POSS species. For POSS systems with more flexible functionalising groups, cooling resulted in amorphous glassy structures. Here, I have characterised crystal formation of in-flexible POSS structures through a number of methods. Due to their the absence of entanglement and shape change due to functionalising group fluctuation, these structures exhibit high temperature crystallisation. I have been able to describe the crystal formation through G(r) analysis. Here, distinct and characteristic peaks have been identified and ascribed to the crystal structure. In addition, at high temperature in the molten state, I have characterised the crystal transition temperature for T_8methyl$_8$ and T_8t-butyl$_8$ through msd analysis and the rotation autocorrelation function as described in section 4.3. The capacity for my simulations to capture this alternative behaviour lends credibility to the effectiveness of the models and methodology employed here. To date, I am not aware of previous simulation studies reporting on POSS crystal structure formation from disordered beginnings in a pure system.

The study of pure and amorphous POSS systems have been reported on to a much lesser

degree. Work carried out by Neyertz *et al* has studied the amino functionalised POSS in the pure and amorphous state at a system size of 15,000 atoms.[49] Here, this group have investigated how macro-scale properties and molecular observations change as a function of the functionalising group. Three distinct POSS systems have been investigated; their molecular structure is given in figure 2.2.4. After annealing at high temperature, these systems are studied at 298 K at 1 Bar in the NPT ensemble for a run length of 5ns. The systems are determined to be amorphous through predicted XRD and G(r) analysis. Effective interaction potentials between the POSS species are described through observations of the behaviour of the functionalising groups. Strong functionalising group entanglement is attributed to the POSS distance of separation. This study is the first in a number of publications from this group concerned with the application of POSS species for POSS-polymer based gas separation.[137–139]

The Neyertz study is similar to the work carried out in section 4.2.1, in that, macro-scale and molecular level observations have been characterised in terms of their functionalising groups. However, there are some crucial differences. Firstly, my simulations have, at their largest, consisted of 25,000 atoms. Within my work, I have also used production level simulations over a range of temperatures which cover two states of matter, glassy and rubbery. This has allowed us to consider the temperature dependant observations with changes in the functionalising groups. I have worked to characterise the molecular level features that lead to the observed glass transition temperature through a number of techniques. The nature of the change in functionalising group is also different as I have altered the linear aliphatic content whereas the Neyertz study has primarily considered the change as a result from the introduction of aromaticity within a cyclic system.

In table 4.3, I present all predicted Tg values for the octa-methacrylate functionalised POSS systems at all system sizes. This study demonstrates the sensitivity of simulation systems

to molecular level change in terms of the impact on maco-scale properties. To characterise these systems, I have also used MSD analysis to quantify the lack of mobility observed within these systems above and below the Tg. Radial distribution function analysis has been used to describe the largely amorphous nature of these systems. Inter-molecular interdigitation between functionalising groups has been quantified through the Voronoi analysis of these systems. Finally, I have identified a molecular level descriptor, namely the breathing mode, that can be used to identify the glass transition temperature for each system in good agreement with the specific volume method of prediction. This systematic analysis has considered many different aspects of the behaviour of octa-functionalised POSS molecules in a pure state. To the best of my knowledge, the analysis of temperature dependant observables has not previously been reported for pure POSS systems. By demonstrating that the breathing mode is the molecular feature that controls the glass transition temperature, I am providing clear understanding for to experimentalist researchers on the key feature to consider for controlling the Tg of pure POSS systems. Further, the identification of this single-molecule degree of freedom as central to determining the glass transition in these systems, explains why very little system size dependence is seen in my simulations of these systems. As discussed in section 2.3, POSS species often undergo phase separation in polymer matrices. In order to control these domains of pure POSS, consideration of the breathing mode will be crucial.

15,000 atoms		
Molecular structure	Specific Volume Tg (K)	SD MOI Tg (K)
T_8Ethyl-Methacrylate$_8$	268.7	275.5
T_8Propyl-Methacrylate$_8$	258.2	274.3
T_8Butyl-Methacrylate$_8$	247.8	270.1
T_8Pentyl-Methacrylate$_8$	262.5	266.1
T_8Hexyl-Methacrylate$_8$	254.2	263
25,000 atoms		
Molecular structure	Specific Volume Tg (K)	SD MOI Tg (K)
T_8Ethyl-Methacrylate$_8$	281.4	283.7
T_8Propyl-Methacrylate$_8$	259.1	269.1
T_8Butyl-Methacrylate$_8$	263.9	263.5
T_8Pentyl-Methacrylate$_8$	261.8	260.8
T_8Hexyl-Methacrylate$_8$	260.1	264.4

Table 4.3: The predicted Tg for all octa-methacrylate functionalised POSS species from the specific volume method and Standard deviation in the moment of inertia method.

In order to bolster my understanding of the contribution from molecular morphology to the observed molecular behaviour and macro-scale properties, I have investigated fundamentally different conformations of the cubic T_8 POSS conformation in the form of tetra-functionalised POSS species. Tetra conformations have appeared in the experimental literature, however, much less frequently than the octa-functionalised counter-parts.[140, 141] Tetra-functionalised POSS have been studied through computational methods by Glotzer *et al* in 2005.[142] To date, this is the only publication I have been able to identify that considers tetra-functionalised systems. Within this study, *ab inito* calculations have been used to generate a coarse-grained model for SC $T_8R_4H_4$ POSS where 'R' represents polymer chains. The model simplifies the POSS cage to 8 united atoms. Through stochastic molecular dynamics, the formation of unique packing arrangements can be observed as a function of the 'R' groups. In addition, the nature of the implicit solvent, the temperature and POSS concentration have all been demonstrated to impact on the observed packing and arrangement of the POSS molecules. The order-disorder transition is measured as a sudden change in the interaction energies between the functionalising groups and the POSS cubes. This is a very interesting paper and demonstrates that SC tetra-functionalised POSS are

able to form unique packing arrangements within suitable implicit solvents.

Within my atomistic study of unsolvated tetra-functionalised POSS, I have investigated how molecular morphology can change the macro-scale properties and molecular level behaviour. In table 4.4, I present the predicted Tg values for tetra methacrylate-functionalised POSS species in the SC and TET morphology from the specific volume method and standard deviation in the MOI method. Here, there is a clear dependence on the morphology in respect to the predicted Tg. This is particularly evident for the T_8Butyl-Methacrylate$_4$Methyl$_4$ systems, where the SC morphology predicts Tg values +28.8 and +28.2 K greater than TET morphology for the specific volume and MOI method respectively. As I have for the octa-functionalised POSS systems, I have characterised the temperature dependent relationships between macro-scale properties and molecular level features.

Shuttlecock (SC) Morphology		
Molecular structure	Specific Volume Tg (K)	SD MOI Tg (K)
T_8Propyl-Methacrylate$_4$Methyl$_4$	258.3	267.6
T_8Butyl-Methacrylate$_4$Methyl$_4$	288.2	292.6
T_8Pentyl-Methacrylate$_4$Methyl$_4$	280	283.7
T_8Hexyl-Methacrylate$_4$Methyl$_4$	255.5	269.9
Tetra (TET) Morphology		
Molecular structure	Specific Volume Tg (K)	SD MOI Tg (K)
T_8Propyl-Methacrylate$_4$Methyl$_4$	271.7	269.6
T_8Butyl-Methacrylate$_4$Methyl$_4$	259.4	264.4
T_8Pentyl-Methacrylate$_4$Methyl$_4$	254.3	272.9
T_8Hexyl-Methacrylate$_4$Methyl$_4$	249	259.1

Table 4.4: The predicted Tg for all Tetra-methacrylate functionalised POSS species from the specific volume method and Standard deviation in the moment of inertia method.

Within this chapter, I have presented results from the atomistic simulation of POSS species as pure entities. I have conducted molecular level analyses relating to the organisation, mobility and interactions of individual molecules. Through this, I have identified that within the temperature range of 130-400 K, POSS molecules exhibit no movement en masse. In systems with long and flexible functionalising groups, this is due to the inter-molecular en-

tanglement between functionalising groups. I have demonstrated that the breathing-mode of these molecules is the principal molecular feature controlling the Tg for these systems. This has been demonstrated for POSS systems of different morphologies as I have covered both octa- and tetra-functionalised POSS. For in-flexible POSS structures, I have demonstrated the formation of highly ordered crystalline species from disordered starting configurations, and discussed the characterisation of their formation at high temperatures. Within this chapter, for a diverse range of structures and morphologies, I have attributed molecular level features to the observed macro-scale properties and material behaviours.

Chapter 5

Polymer-POSS Grafted Nanocomposites

As discussed in Chapter 2, POSS species are often incorporated into polymer matrices to form polymer nanocomposites. In addition to much experimental work, there have been a number of simulation studies on such systems which were reviewed in section 2.3.1. A fundamental choice when developing POSS nanocomposites is that between a blended and grafted approach. These approaches are different in the mechanism of interaction between POSS and polymer matrix. A blended system has dispersed POSS molecules within the matrix without covalent bonding between them. A grafted system has explicitly bonded POSS molecules along the polymer backbone to form pendant groups. Within chapters 4 and 5, I therefore undertake systematic simulation studies to explore the molecular level implications of this choice, with the aim of gaining insight as to what underpins the resultant differences observed at the macroscopic level.

Within this chapter, I present results from simulations of Polymer-POSS grafted systems. I have selected several POSS structures and investigated the molecular differences between these systems and examined the mechanisms that lead to the observed T_g when each is

grafted to a known polymer matrix. This baseline polymer is hydroxy-terminated polybutadiene (HTPB), a system which my research group has previously investigated in the context of binder materials.[110] This work is described and revisited in the context of the PCFF force-field within this section. The remainder of the current chapter then sets out the molecular behaviour observed in chemically grafted POSS-HTPB systems. In Chapter 6, I discuss equivalent simulations carried out on non-grafted POSS + HTPB systems.

5.1 Pure HTPB 311 Study

The selected polymer matrix for this study is hydroxy-terminated polybutadiene (HTPB). These materials have a range of desirable properties, including a low T_g and good environmental resilience. Because of this, HTPB has seen a variety of applications such as binders and thin film coatings.[143, 144] The nature of the HTPB molecule enables the macroscopic behaviour to be influenced directly by the microstructure.[110, 145] Control over the microstructure is typically characterised by the ratio of isomeric *trans, cis* and *vinyl* conformers within the backbone. Microstructures containing high percentage *cis* polybutadienes exhibit high resilience and abrasion resilience. In comparison, high *trans* content leads to higher tensile strength and high *vinyl* content polymers have high tread strength.[146, 147]

In a joint experimental and computational study, my group has previously investigated the molecular mechanisms that govern the glass-transition in HTPB.[110] Within this work, a number of HTPB microstructures (i.e. cis:trans:vinyl ratios) were systematically studied. Their experimentally observed and computationally predicted T_g values were then compared. The suffix attached to HTPB molecules pertains to the conformer ratio (trans:cis:vinyl) of the monomer units that make up the repeating unit of the polymer main chain. The molecular structure of HTPB 311, for example, can be seen in figure 5.1.1. A number of different HTPB microstructures, including HTPB 109 and HTPB 401, were investigated to broaden

the scope of my study.
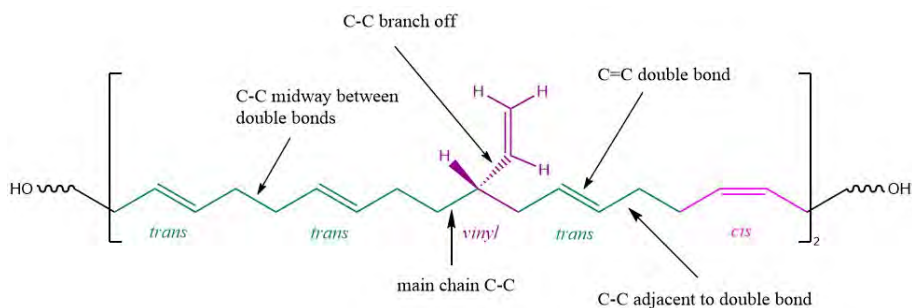
Figure 5.1.1: The Chemical structure of HTPB 311 repeat unit

Using the analysis routine covered in section 3.8.5, I calculated the average number of dihedral rotations over a threshold of 60° for each molecule over the course of each simulation. This dihedral rotation data was then compared with other observables relating to the glass transition. From this data, rotational 'hotspots' along the molecular backbone were identified as the key molecular features for these systems that give rise to the observed macroscale behaviour. In particular, the single C-C bonds adjacent to the *trans* C=C double bonds displayed by far the greatest number of rotations at temperatures above Tg. The presence of this particular group was identified as being critical for the maintenance of the rubbery behaviour of HTPB 311 at lower temperatures. Good agreement was also observed between the experimental and simulation-predicted T_g of 191 K for HTPB 311 as determined by a rotation-counting method. In the same study, the alternative microstructure HTPB 109, which contains a much higher ratio of the *vinyl* conformation, was also investigated. The higher T_g displayed by HTPB 109 was demonstrated to result from the far fewer instances of the in-chain C-C bonds adjacent to the C=C double bond of the *trans* groups. Again, this result was reflected by experimental and computational methods. Finally, this study showed little variation with polymer length beyond 10 butadiene units.

With this work in mind, I decided to utilise the HTPB 311 system for the polymer matrix of my POSS-polymer nanocomposite study, as the previous work provided fundamental

understanding of its molecular behaviour. Our previous study utilised the Dreiding force-field. In a similar fashion to PCFF, Dreiding is a general purpose force-field designed for application within organic and biological systems.[148]

In order to bridge these pieces of work, I have conducted simulations of 10-monomer chains of pure HTPB 311 with PCFF at a systems size of 30,000 atoms. In figure 5.1.2, I provide the specific volume vs temperature relationship for these systems where the Dreiding and PCFF data are shown on the top and bottom bi-linear plots respectively. The Dreiding study did not include the 300 - 350 K temperature range that has been the standard throughout this study. Nevertheless, I see some good agreement between the two force-field regimes. However, as stated in our paper simulation results from volume vs temperature do not predict T_g values in accord with the experimental value of 197K. [110]
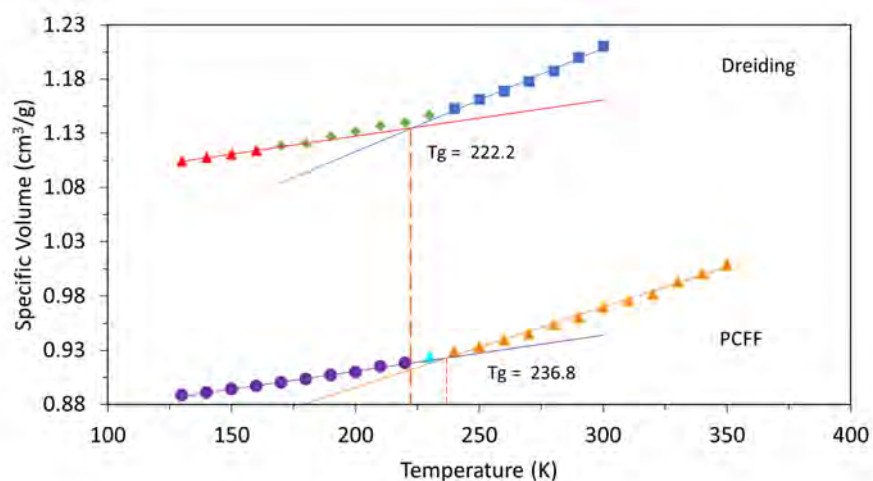
Figure 5.1.2: The specific volume vs Temperature relationship of pure HTPB 311 independently observed with Dreiding (top - red, green blue) and PCFF (bottom - purple, cyan, orange).

In figures 5.1.3a and 5.1.3b, I present the equivalent Dreiding and PCFF bilinear plots and T_g predictions for the same HTPB 311 systems using the number of Dihedral rotations approach. From these data, the Dreiding force-field out performs the PCFF system for predicting Tg. However, for both force-fields, I observe that the number of rotations about

the C-C single bonds adjacent to *trans* C=C double bonds exhibit the same qualitative transition. From this I conclude that the PCFF force-field is able to capture the key molecular mechanisms utilised by HTPB 311.
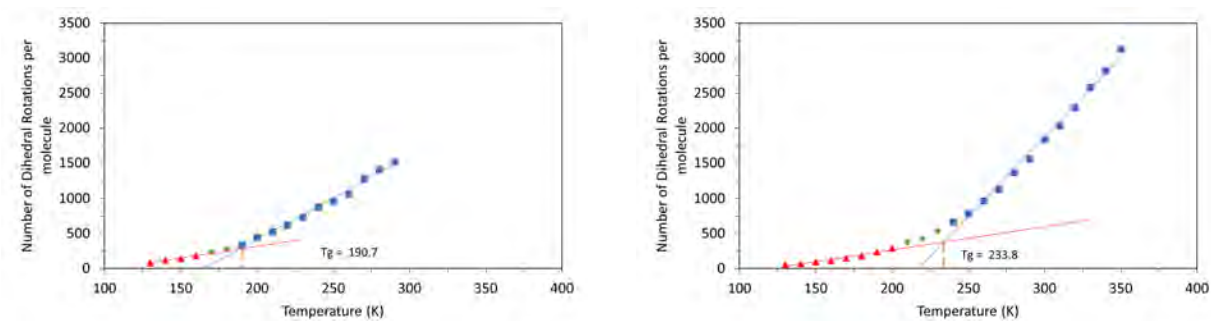
(a) Dihedral Rotation per molecule Temperature relationship for HTPB 311 with Dreiding force-field

(b) Dihedral Rotation per molecule Temperature relationship for HTPB 311 with PCFF

Figure 5.1.3

In figure 5.1.4, the average number of dihedral rotations per molecule are presented for each of the C-C bonds adjacent to the *trans* C=C bonds within the HTPB 311 backbone. This data corresponds to the initial Dreiding simulations at 200K. Figure 5.1.5 provides an alternative representation of the same data as shown in figure 5.1.4 where with the bond index relating to the C-C bonds tracks from left to right. Figure 5.1.5 also shows the equivalent data from the PCFF force-field at 200K. From this, I see the same trends in availability of dihedral rotation along the HTPB backbone, demonstrating that dihedral rotation availability is upheld across force-fields. The Dihedral rotations of C-C bonds midway between double bonds are not included here. This is because, as shown in the previous study, these barely contribute to the molecular motion, even above Tg. Chain motion is dominated by crank-shaft motion involving co-operative rotation of pairs of single-bonds, but the mid-way C-C bond cannot pair up in this fashion.
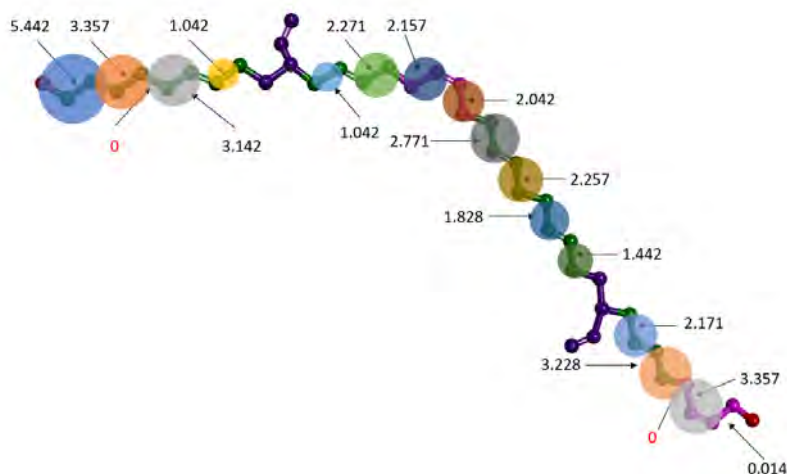
Figure 5.1.4: Molecular structure of a decemer of HTPB 311 with a bubble plot overlaid to depict the number of dihedral rotations about the C-C single bond per molecule. Data has been produced with the Dreiding force-field
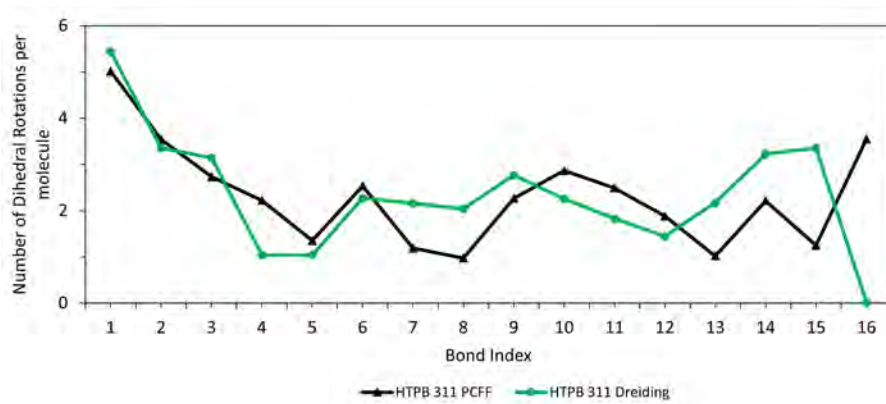
Figure 5.1.5: The number of dihedral rotations per molecule for each C-C bond adjacent to C=C bonds along the backbone of the HTPB 311 molecule. This image relates to figure 5.1.4 as the bond index relates to those seen in this figure. Data provided are derived from simulations at 200 K with Drieding and PCFF force-fields.

The trends in C-C dihedral rotational freedom across the molecule can be ascribed to the proximal intra-molecular chemical environment. For example, from C-C bond index 1 to 4, I observe a gradual decrease in dihedral freedom as the index moves further into the increasingly restrained molecular body. Index 4 and 5 are local minimum due to their immediate proximity to the rotationally constrained vinyl group. At C-C index 6, I see a local maximum, demonstrating the capacity for the *trans* adjacent C-C to exhibit dihedral

rotation. For PCFF, this degree of rotational availability is maintained from index 6 to 11. Dreiding and PCFF exhibit the same availability for the *trans* section from index 9 to 11, with another local minimum surrounding the middle *cis* section at index 7 and 8 (Dreiding). Again, for both force-field regimes, I see local minimum at index 12 and 13 where the second vinyl group is situated. Index 14 and 15 are local maxima due to their proximity to the *vinyl* group. For the Dreiding regime, index 16 has very little rotational freedom. This is due to an error in the original molecular morphology for this system. It is on this basis that I assert the molecular level features observed in the Dreiding simulations are upheld in the PCFF simulations.

To utilise decemer representations of HTPB 311 in the study of grafted POSS-polymer nanocomposites, I have undertaken literature research to determine reasonable basis for the nature and positioning of a grafted unit. A number of different reaction mechanisms are available to the HTPB species. However, based on findings from the literature, I suggest that addition polymerisation would be the most viable route for the introduction of POSS groups. For example, Chang-Tay *et al* have demonstrated that HTPB can be functionalised with methyl methacrylate molecules at the α position of a *trans* monomer within an HTPB oligomer.[149] Given that I have covered many different methyl methacrylate functionalised POSS species in Chapter 4, I have therefore utilised this mechanism and molecular system as the basis for my grafted systems. Figures 5.1.6 provides a visual representation for this graft site along the HTPB 311 backbone at the α carbon position. To investigate how the number of grafted POSS ligands effects the macroscopic properties, I have also introduced a second grafting site, again based on the α position of a *trans* monomer (Figure 5.1.7). Within this work, these two graft sites are used either independently, or together. For the following systems I refer to these grafting sites as site 1 and site 2, respectively. To maintain consistency thoughout my work, I have used the propyl linker length within the methacrylate molecular bridge between HTPB and POSS except for the largest hexyl methacrylate

functionalised POSS grafted system where I have used a hexyl methacrylate linker. The remaining functionalisation sites of the POSS cube have been treated as separate entities.
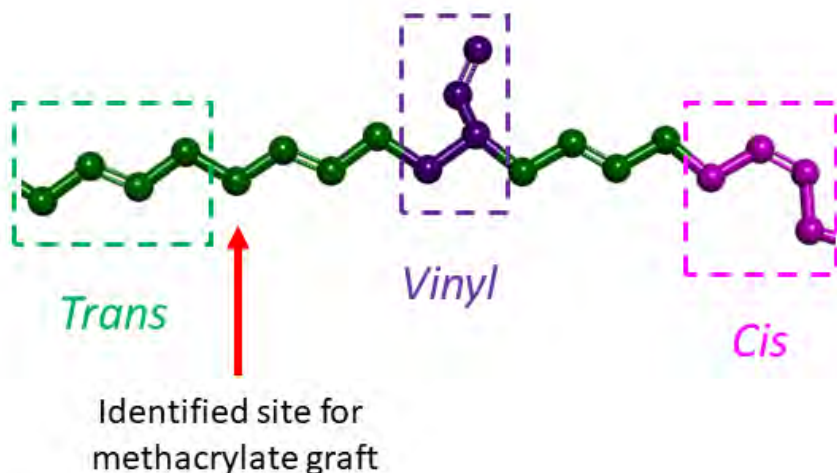
Figure 5.1.6: HTPB 311 repeat unit with identified graft site 1
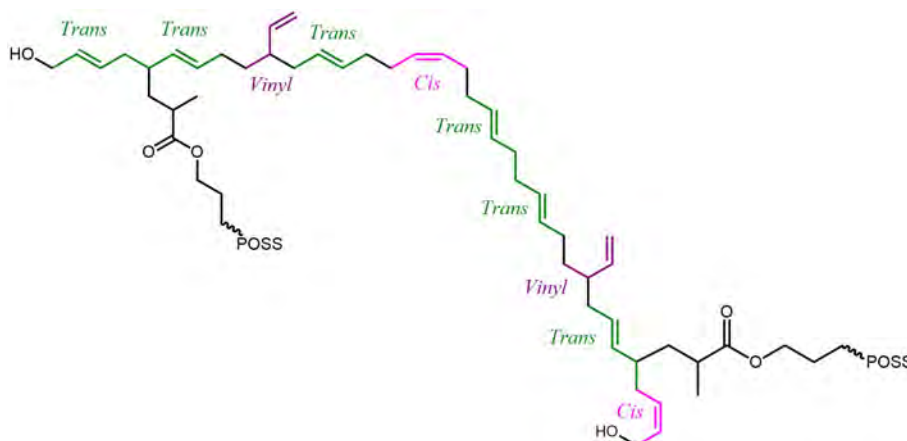
Figure 5.1.7: Whole HTPB 311 molecule with identified graft sites 1 and 2 from left to right.

5.2   Simulation of HTPB with Small Pendant Groups

We have simulated a number of different grafted systems. The smallest grafted pendant group I have studied is the Adamantane structure and the largest is the hexyl methacrylate functionalised POSS. Due to the the presence of a linker from the POSS cube to HTPB backbone, a suitable formula to describe the cube in this context would be, for example,

T_8H_7. This is an alteration to the T_8H_8 descriptions I have used in previous chapters. Within this section I will discuss the predicted T_g values for the smallest grafted systems.

5.2.1   HTPB grafted with Adamantane

We have investigated the addition of adamantane groups to the HTPB 311 molecule. The molecular structure of adamantane can be seen in figure 5.2.1. This structure provides useful comparison with the T_8H_7 grafted systems as it is of similar dimensions and near-cubic in proportions. The moment of inertia of adamantane is significantly smaller than that of POSS, although their molecular radii are similar. These simulations provide insight into the significance of the molecular structure, shape and composition of the pendant group. The Adamantane structures have been grafted to the HTPB molecule in the same fashion as the POSS cubes via a propyl methacrylate linker at graft site 1 and 2.
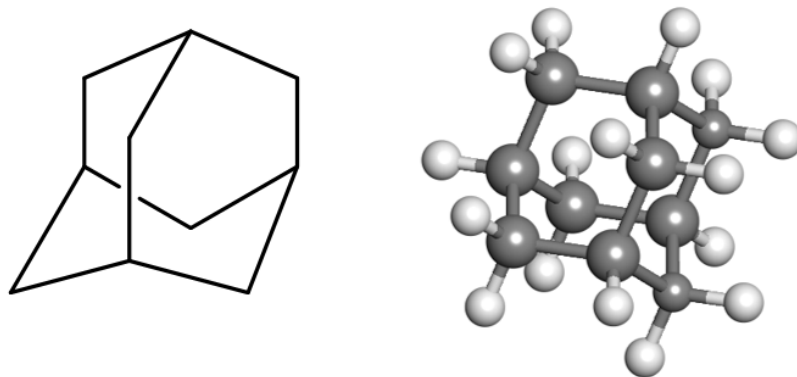
Figure 5.2.1: The molecular structure of adamantane, $C_{10}H_{16}$

Figure 5.2.2 depicts the specific volume vs temperature relationship for HTPB molecules grafted with one and two Adamantane structures. At all temperatures, the two grafted system has higher density than the 1 grafted system. Both systems are significantly less dense than the equivalent T_8H_8 POSS equivalent grafted structures, shown in figure 5.2.5.

From this approach, I predict a T_g of 246.6 K for the single grafted structure. For the double grafted system, I see a decrease of 14.1 K in the T_g to a value of 232.5 K.

(a) 1 grafting adamantane structure at site 1   (b) 2 grafting adamantane structures
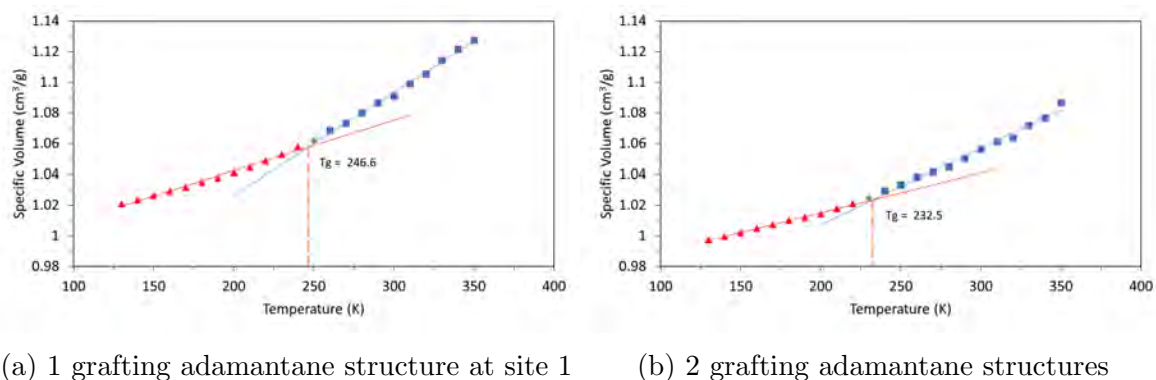
Figure 5.2.2: Specific volume Temperature relationship for HTPB molecules grafted with 1 (left) and 2 (right) Adamantane structures.

The dihedral rotation approach for T_g prediction has also been utilised for these systems as shown in figure 5.2.3. For this method, I predict Tgs of 247 and 247.8 K for single and double grafted systems respectively. Again, I observe an increase for both systems from the pure HTPB predicted value. For the double grafted system, I see that the availability of dihedral rotations is very similar to that of the single grafted system.

(a) 1 grafting adamantane structure in position 1   (b) 2 grafting adamantane structures
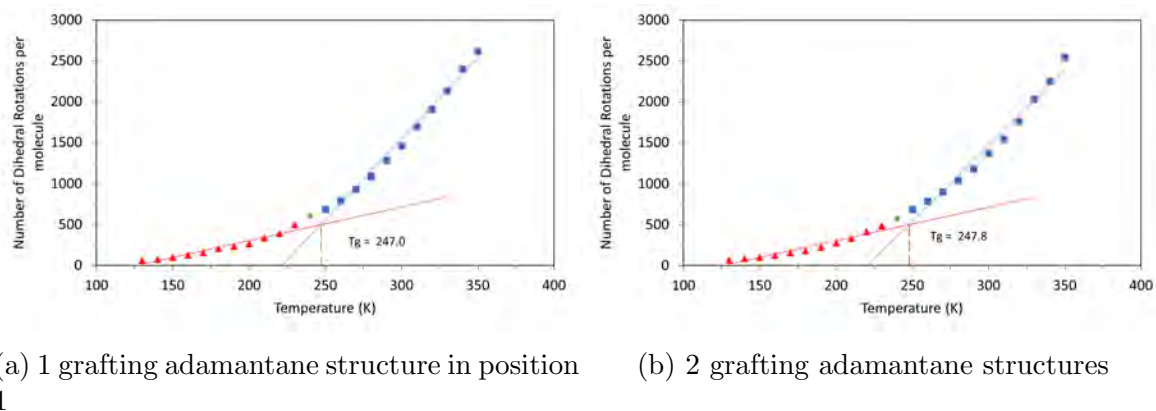
Figure 5.2.3: Total number of dihedral rotations to Temperature relationship for HTPB molecules grafted with 1 (left) and 2 (right) Adamantane structures.

Through the use of Voronoi Analysis, I determine that these molecules are highly inter-penetrating. In figure 5.2.4, I present the number of near neighbours for HTPB-Adamantane

grafted systems as determined through the Voronoi analysis of the centre of mass and hydrogen-stripped molecular structure. From the centre of mass reference, I determine 15.5 and 15.6 near neighbours on average respectively. From the H-stripped molecular structure reference, for both systems, the number of near neighbours is greatly increased to 23 at 130 K with a gradual decrease with temperature to a minimum of 22.0 and 22.3 K at 400 K respectively. Here, as the full molecules are considered, this large number suggests that the molecules are extended and well inter-digitated with one another.

(a) 1 graft HTPB-Adamantane CoM

(b) 1 graft HTPB-Adamantane H-Stripped

(c) 2 graft HTPB-Adamantane CoM

(d) 2 graft HTPB-Adamantane H-Stripped
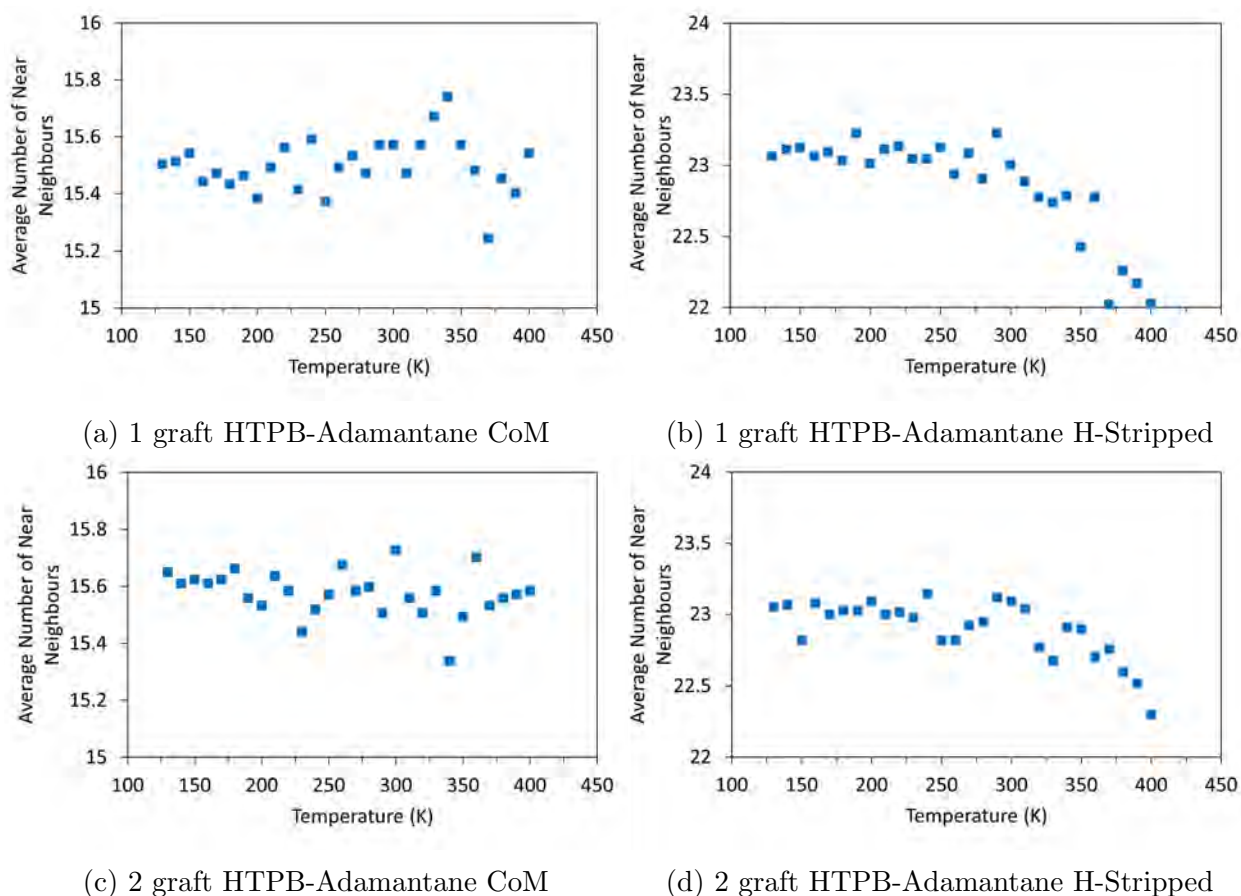
Figure 5.2.4: The average number of the near neighbours for singularly (top) and doubly grafted (bottom) HTPB-Adamantane systems. These values have been determined through the Voronoi analyis from the center of mass (left) and the hydrogen-Stripped molecular structure (right).

5.2.2 HTPB grafted with T_8H_7

In figure 5.2.5, I present the relationship between the specific volume and the temperature for HTPB systems grafted with one and two T_8H_7 POSS cubes. From this data, I predict T_g values of 256.1 and 263.1 K respectively. These values are between 23 and 30 K higher than that predicted for the pure HTPB system. In addition, the doubly grafted system is considerably more dense than the single grafted system. I also observe a flatter relationship in the 2-grafted system as the T_8H_8 character is increasingly expressed. As demonstrated in the pure T_8H_8 simulations covered in Chapter 4, these systems have very little compressibility, resulting in very linear specific volume vs temperature relationships.

(a) 1 grafting T_8H_7 POSS cube in position 1   (b) 2 grafting T_8H_7 POSS cubes
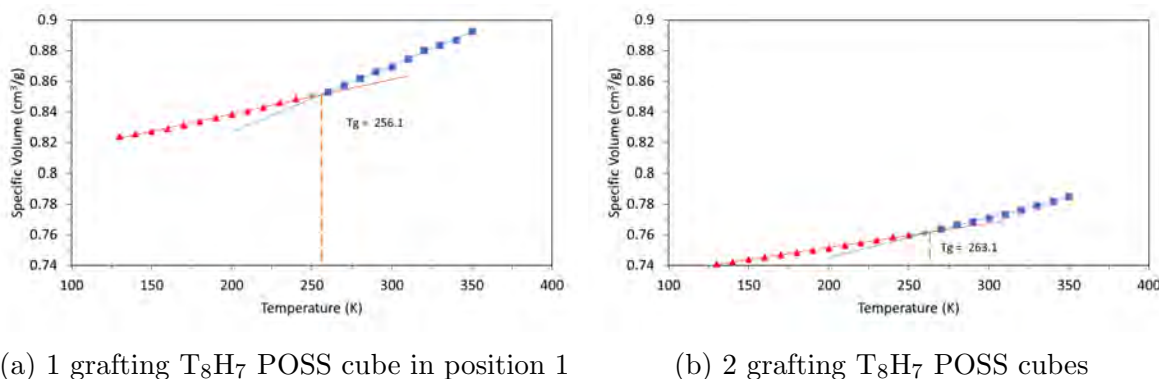
Figure 5.2.5: Specific volume Temperature relationship for HTPB molecules grafted with 1 (left) and 2 (right) T_8H_7 POSS cubes.

Figure 5.2.6 describes the total number of rotations for all T_8H_8 grafted molecules. From this method, I predict a T_g of 250.6 and 256.4 K for each system respectively. Both of these results are consistent with the specific volume method with a 20 K increase from the pure HTPB system. These data demonstrate that the addition of a second T_8H_7 cube has a reductive effect on the availability of molecular dihedral rotations at higher temperatures. This suggests that the pendant groups behave as anchors for the C-C *trans* groups, preventing the rotations observed in the pure HTPB system. Unlike the specific volume approach, very clean bilinear character is obtained with this observable.
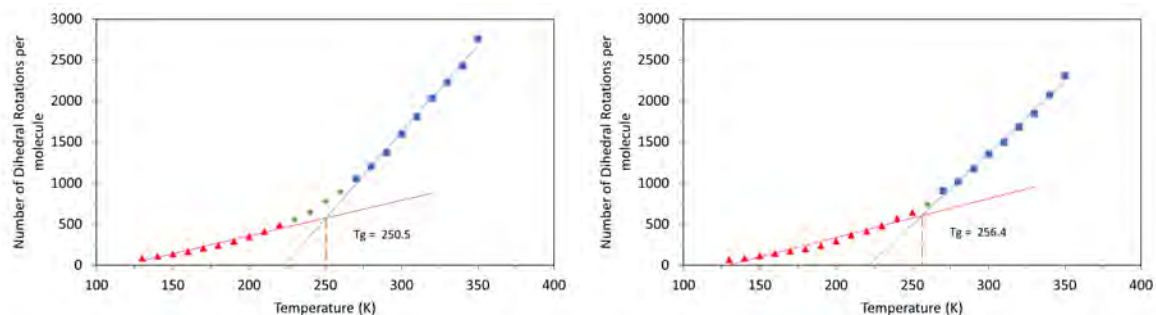
(a) One T_8H_7 POSS cube grafted in position one

(b) Two grafting T_8H_7 POSS

Figure 5.2.6: The total number of dihedral rotations observed in HTPB T_8H_7 grafted systems at varying temperatures.

5.3   Simulation of HTPB with Large POSS Pendant Groups

In addition to adamantane and T_8H_7 grafted systems, I have studied the addition of larger POSS species to the HTPB backbone. Here, I present results from HTPB grafted with T_8t-butyl$_7$ and T_8hexyl-Methacrylate$_7$ independently.

5.3.1   HTPB grafted with T_8t-Butyl$_7$

In figure 5.3.1, the specific volume vs temperature relationship for T_8t-Butyl$_7$ grafted systems are shown. For the singularly grafted system, the T_8t-Butyl$_7$ is grafted at position 2. Refer to figure 5.1.7 for the position of the grafting site. Here, I predict T_g values of 270.2 and 256.8 K for the singular and doubly grafted systems respectively. Similarly to the T_8H_7 grafted systems, these plots have a very linear relationship, indicating that the system is very in-compressible.

(a) One grafting T_8t-butyl$_7$ POSS cube in position two

(b) Two grafting T_8t-butyl$_7$ POSS cubes
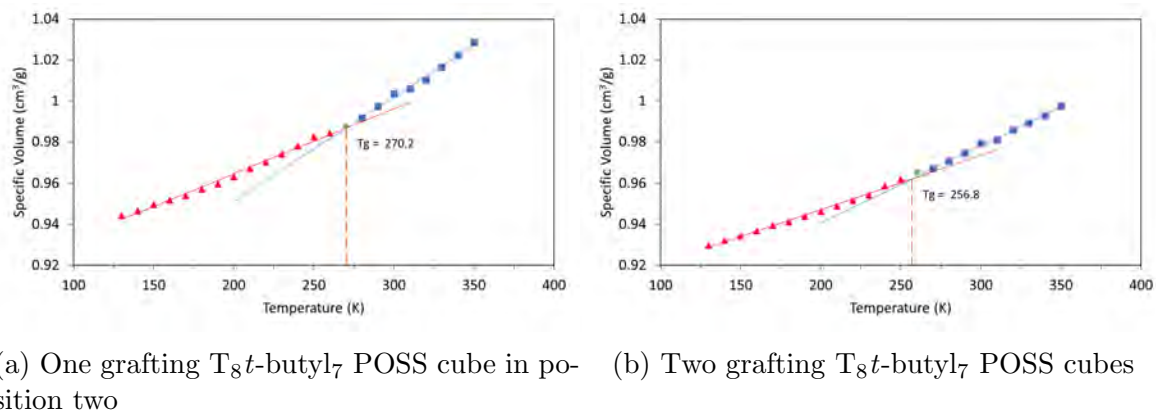
Figure 5.3.1: Specific volume Temperature relationship for HTPB molecules grafted with 1 (left) and 2 (right) T_8t-butyl$_7$ POSS cubes

Figure 5.3.2 presents the predicted T_g from the dihedral rotation method for the same systems. From this method, I predict T_g values of 254.7 and 258.0 K for the single and double grafted systems respectively. For the single grafted system, the predicted T_g values are not in agreement with one another. However, for the doubly grafted system, the predicted T_g are within 1.2 K of one another.

(a)

(b)
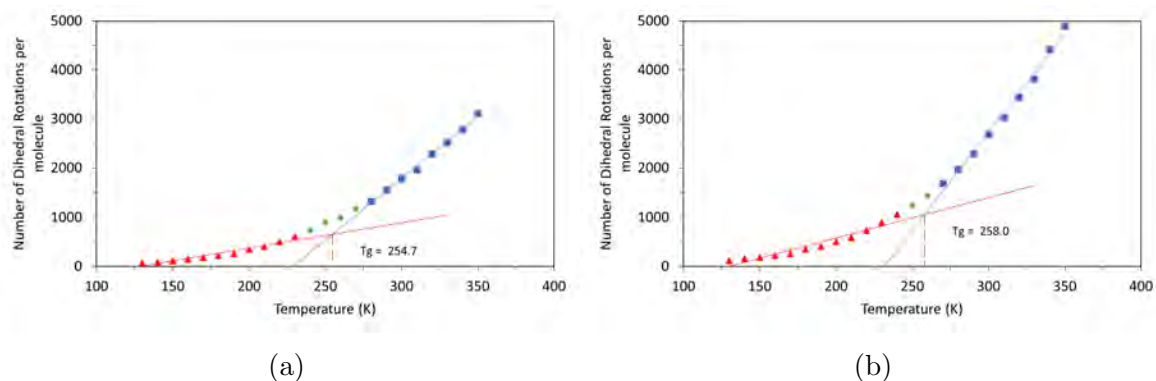
Figure 5.3.2: The total number of dihedral rotations per molecules observed in HTPB T_8t-butyl$_7$ grafted systems at varying temperatures

5.3.2   HTPB grafted with T_8hexyl-Methacrylate$_7$

The largest system that I have studied consists of a singularly grafted hexyl-methacrylate functionalised POSS at position 1. In addition, the usually propyl-methacrylate linker between POSS and HTPB chain has been substituted with a polymerised hexyl-methacrylate

segment. By including this species, I increase the scope of the systems I have studied. Through the inclusion of hexyl-methacrylate groups, I consider a system that has significantly more potential to interact with the HTPB sections of the molecules, which may influence the macro-scale properties. I have chosen to only consider the addition of a single T_8hexyl-Methacrylate$_7$ grafting body as the number of atoms per molecule is quite large, and I would have had a very small number of molecules within the simulation cell in a double grafted system.

In figure 5.3.3 I present the predicted T_g from the specific volume vs temperature relationship for T_8hexyl-Methacrylate$_7$ grafted HTPB. Here, I predict a value of 247.1 K. This value is the lowest observed for this method across the POSS grafted systems.
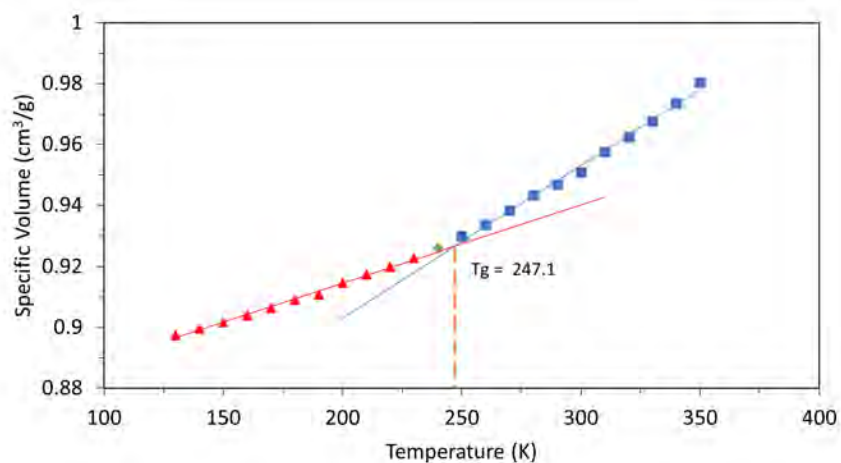
Figure 5.3.3: The specific volume vs Temperature relationship for T_8hexyl-Methacrylate$_7$ grafted HTPB.

In addition, I have predicted the T_g from the number of dihedral rotations per molecule method. Here, I predict a value of 245.8 K. This value is in good agreement with the specific volume method and is also the lowest recorded value for POSS grafts through this method.
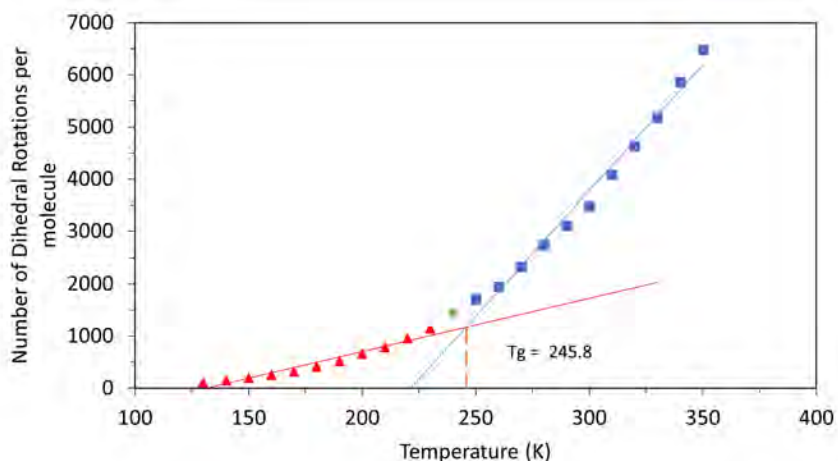
Figure 5.3.4: The predicted T_g for T_8hexyl-Methacrylate$_7$ grafted HTPB for the relationship between the number of dihedral rotations per molecule and temperature.

5.4 HTPB Backbone Analysis in Grafted Systems

In the same way that I have analysed the dihedral rotational freedom of the individual C-C bonds within pure HTPB, as shown in figure 5.1.5, I have also studied this feature for the grafted systems discussed in section 5.2 and 5.3. The methodology and theory behind this analysis is covered in section 3.8.5. Here, I present the results for the dihedral freedom analysis of the HTPB backbone for the grafted systems at 200 and 300 K and compare with that of the pure HTPB system. I have chosen these temperatures as they are both well below and above the predicted Tgs respectively. The singularly and doubly grafted like-systems are presented together.

In figure 5.4.1, I present dihedral rotation analysis of the HTPB backbone of the Adamantane grafted systems. At 200 K, a significant departure from the behaviour observed in the pure HTPB system is observed. Within these systems, grafting site 1 resides at the carbon of bond index 3 closest to the terminus of the molecule. From these data, I see that the there is a significant reduction in the dihedral freedom of bond index 3 and adjacent indices 2 and 4. This departure is visible in both singularly and doubly grafted systems. The same type

of behaviour is seen in the doubly grafted system at bond index 14. Here, the rotational freedom is largely impacted by the presence of the Adamantane. At 300 K, similar behaviour is observed in that the rotational freedom in the immediate vicinity of the grafting site is predominantly affected. At this temperature I also observe that the rotational freedom for the grafted species is also consistently lower than the pure HTPB 311 system across all bond indices.

(a) 200 K   (b) 300 K
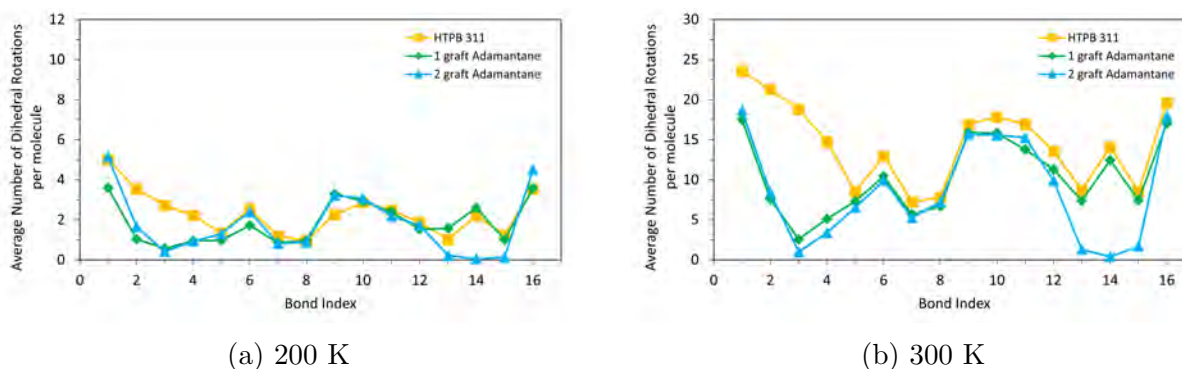
Figure 5.4.1: The number of dihedral rotations per molecule for each C-C bond adjacent to C=C bonds along the backbone of the HTPB Adamantane grafted molecules. Single grafted values are presented in green and the doubly grafted are in Blue.

Figure 5.4.2, presents 200 and 300 K dihedral rotation data for the T_8H_7 grafted system. At 200 K, Again, I see similar behaviour to the Adamantane grafted systems. The rotational freedom of bonds in the vicinity of the grafting sites are the most affected, being significantly reduced by comparison to the pure HTPB 311. This is also the case at 300 K, where both the singularly and doubly grafted systems are rotationally hindered.

(a) 200 K   (b) 300 K
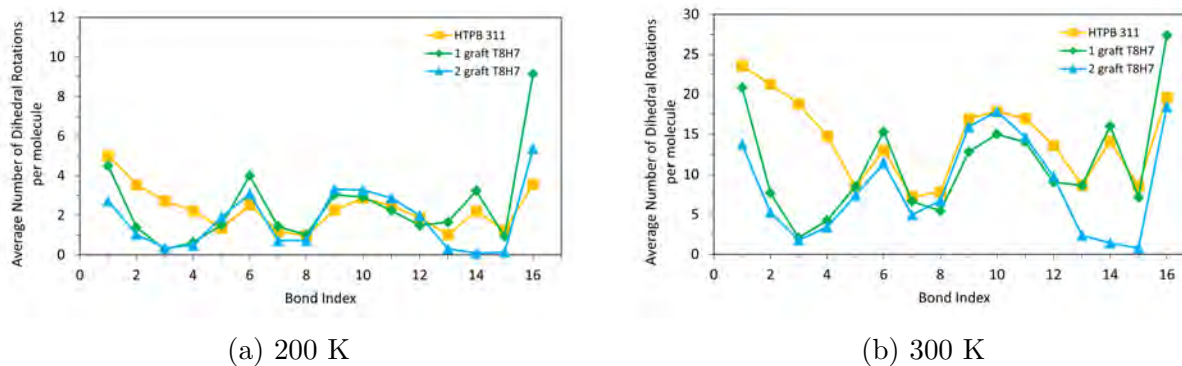
Figure 5.4.2: The number of dihedral rotations per molecule for each C-C bond adjacent to C=C bonds along the backbone of the HTPB T_8H_7 grafted molecules. Single grafted values are presented in green and the doubly grafted are in Blue.

Results from the larger T_8t-butyl$_7$ grafted systems are presented in figure 5.4.3. These graphs describe behaviours that are very similar to the previous systems as the dihedral freedom is significantly impacted at, and adjacent to, the grafting sites. At 200 K, particularly for the singularly grafted system, the dihedral freedom is slightly augmented within the HTPB backbone compared to pure HTPB 311. At 300 K I see similar behaviour in that the dihedral rotations about the graft sites are reduced.

(a) 200 K   (b) 300 K
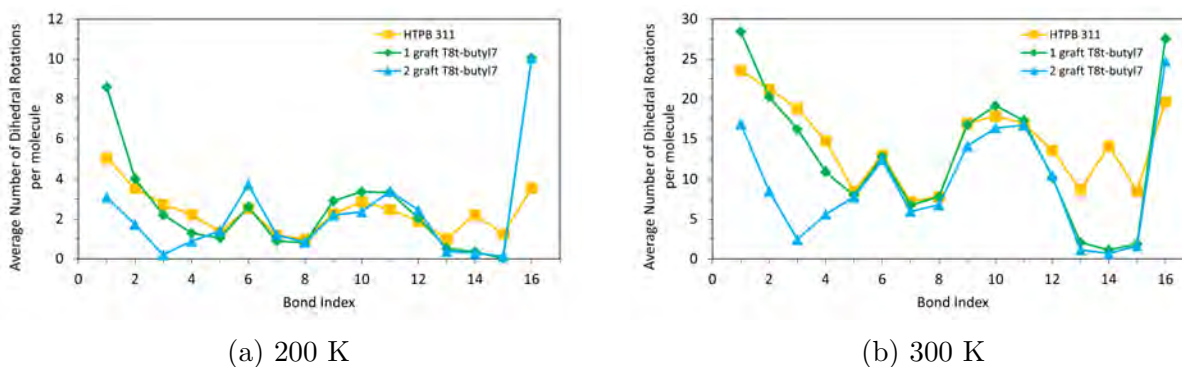
Figure 5.4.3: The number of dihedral rotations per molecule for each C-C bond adjacent to C=C bonds along the backbone of the HTPB T_8t-butyl$_7$ grafted molecules. Single grafted values are presented in green and the doubly grafted are in Blue. The single grafting site was implemented at site 2 (carbon index 14) for this system.

Finally, in figure 5.4.4, I present the same analysis for the T_8hexyl-methacrylate$_7$ grafted system. At 200 K, I see that the dihedrals about the grafting site are locked. In consecutive order, post bond index 4, the dihedrals largely follow those of pure HTPB 311, but enhanced

rotations apparent at indices 9, 10, 11. At 300 K, again, I see that the graft site is rotationally hindered. Here, though, the higher index bonds do not exhibit the enhanced rotation.

(a) 200 K   (b) 300 K
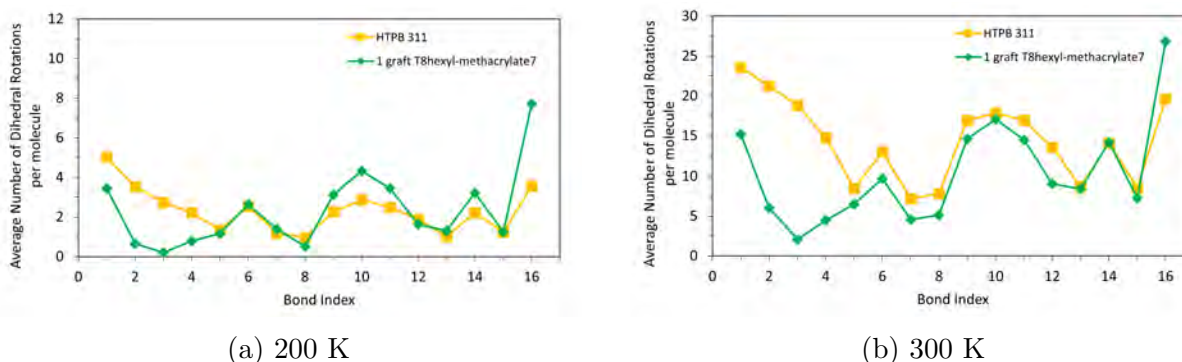
Figure 5.4.4: the number of dihedral rotations per molecule for each C-C bond adjacent to C=C bonds along the backbone of the HTPB T_8hexyl-methacrylate$_8$ grafted molecules. Single grafted values are presented in green and the doubly grafted are in Blue.

5.5 Discussion

Within the previous section, I have presented results from the simulation of a number of HTPB grafted systems. Several different POSS structures have been considered, and the structurally similar 'adamantane' grafting body has also been included.

The fundamental aim of this work was to understand and characterise the implication of including POSS species within the HTPB structure by analysing the microscale behaviour and macro scale properties. In table 5.1, all predicted T_g values are given for each grafted species. As shown, from the specific volume method, the doubly grafted adamantane structure has the lowest predicted Tg, at a values of 232.5 K, followed by the pure HTPB at 236.8 K. The singularly grafted adamantane structure is the third lowest predicted T_g at 246.6 K. These results indicate that the chemical makeup of the grafting species is as important as the shape of the grafting species. There is a clear partition between the Tgs for the systems that contain mostly organic character compared to those which contain inorganic character, contributed by the presence of the silica POSS cube. Moreover, The hexyl-methacrylate

functionalised systems exhibits the lowest T_g of all POSS based systems. Again, this can be attributed to the presence of a higher proportion of organic material. More favourable interaction between HTPB sections and the organic andamantane or hexyl-methacrylate promote the observation of a lower Tg.

We consistently see an increase in predicted T_g values from the specific volume method for the POSS based systems. For the largest system of hexyl-methacrylate functionalised POSS, there is an increase in T_g of 10.3 K from the pure HTPB system. This is the smallest increase in T_g observed for the POSS grafted systems. The contribution of organic character from the large hexyl-methacrylate groups and the longer hexyl-methacrylate linker maintains the softness of the system at lower temperatures. As a result, I see an intermediately low T_g value. Thus, it is the smaller POSS grafts that achieve the maximal increase of 19.3 K from the pure HTPB system for the singularly grafted T_8H_7 system at 256.1 K. This values is further increased to 263.1 K upon the addition of a second T_8H_7 graft. Singularly grafted $T_8 t$-butyl$_7$ has the highest predicted T_g of all systems considered with a value of 270.2 K. While the doubly $T_8 t$-butyl$_7$ grafted system also exhibits a a predicted T_g value of 256.8 K. However, very small gradient changes obtained using the specific volume method, particularly for the doubly grafted systems, reduces the reliability of those reported Tgs.

Grafting Species	Number of grafting bodies	Specific Volume method (K)	Dihedral Rotation method (K)
HTPB	N.A	236.8	233.8
Adamantane	1	246.6	247
	2	232.5	247.8
T_8H_7	1	256.1	250.5
	2	263.1	256.4
$T_8 t$-butyl$_7$	1	270.2	254.7
	2	256.8	258
T_8hexyl-methacrylate$_7$	1	247.1	245.8

Table 5.1

Similar trends are observed from the dihedral rotation method of T_g prediction. As

shown in table 5.1, the adamantane and T_8hexyl-methacrylate$_8$ POSS grafts have the lowest predicted Tgs of the cohort of systems. For these systems, there is good agreement between the two methods for T_g prediction for these systems. For the smaller POSS systems, again I see some good agreement between the methods of T_g prediction, with single grafts increasing T_g by 16.7 (T_8H_7) and 20.9 K (T_8t-butyl$_7$). For the T_8H_7 grafted system, I observe further increase of 5.9 K from the singularly to doubly grafted system. For the T_8t-butyl$_7$ grafted system, the predicted T_g increases by 3.3 K with the addition of a second T_8t-butyl$_7$ grafting body.

As described in section 5.1, the dihedral freedom of *trans* C=C adjacent C-C bonds are the crucial molecular feature in HTPB 311 to enable its observed low Tg. In our published study, I have demonstrated this by substituting the *trans* groups with *vinyl* monomers, and observing large shifts in Tg. By tracking the frequency of the dihedral rotations along the HTPB back-bone within my grafted system, I am able to characterise the impact of POSS grafting on this mechanism. In section 5.4, I have presented this analysis. For all grafted species, the addition of a grafting body dramatically reduces the dihedral freedom about the grafting site. This grafting also reduces the dihedral freedom of the adjacent dihedral sites. This reduction is present above and below the Tgs identified for each system. However the region of significant rotational reduction is limited to just the graft site and the C-C bond that immediately neighbours it.

A graft may also influence the dihedral rotation of the C-C bonds within the HTPB back-bone away from the vicinity of the binding site. For the adamantane grafted system, at 300 K, the dihedral freedom of all bond indices are lower than those available to the un-grafted HTPB 311 system. This is also true of the doubly grafted T_8H_7, T_8t-butyl$_7$ and singularly grafted T_8hexyl-methacrylate$_7$ systems. However, slightly enhanced rotational freedom is seen for the singularly-grafted POSS systems, particularly around bond index 10. Thus,

where grafting density is low, there appears to be a secondary effect where rotations become more likely away from the strongly anchored graft site.

Within their publication, Bharadwaj *et al* studied improvements to the material properties of norborene-POSS polymer through simulation methods.[66] As this is a relatively old publication, the systems are small being at most 3142 atoms with intervals of the cooling sequence being 30 K for a run length of 500ps. Their characterisation highlighted that the non-polar but sterically bulky cyclopentyl and cyclohexyl functionalised POSS pendant groups behaved as anchoring points for the norborene polymer chain and produced a higher T_g than that of the pure system. By comparing with simulations of pure poly-norborene, they showed that chain dynamics were slowed by the presnce of pendant POSS grafts through analysis via the torsional autocorrelation function. While my findings are generally consistent with this, they provide greater detail on the extent and reach of the effect of the grafting, including more nuanced behaviours associated with the choice of grafted entity and the density of the grafting sites. In more recent studies of grafted POSS systems, R. Pan *et al* have simulated blends of Trisilanolisobutyl POSS in polyurethane.[150] The POSS structures considered here are slightly different in that a single silicon vertex is missing from the T_8 cubic structure. Thus, the bridging oxygen atoms between silicon atoms at this vertex are hydroxyl groups, which are used for co-polymerisation with the polyurethane chains. Within The computational section of this paper, the agglomeration of POSS cages has been characterised through the use of simulated X-ray scattering profiles and radial distribution analysis. At the highest concentration of 22% POSS, the average neighbour distance for the polymer chains is lower than the 13% POSS concentration due to the lower dispersion of POSS cages within the polymer matrix. MSD analysis at 500 K has been used to identify that the POSS molecules have significantly less mobility than the polyurethane chains. The mobility of POSS also decreases with POSS concentration. From the specific volume vs temperature relationship, the predicted T_g value increases with POSS concentration. This trend is ex-

plained by the reduced mobility within the polyurethane chains. Within my work, I observe similar trends in that grafting POSS cubes results in an increase to the T_g for HTPB 311. As discussed, the dihedral rotation about specific bonds within the HTPB backbone are critical for the low T_g observed for these systems. I have been able to characterise the impact of POSS grafting on this mechanism, and utilise this molecular feature for the prediction of Tg.

The results presented in this chapter clearly demonstrate that, whilst synthetically challenging, grafting of POSS molecules has a signifcicant and direct effect on the material properties of HTPB. By suppressing the cooperative crankshaft dihedral rotation in the vicinity of the grafting site, the material compressibility and the T_g can be controlled. However, since the effect of grafting is apparent both above and below Tg, a further consequence is that the compressibility change at T_g is reduced - that is, the transition is still apparent, but it doesn't involve the same material property changes as are seen for pure HTPB.

In the next chapter, I investigate alternative polymer nanocomposites based on blends rather than grafting.

Chapter 6

Polymer-POSS Blended Nanocomposites

Within chapters 4 and 5, I have discussed simulations of pure POSS systems comprising the entire simulation body, and simulations of POSS as a grafting species within the backbone of a polymer matrix. In both of these chapters, all of the simulated molecules have been chemically identical in nature. To broaden my understanding of POSS systems, I have also carried out studies on blended systems. That is to say the POSS species are distributed within a matrix as individual molecules with no chemical bonding to that surrounding matrix. For consistency and comparison with chapter 5, I have again chosen HTPB as the primary matrix. In addition, I have also carried out simulations with octatetraene forming the matrix material as a short chain organic alkene. For both regimes, I have performed cooling simulations at 10%, 30% and 50% POSS concentration by mass. Herein I discuss the macro and micro scale behaviours of the resultant bulk material and different molecular species properties.

6.1   Chapter Overview

In chapter 4, I have presented a study of a range of POSS molecules as single-component systems. From this, I have identified that the molecular breathing mode can be used to predict the T_g for the given system. In chapter 5 I investigated the effect of grafting POSS molecules onto a well studied polymeric system. This study showed that the POSS molecules behave as anchor points for the HTPB molecules, do not have a strong tendency to phase separate and have a significant effect on the glass transition of these species. Within the following chapter, I aim to elucidate the molecular mechanisms and behaviour of POSS molecules in blended nanocomposites that lead to the production of their characteristic nanomaterial properties. I have again chosen HTPB 311 for my polymer matrix as this molecule is well studied and has been included in chapter 5. From simulation, I have seen that HTPB 311 has a strong tendency to become entangled. Also, the persistent availability of dihedral rotation of *trans* C-C bonds within the HTPB backbone enables the system to have a particularly low Tg. From literature summarised above, it has been shown that POSS are able to increase the T_g by interrupting the regular packing of certain polymers. The HTPB system is distinct from this in that the structure is amorphous. This work describes the relationship between entangled HTPB 311 and a range of POSS species over a range of concentrations.

To understand the behaviour of POSS within a system that exhibits much less entaglement, I initially ran simulations of butadiene-POSS blends. However, the boiling point of butatdiene was too low to enable condensed phase simulation in the desired temperature range. As a compromise, therefore, I have also studied the addition of POSS within octatetraene, which is effectively the combination of two butatdiene molecules. These systems, with HTPB and octatetraene matrices, respectively, offer unique insight into the behaviour of POSS molecules in different chemically consistent but morphologically distinct environments.

6.2   HTPB-POSS nanocomposite

I have simulated a number of different POSS species as a discrete nanofiller within a polymer matrix. Herein I discuss results from the simulation of three different POSS systems blended with the polymer HTPB 311. The simulation of pure HTPB has been covered extensively in section 5.1.

6.2.1   HTPB T_8H_8 blend

I first discuss results from simulations featuring the smallest POSS, the T_8H_8 structure at 10% wt POSS. As mentioned in previous chapters, each system has undergone high temperature annealing before being passed to the production cooling sequence. Annealing begins at 700 K and decreases by 50 K intervals until 400 K is reached. The production phase of the cooling sequence is between 400 K and 130 K with 10 K intervals. Each temperature has a run length of 0.5ns and is 30,000 atoms in size. As I have covered in previous chapters, a number of methods have been used to predict the T_g for the bulk material. In figure 6.2.1, I present the specific volume vs temperature relationship. From this method, I predict a T_g of 244.1 K. This is a slight increase of 7.3 K with this method from the predicted T_g of the pure HTPB 311 system.
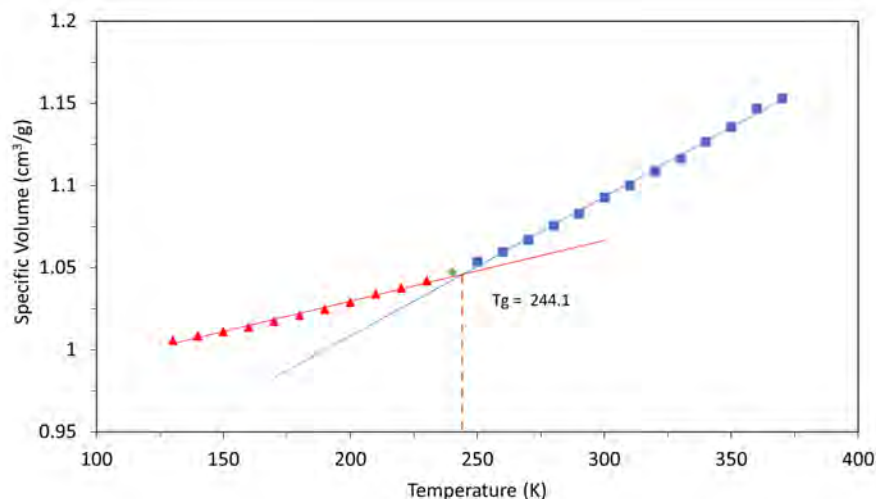
Figure 6.2.1: Tg prediction from specific volume and Temperature relationship for 10% wt T_8H_8 in HTPB 311

In conjunction with this method, I have also employed the standard deviation in the moment of inertia method and number of dihedral flips per molecule method. Each of these methods have proven useful for the HTPB and POSS systems respectively. As these systems are blended, I collect two distinct sets of measurements; those of the HTPB and those of the POSS. In figure 6.2.2, I see the relationship between the standard deviation in the moment of inertia and temperature for HTPB (left) and T_8H_8 POSS molecules at 10% wt. For the HTPB data, I observe a bilinear plot as I have seen in previous systems, which predicts a T_g of 264.5 K. For the POSS data (right), the trend in data is very similar to the pure T_8H_8 system covered in chapter 4. I observe a very linear relationship due to the rigidity of the molecule and maintenance of the cubic structure well into higher temperatures.

(a) Standard deviation in the Moment of inertia for HTPB molecules

(b) Standard deviation in the Moment of inertia for T_8H_8 molecules
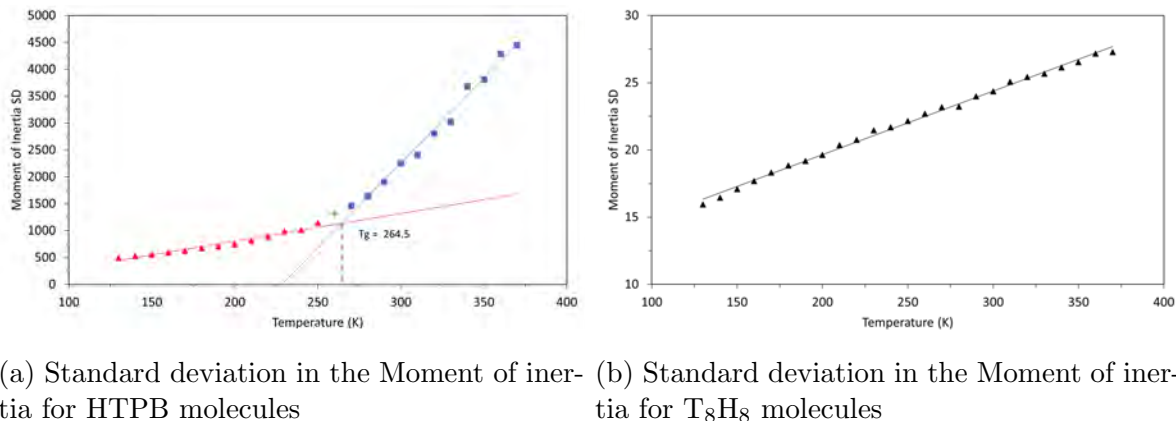
Figure 6.2.2: The Standard Deviation in the moment of inertia over a range of temperatures for HTPB molecules (left) and T_8H_8 (right) in a blended system at %10 wt POSS.

In figure 6.2.3, I present data for both the HTPB (left) and T_8H_8 (right) describing the average number of dihedral rotations per molecule. The Dihedral rotation is counted as a 'flip' when the dihedral angle passes through 60°. Details of this method are covered in section 3.8.5. From the HTPB data, I see a predicted T_g of 238.5 K. This value is very close to the value predicted in Chapter 5 (Figure 5.1.3b) where I employed the same methodology to a pure HTPB system and predict a T_g of 233.8 K. By comparing these graphs, I can also see that the scale of the number of dihedral rotations are in good agreement with one another. The POSS data is also congruent with previous observations that there are very few dihedral flips observed within these molecule. Again, this is due to the rigity and cubic conformation of the T_8H_8 structure. This data tells us that the POSS cubes are behaving as expected, however these methods cannot be applied to the T_8H_8 molecules for the prediction of Tg.
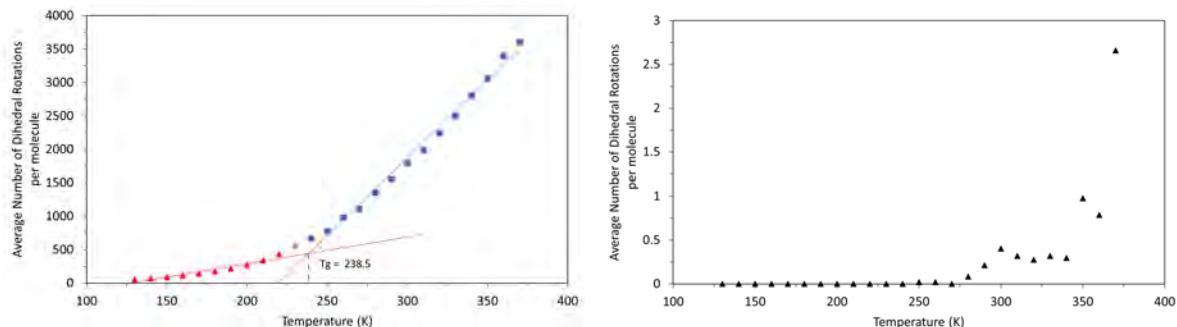
(a) The average number of dihedral rotations per molecule for HTPB molecules

(b) The average number of dihedral rotations per molecule for T_8H_8 molecules

Figure 6.2.3: The average number of dihedral rotations per molecule over a range of temperatures for HTPB molecules (left) and T_8H_8 (right) in a blended system at %10 wt POSS.

The molecular level behaviour of these systems has also been considered. I first analyse the packing of these blended systems through radial distribution analysis of HTPB and POSS as separate entities. Figure 6.2.4 displays the radial distribution function for HTPB (left) and POSS (right) at 130, 200 and 310K. For the HTPB system, I can see that these molecules are in close proximity to one another from a distance of 1 Å. These values are calculated from the centre of mass for each molecule. Due to the molecular entanglement, the centre of mass are able to overlap. At 130K, I see sharp peaks, indicating that there is minimal movement of HTPB molecules en masse. This type of analysis for polymeric systems is a highly involved procedure. I am unable to speak to the reproducibility of these data and ommit this method for HTPB analysis for all future systems.

For the POSS sub-system, I see that there is a minimum distance of 7 Å before another T_8H_8 is observed. In the POSS cage structure there is 4 Å between Si atoms on opposing faces. With the addition of bonded hydrogen atoms at the POSS vertices, I observe an effective molecular diameter of 7 Å. At 130 K, as is observed for the HTPB molecules, I see very sharp peaks. This suggests that the entire systems is conformationally locked. At 220 K, the peaks become more rounded, although the shape and position is maintained, indicating some molecular movement. At 310 K I observe a smooth G(r) which appears to be trending

towards a typical fluid structure. The peak observed at 7 Å with a shoulder at 8 Å at 130 and 220 K is still maintained at 310 K. Equally, a very strong peak in G(r) value suggests there is a strong tendency for these molecules to aggregate. As this peak appears at higher temperatures, I determine that there is a strong effective potential between POSS species in this medium as there is a propensity for low level clustering.

(a) HTPB 130K

(b) POSS 130K

(c) HTPB 220K

(d) POSS 220K

(e) HTPB 310K

(f) POSS 310K
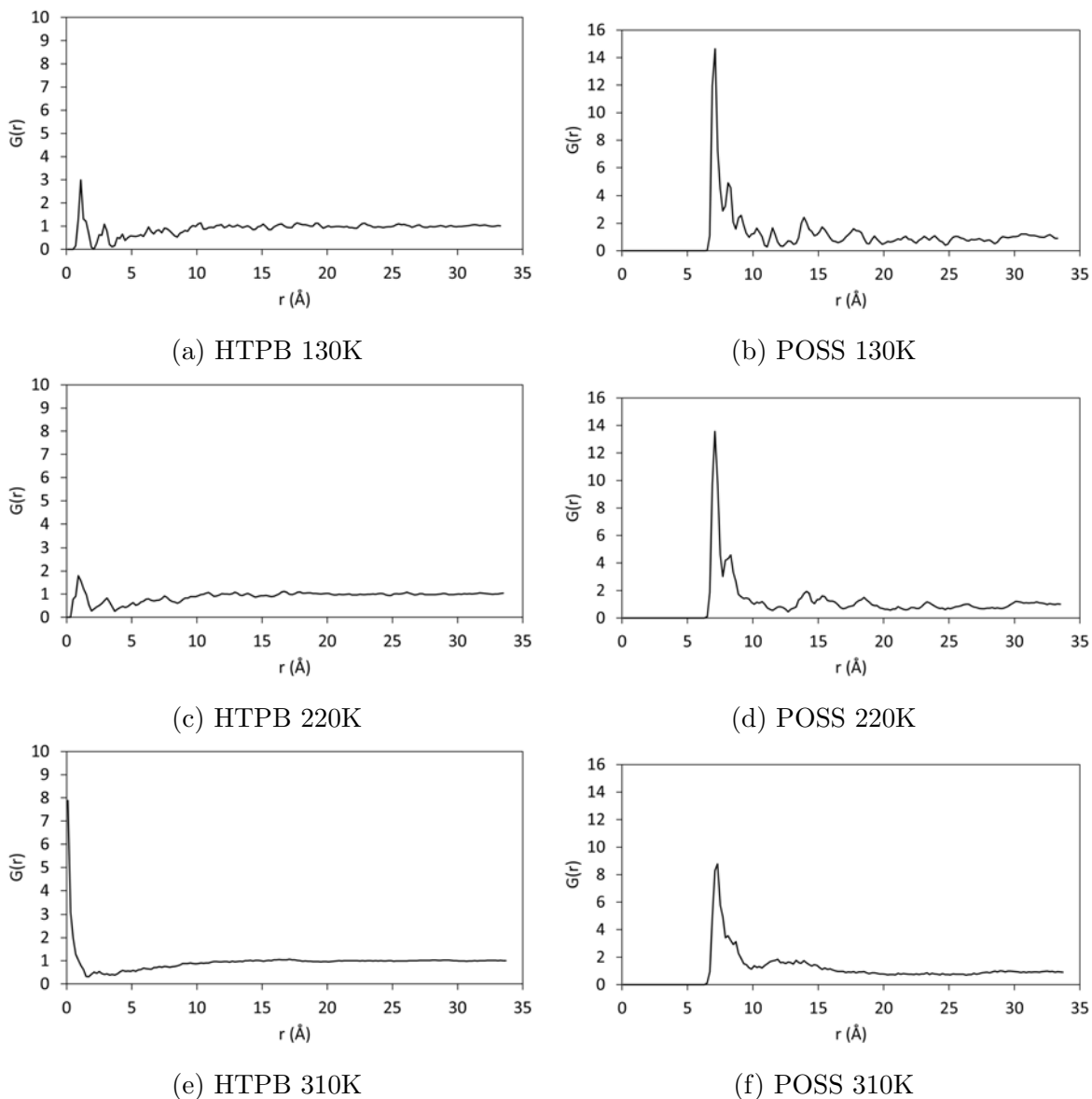
Figure 6.2.4: The radial distribution functions for HTPB (left) and T_8H_8 (right) at 10% wt POSS over the course of a cooling sequence taken at 130, 220 and 310 K.

To quantify the degree of movement available to both HTPB and POSS, at a range

of temperatures, I have carried out Mean Squared Displacement (MSD) analysis on both species. In figure 6.2.5a I can see that there is very little translational movement available to these systems, even well above the T_g for this system. The trend in behaviour can be seen for the POSS species in figure 6.2.5b. However, the relative translational freedom of the POSS is greater than that of the HTPB.

(a) HTPB MSD   (b) POSS MSD
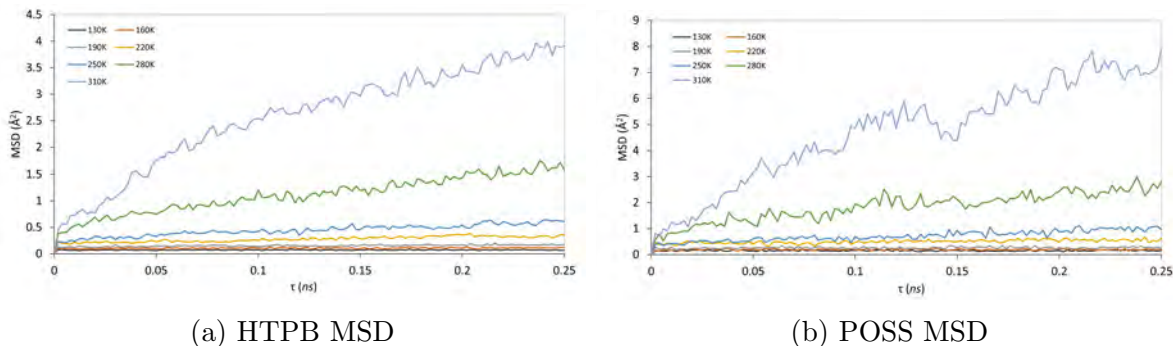
Figure 6.2.5: The MSD for HTPB (left) and T_8H_8 POSS (right) at 10% wt over a range of temperatures and the MSD gradients for both species.

These analyses form the foundation of which I have used to inspect these systems. At 30% wt POSS in HTPB, as shown in figure 6.2.6, I see that the predicted T_g has risen by 15.2 K from the pure HTPB value of 236.8 K to 252.0 K. Again, I observe the influence of the T_8H_8 structure as the bilinear curve is relatively flat.
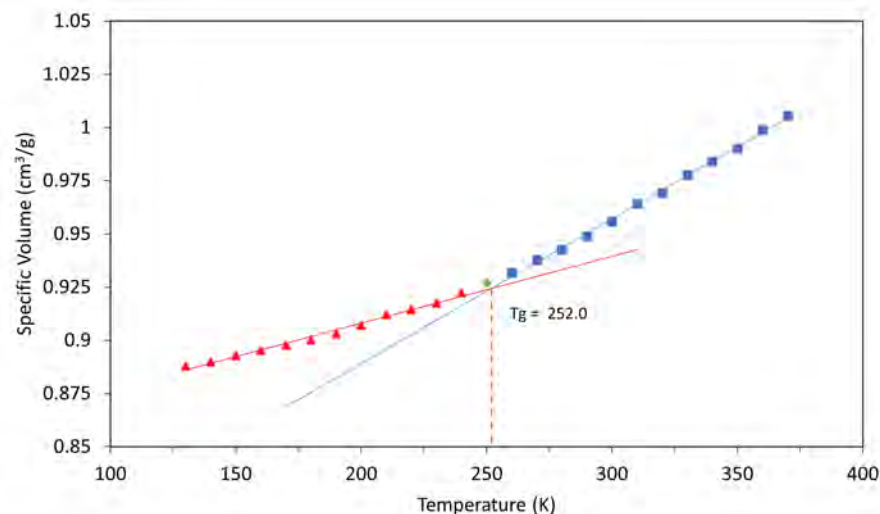
Figure 6.2.6: Tg prediction from specific volume and Temperature relationship for 30% wt T_8H_8 in HTPB 311

As discussed, the standard deviation in MOI and number of dihedral rotations method of predicting the T_g from T_8H_8 POSS data does not function as desired and will no longer be described. However, when applied to the HTPB system, the number of dihedral rotations is still a valid measure as rotations are still detected at all temperatures. In figure 6.2.7, I present the predicted T_g of 252.4 K from the average number of dihedral rotations per molecule for the HTPB molecules only when blended with T_8H_8 POSS at 30% wt POSS. This value is in good agreement with the specific volume method and denotes a 14.9 K increase from the 10% wt POSS blend. Again, I see that the number of dihedral rotations is similar to that of the pure HTPB system and 10% POSS blended system.
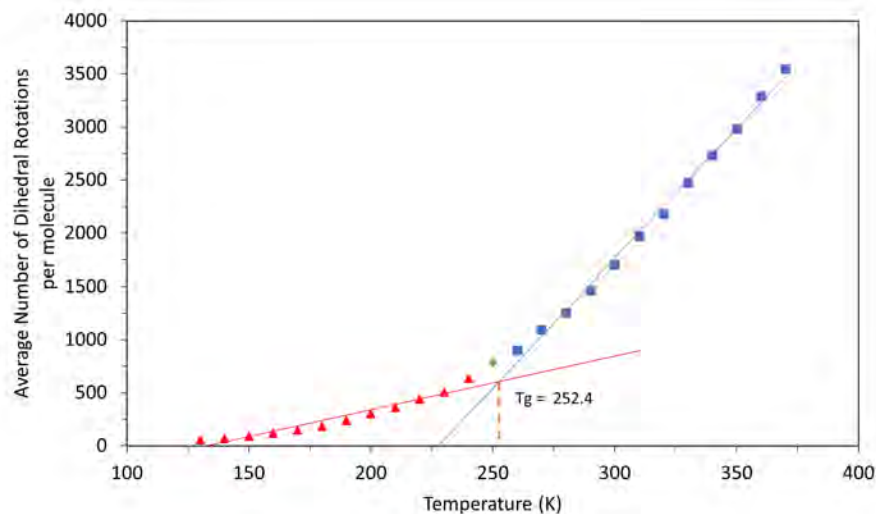
Figure 6.2.7: The average number of dihedral rotations per molecule over a range of temperatures for HTPB molecules (left) in a blended system of T_8H_8 at 30% wt POSS.

In figure 6.2.8, I present the G(r) data for the T_8H_8 molecules as a blended system at 30% wt POSS at 130, 220 and 310 K. The distribution of POSS is highly indicative of a well ordered system. In 130 K, At 7 Å, I see a steep initial rise to a value of 14 followed by a second peak at 8.5 Å. These peaks describe the initial coordination sphere of closely packed POSS molecules. At 14 Å, I see evidence of longer range packing. The value of 14 Å is also significant as it is twice that of the effective POSS diameter, suggesting the existence of a secondary coordination sphere. These peaks also consistently appear at 220 and 310 K, indicating that the POSS molecules are agglomerating at high temperatures.

(a) POSS 130 K

(b) POSS 220 K

(c) POSS 310 K
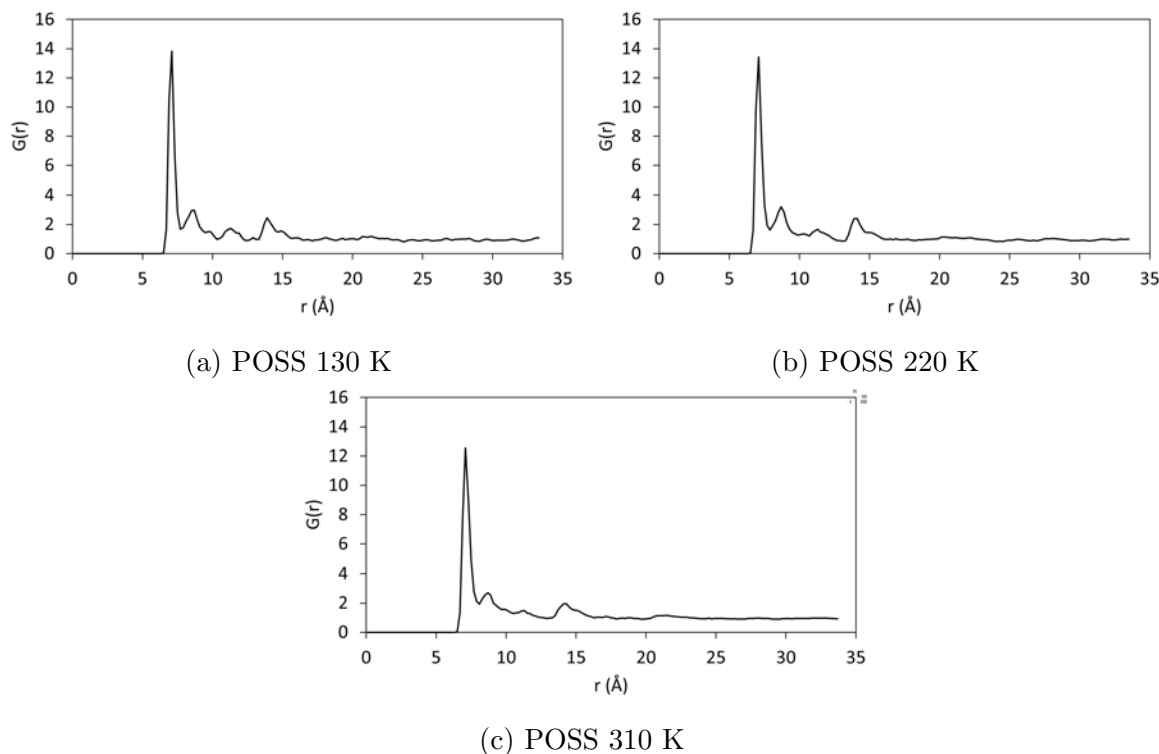
Figure 6.2.8: The radial distribution functions for T_8H_8 at 30% wt POSS over the course of a cooling sequence taken at 130, 220 and 310 K.

From the figures in 6.2.9, the mobility of the HTPB and POSS species are in step with one another. Specifically, at 310 K, I see that between 0.1 and 0.15 ps both the HTPB and POSS both undergo an increase in displacement, suggesting that the POSS species is having more of an influence on the organisation of the HTPB molecules.

(a) HTPB MSD

(b) POSS MSD
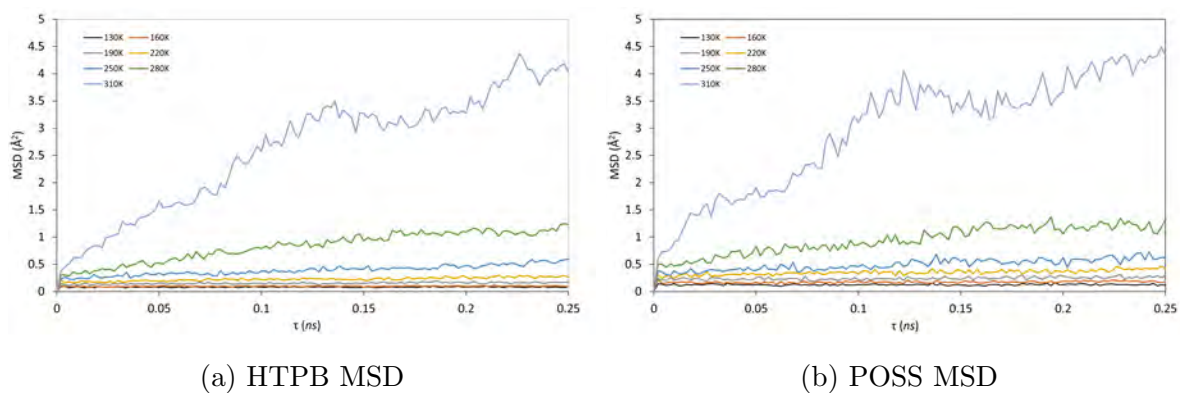
Figure 6.2.9: The MSD and MSD gradient for HTPB (left) and T_8H_8 POSS (right) at 30% wt over a range of temperatures.

As the concentration of POSS is increased from 30% to 50%, I see the predicted T_g from the specific volume method rise from the pure HTPB value of 236.8 to 257.6 K, demonstrating a monotonic increase in T_g with POSS concentration. Due to the substitution of predominantly carbon and hydrogen found in HTPB with the silicon and oxygen atoms of T_8H_8, the overall system density also increases.
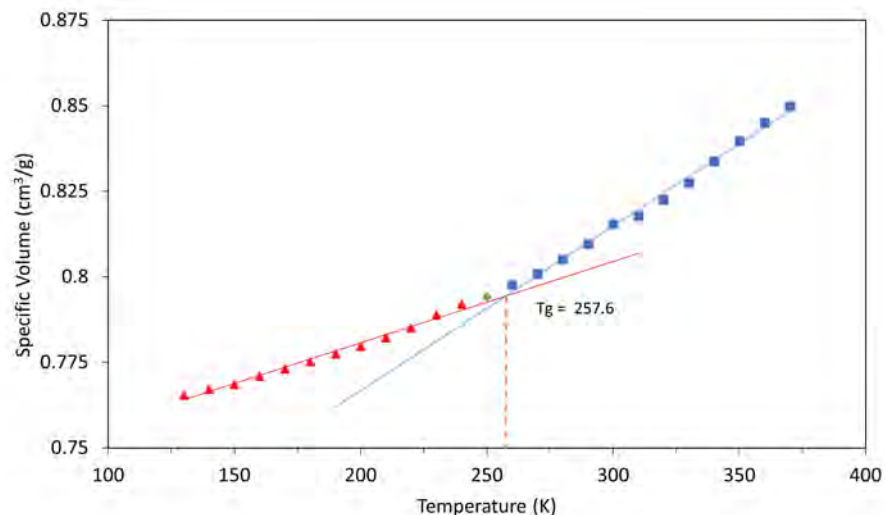
Figure 6.2.10: Tg prediction from specific volume and Temperature relationship for 50% wt T_8H_8 in HTPB 311

In figure 6.2.11, the average number of dihedral rotations per molecule is used to predict the T_g through the HTPB molecules. Here, I predict the T_g to be 243.3 K. This is close to the T_g predicted by the specific volume method of 244.1 K, however the similarity observed for these methods in the 30% system is not as well maintained at 50%.
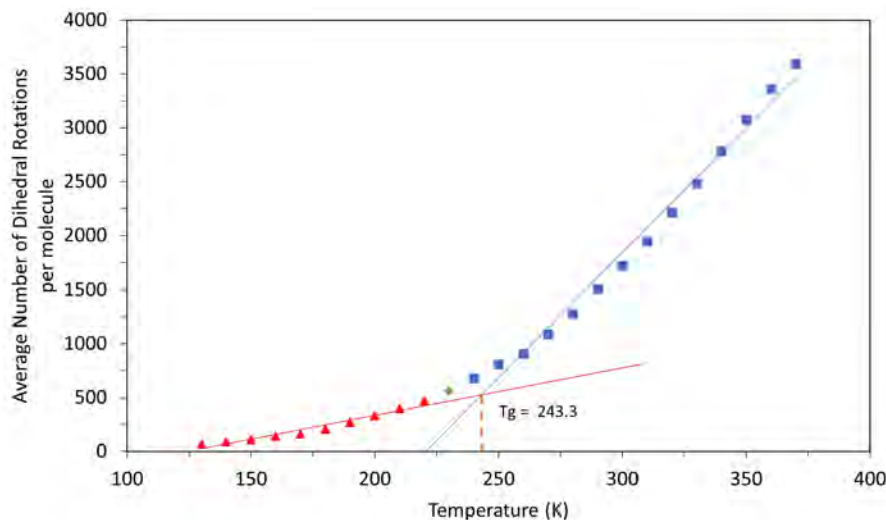
Figure 6.2.11: The average number of dihedral rotations per molecule over a range of temperatures for HTPB molecules (left) in a blended system of T_8H_8 at 50% wt POSS.

For all concentrations, I see that the average number of dihedral flips are consistent with one another. In figure 6.2.12, I see the same type of plot as shown in figure 5.1.5 where I measure the average number of Dihedral rotations for each C-C bond within the HTPB backbone. Each index within this plot denotes the C-C bond position from the *trans* terminus of the HTPB 311 molecule. Here, the pure HTPB 311 (black) data is taken from the pure HTPB simulations covered in section 5.1. These data indicate that the dihedral freedom is mostly unaffected by the presence of T_8H_8 molecules as discrete molecules as for most C-C sites, the number of dihedral rotations are in agreement. However, At some positions of the HTPB molecules, I see an increase in dihedral freedom. This is particularly true at index 6 and 9 which are both maximised at the highest concentration of POSS. These indices are both adjacent to *trans* groups and are positioned within the central region of the molecule. Results from the blended systems are some what similar to the dihedral rotations study covered in section 5.4 concerned with grafted HTPB-T_8H_8 systems. For this system, index 6 and 9 are elevated above the pure HTPB 311 system. Data from the T_8H_8 grafted system are also given in figure 6.2.12. Interestingly, the presence of POSS within HTPB, be it physically blended or grafted seems to enhance the crankshaft motion of certain C-C

bonds across the HTPB backbone.
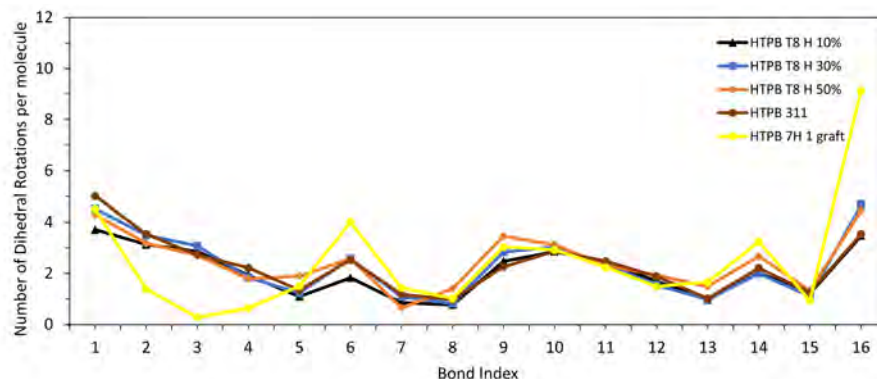
Figure 6.2.12: The average number of C-C Dihedral rotations that occur along the back bone of the HTPB molecule at different concentation of T_8H_8 at 200K. The bond index relates to the position of the C-C bond in relation to the *trans* terminus of the molecule.

In terms of packing, the 50% system shows the same trends in the 10 and 30%. G(r) analysis for T_8H_8 at 130, 220 and 310 K, be seen continuing the trend in figure 6.2.13. In the lower concentrations, there are four well defined peaks in each G(r), strongly indicative of clustering. This packing extends to up to 15 Å even at the highest given temperature of 310 K. This is due to the high degree of agglomeration exhibited by these systems. The progressive positional ordering observed in simulationas POSS concentration has been increased, indicates highly ordered domains of microcrystallites caused by microphase separation of the POSS and HTPB. This phenomenon is well documented within the POSS literature and is a significant interest for chemists working with materials that contain POSS. The HTPB molecules are in an amorphous phase as I have previously observed. The associated arrival of higher dihedral rotational freedom may be due to an increase in the effective specific density of the HTPB subspace when the POSS material adopts a highly ordered arrangement.

(a) POSS 130K

(b) POSS 220 K

(c) POSS 310 K
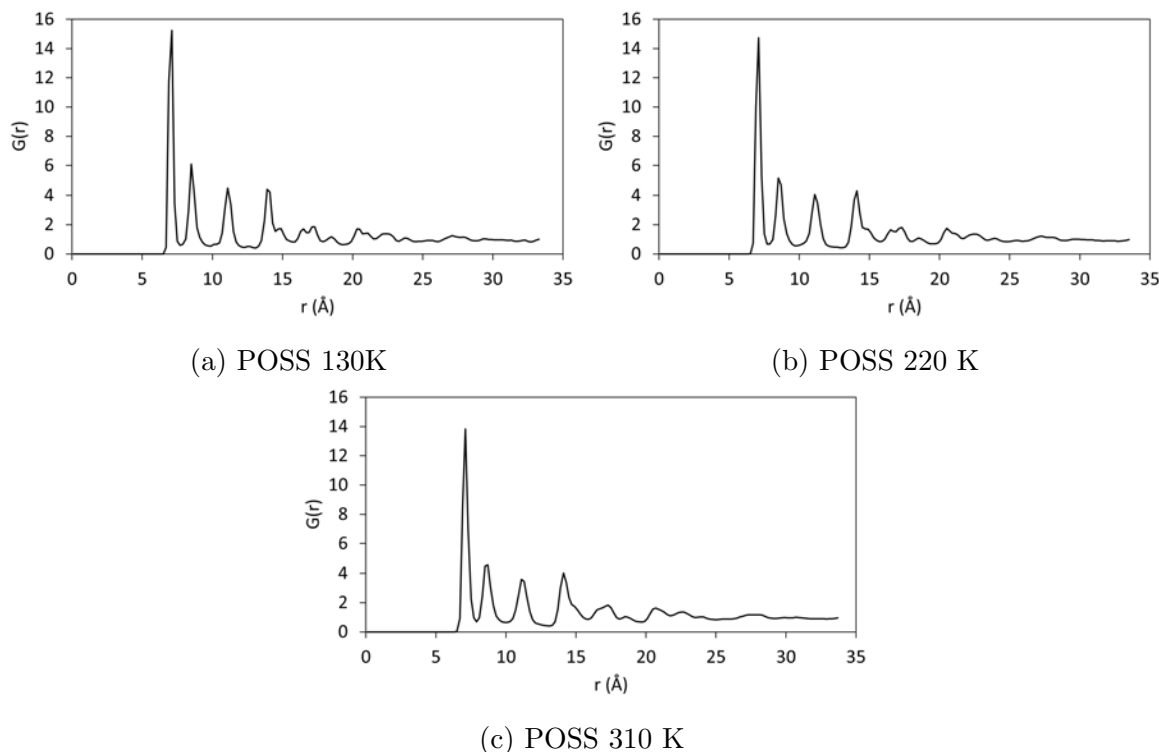
Figure 6.2.13: Radial distribution function for T_8H_8 at 50% wt POSS over the course of a cooling sequence taken at 130, 220 and 310 K.

In figure 6.2.14, I depict several POSS molecules and their coordinates taken from the 130 K temperature final configuration file. Hydrogen atoms and HTPB molecules have been ommitted for clarity. Here I present 3 distinct planes, and their uniform packing. The orange, cyan and purple spheres represent the centres of mass for each POSS molecule. The orange POSS cages are not shown. This group of POSS demonstrates the first coordination sphere of T_8H_8. The calculated distances between the in plane centres of mass (7.08 and 8.63 Å) correspond to the first two G(r) peaks given in figure 6.2.13a and the third peak corresponds to the long diagonal neighbour. This image also highlights the orientation of the POSS molecules in reference to one another. Those in direct contact are slightly offset from each facet. This is due to the hydrogen atoms preferentially interacting with the exposed oxygen atoms of different POSS molecules.
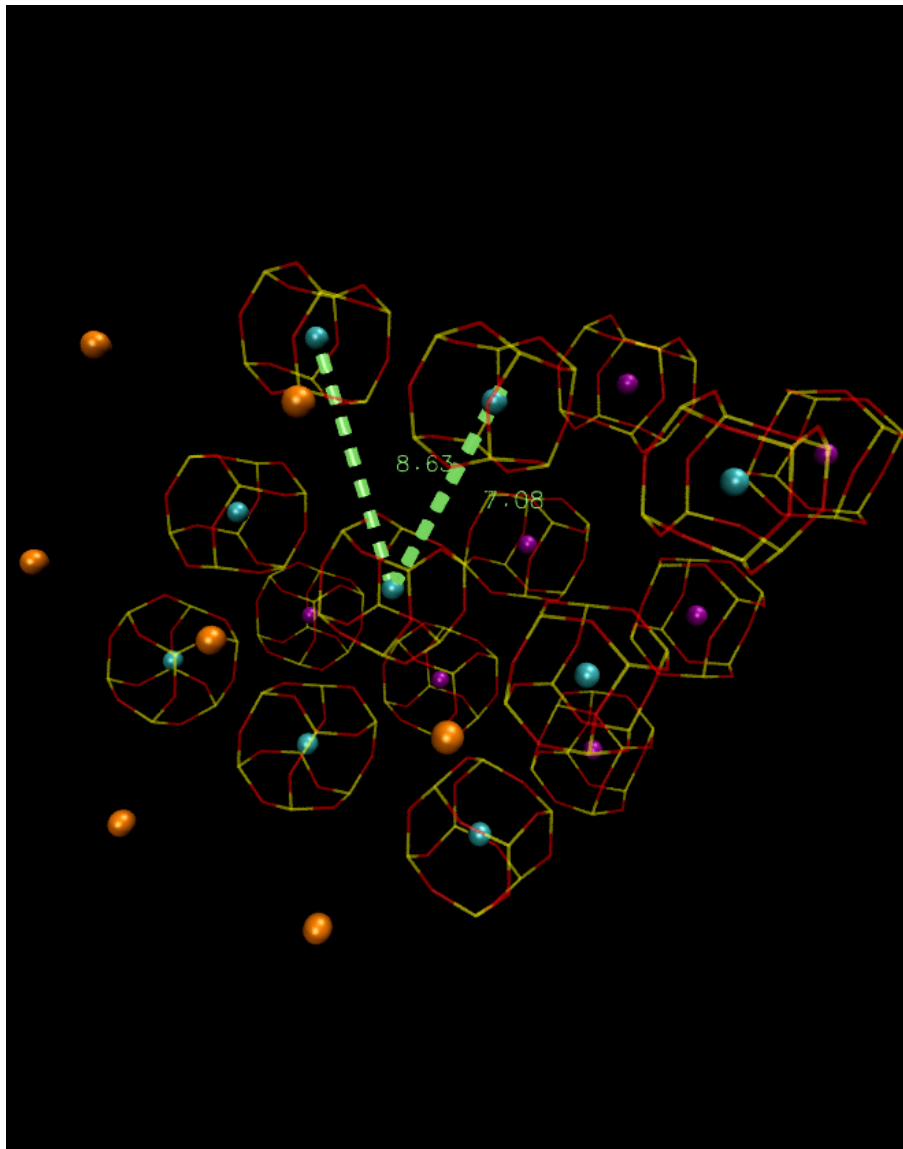
Figure 6.2.14: Rendering of several POSS molecules and their centres of mass from HTPB T_8H_8 blend at 50% wt POSS. This image depicts several POSS molecules that had agglomerated over the course of the cooling sequence. These show 3 distinct planes, as indicated by the colours of the centres of mass. orange is the closest plane, cyan is in the middle and purple is the furthest. Measurements of centre of mass distances are in Angstroms.

In addition, I have also carried out Voronoi analysis on the POSS and HTPB molecules. For these blended systems, my Voronoi regime is slightly different to that which I have used for previous systems. As these systems are mixed, the Voronoi algorithm generates Voronoi tessellations which consider both POSS and HTPB molecules. However, I am interested in the number of like neighbours. To address this, in the final analysis, I only consider the

Voronoi facets generated between like molecules. This analysis provides further insight into the packing of these systems. In figures 6.2.15a and 6.2.15b, I present the average number of like near neighbours for the HTPB and POSS molecules at all concentrations over the course of the cooling sequence. From the HTPB data, I see that, at all POSS concentrations, the HTPB molecules are highly entangled with each molecule in contact with at least 18 other HTPB molecules. The linear structure of HTPB enables the observed entanglement. As the number of near neighbours is maintained from the highest temperature and the MSD is very low, I can determine that the this molecular arrangement is established prior to passing through the Tg. Within these blended systems, I see that the Voronoi analysis greatly reflects the data seen in the G(r). At 10% loading, the average number of POSS near neighbours is approximately two. This demonstrates the strong effective potential between POSS molecules. As the concentration is increased to 30% and 50% I see further evidence that these molecules are strongly attracted to one another within the HTPB medium, as the number of immediate near neighbours climbs to 5 and 8, respectively.

(a) HTPB number of near neighbours   (b) POSS number of near neighbours
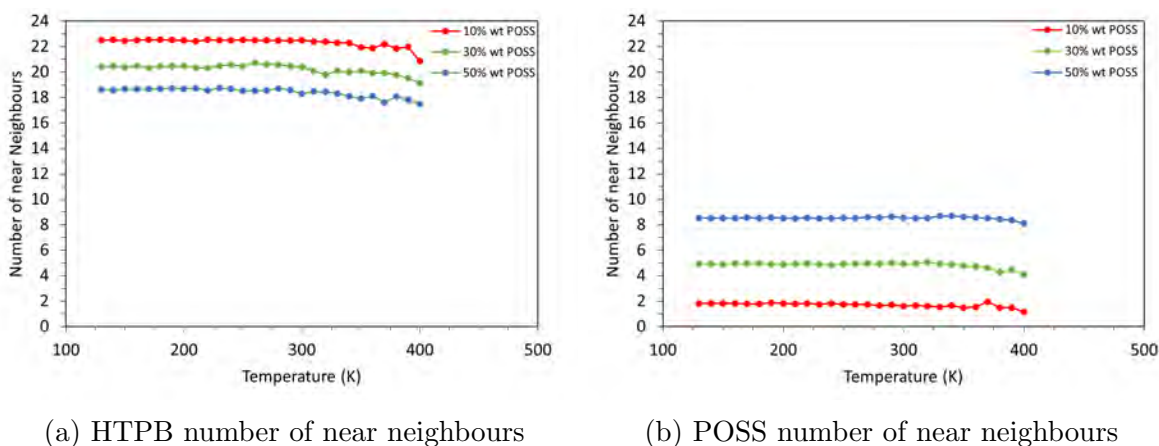
Figure 6.2.15: The number of like near neighbours for the HTPB (left) and POSS T_8H_8 (right) molecules over the course of the cooling sequnce.

6.2.2   HTPB T_8t-butyl$_8$ blend

In addition to T_8H_8 blended systems, I have also studied the behaviour of T_8t-butyl$_8$ POSS blended within HTPB at 10, 30, 50% wt. This molecular structure is denoted by an increase

in the organic ratio within the POSS structure. The t-butyl functional groups enable molecular symmetry to be upheld while increasing the molecular radius of the structure. Like in the T_8H_8, due to molecular symmetry and rigidity, the moment of inertia measures for T_8t-butyl$_8$ do not exhibit a bilinear relationship with temperature.

In figure 6.2.16a, I present the specific volume vs temperature relationship for T_8t-butyl$_8$ within HTPB at 10% wt. Similarly to the 10% T_8H_8 predicted T_g of 244.1 K, here, I predict a T_g of 236.9 K. This value is also very similar to the pure HTPB 311 value of 236.8 K from this method. The predicted T_g from the dihedral rotations method for the HTPB molecules is 244.9 K, in reasonable agreement with the specific volume method. As is observed in the T_8H_8 blended systems, I see that the availability of dihedral rotation is relatively unaffected by the presence of this POSS species.

(a)   (b)
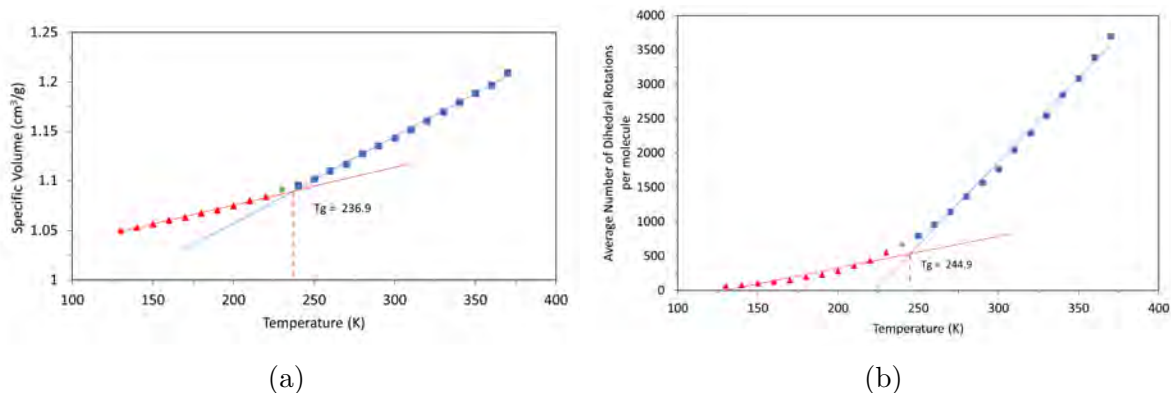
Figure 6.2.16: predicted from the specific volume and Temperature relationship for 10% wt T_8t-butyl$_8$ in HTPB (left) and predicted T_g from the average number of dihedral rotations per HTPB molecule (right) at 10% wt POSS.

Surprisingly, I also see that a bilinear relationship exhibited from the dihedral rotation method when applied to the T_8t-butyl$_8$ POSS molecules. In figure 6.2.17, I present the results from the dihedral rotation analysis of T_8t-butyl$_8$ at 10% wt. Here I predict a T_g of 268.1 K, however, 10 K above and below this value, there are clear discrepancies from the bilinear ideal. Although this method does predict a T_g in agreement with the other methods, I interpret this as the sudden availability of certain dihedrals. From the T_8H_8 study, I know

that the contribution from the POSS cage to the dihedral rotation count is negligible. The t-butyl functional group introduces two types of dihedral to the molecular structure. The first type is that which is introduced at the C-C bond at the terminal carbon atom. The second type relates to dihedral rotation occurring at the Si-C bond. Alternatively, type one describes the rotation of the methyl groups about the central carbon atom and the second type describes the rotation of the all three methyl groups about the silicon atom.
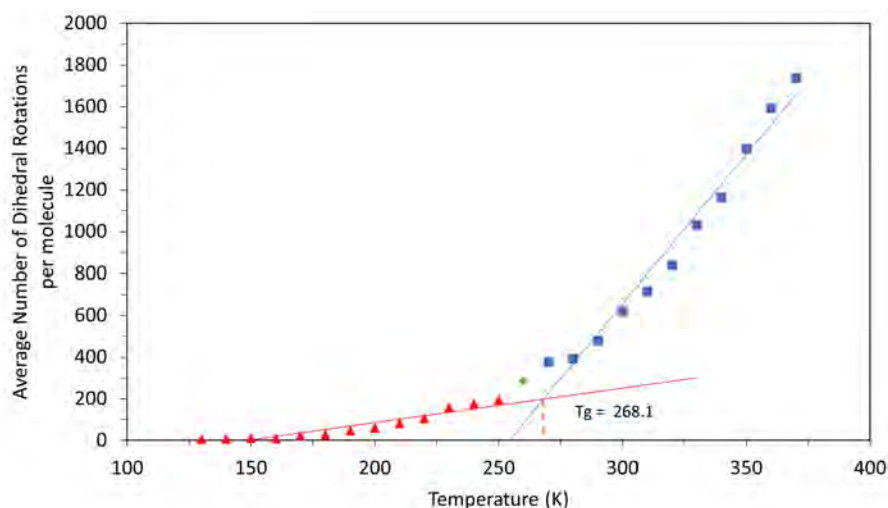
Figure 6.2.17: The average number of dihedral rotations per molecule over a range of temperatures for $T_8 t$-butyl$_8$ molecules in a blended system of at 10% wt POSS.

In terms of packing, this system exhibits similar tendencies to those seen in $T_8 H_8$ blended systems. At this concentration of POSS, I see that the molecules exhibit increased clustering on cooling. At approximately 12 and 14 Å, at 310 K, I observe initial indication of clustering behaviour. At 130 K, the G(r) consists of very sharp peaks, indicating very little movement is available to the molecules, but the dominant feature of 12-13 Å suggests molecular association.

(a) POSS 130 K

(b) POSS 220 K

(c) POSS 310 K
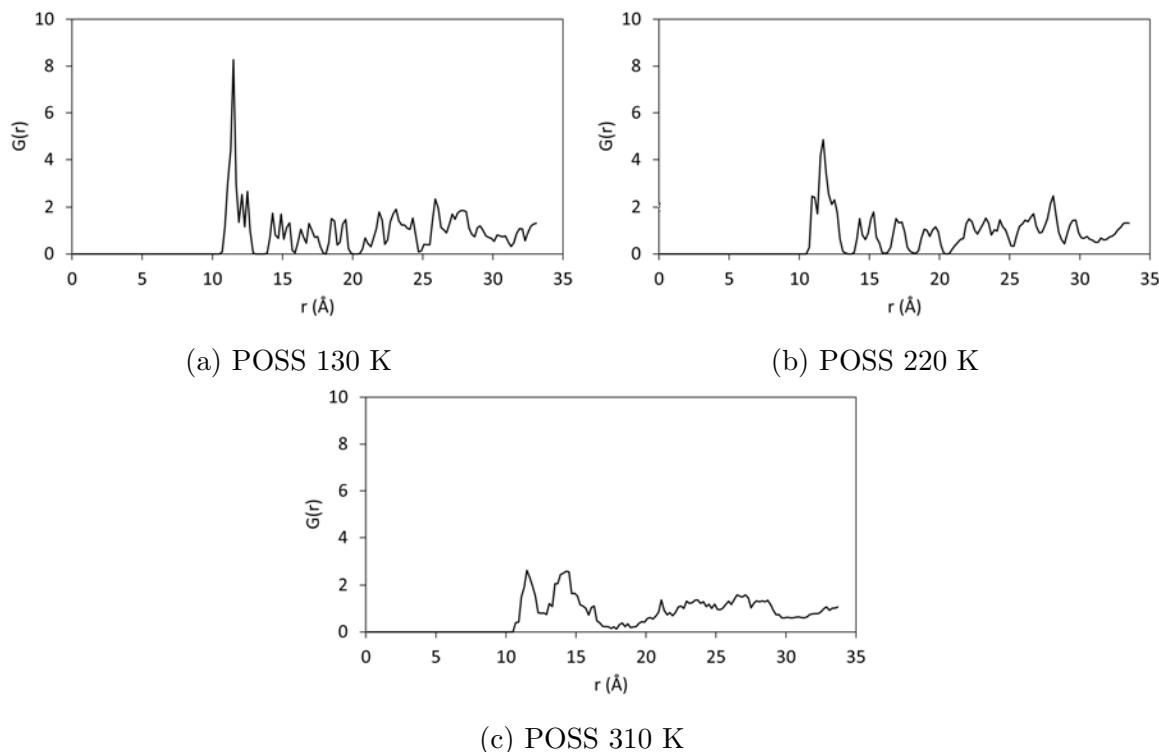
Figure 6.2.18: Radial Distribution analysis for T_8t-butyl$_8$ molecules at 10% wt POSS at 130, 220 and 310 K.

For these systems, I have also investigated the mean squared displacement. Here, the 10% wt T_8t-butyl$_8$ blended system exhibits less mobility than its T_8H_8 10% counter part. From a sterics perspective, the T_8t-butyl$_8$ system has much more opportunity to become entrapped by the HTPB molecules, lending to an overall lower mobility.

(a) HTPB MSD

(b) POSS MSD
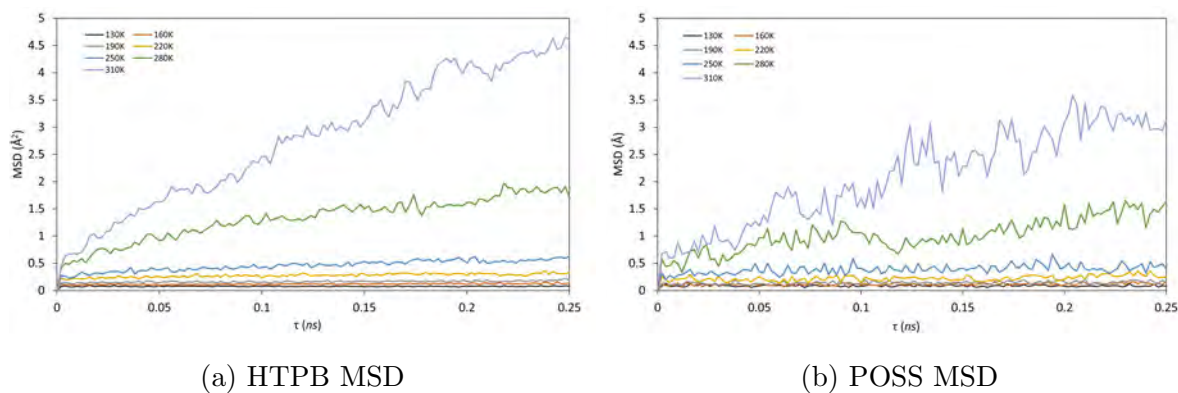
Figure 6.2.19: MSD data for HTPB (left) and T_8t-butyl$_8$ (right) at 10% wt over a range of temperatures

I will now discuss results from the 30% and 50% wt $T_8 t$-butyl$_8$ blended systems in tandem with one another. At 30% wt $T_8 t$-butyl$_8$ POSS loading, specific volume measurements predict a T_g of 246.1 K as seen in figure 6.2.20a. This value is 9.2 K higher than the 10% wt $T_8 t$-butyl$_8$ system and 9.3 K higher than the pure POSS system. Similarly to the $T_8 H_8$ blended system, I observe that increase in POSS concentration results in an increased predicted T_g value though the specific volume method. As shown in figure 6.2.20b, At 50% wt, I predict a further marked rise to T_g to 263.4 K. It should be noted that as the angle between the trend lines becomes smaller, as a result, measurement error for T_g becomes greater.

(a) 30% $T_8 t$-butyl$_8$ HTPB blend   (b) 50% $T_8 t$-butyl$_8$ HTPB blend
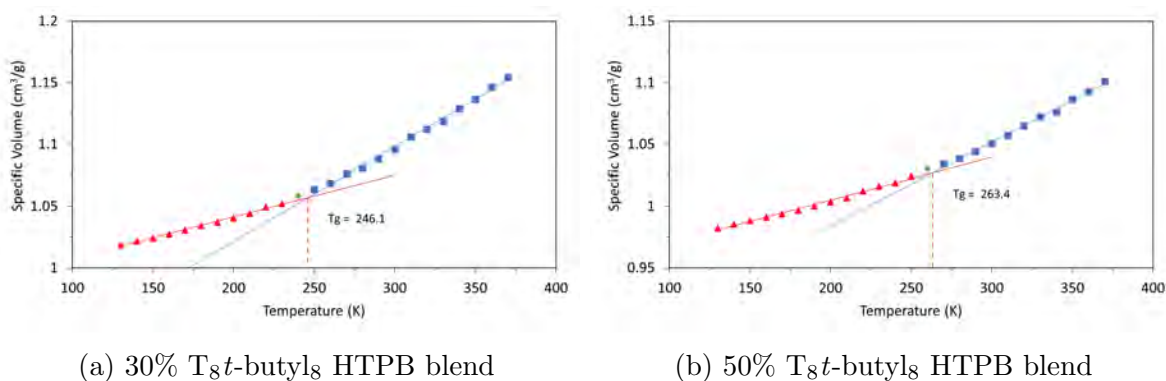
Figure 6.2.20: Specific volume vs temperature relationship for $T_8 t$-butyl$_8$ blended in HTPB 311 at 30% (left) and 50% wt loadings.

Through the Dihedral rotation of HTPB analysis method, I am also able to predict a T_g for both the 30% and 50% systems. As shown in figure 6.2.21, I predict Tgs of 253.3 and 253.0 K for the 30% and 50% systems respectively. These values are remarkably similar and are also relatively close to the 10% predicted T_g of 244.9 K.

(a) 30% T$_8$$t$-butyl$_8$ HTPB blend

(b) 50% T$_8$$t$-butyl$_8$ HTPB blend
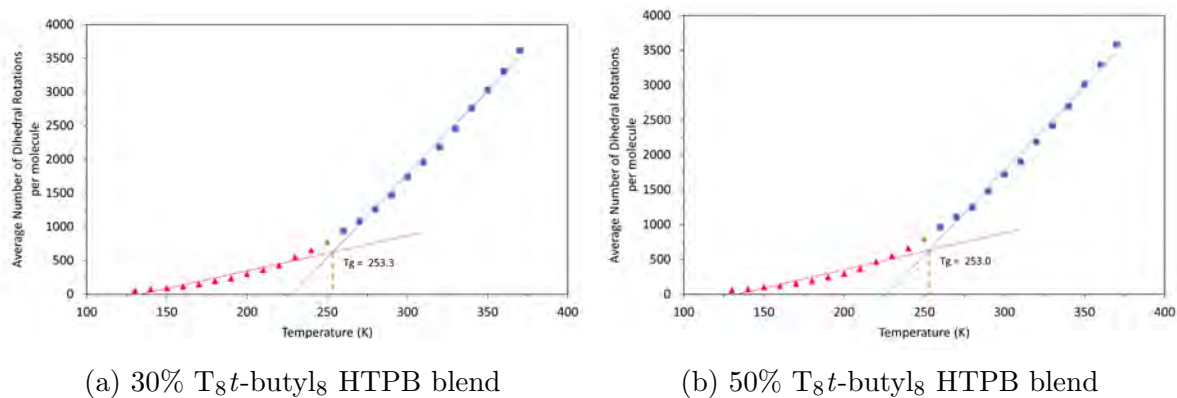
Figure 6.2.21: The average number of Dihedral Rotations per HTPB molecule at 30% and 50% wt T$_8$$t$-butyl$_8$ POSS loadings

These findings provide a further indication that the HTPB dihedral rotation is not impeded by the presence of POSS. Again, for each temperature, the average number of dihedral rotations are in step for all concentrations. In figure 6.2.22, I present the dihedral rotations for each C-C bond within the HTPB backbone for all HTPB molecules. As is shown, at several positions, the HTPB molecules that form part of the T$_8$$t$-butyl$_8$ blended systems experience a higher frequency of dihedral rotations than they do in the pure HTPB system. For example, C-C index 9 and 10. However, this trend is not as distinct as that observed in the T$_8$H$_8$ blended systems.
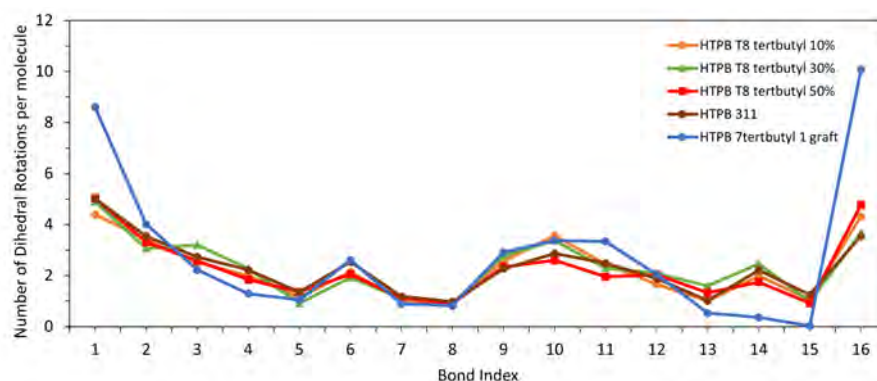
Figure 6.2.22: The average number of C-C Dihedral rotations that occur along the back bone of the HTPB molecule at different concentration of T$_8$$t$-butyl$_8$ at 200K. The bond index relates to the position of the C-C bond in relation to the *trans* terminus of the molecule

In figure 6.2.23, I present the radial distribution function for 30% (left) and 50% (right)

wt T_8t-butyl$_8$ HTPB blended systems. For the POSS molecules, I see similar behaviour to the T_8H_8 blended systems in that short-ranged peaks suggest some level of agglomeration. At all three concentrations, two clear peaks are observed at 11 Å and 13 Å for T = 130, 220 and 310 K. However, the peak heights are significantly lower than those observed in the T_8H_8 systems and the long range increase in the number peaks with increased POSS concentration has been lost with the addition of the *tert*-butyl functional group. While there is some indication of longer range ordering, with peaks at 18 and 23 Å, these features are very small and broad.

(a) 30% T_8t-butyl$_8$ POSS 130K G(r)

(b) 50% T_8t-butyl$_8$ POSS 130K G(r)

(c) 30% T_8t-butyl$_8$ POSS 220K G(r)

(d) 40% T_8t-butyl$_8$ POSS 220K G(r)

(e) 30% T_8t-butyl$_8$ POSS 310K G(r)

(f) 50% T_8t-butyl$_8$ POSS 310K G(r)
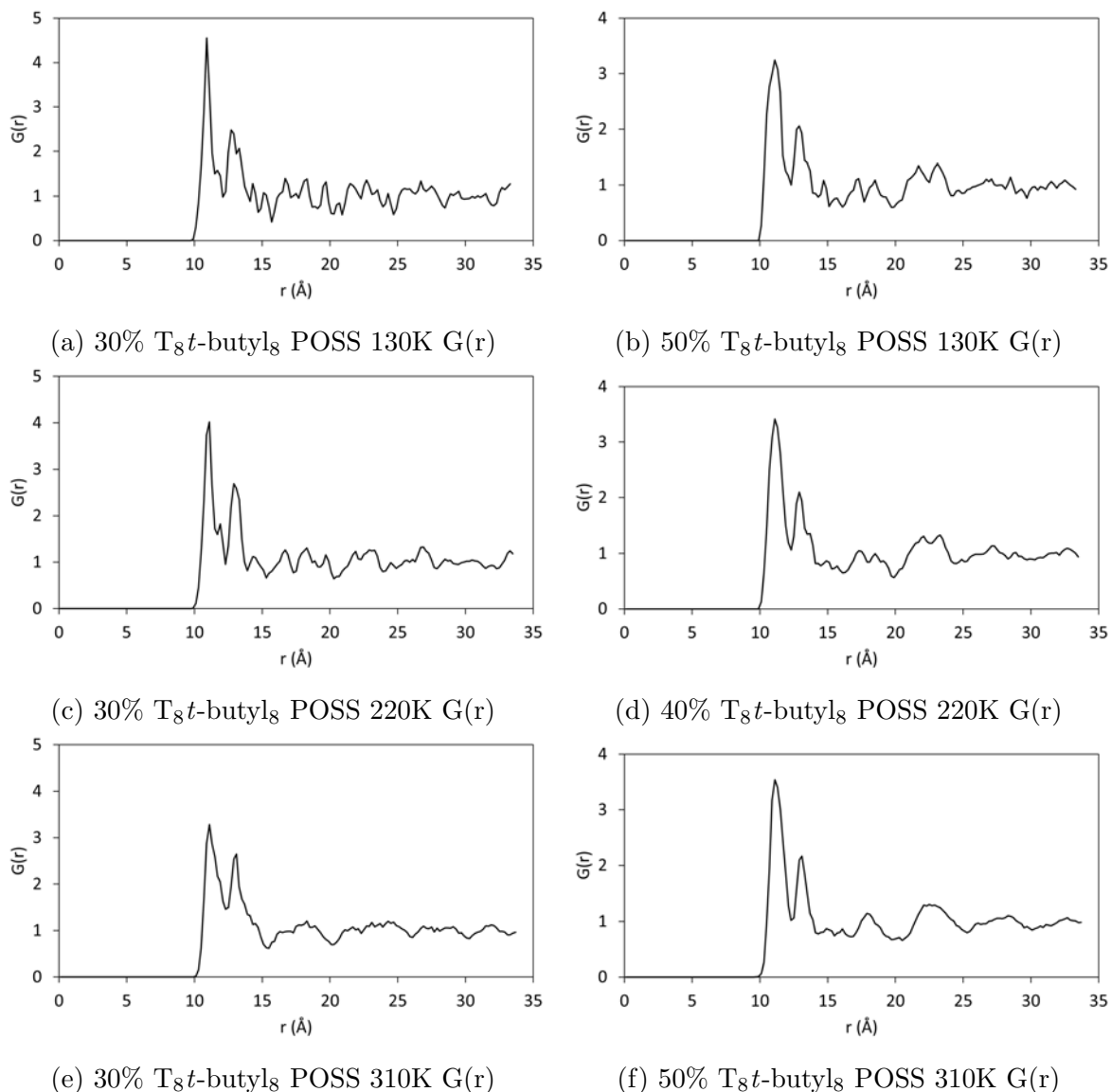
Figure 6.2.23: Radial Distribution function analysis for T_8t-butyl$_8$ in HTPB 311 at 30% (left) and 50% wt (right) concentration at 130, 220 and 310K.

I have also performed Voronoi analysis of the like neighbours for the HTPB and POSS molecules. For the T_8H_8 system, I saw for POSS molecules the average number of near neighbours of approximately 2.0, 5.0 and 8.5 for 10, 30 and 50% respectively. Here, for T_8t-butyl$_8$, I see a clear decrease in these values at all percentages to 0.5, 3.8 and 6.2. Thus, despite the molecular radius being larger than that of the T_8H_8 system, fewer neighbours are observed for T_8t-butyl$_8$.
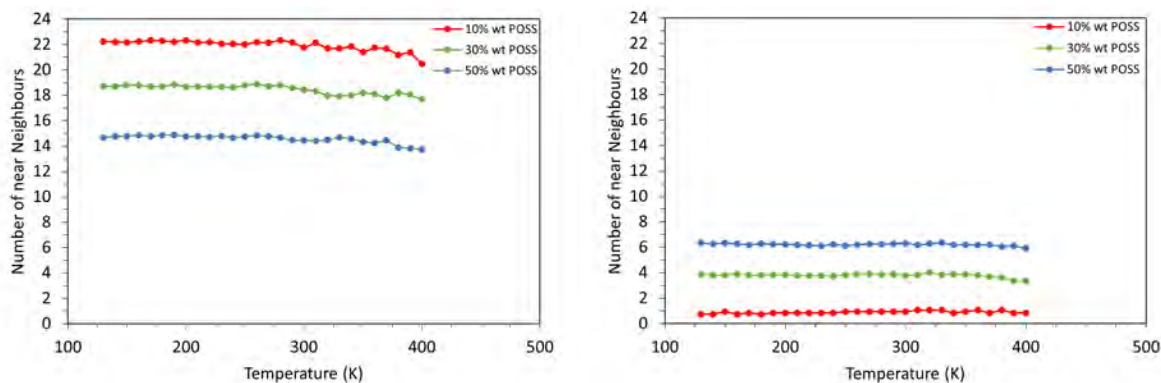
(a) HTPB number of near neighbours

(b) POSS number of near neighbours

Figure 6.2.24: The number of like near neighbours for the HTPB (left) and POSS T_8t-butyl$_8$ (right) molecules over the course of a cooling sequence determined through voronoi tessellation diagrams.

6.2.3   HTPB T_8propyl-methacrylate$_8$ blend

To complete my POSS-HTPB nanocomposite blend study, I have also used the much larger T_8propyl-methacrylate$_8$ POSS species. By comparison to the previous two POSS structures T_8propyl-methacrylate$_8$ has a much larger molecular weight, molecular radius and capacity for interdigitation. The much longer and sterically cumbersome propyl-methacrylate functional group offers an interesting contrast to the much smaller hydrogen and t-butyl groups.

At 10% wt POSS, from the specific volume method, I predict a T_g of 244.5 K as shown in figure 6.2.25. The T_8propyl-methacrylate$_8$ systems is predicted to have the highest T_g at the 10% concentration as this value is 0.4 and 7.9 K higher than the predicted T_g from the same method for the 10% T_8H_8 and T_8t-butyl$_8$, respectively. This value is also 7.7 K higher than the pure HTPB 311 system.
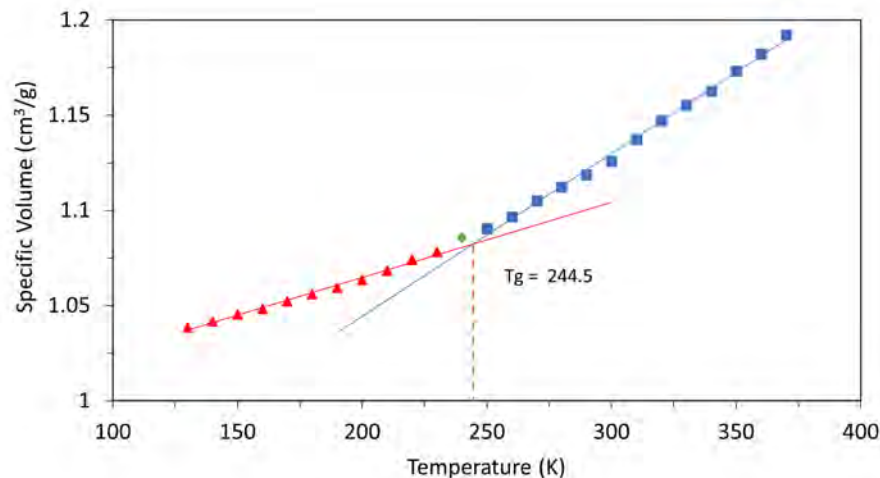
Figure 6.2.25: Specific volume vs temperature relationship for T_8propyl-methacrylate$_8$ blended in HTPB 311 at 10% wt POSS

I have also carried out dihedral rotation analysis for the prediction of Tg. Results from both the HTPB and POSS molecules are presented in figure 6.2.26. Due to the dihedral freedom of the propyl linker chain of the propyl-methacrylate functional group, I am able to use the same methodology for POSS molecules. The predicted value from the HTPB data is in excellent agreement with the specific volume method, being only 0.4 K higher than the specific volume predicted Tg. The POSS data, however, over predicts the T_g with a value of 254.3 K.

(a) HTPB   (b) POSS
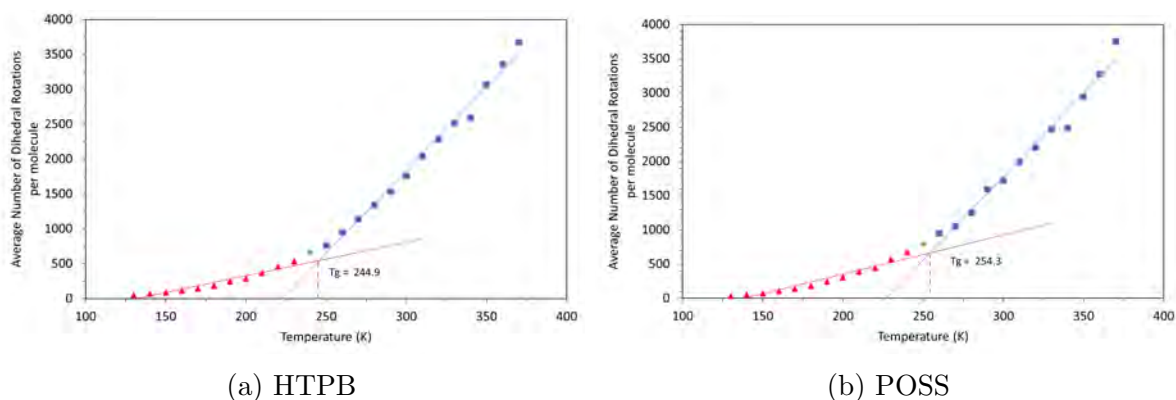
Figure 6.2.26: The average number of dihedral rotations per molecule for HTPB (left) and T_8propyl-methacrylate$_8$ molecules at 10% wt concentration with a HTPB blend.

In figure 6.2.27 I present the predicted T_g from the standard deviation in the moment

of inertia method for the POSS molecules. Here I predict a T_g of 243.6 K. Again this number is in good agreement with the specific volume method of 244.5 K. This result is particularly encouraging for the efficacy of this methods for the HTPB and POSS system on an individual basis. For the pure T_8propyl-methacrylate$_8$ system, as shown in figure 4.2.12, I predict T_g values of 259.1 and 268.1 K for the specific volume and moment of inertia method respectively. These values denote a decrease in predicted T_g values of 14.6 and 24.5 K for the respective methods with the dispersion within POSS.
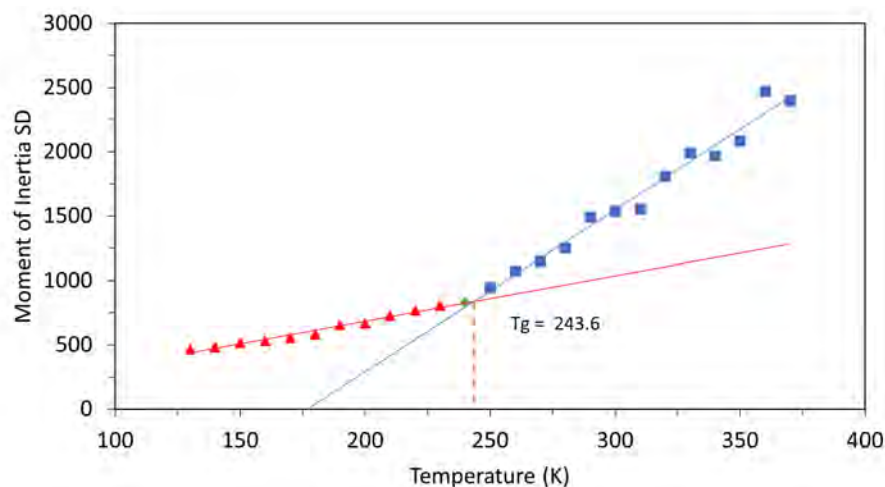
Figure 6.2.27: The standard deviation in the moment of inertia of a range temperatures for T_8propyl-methacrylate$_8$ POSS molecules in a HTPB blended system at 10% wt.

Structurally, this system is distinct from the previous 10% blends. In figure 6.2.28, I present the G(r) for the T_8propyl-methacrylate$_8$ molecules at 130 K. Here, I see two initial sharp peaks at   9 and 11.5 Å. Although these peaks may be indicative of high order packing, each of these is in fact likely due to the interaction of just two POSS molecules. Because of the larger number of atoms in T_8propyl-methacrylate$_8$, I have 13 molecules within the system. The observed initial sharp peaks within this plot are due to the interactions between a limited number of molecules.
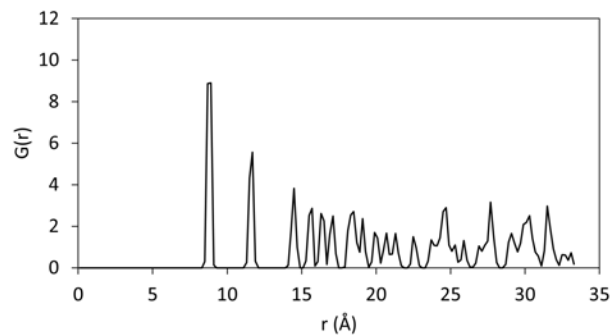
Figure 6.2.28: The radial distribution function analysis at 130 K for HTPB 311 (left) and T_8propyl-methacrylate$_8$ (right) at 10% wt POSS.

In figure 6.2.29, I present the mean square displacement for the HTPB and T_8propyl-methacrylate$_8$ molecules at 10% wt loading. Again, for both molecules, I see very little movement en masse above and below the Tg.

(a) HTPB MSD

(b) POSS MSD
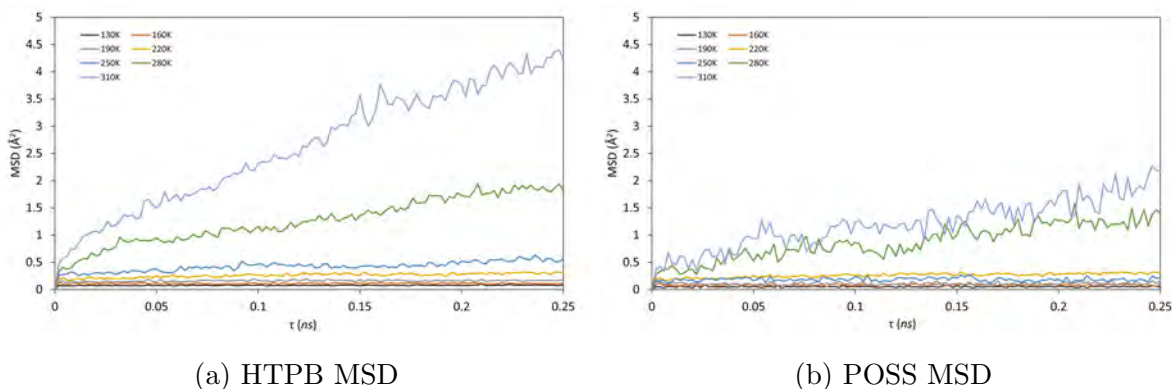
Figure 6.2.29: The mean square displacement for HTPB 311 (left) and T_8propyl-methacrylate$_8$ at 10% over a range of temperatures

At 30% and 50% wt concentration, I observe an increase in T_g from 244.5 K to 249.1 and 250.6 K from the specific volume method as shown in figure 6.2.30. These increases maintain the trends described for the T_8H_8 and T_8t-butyl$_8$ systems. This increase, however, is over a much narrower temperature range than the previous systems, with T_8t-butyl$_8$ blended systems having the greater T_g increase from 236.9 to 263.4 K on changing the POSS wt percentage from 10% to 50% respectively.

(a) HTPB T_8propyl-methacrylate$_8$ 30%   (b) HTPB T_8propyl-methacrylate$_8$ 50%
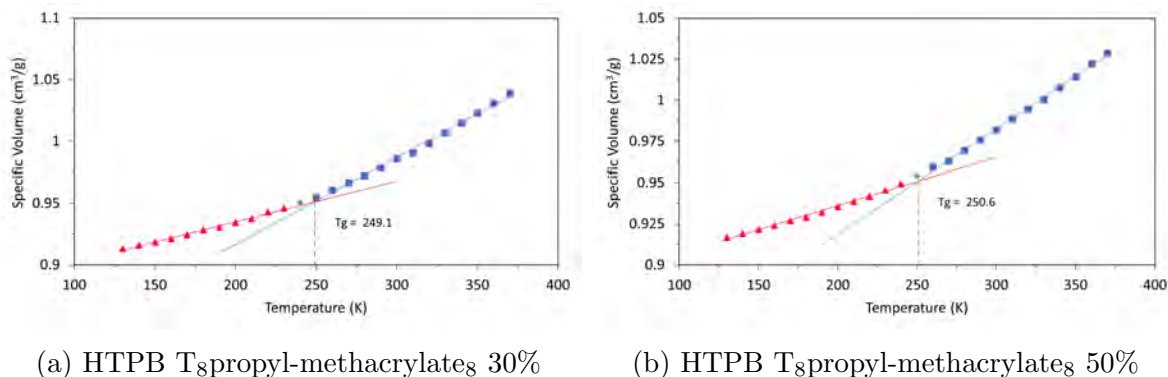
Figure 6.2.30: The specific volume vs temperature relationship for HTPB T_8propyl-methacrylate$_8$ blends at 30% (left) and 50% (right) loading

For the 30% POSS system, from the number of dihedral rotations method applied to HTPB, and the standard deviation of the moment of inertia method applied to the POSS molecules, I predict Tgs of 247.2 and 257.0 K respectively; as shown in figures 6.2.31a and 6.2.31b. Here, the dihedral rotations analysis predicts a T_g in much closer agreement to the specific volume method of 249.1 K. At 50% wt POSS, I predict Tgs of 246.9 and 272.3 K from the respective methods. For the equivalent pure T_8propyl-methacrylate$_8$ system, as shown in figures 4.2.11b and 4.2.11d in chapter 4, I predict Tgs of 259.1 and 268.1 K from the specific volume and moment of inertia methodology respectively. Here, the 50% T_8propyl-methacrylate$_8$ blend has good agreement with the pure system when I consider the standard deviation method results. However, when blended with HTPB at this concentration, the T_g is reduced by 9.1 K when the specific volume method is employed. Through the blending of T_8propyl-methacrylate$_8$ with HTPB, therefore, the breathing mode of the POSS species no longer appears to be the dominant molecular mechanism in the determination of Tg.
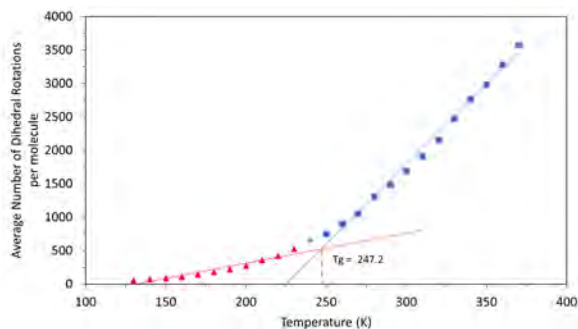
(a) T_8propyl-methacrylate$_8$ 30% HTPB Dihedral rotation analysis
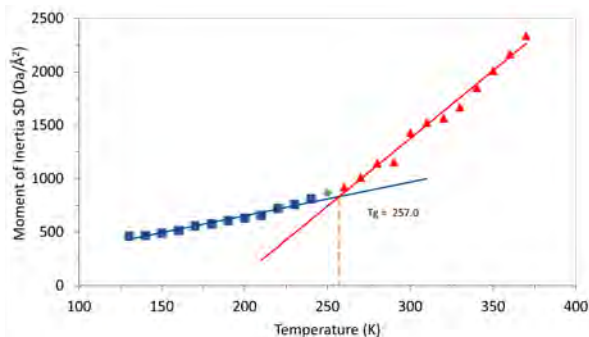
(b) T_8propyl-methacrylate$_8$ 30% POSS standard deviation in moment of inertia analysis
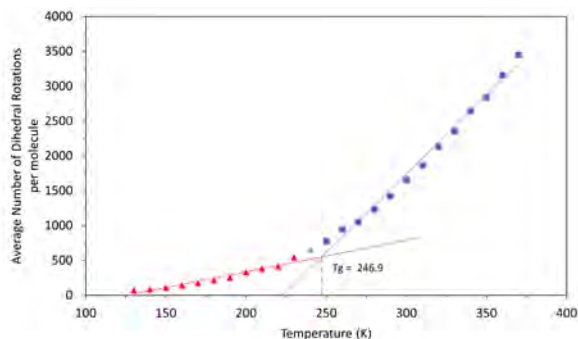
(c) T_8propyl-methacrylate$_8$ 50% HTPB Dihedral rotation analysis
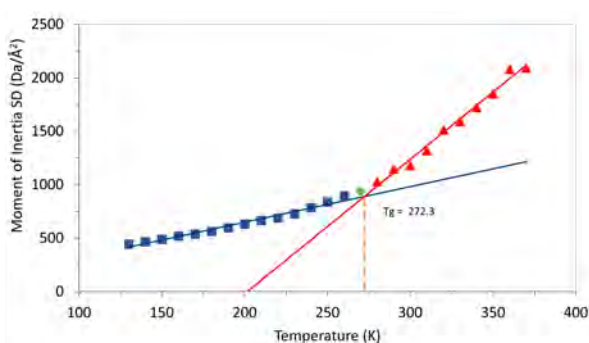
(d) T_8propyl-methacrylate$_8$ 50% POSS standard deviation in moment of inertia analysis

Figure 6.2.31: Predicted T_g from the average number of dihedral rotations per HTPB molecule (right) and the standard deviation in the moment of inertia of POSS (right) at 30% wt loading (top) and 50% wt loading (bottom)

In addition, as I have also analysed the molecular packing of these systems. For the POSS molecules of these systems, as shown in figure 6.2.32, I observe amorphous packing. For both concentrations, I observe an initial exclusion region, due to the effective molecular radius, until 9.5 Å where I see the first peak. The G(r) plots for these systems are qualitatively different from those of the previous systems as the interdigitating propyl-methacrylate functional groups have much higher tendancy to entangle with the HTPB molecules, thereby reducing the capacity for phase separation. These plots are also very similar to those of the pure T_8propyl-methacrylate$_8$ system as shown in figure 4.2.14.

(a) 30% T_8propyl-methacrylate$_8$ 130 K

(b) 50% T_8propyl-methacrylate$_8$ 130 K

(c) 30% T_8propyl-methacrylate$_8$ 220 K

(d) 50% T_8propyl-methacrylate$_8$ 220 K

(e) 30% T_8propyl-methacrylate$_8$ 310 K

(f) 50% T_8propyl-methacrylate$_8$ 310 K
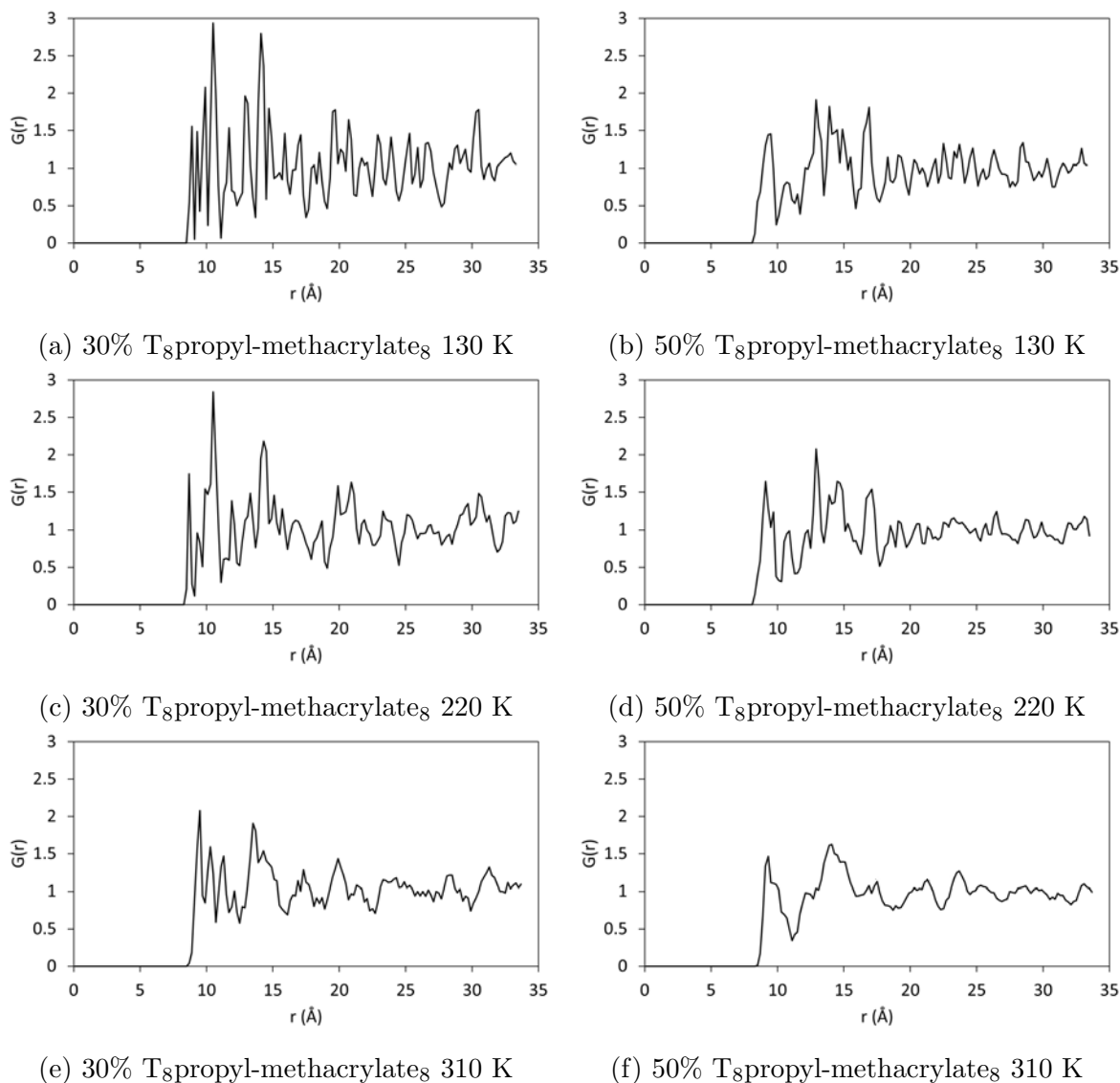
Figure 6.2.32:   Radial distribution function analysis for T_8propyl-methacrylate$_8$ POSS molecules at 30% (left) and 50% wt (right) at 130, 220 and 310 K.

Voronoi analysis has also been carried out on these systems. In figure 6.2.33, I present the average number of like near neighbours for the HTPB and T_8propyl-methacrylate$_8$ POSS molecules at all concentrations. Interestingly, I see that the average number of like neighbours for the POSS molecules is quite similar to that of the T_8t-butyl$_8$ and T_8H_8 systems. For a binary amorphous system, it might be expected that these values would be lower. However, the capacity of these molecules to interdigitate with one another and the POSS molecules, means they are able to form close contacts with one another through their propyl-

methacrylate functional groups, despite the separation of their silica cores being spread over a range of distances. Further more, I see that the number of near neighbours for the HTPB molecules at 50% wt concentration is significantly lower than that of the 50% T_8H_8 system. Again, this feature can be attributed to the degree of interdigitation by the propyl-methacrylate functional groups.
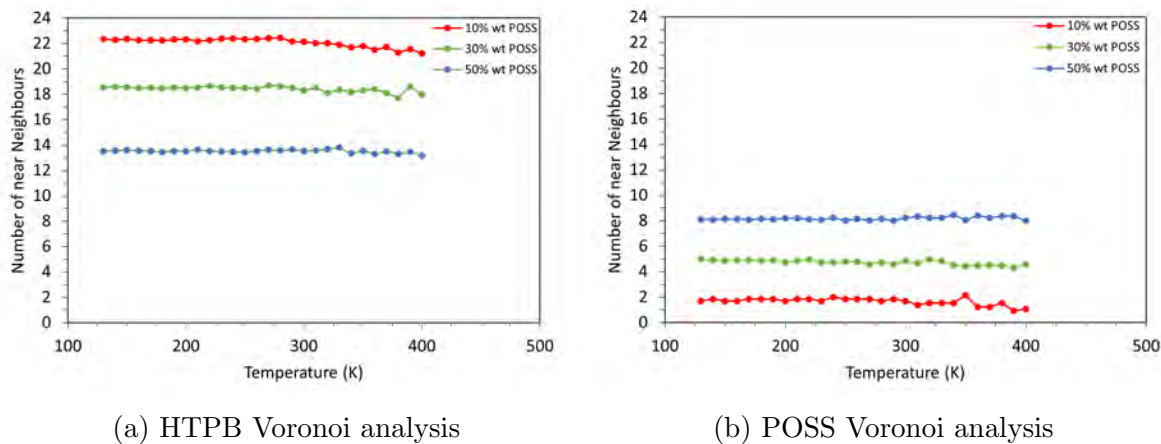
(a) HTPB Voronoi analysis   (b) POSS Voronoi analysis

Figure 6.2.33: The average number of like near neighbours for the HTPB and T_8propyl-methacrylate$_8$ molecules at 10, 30 and 50% wt concentration over the course of a cooling sequence. These values are determined from Voronoi tesselation diagrams.

Finally, I have analysed the dihedral freedom of the HTPB molecules across all POSS concentration at 200 K as shown in figure 6.2.34. Here, I see that the dihedral freedom follows the same trend as bulk HTPB between indices. Interestingly, I see that the greatest degree of freedom is observed in the 50% concentration, where the number of dihedral rotations are mostly higher than within the pure system.
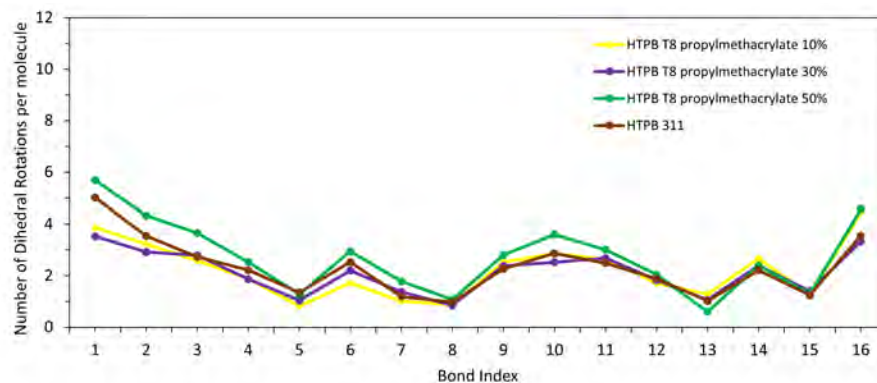
Figure 6.2.34: The average number of C-C Dihedral rotations that occur along the back bone of the HTPB molecule at different concentation of T_8propyl-methacrylate$_8$ at 200K. The bond index relates to the position of the C-C bond in relation to the *trans* terminus of the molecule

6.3   Octetraene-POSS Nanocomposite

In addition to HTPB, I have also studied the use of octatetraene as a nanocomposite matrix with POSS. Octetraene is the smallest molecule with nearly equivalent chemistry to HTPB which is in condensed phases at standard conditions. I can use it to investigate whether the phase separation behaviour seen in section 6.2 is significantly influenced by the intrinsic mobility of the matrix component. Here, therefore, I investigate how the difference in properties between HTPB and octetraene impact the behaviour of the POSS molecules during simulation. As discussed, HTPB has a strong tendency to become entangled due to the long and flexible nature of the molecular backbone containing 36 Carbon atoms from end-to-end. In contrast, octatetraene is a much shorter and, by nature, a more linear molecule.

The molecular structure for octatetraene is given in figure 6.3.1. This structure has 4 double bonds at equal spacing within the molecular backbone. This means there are only 3 sites available for dihedral rotation. Through the use of this molecule, I aim to further understand the molecular mechanisms that influence the bulk behaviour of POSS containing materials and how they interact with the matrix of a nanocomposite. For this section of the study, I

have focused on the all *Trans* morphology of octatetraene. For comparison, I have also conducted the same types of analyses on pure octatetraene, which I will discuss in the following section.
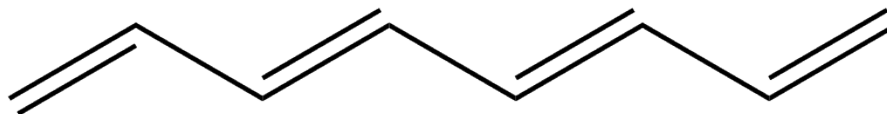
Figure 6.3.1: Molecular structure of octatetraene

6.3.1 The Simulation of pure Octatetraene

In the same fashion as my previous simulation studies, this system has 30,000 atoms and is first annealed at a high temperature before being subjected to a cooling sequence in the range 400 - 130 K. One key fundamental difference between octetraene and HTPB is that at standard conditions, octatetraene is a colourless liquid, where as HTPB 311 is a rubbery material. However, I have identified this species as a viable candidate as according to the literature, the boiling point of octatetraene is 362.2 K, which is at the upper limit of my cooling sequence.[151]

From my simulations, I identify what may be considered condensation from the gas phase at approximately 310 K. In figure 6.3.2a, I present the specific volume temperature relationship from the simulation of pure octatetraene. Within this plot, I have omitted the values from 300 K upwards as the system is not fully condensed, and the value of the specific volume is much larger than that of the condensed phase, meaning the bilinear plot that has been identified would not be visible. As is shown, this system appears to exhibit transition from liquid to solid behaviour at 244.3 K. Effectively, this is the melting temperature (T_m)

In figures 6.3.2b and 6.3.2c I analyse the standard deviation in the moment of inertia and average number of dihedral rotations per molecule as a function of temperature. For both

methods, I am able to retain data through the temperatures where the system is not fully condensed. Within this region, as shown in the MOI plot, the rate of increase in the change of shape is reduced. I postulate that this is due to the absence of close packing in none condensed systems. Close range forces that would be experienced by each molecule on each molecule are reduced, meaning there is less cause to undergo change in shape. That said, I do observe an increase in the number of dihedral rotations per molecule. The observed trend is displacement of the gradient in the condensed phase to a higher order. The overall gradient is maintained.

(a)

(b)

(c)
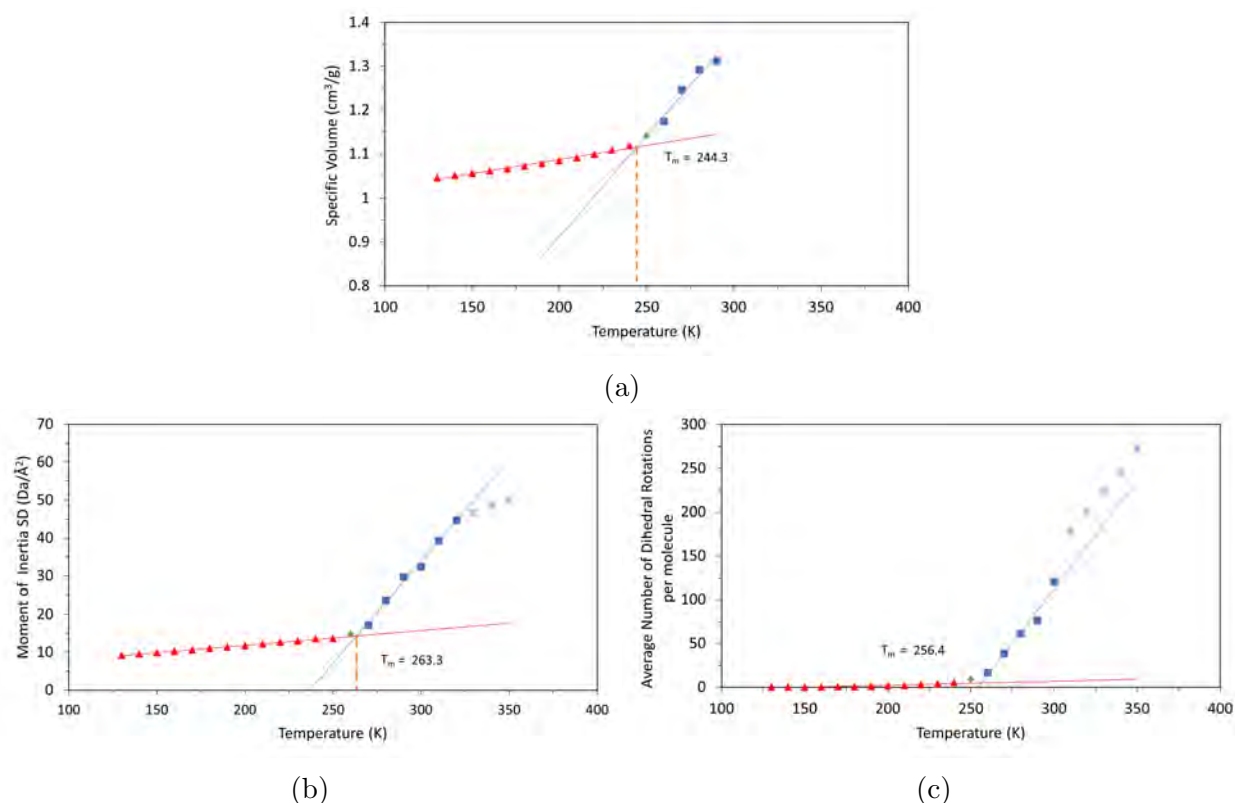
Figure 6.3.2: The prediction of the T_m for octatetraene from three different methods.

In figure 6.3.3, I present the average number of C-C dihedral rotations per C-C bond of the octatetraene molecule at 200, 260 and 320 K. Bond index 2 is the central C-C bond and index 1 and 3 are the peripheral single C-C bonds. Here, the system is transitioning through all three states as shown in figure 6.3.2. I observe an interesting paradigm shift in that the central C-C bond becomes increasingly active as the temperature increases compared to the

other C-C bonds.

Bond Index	Temperature (K)		
	200	260	320
1	0.042	0.673	7.303
2	0.020	0.604	11.488
3	0.052	0.662	7.281

Figure 6.3.3: The average number of dihedral flips for each C-C single bond of the octatetraene molecule at 200, 260 and 310 K.

In terms of packing, these molecules also exhibit interesting behaviour. In figure 6.3.4, I present the radial distribution function analysis for octatetraene molecules at 290, 270 and 250 K. At 290 K, the system exhibits amorphous liquid like behaviour with an amorphous spherical liquid like G(r) curve. as the system is cooled, I begin to see some long range order being introduced. At 250 K I see a great deal of order. In fact, the structure of these systems is near crystalline. For all molecules at 250 K, I calculate that the mean eigen-values from the moment of inertia are 34.2, 883.8 and 910.4, with standard deviation scores of 5.2, 24.1, 23.4 respectively. These results strongly suggest that these molecules are in a linear conformation and have highly regular packing.

(a) 290 K

(b) 270 K

(c) 250 K
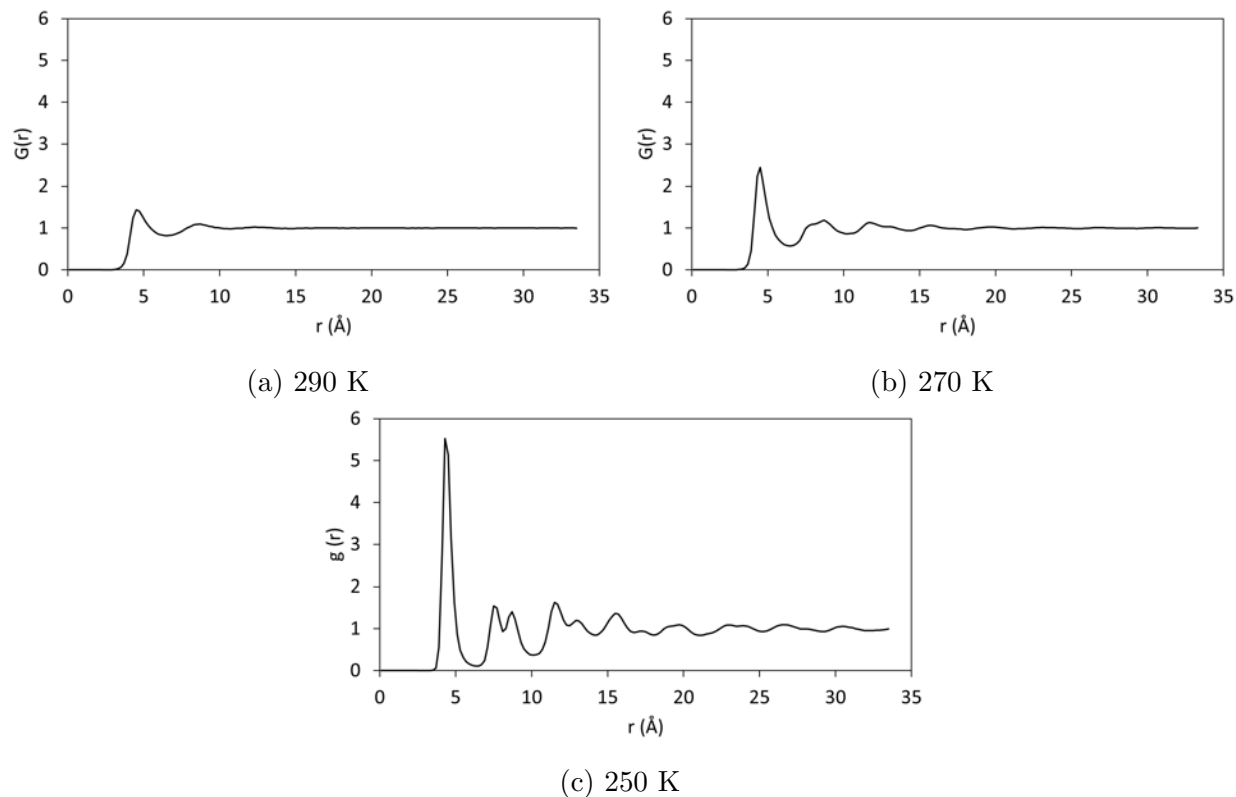
Figure 6.3.4: The radial distribution analysis for octatetraene at 290, 270 and 250 K.

With this fundamental understanding of octatetraene, I now analyse the effect of POSS incorporation. As I have carried out for the HTPB nanocomposite systems, I have 3 concentrations of POSS within each blend, 10%, 30% and 50% wt. Firstly, I will discuss results from the T_8H_8 blends starting with 10% wt concentration before moving onto the T_8t-butyl$_8$ and T_8propyl-methacrylate$_8$ blend.

6.3.2   Octatetraene T_8H_8 POSS blend

For the 10% wt POSS concentration system, as I have observed for the pure system, during the early steps of my cooling sequence, the system is not condensed. However this system does condensed at a higher temperature of 330 K. In figure 6.3.16, I present the predict T_m from the specific volume method, dihedral rotations method and moment of inertia method, the latter two of which use the octatetraene data only. As before, I have omitted the data

points for the specific volume method where the system is not condensed. Here I predict a T_m of 246.4 K, which is very similar to the pure octatetraene value of 244.3 K. In addition the other methods are also in agreement with the number of dihedral rotations method slightly over estimating with a value of 253.0 K.

(a)

(b)

(c)
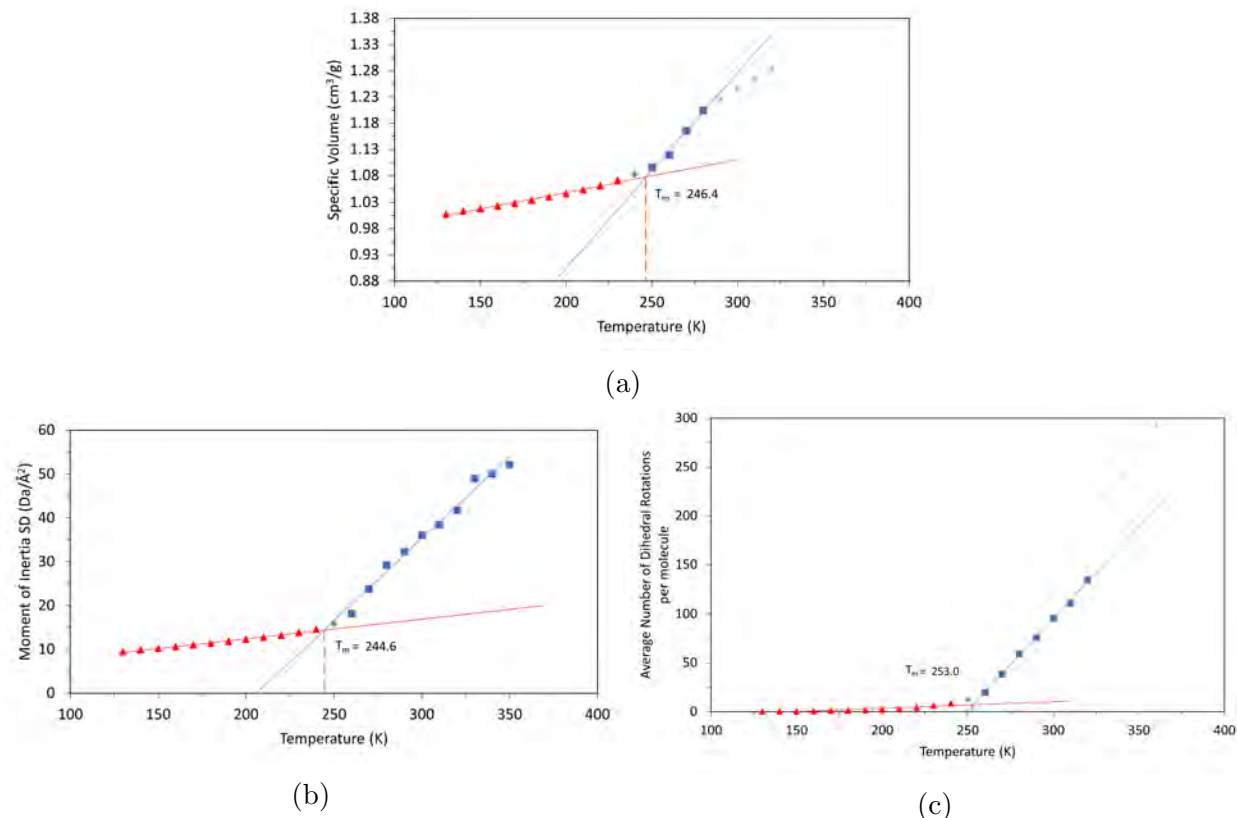
Figure 6.3.5: The T_m prediction from the specific volume temperature relationship (a), the standard deviation in the moment of inertia of octatetraene molecules (b) and the average number of dihedral rotations per octatetraene molecule (c) methods for Octatetraene-T_8H_8 10% POSS wt blends.

Within these data I observe some interesting differences with the pure system. From the specific volume relationship (figure 6.3.5a) I now see a triple linear pattern. The solid phase is denoted by red triangles, the second phase is denoted by blue squares and the third phase is blue stars. After 330 K, the data is omitted as the system is in the gas phase. To try to understand the means of this behaviour, I first look at the mean square displacement. In figure 6.3.6 I present the MSD for the octatetraene and POSS molecules. From these data,

I can see that for the POSS system, between the temperatures of 290 and 280 K, there is a decrease in the MSD, suggesting that there is a significant loss in the rate of increase in the mobility for the POSS molecules.

(a) octatetraene   (b) T_8H_8
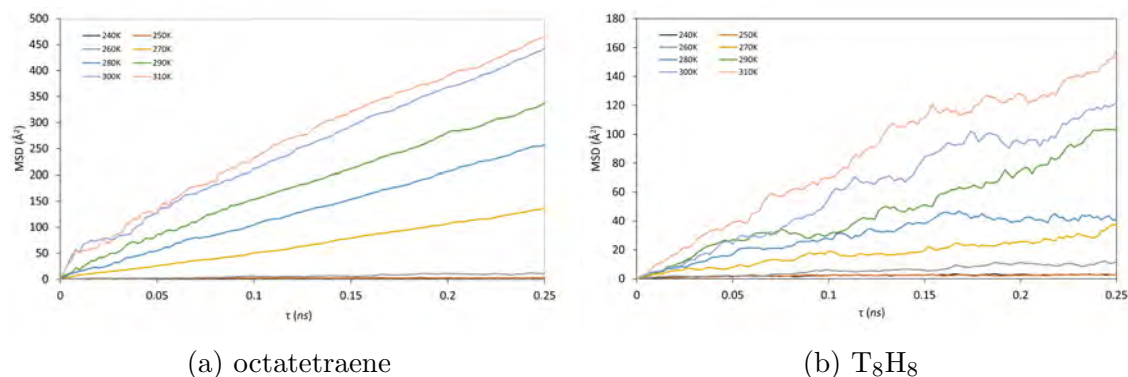
Figure 6.3.6: The MSD for the octatetraene (left) and T_8H_8 molecules (right) at 10% wt POSS concentration.

In addition, I have also considered the packing of these molecules. In figure 6.3.7, I present the radial distribution function of the octetraene and T_8H_8 molecules at 220 and 310 K. Here, the Octetraene data is highly reminiscent of the pure octatetraene system, where at the higher temperature I have amorphous liquid like behaviour, and at the lower temperature I have a highly ordered structure. The POSS molecules on the other hand do not present liquid like behaviour. Instead, there is a very strong peak at 7.5 Å that is retained at 220 K. This peak to be an artefact of the POSS molecules forming agglomerations whilst exhibiting the high mobility of the gaseous phase and liquid phase.

(a) Octetraene 220 K

(b) POSS 220 K

(c) Octetraene 310 K

(d) POSS 310 K
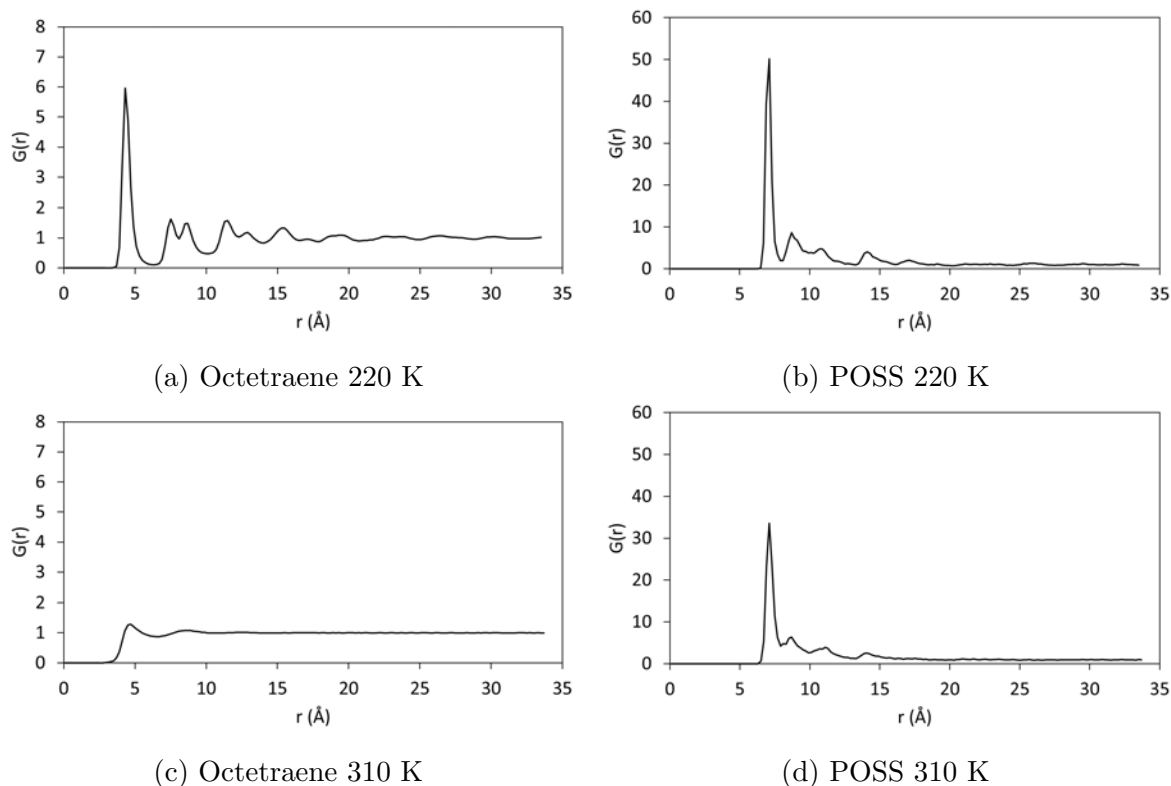
Figure 6.3.7: Radial distribution function for Octetraene (left) and T_8H_8 (right) molecules at 220 and 310 K at 10% wt POSS loading.

At 30% T_8H_8 POSS, I observe a continuation in the change to the bulk material. As shown in figure 6.3.8b, this system exhibits the same three phases behaviour as the 10% blend to produce a T_m prediction of 253.6 K. This value is 7.2 K higher than the 10% system and 9.3 K higher than the pure octatetraene system. I also see that this system condenses at a much higher temperature of 370 K. From the moment of inertia method, I predict a T_m of 259.2 K. Interestingly, in contrast to the 10% system, this plot follows the trend of the specific volume relationship, depicting a three phase system. From the dihedral rotations method I predict a T_m of 253.0 K however I observe a much more linear relationship.

(a)

(b)

(c)
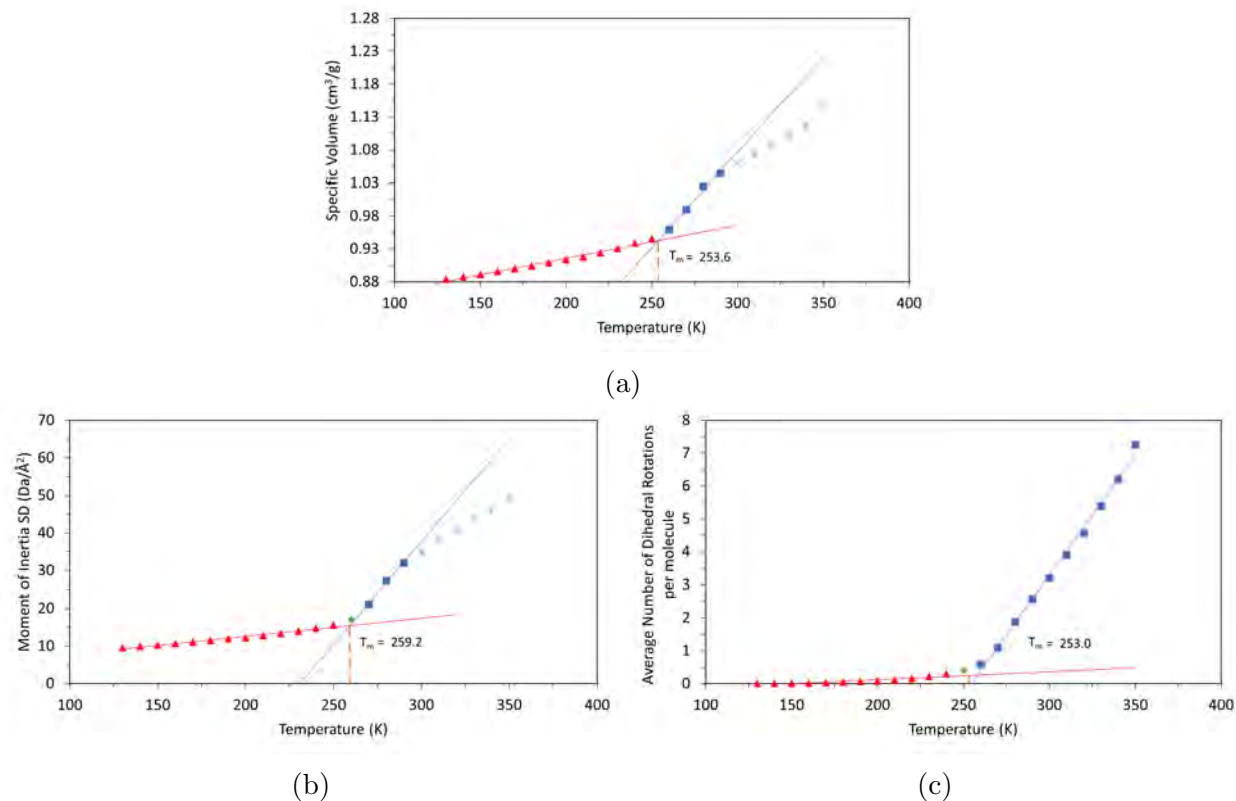
Figure 6.3.8: The T_m prediction from the specific volume temperature relationship (a), the standard deviation in the moment of inertia of octatetraene molecules (b) and the average number of dihedral rotations per octatetraene molecule (c) methods for Octatetraene-T_8H_8 30% POSS wt blends.

At a finer level of analysis, in figure 6.3.9, I present the dihedral rotations of each single C-C bond for octatetraene at 230, 270 and 310 K. For these molecules, similarly to he pure system, I see that at higher temperatures the central single C-C bond becomes more active in terms of dihedral rotations. Although the gradient in the number of dihedral rotations per molecule after T_m is constant with temperature, I see, in figure 6.3.9, that the bulk of the rotation shifts to the central C-C single bond, in step with the change in the gradient of the standard deviation in the moment of inertia. This gradient change in the standard deviation of the moment of inertia and the specific volume temperature relationship is explained by the shift in the position of higher dihedral rotational freedom. Certainly, if the central C-C bond becomes more active, a greater amount of mass is covering a larger distance per rotation than the terminal rotors of the octatetraene molecule. In principle, this would explain the

arrival of the observed trend.

	Temperature (K)		
Bond Index	230	270	310
1	0.226	1.166	4.152
2	0.129	1.243	5.970
3	0.250	1.165	4.203

Figure 6.3.9: The average number of dihedral flips for each C-C single bond of the octate-traene molecule at 230, 270 and 310 K.

In figure 6.3.10, I present the mean squared displacement. Overall the mobility of the octatetraene molecules is very similar to the 10% loading system. For the POSS molecules I see some divergence from the behaviour observed in the 10% system. Here, I see much less molecular mobility by comparison.

(a) Octatetraene   (b) T_8H_8
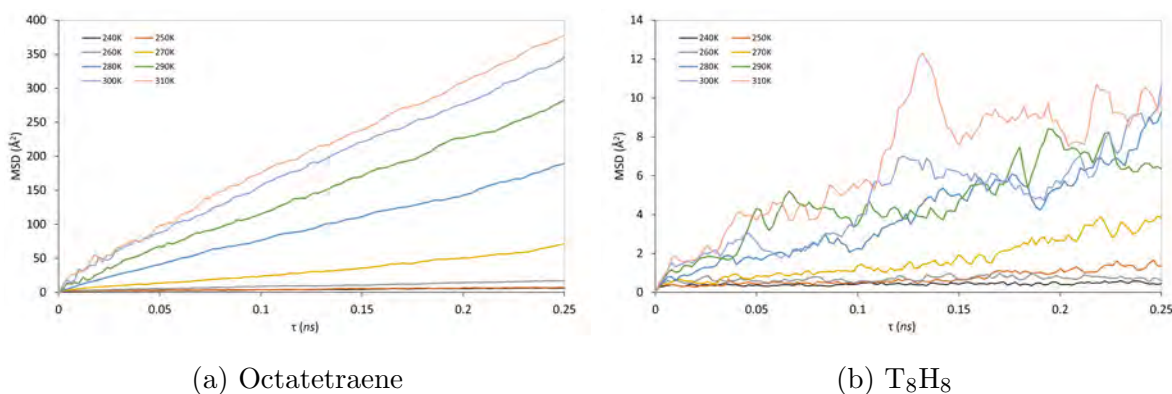
Figure 6.3.10: The MSD for the octatetraene (left) molecules and T_8H_8 (right) molecules at 30% wt loading.

The observed molecular mobility can be explained by the packing of the system. In figure 6.3.11 I can see that at 310 K, the octatetraene exhibit liquid like behaviour whilst the POSS molecules appear to high level packing. The POSS molecules have again agglomerated to form larger micro-crystallites than in the 10% system. The long range packing indicates that there is at least one complete layer of POSS molecules within the initial coordination sphere. As a collected unit, each individual POSS molecule is not as able to exhibit a great deal of molecular mobility.

(a) Octatetraene 220 K

(b) T_8H_8 220 K

(c) Octatetraene 310 K

(d) T_8H_8 310 K
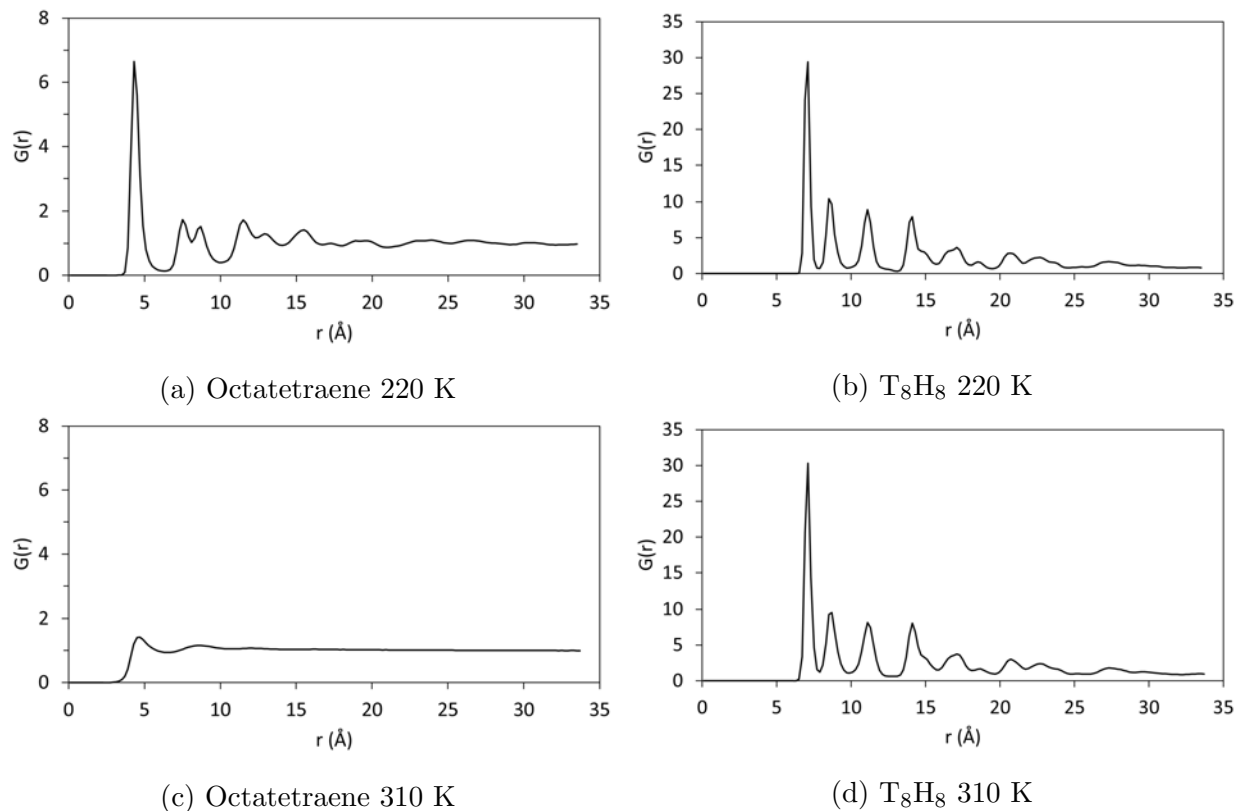
Figure 6.3.11: Radial distribution function for octatetraene (left) and T_8H_8 (right) molecules at 220 K and 310 K at 30% POSS loading.

At 50% T_8H_8 POSS, I observe a continuation of the trends in behaviour. As shown in figure 6.3.12a, from the specific volume method, I predict a T_m of 252.1 K with the three phases of the system being exhibited. From the number of dihedral rotations and moment of inertia method from the octatetraene molecules, I predict T_m of 260.6 and 253.8 K respectively. These temperatures are within 8.5 K of one another. However, the trend observed from 10% to 30% that the T_m is increasing has stopped. From 30% to 50%, I observe a decrease of 1.5 K for the specific volume method, and a 1.4 K and 0.8 K increase for the dihedral and moment of inertia methods respectively.

(a)

(b)

(c)
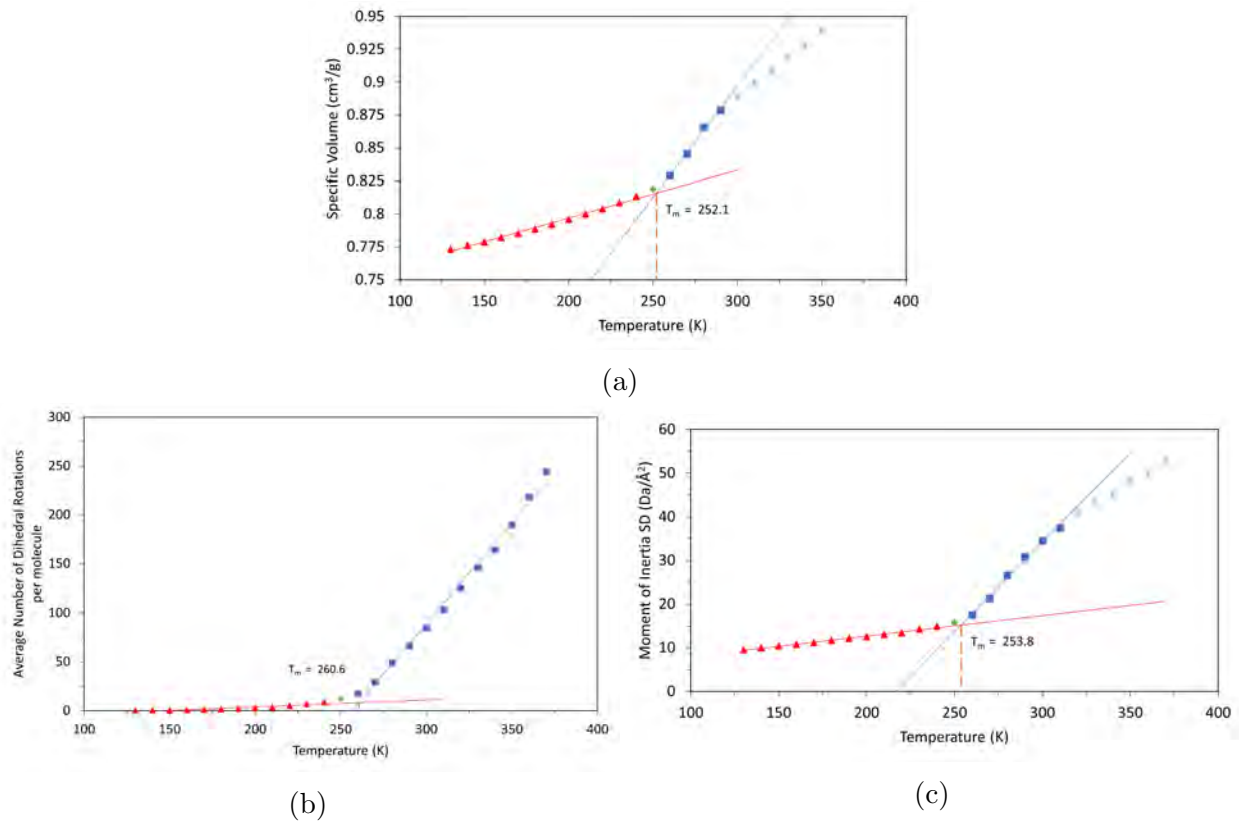
Figure 6.3.12: The T_m prediction from the specific volume temperature relationship (a), the standard deviation in the moment of inertia of octatetraene molecules (b) and the average number of dihedral rotations per octatetraene molecule (c) methods for octatetraene-T_8H_8 50% POSS wt blends.

In figure 6.3.13, I present the mean squared displacement for the 50% T_8H_8 blend. As I see in the 30% system, the octatetraene molecules exhibit high mobility where as the POSS molecules are much more restricted in their movement.

(a) Octetraene   (b) POSS
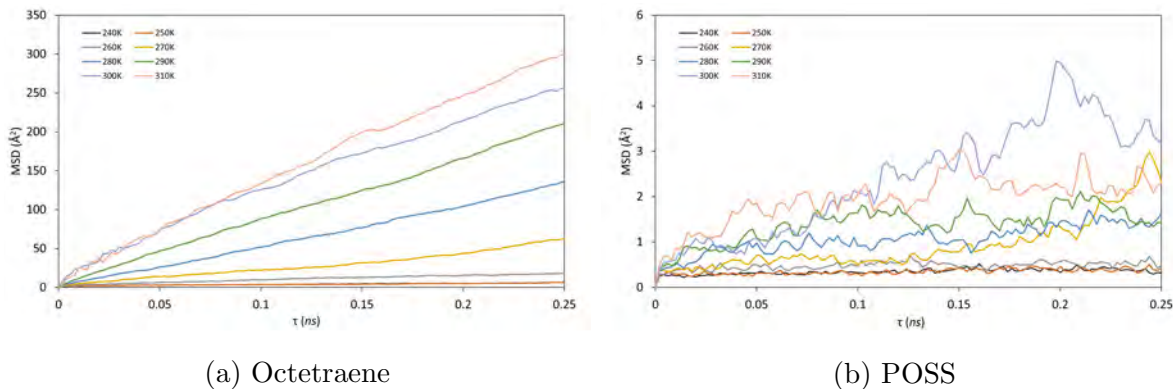
Figure 6.3.13: The MSD for octatetraene (left) molecules and T_8H_8 (right) molecules at 50% wt loading.

From the radial distribution function analysis of these systems, I can see similar behaviour to the 30% system. As shown in figure 6.3.14, I see that at 220 K, both systems have long range ordering in packing that is unique to the molecule type. This suggests that the systems are highly phase separated and both near crystalline in structure. At 310 K, for the octatetraene molecules I have a liquid like regime. For the POSS molecules, as I have seen in the 30% system, the crystal phase has been generated at a higher temperature and maintained through the cooling sequence.

(a) Octatetraene 220 K

(b) T_8H_8 220 K

(c) Octatetraene 310 K

(d) T_8H_8 310 K
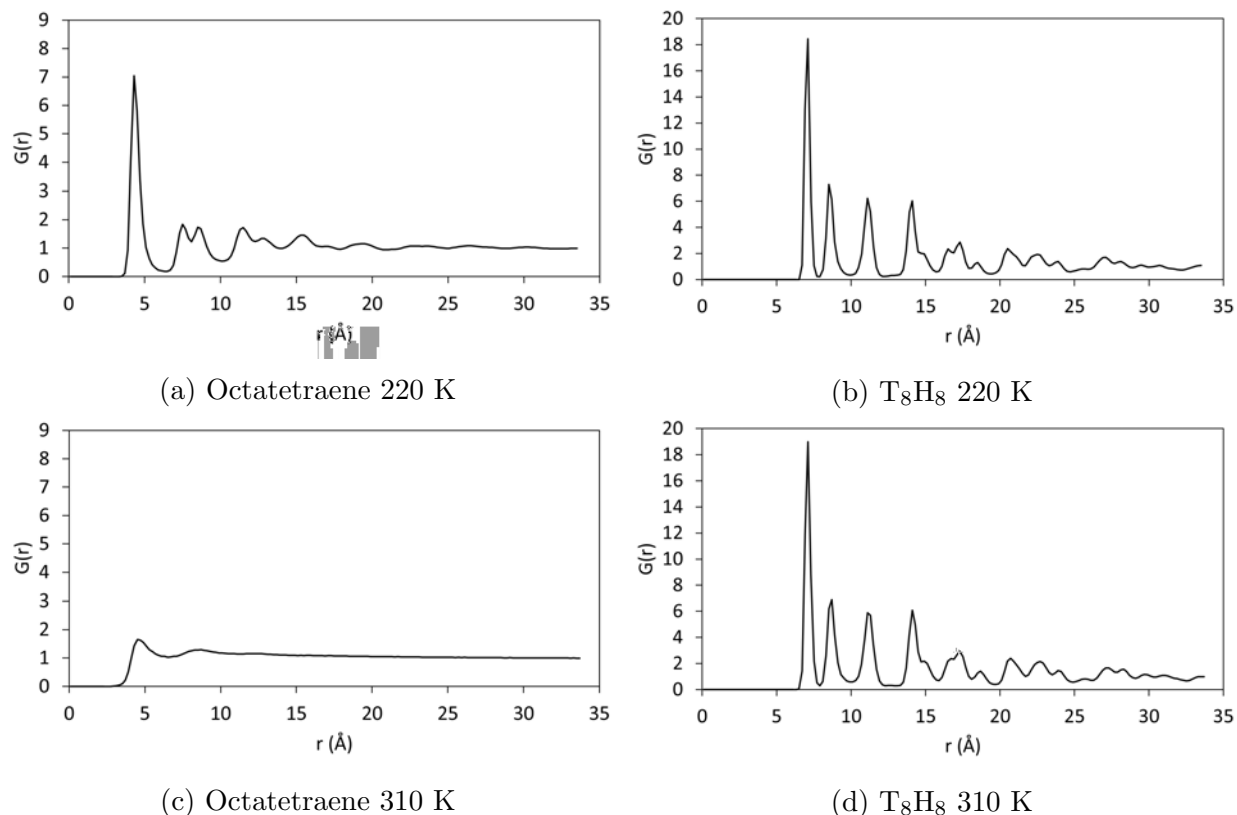
Figure 6.3.14: Radial distribution function for octatetraene (left) and T_8H_8 (right) molecules at 220 K and 310 K at 50% POSS loading.

From the number of like near neighbour analysis shown in figure 6.3.15, I see that the octatetraene molecules remain in close proximity to one another over the course of the cooling sequence at all temperatures. For the POSS molecules however, I can observe the agglomeration through the cooling sequence. Even at low concentration, I can observe the tendency for these molecules to agglomerate until 290 K where the system becomes much less mobile.

(a) Octetraene   (b) T_8H_8
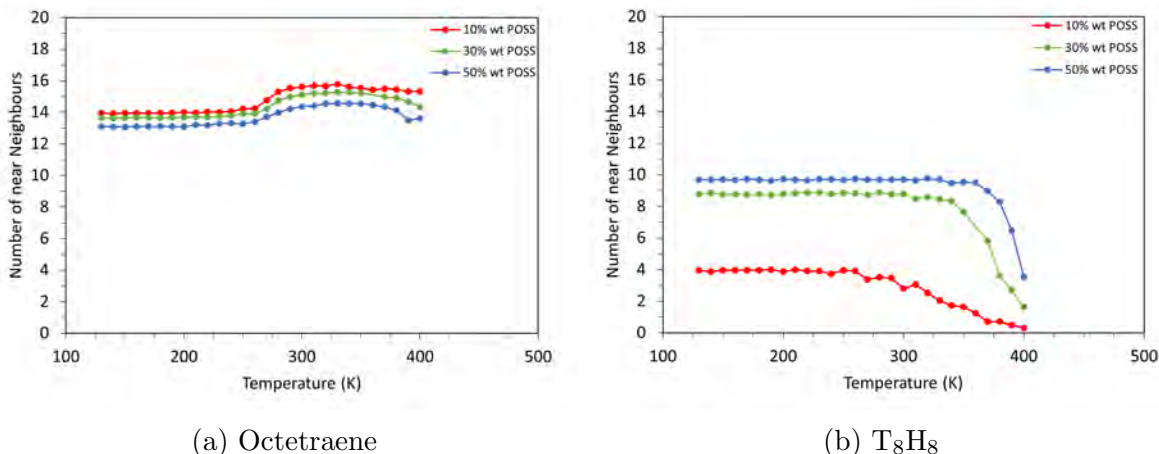
Figure 6.3.15: The number of like near neighbours for the HTPB (left) and POSS T_8H_8 (right) molecules over the course of a cooling sequence determined through voronoi tessellation diagrams.

6.3.3   Octatetraene T_8t-butyl$_8$ POSS blend

Within the following section, I will present the restults from simulations containing octatetraene and T_8t-butyl$_8$ molecules at 10, 30 and 50% wt.

At 10% T_8t-butyl$_8$, I predict a T_m of 242.4, 250.1 and 241.2 K from the specific volume, dihedral rotation and moment of inertia method respectively. The latter two methods utilise the trajectory data from the octatetraene molecules only. The specific volume method predicts values that are in close agreement with the pure and 10% T_8H_8 system which predict values of 244.3 K and 246.4 K respectively. This system also exhibits similar condensation behaviour to the T_8H_8 system, forming a liquid phase at 340 K. I also see that this system has three phases by comparison to the two phases exhibited in the HTPB systems.

(a)

(b)

(c)
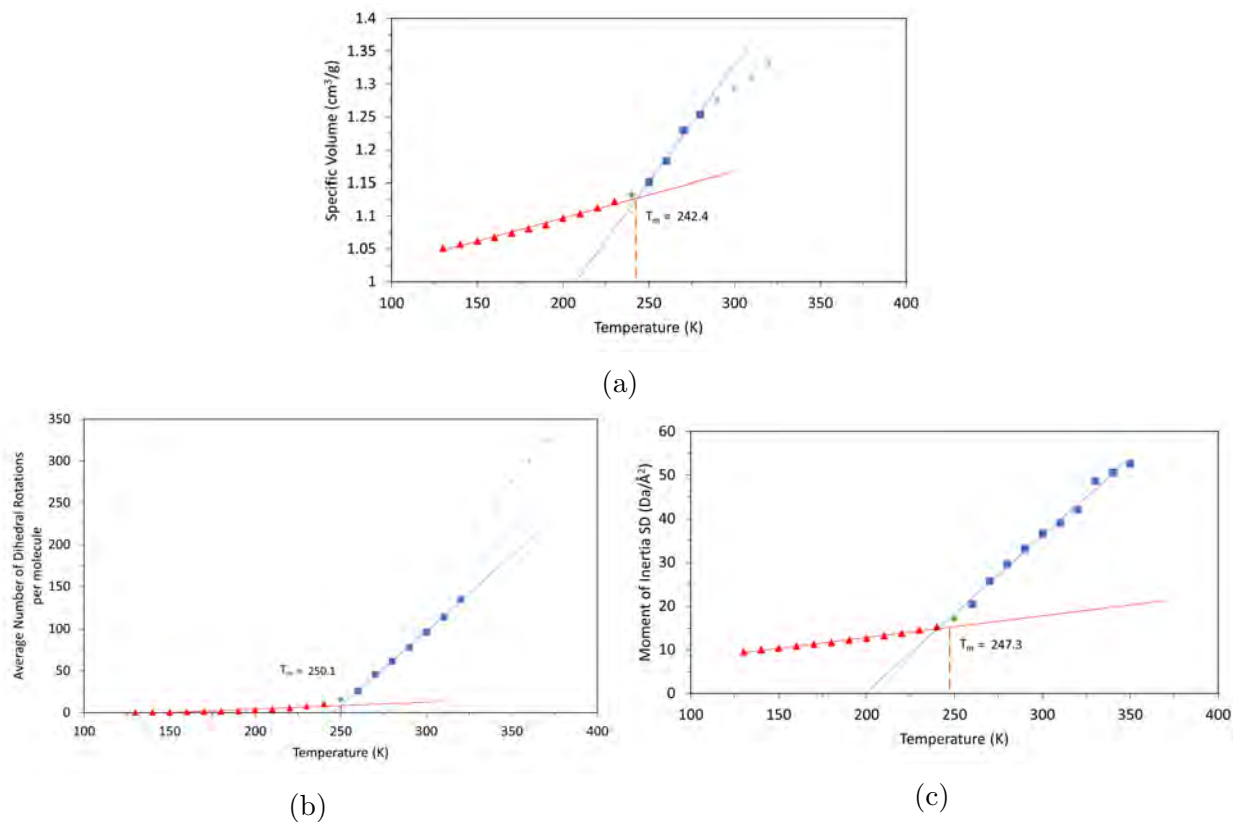
Figure 6.3.16: The T_m prediction from the specific volume temperature relationship (a), the standard deviation in the moment of inertia of octatetraene molecules (b) and the average number of dihedral rotations per octatetraene molecule (c) methods for octatetraene-T_8t-butyl$_8$ 10% POSS wt blends.

In figure 6.3.17, I present the MSD of the octetraene and T_8t-butyl$_8$ molecules over a range of temperatures at 10% wt POSS loading. Similarly to the 10% T_8H_8 blended system, I see that the octatetraene molecules exhibit higher mobility than the POSS molecules. Both components of the system blends appear to have very similar mobility to the 10% T_8H_8 blended system.

(a) Octetraene

(b) POSS
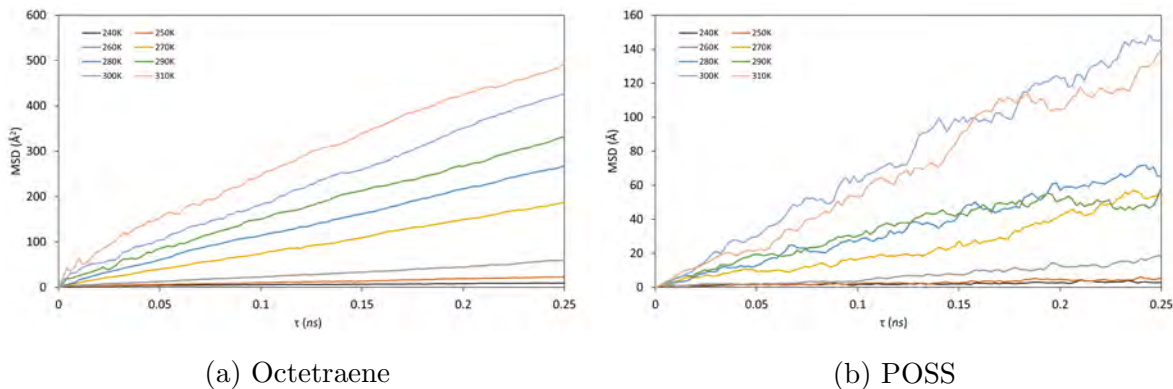
Figure 6.3.17: The MSD for the octatetraene molecules and $T_8 t$-butyl$_8$ molecules at 10% wt loading.

In figure 6.3.18, I present the radial distribution function analysis for octatetraene and $T_8 t$-butyl$_8$ molecules at 220 K and 310 K at 10% wt POSS loading. For the octatetraene molecules, I see liquid like behaviour at the higher temperature and long range crystalline packing below the T_m. Here, at 310 K, the $T_8 t$-butyl$_8$ POSS molecules exhibit a very flat G(r). From this G(r) data, and through visualisation of the molecular trajectory, I know that these molecules are in an amorphous arrangement.

(a)

(b)

(c)

(d)
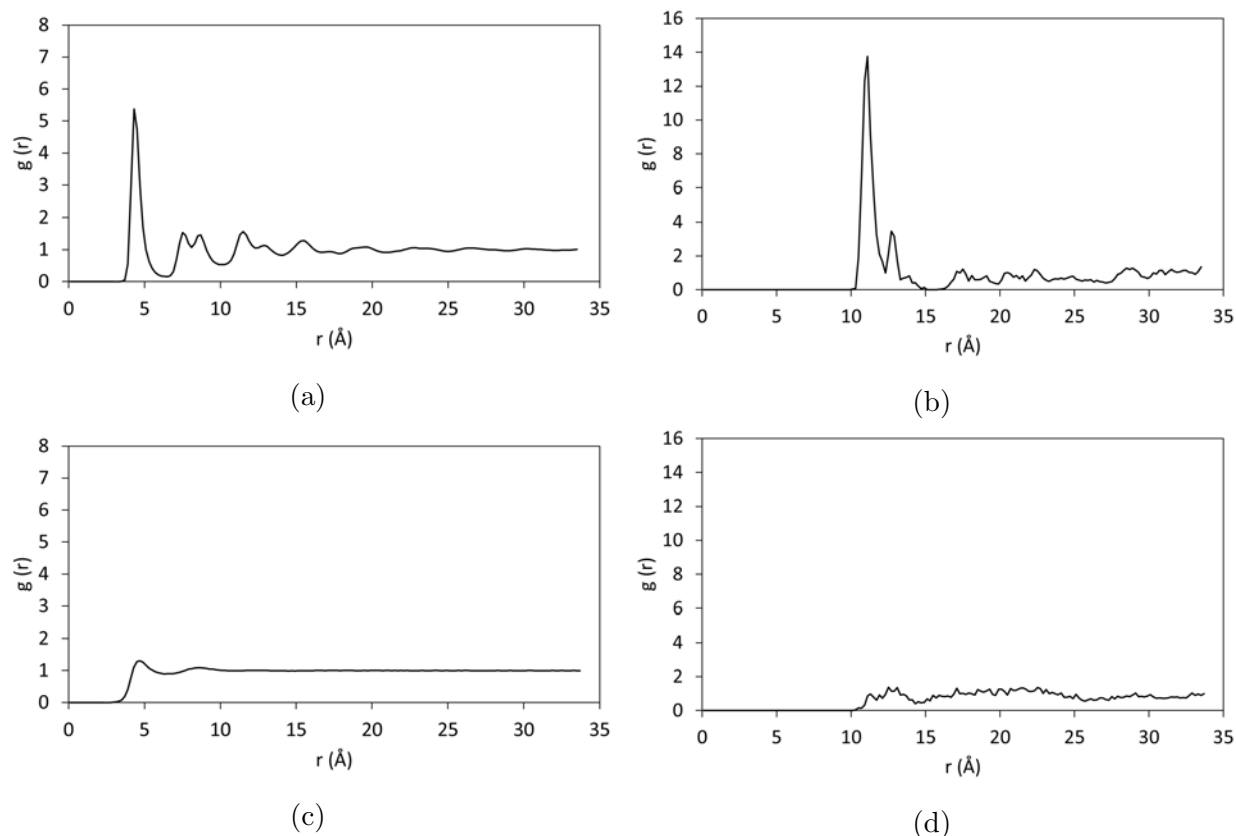
Figure 6.3.18: Radial distribution function for octatetraene (left) and T_8t-butyl$_8$ (right) molecules at 220 K and 310 K at 10% POSS loading.

I now present the 30 and 50% octetraene-T_8t-butyl$_8$ blended data in tandem with one another. In figure 6.3.19a and 6.3.19b, I see the specific volume relationship of the 30% and 50% blended systems respectively. For the 30% system, I see a continuation of the behaviour observed in the 10% system. The predicted T_m is 241.9 K and the system exhibits the previously described three phases. For the 50% system, I observe a change in the behaviour of the compressability of the system. Here, the three phase mode has changed to a two phase system, as I have observed in the HTPB systems. Interestingly, with this method I predict a very low T_m of 229.7 K. From the dihedral rotation method, utilising the octatetraene data only, I predict a T_m of 253.6 and 254.5 K respectively. For both systems, there is a large disparity of 11.7 K and 24.8 K between the specific volume and dihedral for the 30% and 50% systems respectively. At 30% wt POSS, the standard deviation in the moment of inertia

describes similar trends as the specific volume as I see three phases. The T_m predicted with this method is 241.8 K, which is in agreement with the specific volume method value of 241.9 K. At 50%, I see that the three phases is no longer present. Here, I predict a T_m of 231.7 K, which is in good agreement with the specifc volume method of 229.7 K.
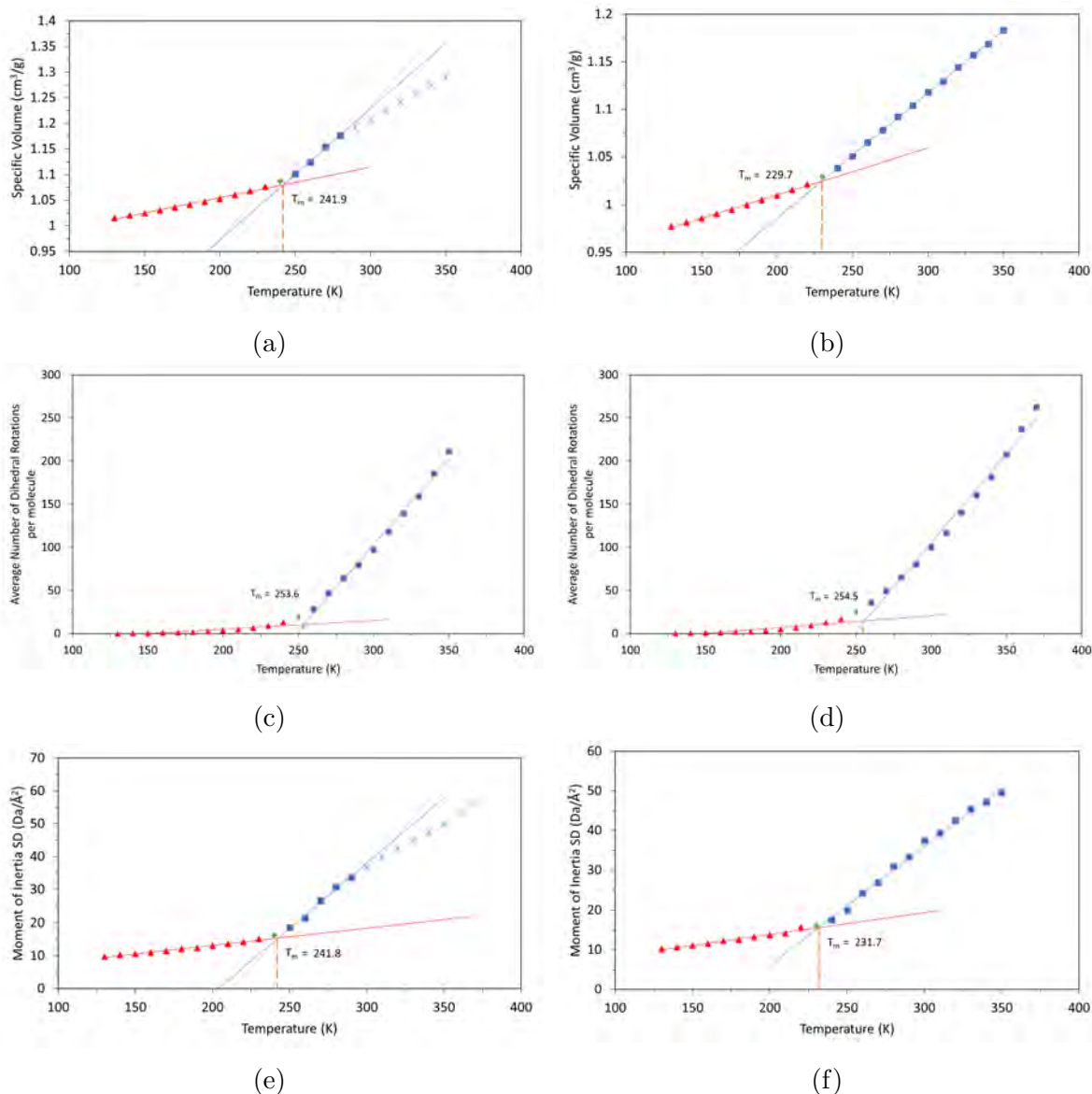
Figure 6.3.19: Three methods used to predict the T_m of the octetraene-$T_8 t$-butyl$_8$ blended systems at 30% (left) and 50% wt (right) POSS. The top graphs describe the specific volume temperature relationship, the middle graph describes the average number of dihedral per octatetraene molecule and the bottom graphs describe the standard deviation in the moment of inerta of the octatetraene molecules as a function of temperature.

In figure 6.3.20, I present the radial distribution function of the octatetraene molecules, at 220 K and 310 K, at 30% and 50% wt POSS loading. For both systems I see very similar packing behaviour. At 220 K I see well defined peaks at regular intervals suggesting the formation of a crystalline structure. At 50% I see a reduction in the intensity of the peaks. At 310 K, for both blended systems, the octatetraene molecules exhibit liquid like behaviour.

(a) 30% 220 K

(b) 50% 220 K

(c) 30% 310 K

(d) 50% 310 K
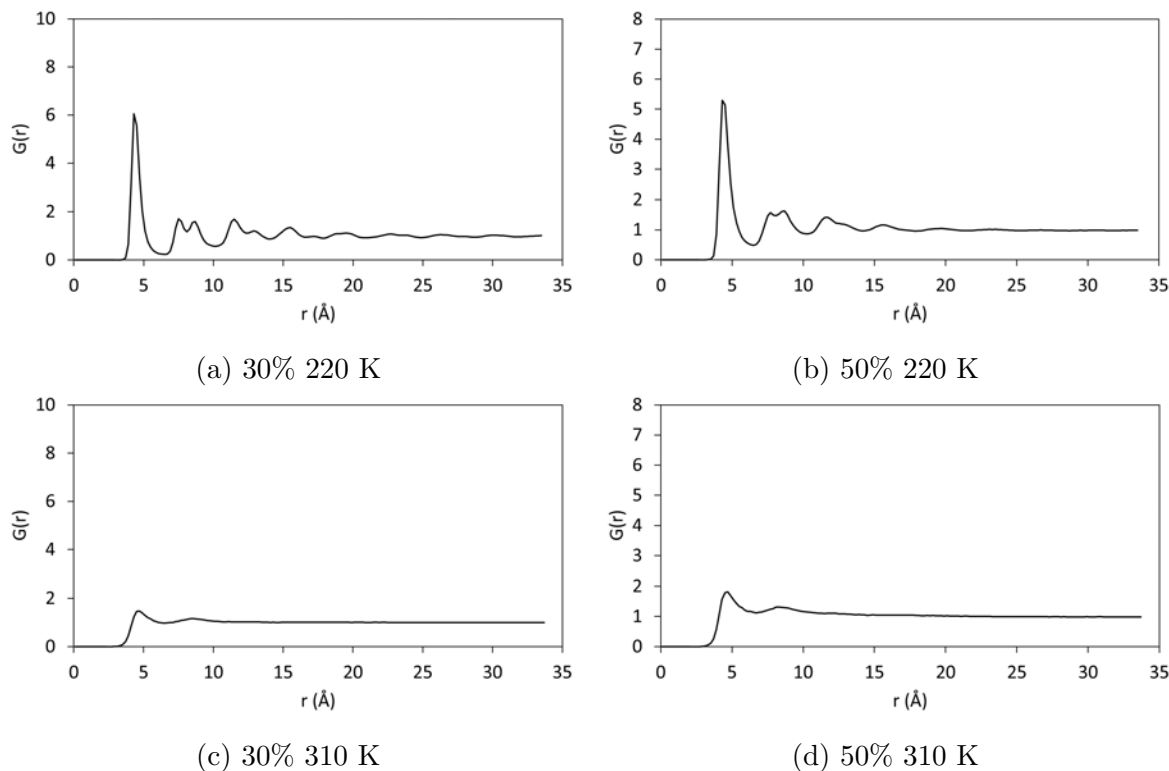
Figure 6.3.20: The radial distribution function analysis of octatetraene molecules at 30% (left) and 50% (right) $T_8 t$-butyl$_8$ POSS loading at 220 K (top) and 310 K (bottom).

In figure 6.3.21, I present the equivalent radial distribution function analysis for the POSS molecules at 30% and 50% wt POSS within the octetraene-$T_8 t$-butyl$_8$ blended systems. Within these plots, I can see that both systems at both temperatures have very similar G(r) curves. There are two well defined peaks at 11 and 13 Å and, particulary for the 50% system, broader secondary peaks at 18 Å and 23 Å. Similarly to to the octatetraene molecules, these peaks suggest the formation of crystalline regions. However the nature of the crystal packing is different between the two systems.

(a) 30% 220 K

(b) 50% 220 K

(c) 30% 310 K

(d) 50% 310 K
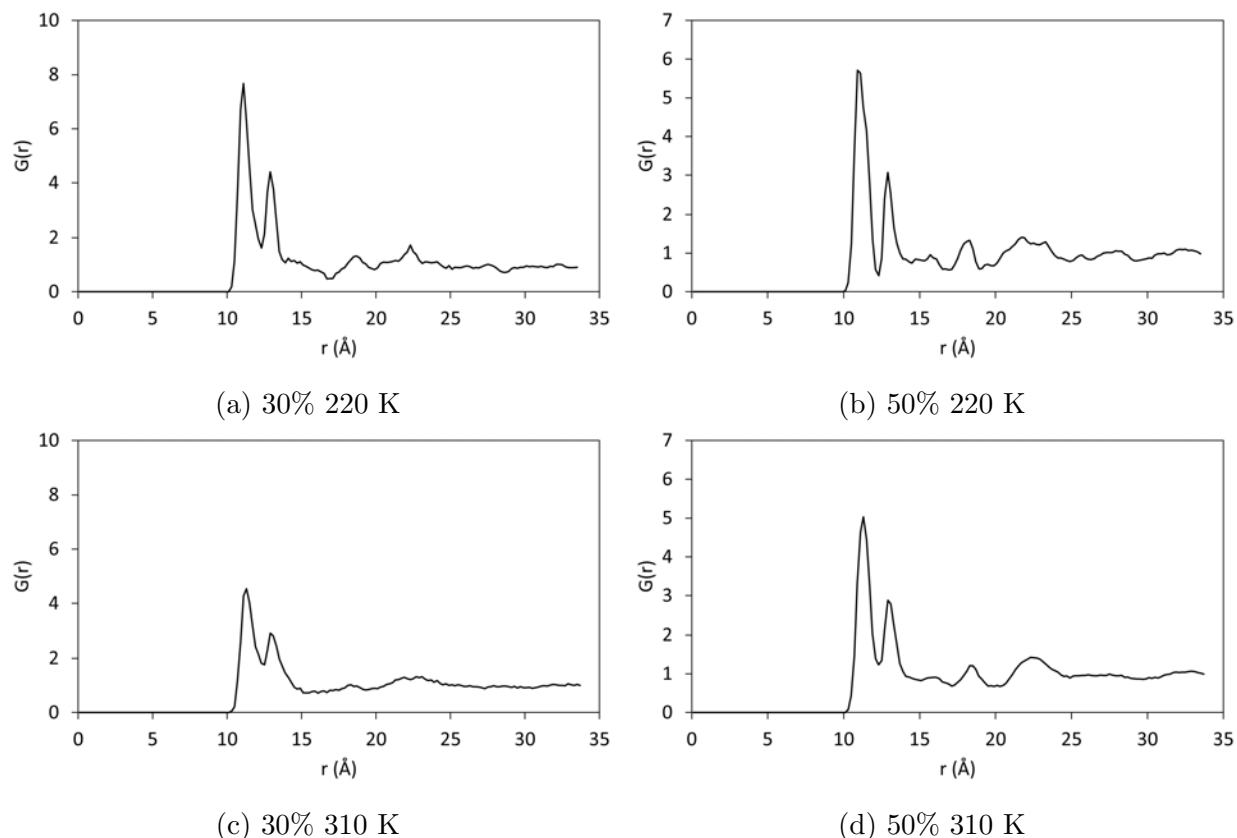
Figure 6.3.21: The radial distribution function analysis of T_8t-butyl$_8$ molecules at 30% (left) and 50% (right) T_8t-butyl$_8$ POSS loading at 220 K (top) and 310 K (bottom).

I have also studied the molecular mobility of these systems. In figure 6.3.22, I present the MSD data for both octatetraene and POSS molecules at 30% and 50% T_8t-butyl$_8$. Here, I see a less mobile system at 50% wt POSS. I also see a difference in mobility behaviour, particularly for octatetraene. Within the 30% system, between the temperatures 260 K and 280 K, I see an increase in the MSD, indicating a more rapid increase in the mobility within this temperature range than between 280 and 310 K. This behaviour is not observed within the 50% system; instead, I see a much more linear relationship with temperature.

(a) octatetraene

(b) $T_8 t$-butyl$_8$

(c) octatetraene
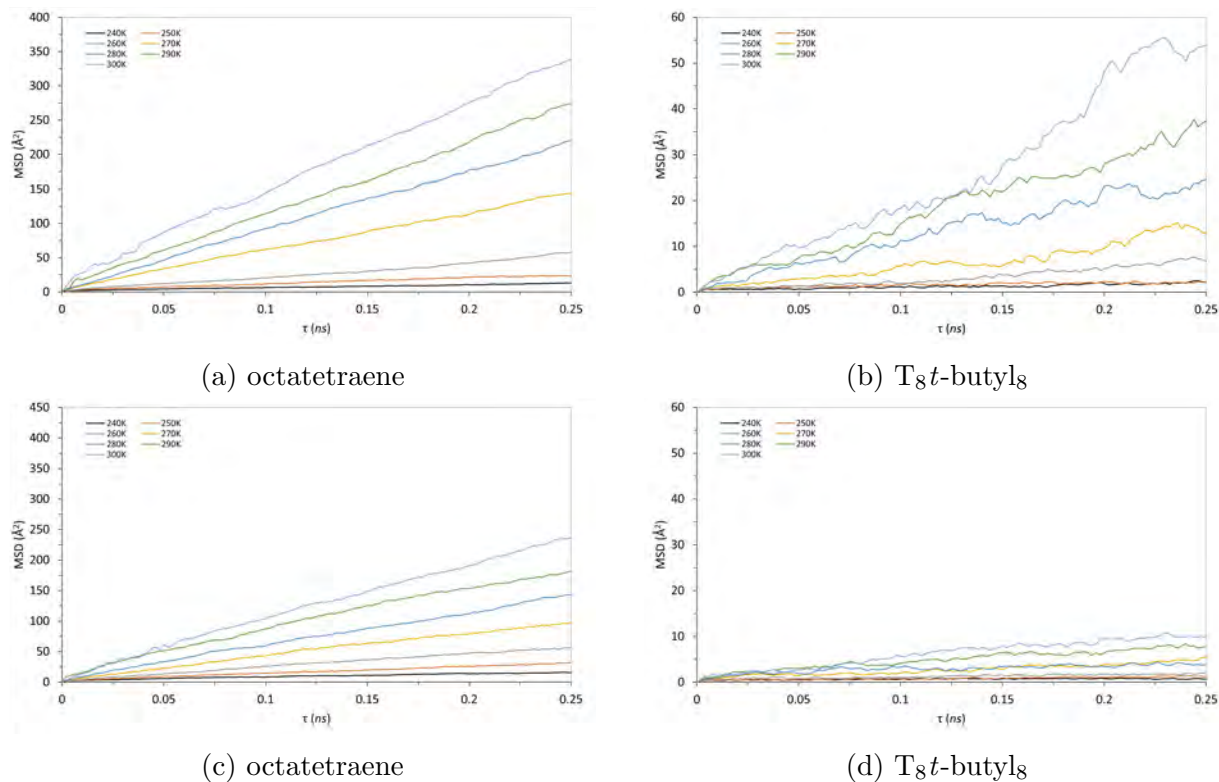
(d) $T_8 t$-butyl$_8$

Figure 6.3.22: The MSD for octatetraene molecules (left) and $T_8 t$-butyl$_8$ molecules (right) over the transition region. The top graphs contains data from the 30% $T_8 t$-butyl$_8$ system and the bottom graph contains data from the 50% $T_8 t$-butyl$_8$ system.

Through like near neighbour analysis from Voronoi tessellation diagrams (figure 6.3.23), I see that for all POSS concentrations, the octatetraene molecules experience two distinct levels of likelihood for encountering like molecules. At higher temperatures, where I observe liquid like mobility, on average, each molecule is in contact with more like neighbours than lower temperatures. As discussed, from 240 K and below, the octatetraene are in a near crystalline configuration. This regularity is also present in the molecular structure as each molecule exhibits a very linear conformation. This regularity in structure explains the observed trend as the molecules form distinct layers with very little inter-layer penetration. For the POSS molecules, I observe a gradual increase in the number of like neighbours encountered as temperature is decreased, until a steady state is achieved. In part, this is likely due to the gradual agglomeration of the POSS molecules over the course of the simulation. However, as the packing of the octatetraene molecules becomes more regular, the number of octatetraene

near neighbours also decreases.

(a) Octatetraene
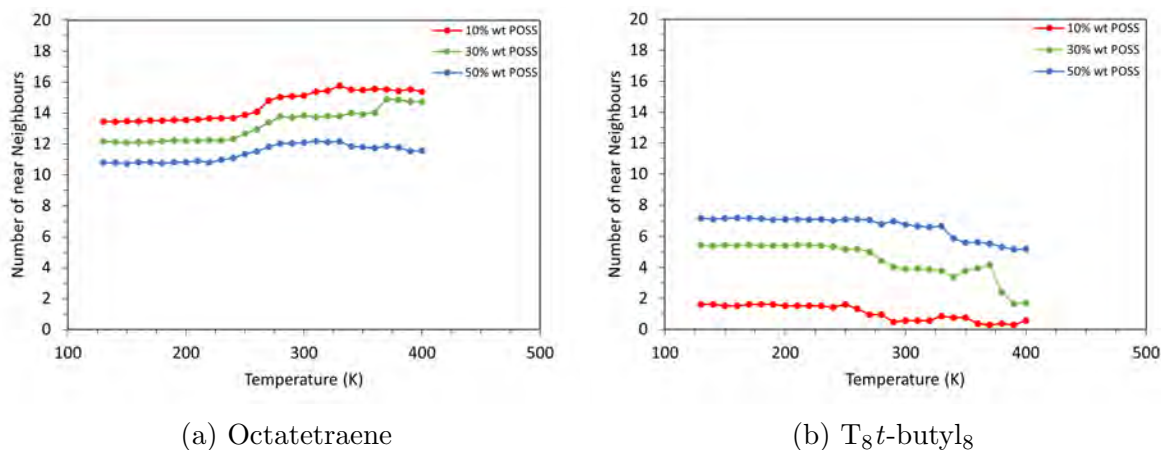
(b) T_8t-butyl$_8$

Figure 6.3.23: Near neighbour analysis for octatetraene (left) and T_8t-butyl$_8$ (right) molecules from voronoi tessellation diagrams of the molecular structures.

6.3.4 Octatetraene T_8propyl-methacrylate$_8$ blend

The final collection of systems to be studied in this section contain T_8propyl-methacrylate$_8$ molecules blended with octatetraene at 10%, 30% and 50% wt POSS concentration. The T_8propyl-methacrylate$_8$ structure has been studied as a pure system in section 4.2.1. These systems exhibit much more organic/polymeric behaviour by comparison to the T_8H_8 and T_8tert-butyl$_8$. Each propyl-methacrylate group has significant mobility and enables interdigitation within the pure system.

At 10% wt T_8propyl-methacrylate$_8$, from the specific volume method as shown in figure 6.2.25, I predict a T_m of 237.8 K. As is shown in previously discussed octatetraene blended system, this system also exhibits a gas phase from upward of 340 K. Also, I observe three phases for this system in the condensed phase. From the standard deviation in the moment of inertia method, I predict T_m of 224.8 K and 240.3 K for the POSS and octatetraene molecules, respectively. The agreement between the specific volume method temperature and octatetraene is an indication of the dominant octatetraene characteristic being exhibited by the system. However, interestingly, the POSS data exhibits the same three phase

trend. Until now, this is a behaviour I have not observed within these systems. The efficacy of the number of dihedral rotations method from the octatetraene data seems to be lost as from this method I predict a T_m of 254.5 K.

(a)

(b) T_8propyl-methacrylate$_8$ data

(c) Octatetraene data

(d) Octatetraene data
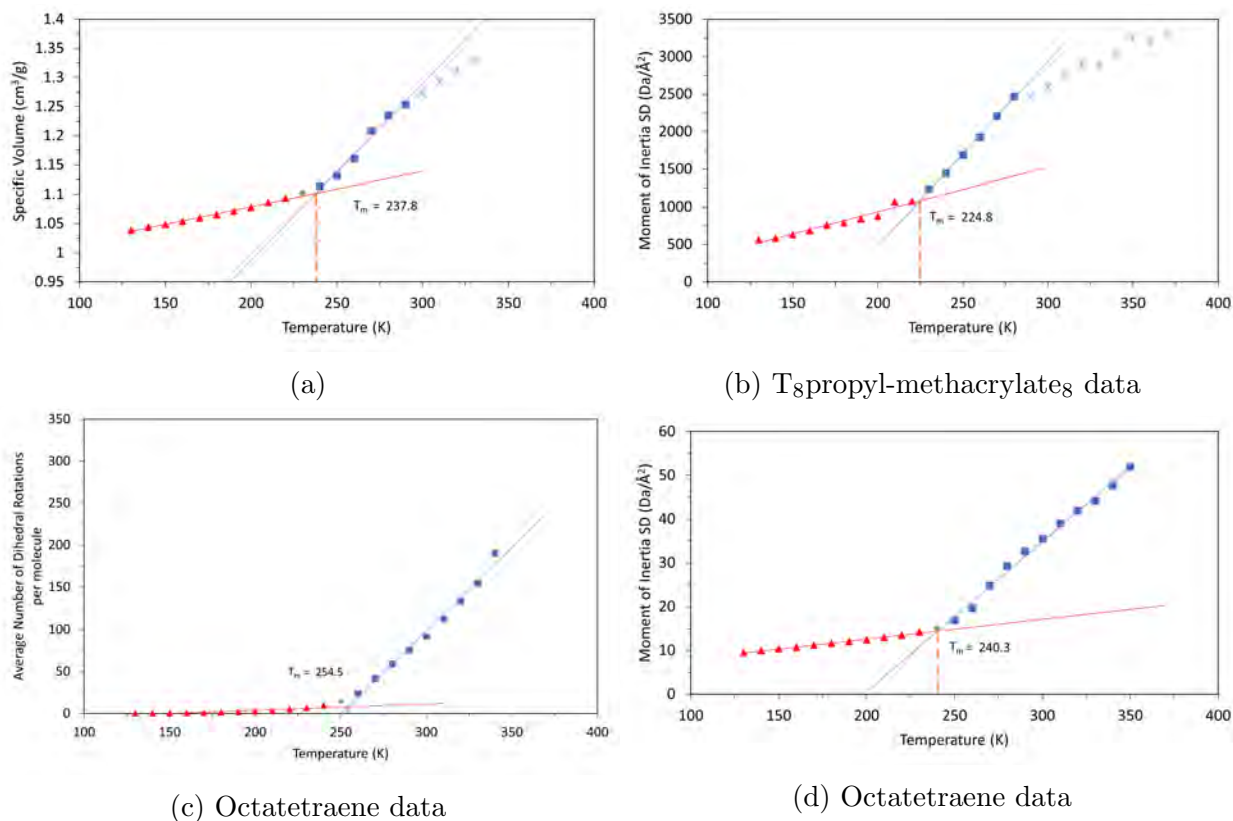
Figure 6.3.24: Prediction of the T_m from the specific volume method, standard deviation in the moment of inertia and number of dihedral rotations applied to the octatetraene and T_8propyl-methacrylate$_8$ molecules separately at 10% POSS concentration.

Within these systems, I see the same crystallisation behaviour I have characterised for the previous octatetraene blended systems. In figure 6.3.25, I present the radial distribution function analysis for octatetraene molecules and T_8propyl-methacrylate$_8$ molecules. For the octatetraene molecules, I observe a liquid-like G(r) curve at 310 K and a highly ordered packing arrangement at 220 K. This is very similar to the previous systems. At this concentration of POSS, I have a very low number of molecules present during the simulation. As a result the G(r) curve at 220 K has what may appear to be high ordering, however is only an artefact from the low number of molecules.

(a) Octatetraene 220 K

(b) T$_8$propyl-methacrylate$_8$ 220 K

(c) Octatetraene 310 K

(d) T$_8$propyl-methacrylate$_8$ 310 K
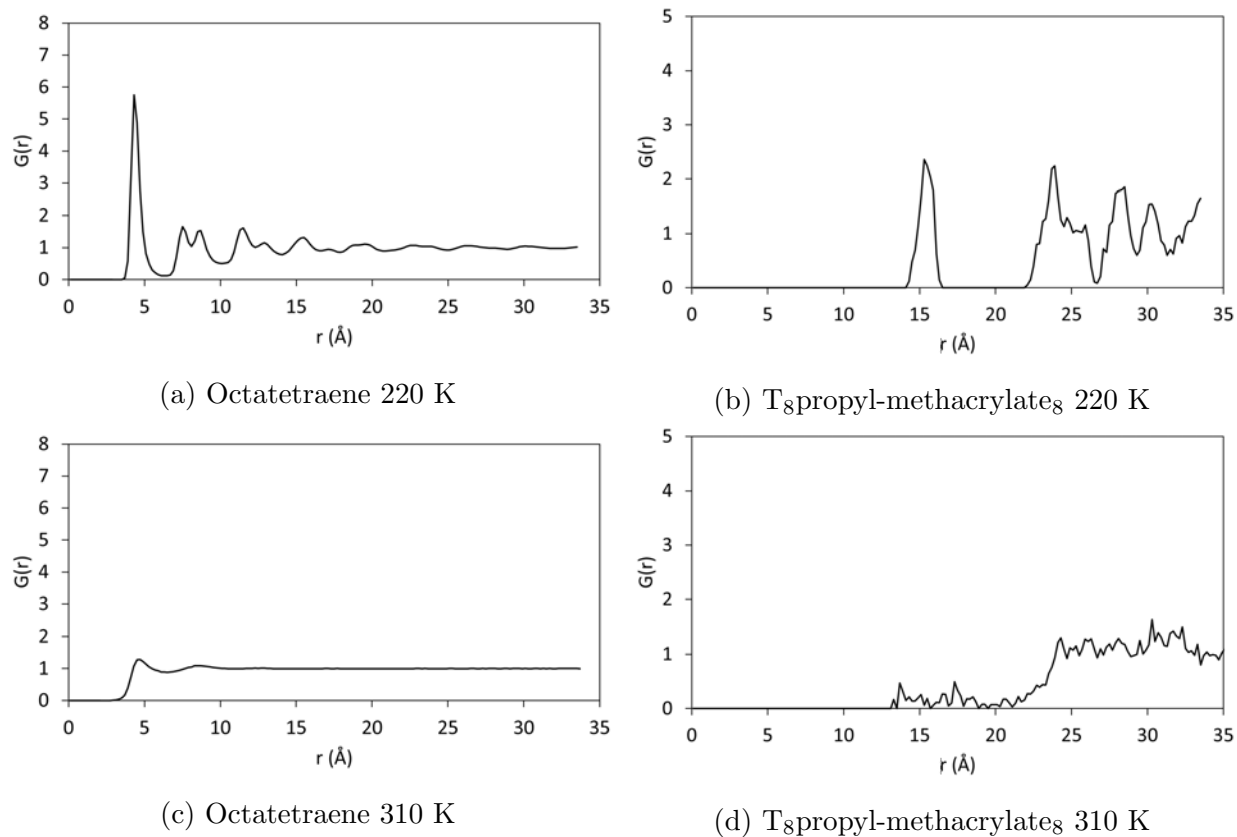
Figure 6.3.25: The radial distribution function analysis for octatetraene (left) and T$_8$propyl-methacrylate$_8$ (right) at 220 K and 310 K.

The molecular mobility for these species are defined in figure 6.3.26. Here, I see that the behaviour of these systems is very similar to the previously discussed octatetraene blends in that I see high mobility for the octatetraene molecules and comparatively less mobility in POSS molecules. At this concentration, I see less mobility than for the smaller T$_8$H$_8$ and T$_8$tert-butyl$_8$ species.

(a)   (b)
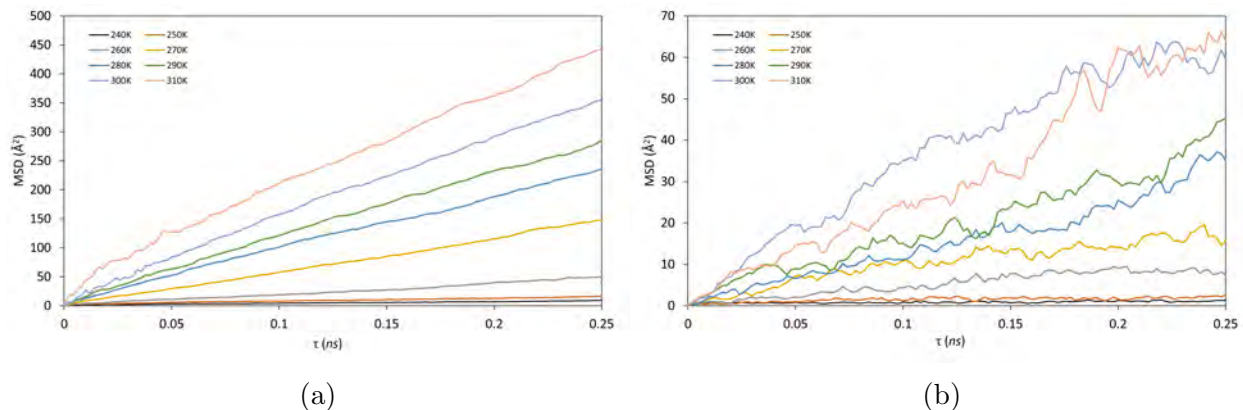
Figure 6.3.26: The MSD for octatetraene molecules (left) and T_8propyl-methacrylate$_8$ molecules (right).

At 30% and 50% wt T_8propyl-methacrylate$_8$, I predict a T_m of 220.8 K and 232.7 K respectively as shown in figures 6.3.27a and 6.3.27b. From this method, as the concentration of POSS is increased from 10%, I see an intial decrease in the T_m from 237.8 K to 220.8 K followed by an increase to 232.7 K. interestingly, the behaviour observed for these system appears to be quite different in that the 30% and 50% blends no longer exhibit the three phases observed at the 10% POSS level. Furthermore, in figure 6.3.27, I also present the predicted T_m from the average number of dihedral rotations per octatetraene molecule and standard deviation in the moment of inertia for all octatetraene molecules as a function of temperature. Here, I see that for both thee 30% and 50% system, there is little agreement between the predicted values from the dihedral method and specific volume method. At all concentrations, I see that from this method, I consistently predict a T_m close to 255 K. From the moment of inertia method, I see better agreement with the specific volume method as at 30% and 50% I predict T_m of 232.3 K and 234.4 K. Again, from these plots, I see that for 30% and 50% POSS, the three phase behaviour is lost.
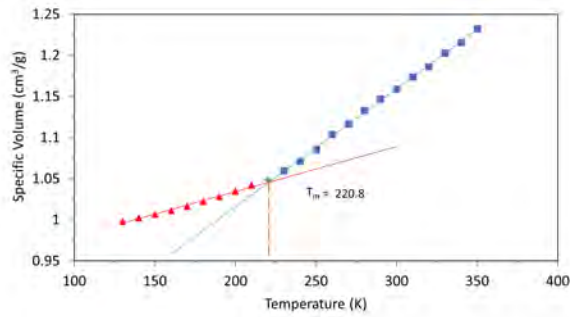
(a) Octetraene data 30% POSS
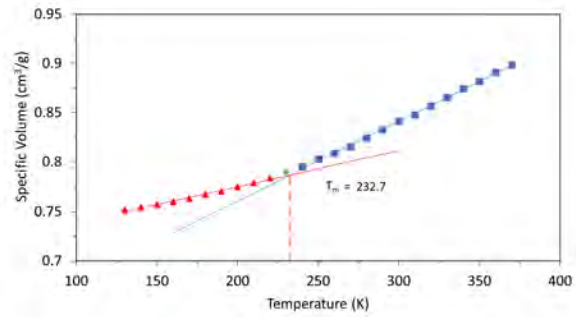
(b) Octetraene data 50% POSS
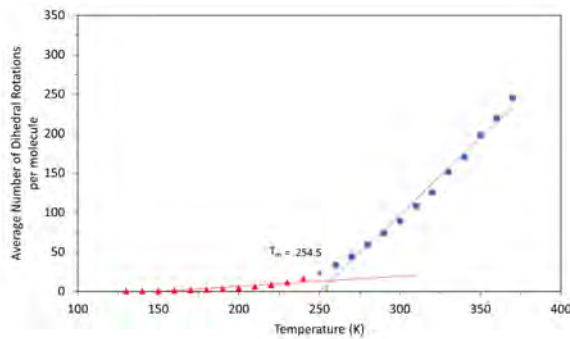
(c) Octetraene data 30% POSS
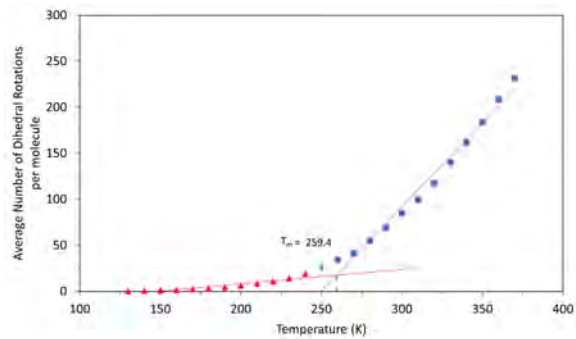
(d) Octetraene data 50% POSS
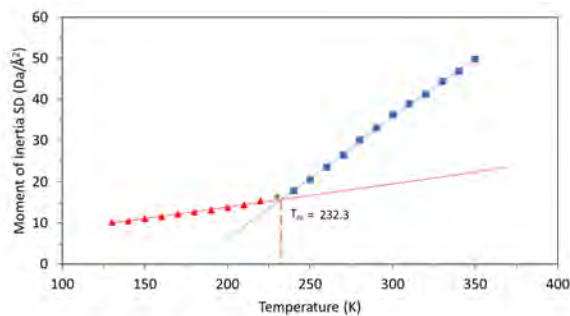
(e) Octetraene data 30% POSS
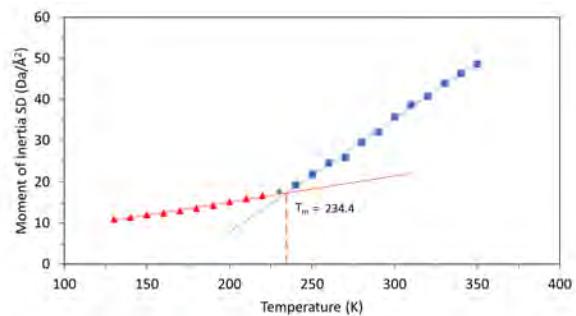
(f) Octetraene data 50% POSS

Figure 6.3.27: The predicted T_m for 30% (left) and 50% (right) T_8propyl-methacrylate$_8$ loading utilising the specific volume method (top), number of dihedral roations per octate-traene molecules method (middle) and the standard deviation in the moment of inertia for all octatetraene molecules method (bottom).

In addition, in figure 6.3.28, I also present the predicted T_m for 30% and 50% T_8propyl-methacrylate$_8$ blends from the moment of inertia method from the POSS molecule data only. Here, I predict values of 206.5 K and 215.6 K for 30% and 50% respectively. At the 30% level, I observe some very interesting behaviour as three phases can be observed in a similar fashion to that shown in figure 6.3.24b. For both blended systems, the predicted values

are significantly lower than the specific volume method for the respective systems and pure

T_8propyl-methacrylate$_8$ system.
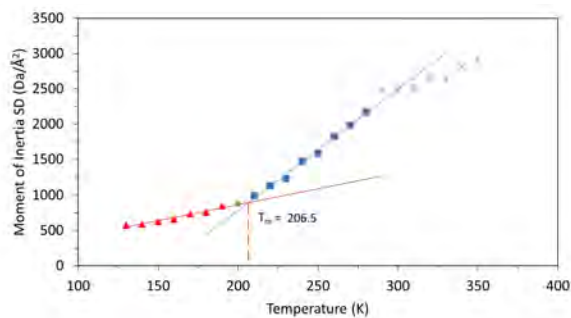
(a) 30% T_8propyl-methacrylate$_8$
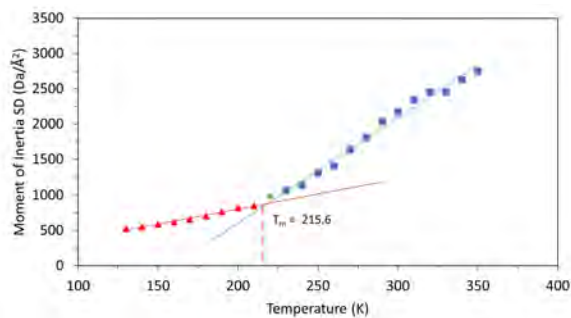
(b) 50% T_8propyl-methacrylate$_8$

Figure 6.3.28: The predicted T_m from the standard deviation in the moment of inertia method for 30% (left) and 50% (right) T_8propyl-methacrylate$_8$ octatetraene blends where POSS data has been considered only.

In figure 6.3.29, I present the radial distribution function analysis for 30% and 50%

T_8propyl-methacrylate$_8$ octatetraene molecules. To observe the packing behaviour above

and below the T_m, I have analysed these data at 190 K and 310 K. At 30%, I see that the

octatetraene molecules are able to form the the crystalline phase I have seen for the T_8H_8

and T_8*tert*-butyl$_8$ blended systems. However, at 50% T_8propyl-methacrylate$_8$, at 190 K, I

see that high order for these systems is lost. Instead I see a much more amorphous condensed

system.

(a) 30% POSS 190 K

(b) 50% POSS 190 K

(c) 30% POSS 310 K

(d) 50% POSS 310 K
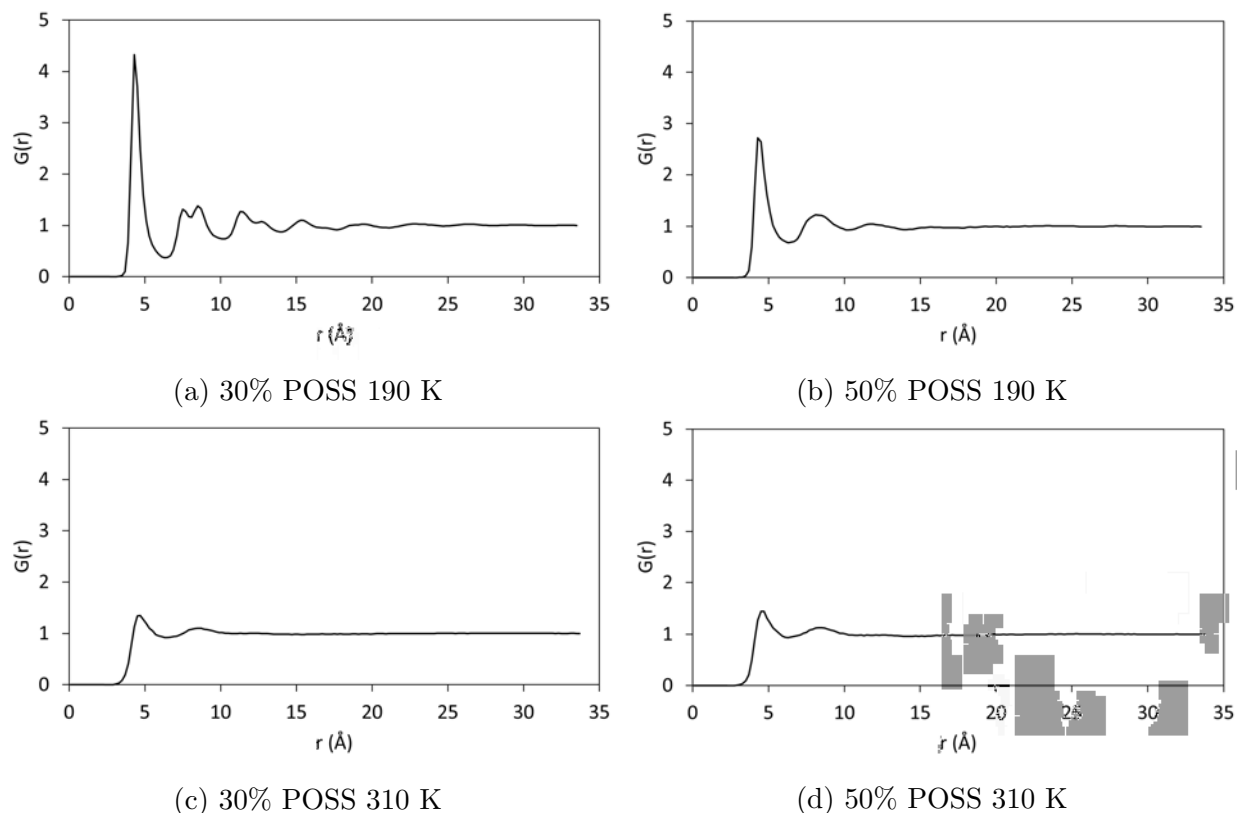
Figure 6.3.29: The radial distribution function of Octatetraene molecules at 30% (left) and 50% (right) T_8propyl-methacrylate$_8$ loading at 190 K and 310 K.

Results from the radial distribution function analysis of the T_8propyl-methacrylate$_8$ molecules are also presented in figure 6.3.30. At 30% and 50% T_8propyl-methacrylate$_8$ blends, I have 41 and 74 POSS molecules, respectively. This relatively low number of POSS molecules means that describing reproducible packing patterns may be difficult. However, from these data I see that at 190 K, both systems exhibit sharp peaks after 9 Å due to the lack of molecular mobility. The observed void region prior to 9 Å is due to the inability for POSS molecules to be closer than the POSS cage will permit. At 310 K, I see smoother curves as the molecules are permitted slightly more mobility. However, the curves are featureless. For the 30% blend, I see a sudden drop at 12 Å, however, this is likely due to the low number of molecules.

(a) 30% POSS 190 K

(b) 50% POSS 190 K

(c) 30% POSS 310 K

(d) 50% POSS 310 K
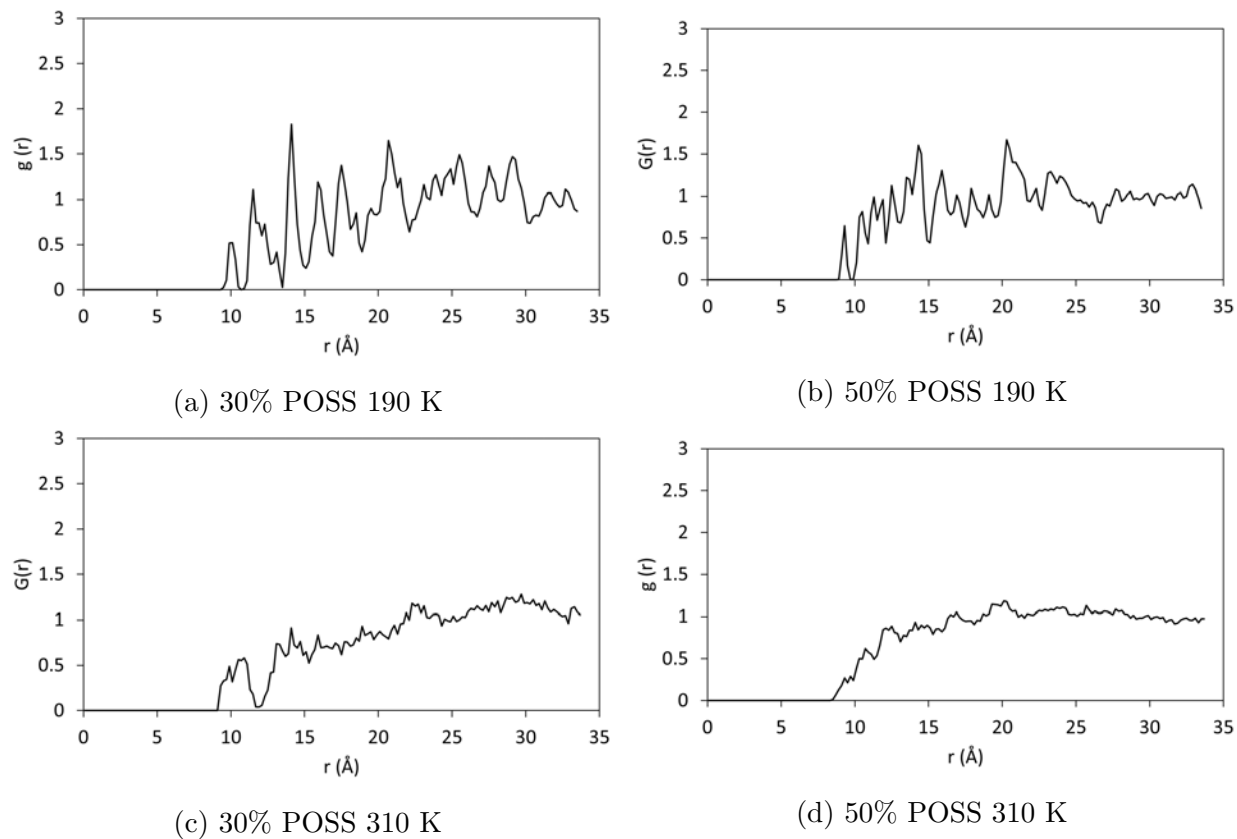
Figure 6.3.30: The radial distribution function of T_8propyl-methacrylate$_8$ molecules at 30% (left) and 50% (right) T_8propyl-methacrylate$_8$ loading at 190 K and 310 K.

In figure 6.3.31, I present the MSD for the octetraene and T_8propyl-methacrylate$_8$ molecules at 30% and 50% POSS loading. Here, I see a significant reduction in the octatetraene mobility as the percentage of T_8propyl-methacrylate$_8$ is increased. In addition, I also observe that the POSS mobility is reduced with concentration increase.

(a) octetraene

(b) T_8propyl-methacrylate$_8$

(c) octetraene

(d) T_8propyl-methacrylate$_8$
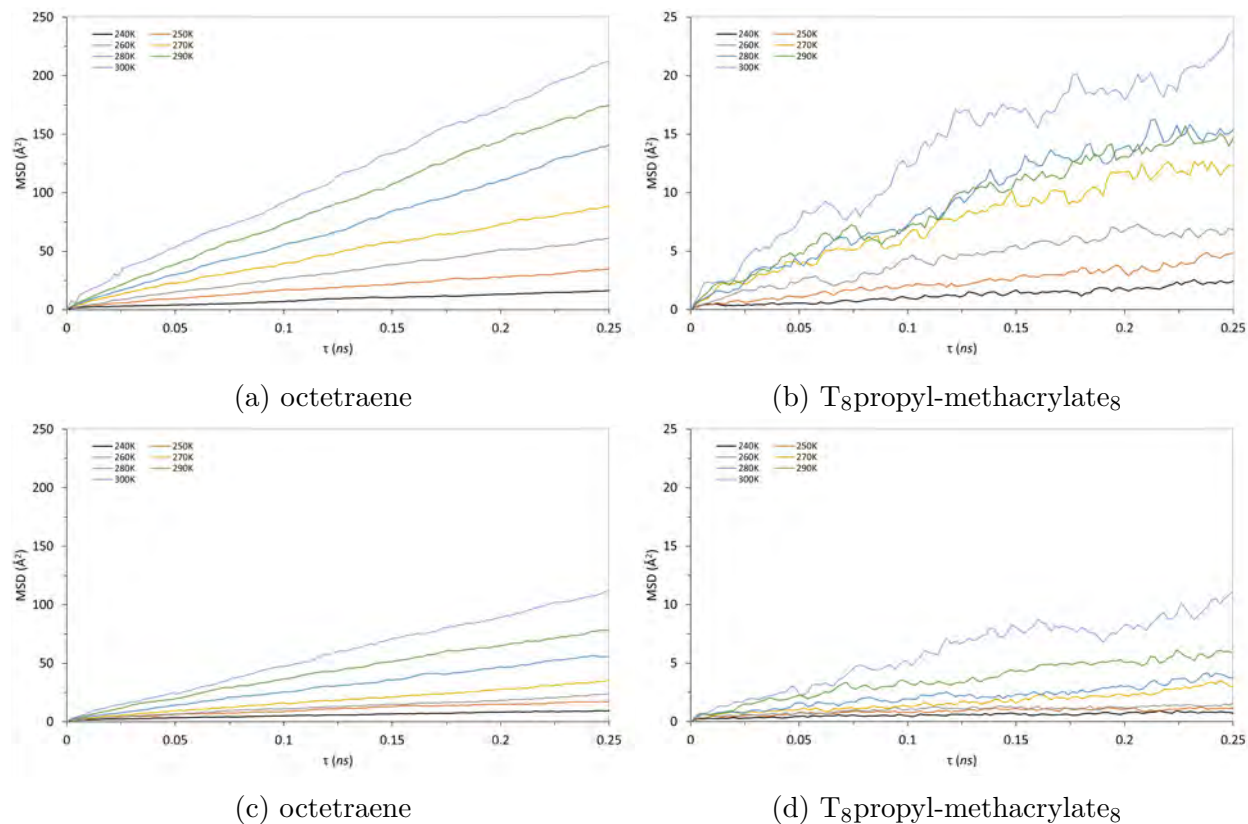
Figure 6.3.31: The MSD for octatetraene (left) and T_8propyl-methacrylate$_8$ (right) molecules as part of 30% (top) and 50% (bottom) POSS blends over a range of temperatures.

The final characterisation of this system is the Voronoi analysis shown in figure 6.3.32. Here, I see the lowest number of near neighbours observed in all octatetraene blends with between 9 and 10 being reported for the 50% system. At 30% and 50% I see that although the number of molecules is relatively small, the POSS molecules are inter-penetrating octatetraene molecules as the number of near neighbours increases.
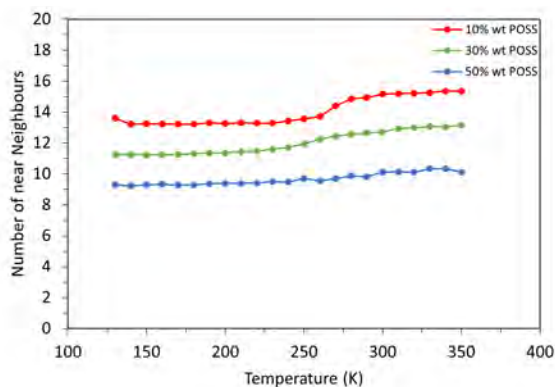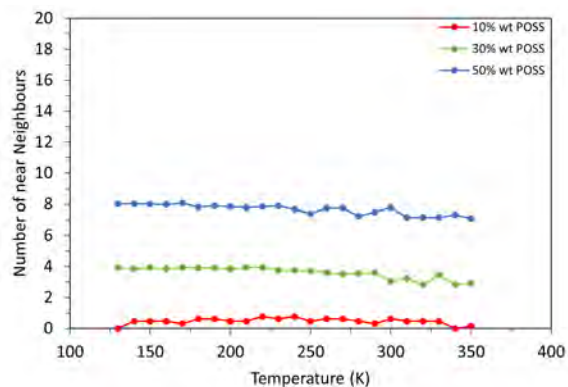
(a) Octatetraene   (b) T_8propyl-methacrylate$_8$

Figure 6.3.32: Near neighbour analysis for Octatetraene (left) and T_8propyl-methacrylate$_8$ (right) molecules from voronoi tessellation diagrams of the molecular structures.

In figure 6.3.33, I present 4 images that illustrate the atomic positions of the pure octatetraene system and the respective blended systems at 50% wt loading and 130 K. Here, the impact of POSS functionalisation is evident. In a pure octatetraene system, I see a highly ordered system. As the complexity in the functional group increases, the crystallinity in POSS and the octatetraene is gradually lost. Although not perfect, in the *tert*-butyl functionalised system, there is still evidence of ordered packing in the octatetraene.
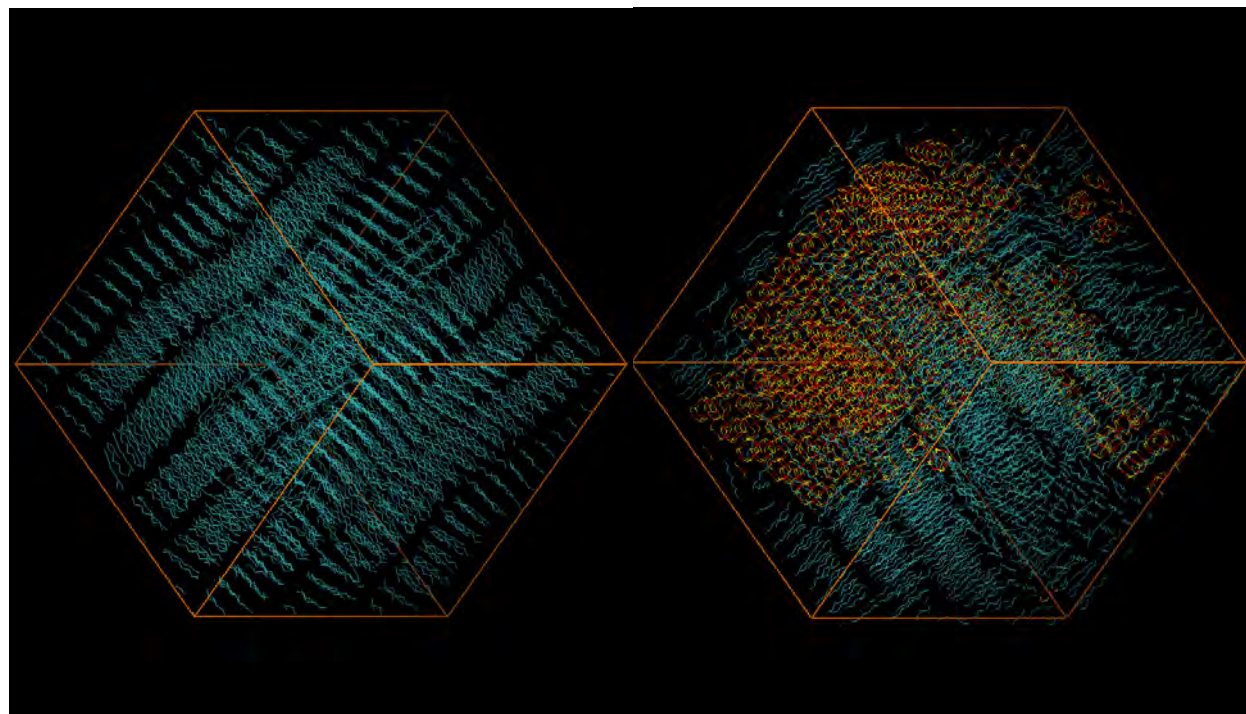
(a) pure octatetraene

(b) 50% T_8H_8 blend
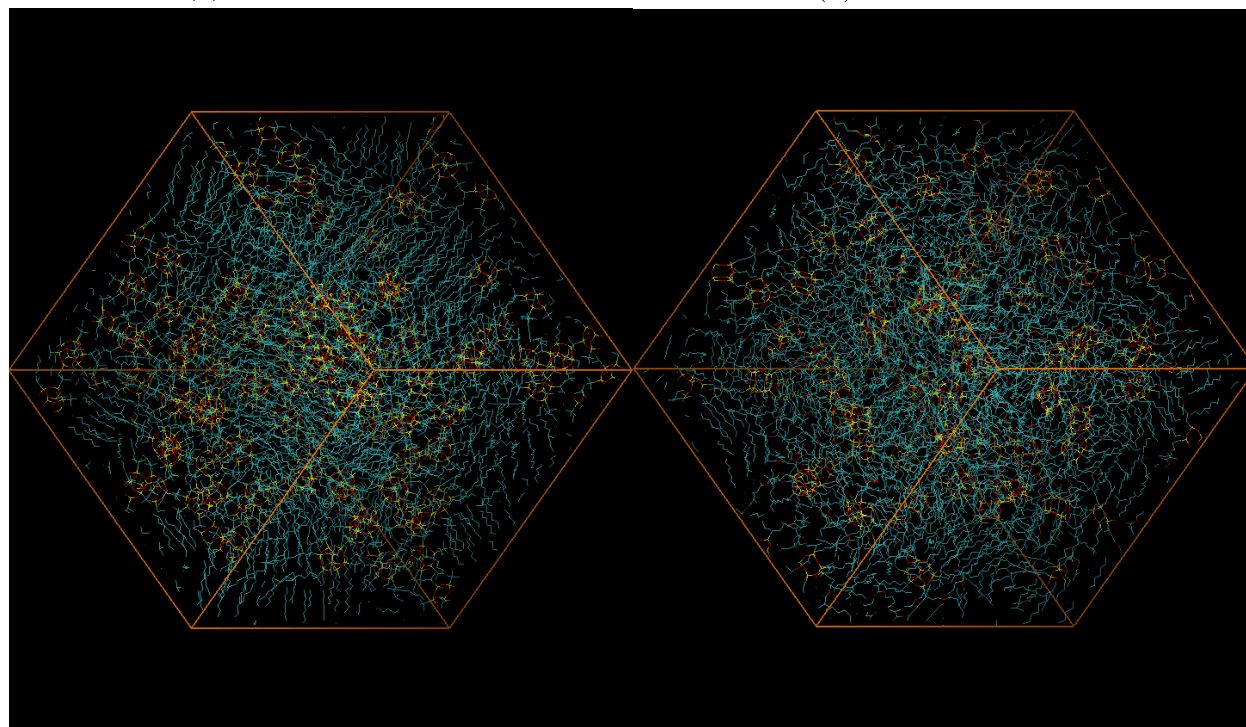
(c) 50% T_8*tert*-butyl$_8$ blend

(d) 50% T_8propyl-methacrylate$_8$ blend

Figure 6.3.33: Renderings of blended octatetraene systems at 50% wt POSS concentration and 130 K.

6.4   Discussion

Within the previous sections of Chapter 6, I have covered the systematic analysis of HTPB and octatetraene blended systems with different POSS species at 10%, 30% and 50% wt POSS. I now discuss the results from these simulations in relation to one another and the surrounding literature.

In table 6.1, I present a collection of the predicted T_gs and T_m for the HTPB and octatetraene blends. Results from the specific volume method, the number of dihedral rotations per molecule method and the standard deviation in the MOI from the POSS molecules method are included.

For the HTPB blended systems, from the specific volume method, the T_g value consistently increases with POSS concentration. All blends have a higher T_g than the pure HTPB system. For each blend, there is some good agreement between the specific volume method and the number of matrix dihedral rotations method. For each of the different POSS species, the greatest difference between specific volume and dihedral rotation is at 50% POSS concentration, with the dihedral method predicting the lower T_g value. This difference is greatest for the rigid T_8H_8 POSS. As POSS concentration increases and predicted T_g increases, the contribution of HTPB to the bulk material can be expected to decrease. Thus, there is a general effect that the addition of POSS character augments the Tg.

Matrix	POSS Species	% POSS	Specific Vol	Matrix nRot	POSS MOI
HTPB	T8 H	10	244.1	238.5	
		30	252	252.4	
		50	257.6	243.3	
	T8 t-Butyl	10	236.9	244.9	
		30	246.1	253.3	
		50	263.4	253	
	T8 propyl-methacrylate	10	244.5	244.9	243.6
		30	249.1	247.2	257
		50	250.6	246.9	273.3
pure HTPB		0	236.7	233.8	
Octatetraene	T8 H	10	246.4	253	
		30	253.6	253	
		50	252.1	260.6	
	T8 t-Butyl	10	242.4	250.1	
		30	241.9	253.6	
		50	229.7	252.8	
	T8 propyl-methacrylate	10	237.8	254.5	224.8
		30	220.8	254.5	206.5
		50	232.7	259.4	215.6
pure Octatetraene		0	244.3	256.4	

Table 6.1: The predicted transition temperatures for HTPB and octatetraene blended systems. The final three columns present the T_g and T_m for HTPB and octatetranen blends from the specific volume temperature method, number of molecular dihedral rotations method and standard deviation in the moment of inertia of the POSS molecules respectively.

The octatetraene blended systems exhibit different trends in predicted T_m. For the octatetraene T_8H_8 blended systems, the specific volume method predicts an increase in T_m with increasing POSS concentration. However, the T_8t-butyl$_8$ blended systems exhibit a decrease in T_m with POSS concentration from 242.4 K at 10% to 229.7 K at 50% POSS. T_8propyl-methacrylate$_8$ octatetraene blended systems also have a lower T_m than the pure octatetraene system. Here, the T_m does not linearly decrease with POSS concentration. The lowest predicted T_m is for 30% POSS with a value of 220.8 K. T_m prediction from the number of dihedrals of rotations in the octatetraene molecules has proved to be quite unreliable for these systems. The moment of inertia method for the POSS molecules also predicts low T_m, which are more consistent with the predicted values from the specific volume method. Such

low values have not been seen previously for POSS systems in my study. This observation reflects on the efficacy of my models and the utility of the breathing mode in characterising flexible POSS systems.

Several of the octatetratene blended systems demonstrate rich phase behaviour. For the T_8t-butyl$_8$ blended systems, the 10% POSS blend has three phases and the 50% has two phases, as shown in figure 6.3.24. This three phase system is indicative of a liquid crystal like regime. Where, at high temperatures, I have an isotropic system, followed by a nematic phase of extended octatetraene molecules in the intermediate phase and a crystal phase at the lower temperature. In figure 6.4.1, visualisation of the octatetraene 10% T_8t-butyl$_8$ blended system at 200, 260 and 320 K are presented. These images reinforce interpretations that this system exhibits liquid crystal behaviour, from the configuration snapshots of each of the three identified phases. At 50%, the bulk material behaves in a bi-phasic manner. This particular blend is an interesting combination of the two species opening up novel behaviour within this system as the single component T_8t-butyl$_8$ system is incompressible at this temperature range, resulting in a flat specific volume vs temperature relationship.
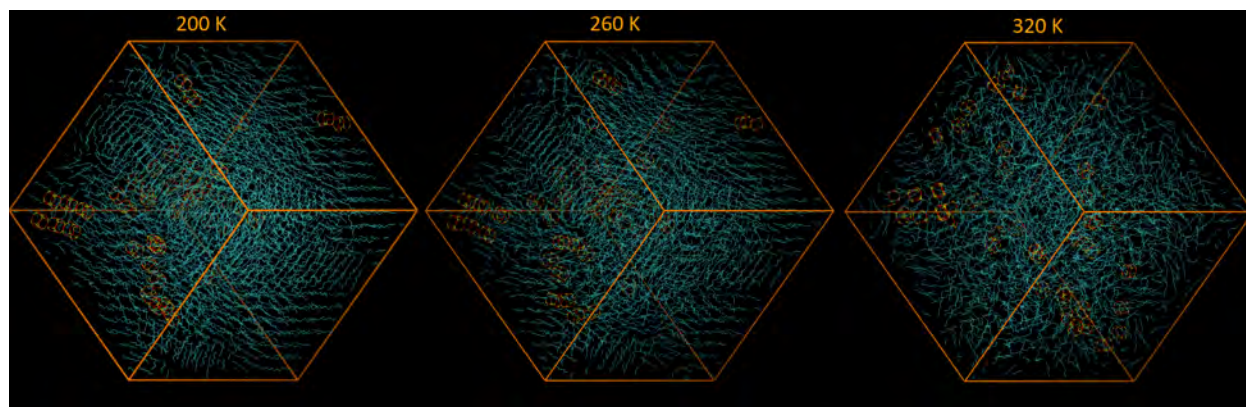
Figure 6.4.1: Octatetraene T_8t-butyl$_8$ 10% POSS blended system at at 200, 260 and 320 K from left to right respectively.

As shown from figures 6.4.9, 6.4.3, 6.4.4 and 6.4.5, HTPB mobility consistently decreases with the increased concentration of POSS. The mobility for all of these systems are very low,

even at 310 K.
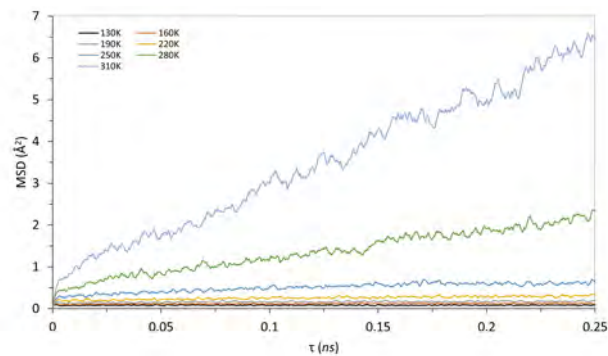
Figure 6.4.2: The MSD for pure HTPB 311 at a range of temperatures.
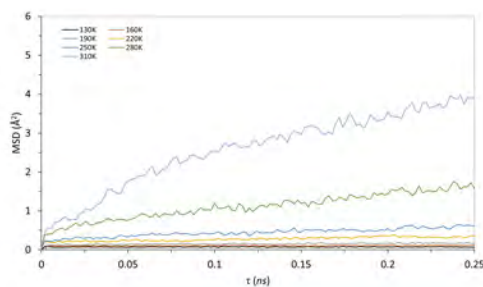
(a) HTPB with T_8H_8 at 10%
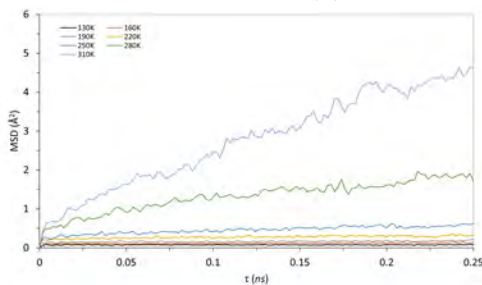
(b) T_8t-butyl$_8$ 10% load
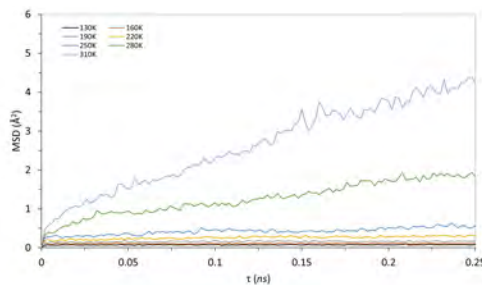
(c) T_8propyl-methacrylate$_8$ 10% load

Figure 6.4.3: The MSD for HTPB molecules in T_8H_8 (a), T_8t-butyl$_8$ (b) and T_8propyl-methacrylate$_8$ (c) blends at 10% wt POSS.
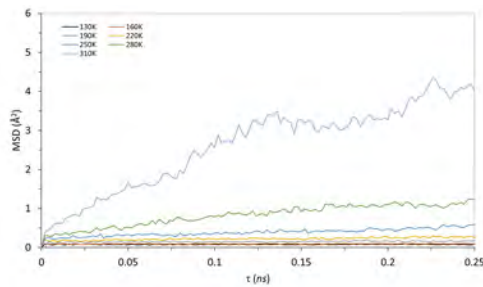
(a) T$_8$H$_8$ 30% load
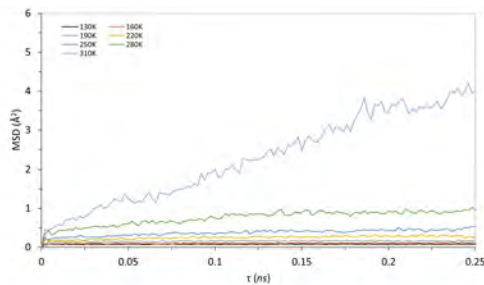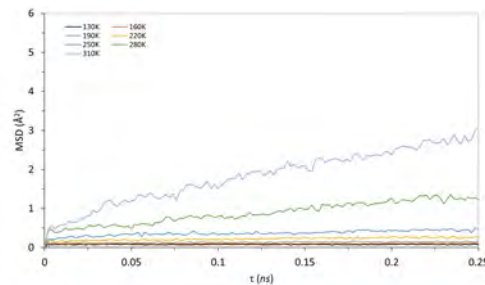
(b) T$_8$t-butyl$_8$ 30% load

(c) T$_8$propyl-methacrylate$_8$ 30% load

Figure 6.4.4: The MSD for HTPB molecules in T$_8$H$_8$ (a), T$_8$t-butyl$_8$ (b) and T$_8$propyl-methacrylate$_8$ (c) blends at 30% wt POSS.
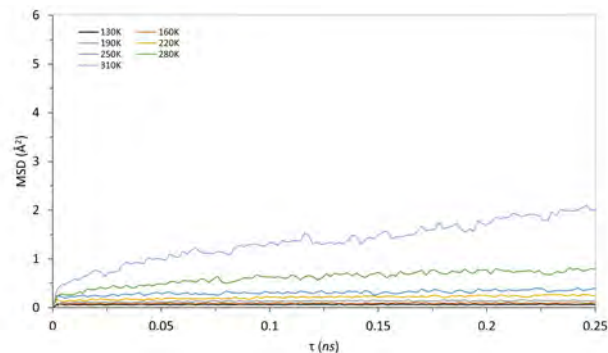
(a) T_8H_8 50% load
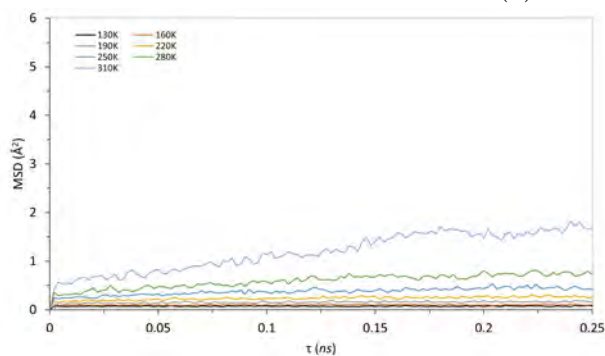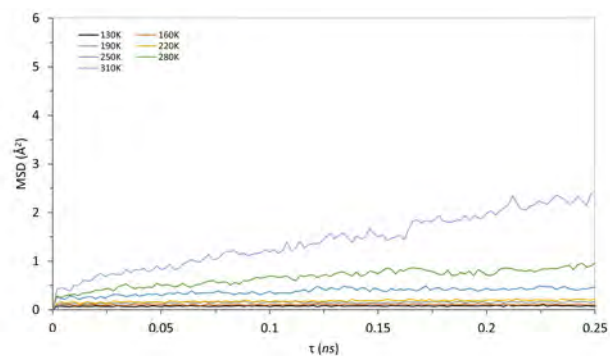
(b) T_8t-butyl$_8$ 50% load

(c) T_8propyl-methacrylate$_8$ 50% load

Figure 6.4.5: The MSD for HTPB molecules in T_8H_8 (a), T_8t-butyl$_8$ (b) and T_8propyl-methacrylate$_8$ (c) blends at 50% wt POSS.

In figures 6.4.6c, 6.4.6, 6.4.7, 6.4.8 I present the equivalent MSD data for the POSS molecules in the same HTPB blends. Here, similarly to the HTPB molecules, I see that the POSS mobility decreases on average with increase in POSS concentration. However, at 10% loading for the T_8H_8 blended system as shown in figure 6.4.6a, I see that the POSS mobility on is similar to the pure HTPB system.
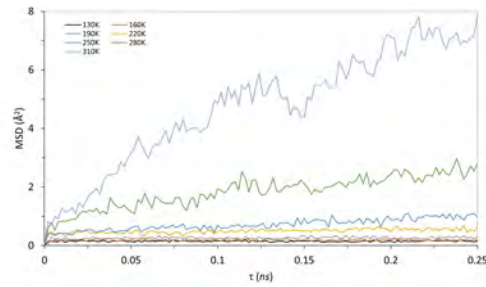
(a) T_8H_8 10% load
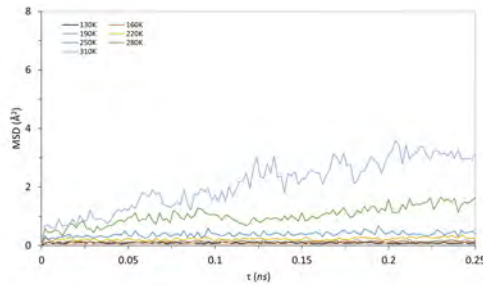
(b) T_8t-butyl$_8$ 10% load
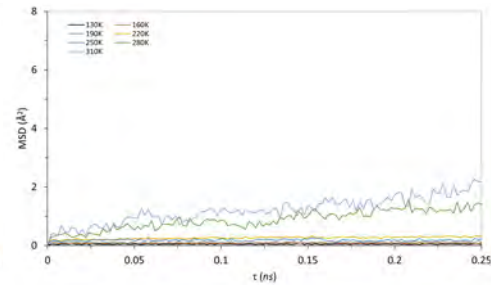
(c) T_8propyl-methacrylate$_8$ 10% load

Figure 6.4.6: The MSD for POSS molecules in T_8H_8 (a), T_8t-butyl$_8$ (b) and T_8propyl-methacrylate$_8$ (c) blends with HTPB 311 at 10% wt POSS.
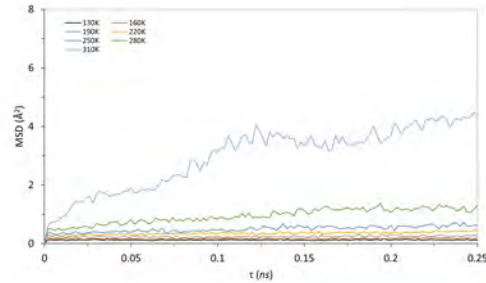
(a) T_8H_8 30% load
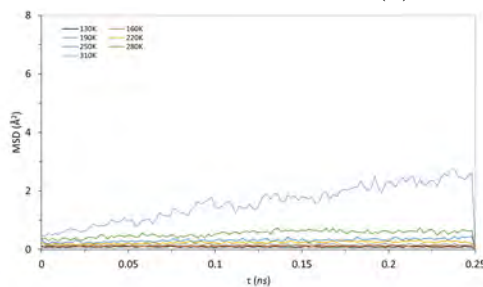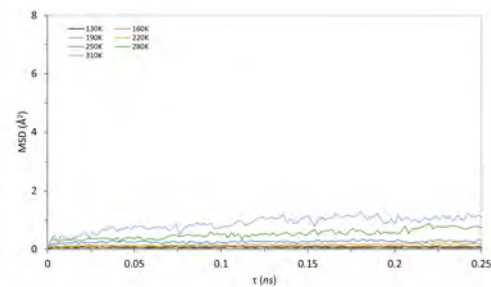
(b) T_8t-butyl$_8$ 30% load

(c) T_8propyl-methacrylate$_8$ 30% load

Figure 6.4.7: The MSD for POSS molecules in T_8H_8 (a), T_8t-butyl$_8$ (b) and T_8propyl-methacrylate$_8$ (c) blends with HTPB 311 at 30% wt POSS.
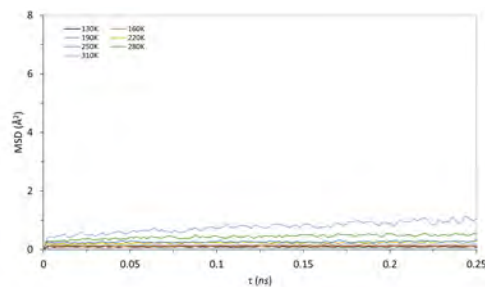
(a) T_8H_8 50% load
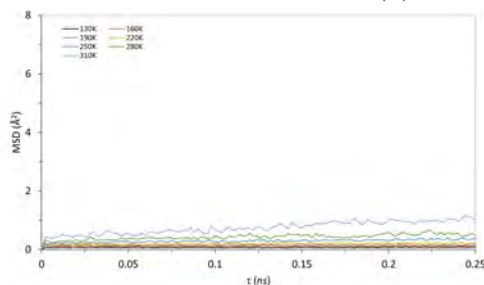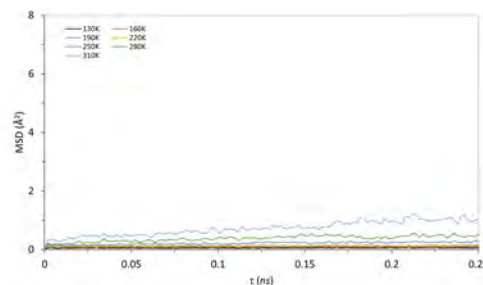
(b) T_8t-butyl$_8$ 50% load

(c) T_8propyl-methacrylate$_8$ 50% load

Figure 6.4.8: The MSD for POSS molecules in T_8H_8 (a), T_8t-butyl$_8$ (b) and T_8propyl-methacrylate$_8$ (c) blends with HTPB 311 at 50% wt POSS.

An overview of the octatetranene mobility in different blended systems can be seen in figure **??**. For the pure octatetraene data, the 310 K data point has been omitted as the system is in a gaseous state. For each system I see that octatetraene mobility decreases with increasing POSS concentration. The T_8H_8 and T_8t-butyl$_8$ blends demonstrate similar trends in octatetraene mobility with temperature. T_8propyl-methacrylate$_8$ blends demonstrate the lowest octatetraene mobility, however there is still significant mobility within the system.
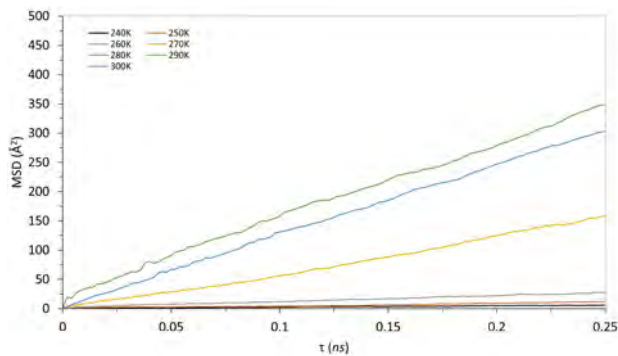
Figure 6.4.9: The MSD for pure octatetraene at a range of temperatures.
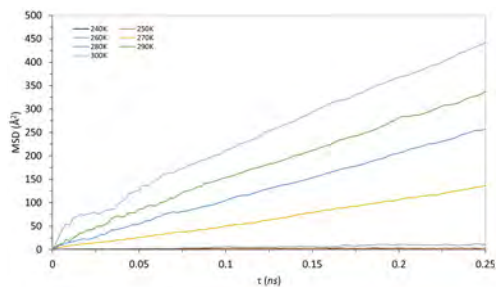
(a) T_8H_8 10% load
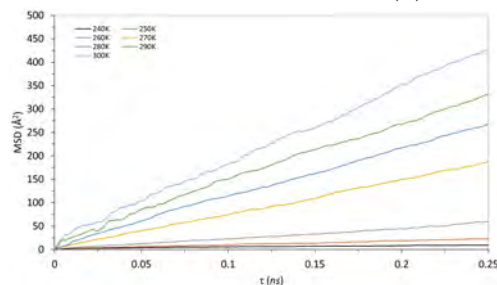
(b) T_8t-butyl$_8$ 10% load
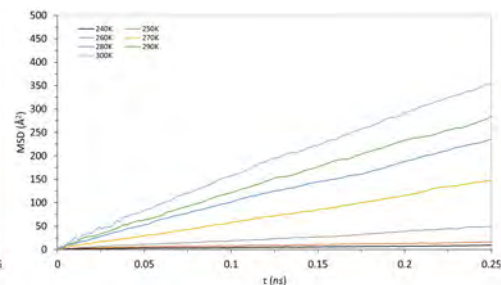
(c) T_8propyl-methacrylate$_8$ 10% load

Figure 6.4.10: The MSD for octatetraene molecules in T_8H_8 (a), T_8t-butyl$_8$ (b) and T_8propyl-methacrylate$_8$ (c) blends with octatetrane at 10% wt POSS.
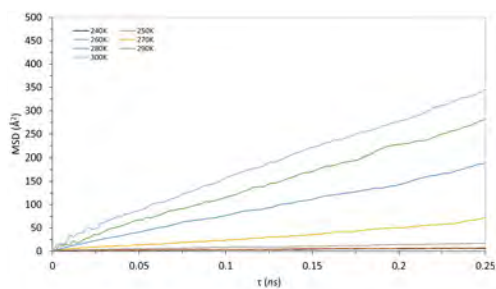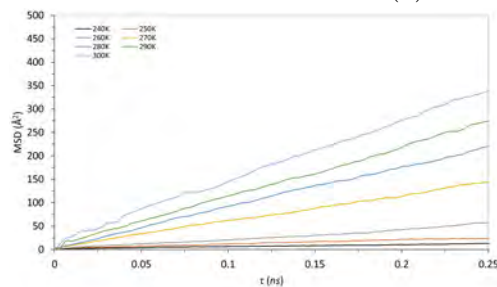
(a) T_8H_8 30% load
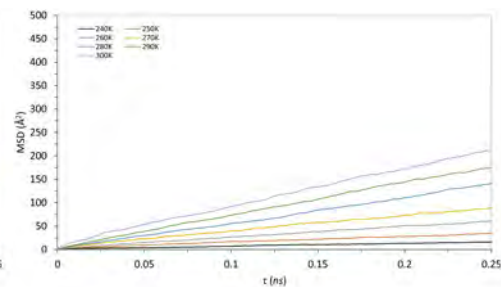
(b) T_8t-butyl$_8$ 30% load

(c) T_8propyl-methacrylate$_8$ 30% load

Figure 6.4.11: The MSD for octatetraene molecules in T_8H_8 (a), T_8t-butyl$_8$ (b) and T_8propyl-methacrylate$_8$ (c) blends with octatetrane at 30% wt POSS.
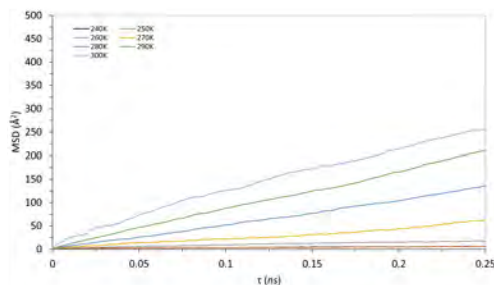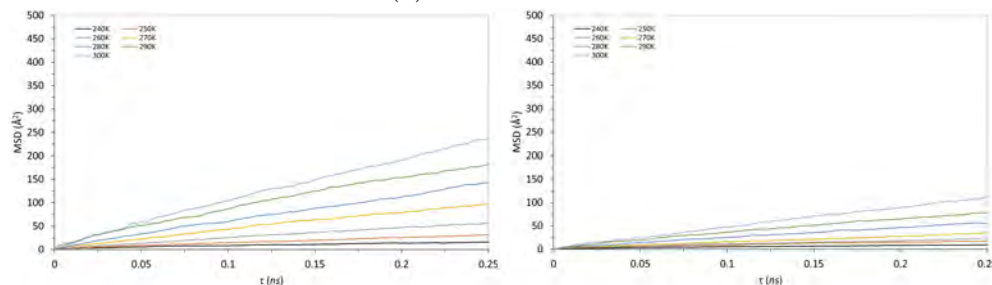
(a) T_8H_8 50% load

(b) T_8t-butyl$_8$ 50% load

(c) T_8propyl-methacrylate$_8$ 50% load

Figure 6.4.12: The MSD for octatetraene molecules in T_8H_8 (a), T_8t-butyl$_8$ (b) and T_8propyl-methacrylate$_8$ (c) blends with octatetrane at 50% wt POSS.

In figure 6.4.13, 6.4.14 and 6.4.15, I present the mobility of POSS molecules in octate-traene blended systems. Again, the mobility consistently decreases with POSS concentration. 30% and 50% concentrations of T_8H_8 blended systems have significantly lower mobility than the other POSS species at this concentration. This is a product of phase separation and POSS crystallisation within this system. Due to this agglomeration, the microcrystallites mobilise as a large and slow single unit. The equivalent T_8t-butyl$_8$ system at 30 and 50% system demonstrates greater mobility than the T_8H_8 blends. Here, due to the reduced tendency to form aggregates, smaller clusters and individual molecules are able to be more mobile.
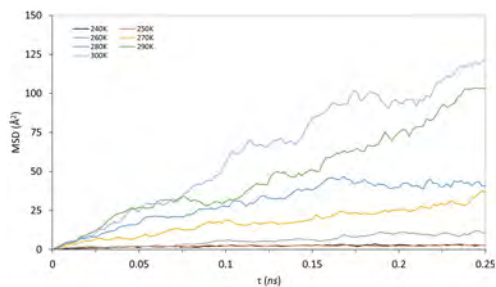
(a) T_8H_8 10% load
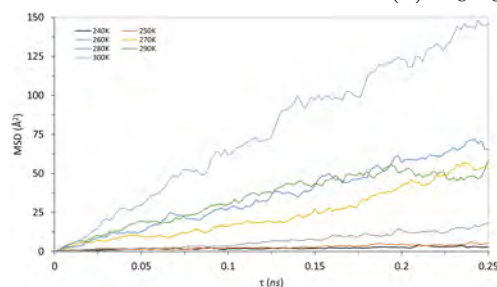
(b) T_8t-butyl$_8$ 10% load
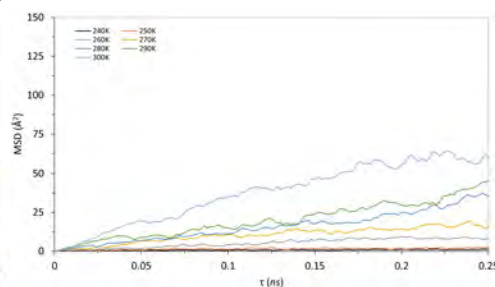
(c) T_8propyl-methacrylate$_8$ 10% load

Figure 6.4.13: The MSD for POSS molecules in T_8H_8 (a), T_8t-butyl$_8$ (b) and T_8propyl-methacrylate$_8$ (c) blends with octatetrane at 10% wt POSS.
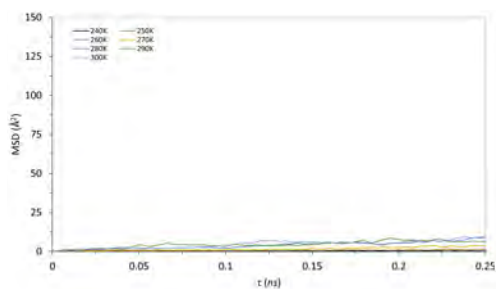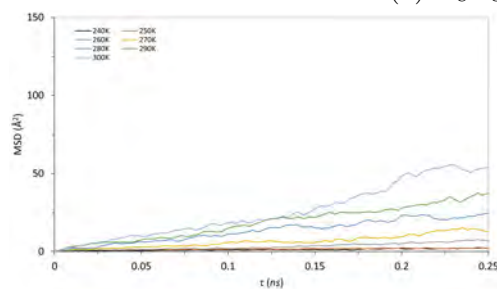
(a) T_8H_8 30% load
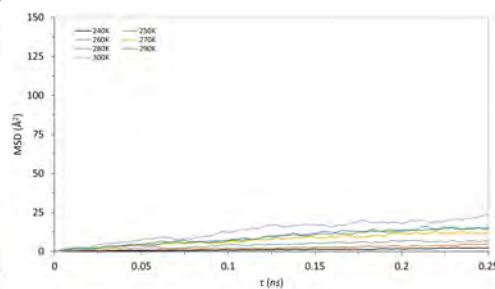
(b) T_8t-butyl$_8$ 30% load

(c) T_8propyl-methacrylate$_8$ 30% load

Figure 6.4.14: The MSD for POSS molecules in T_8H_8 (a), T_8t-butyl$_8$ (b) and T_8propyl-methacrylate$_8$ (c) blends with octatetrane at 30% wt POSS.
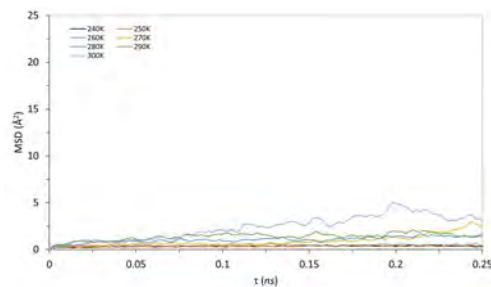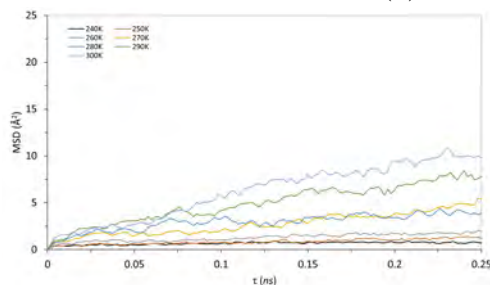
(a) T_8H_8 50% load
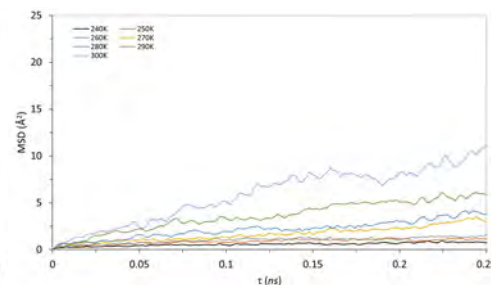
(b) T_8t-butyl$_8$ 50% load

(c) T_8propyl-methacrylate$_8$ 50% load

Figure 6.4.15: The MSD for POSS molecules in T_8H_8 (a), T_8t-butyl$_8$ (b) and T_8propyl-methacrylate$_8$ (c) blends with octatetrane at 50% wt POSS.

From the Voronoi analysis of these systems, I have demonstrated the propensity for favourable interaction between the POSS and polymer matrix. In table 6.2, I present the number of near neighbours for the POSS and matrix of each blend at 130 K. For HTPB blends, at 10% POSS concentration, the number of near neighbours for POSS is between 22 and 22.5. As POSS concentration increases, the average number of near neighbours decreases. The T_8propyl-methacrylate$_8$ blended system has the greatest reduction in the number of near neighbours. This is due to the more favourable interactions between the POSS and polymer, as the propyl-methacrylate groups are able to inter-penetrate the HTPB molecules. This trend can also be seen in the octatetraene blended systems.

Matrix	POSS Type	POSS conc	Number of Near Neighbours	
			POSS	HTPB
HTPB 311	T_8H_8	10%	1.8	22.5
		30%	4.9	20.4
		50%	8.6	18.6
	T_8t-butyl$_8$	10%	0.7	22.2
		30%	3.9	18.7
		50%	6.3	14.7
	T_8propyl-methacrylate$_8$	10%	1.7	22.4
		30%	5.0	18.5
		50%	8.1	13.5
octatetraene	T_8H_8	10%	4.0	13.9
		30%	8.8	13.6
		50%	9.7	13.1
	T_8t-butyl$_8$	10%	1.6	13.4
		30%	5.4	12.1
		50%	7.2	10.8
	T_8propyl-methacrylate$_8$	10%	0.0	13.6
		30%	4.0	11.3
		50%	8.0	9.3

Table 6.2: The number of near neighbours for all components within the blended systems at 130 K from H-stripped structures.

Simulation studies of blended POSS systems by Capaldi *et al* have described the early stages of POSS microcrystallite formation in T_8cyclo-pentyl$_8$ and polyethylene blends.[71] Cooling sequences from 500 to 300 K have been employed, with analyses being conducted at these temperatures only. This publication provides excellent insight into the interaction between the POSS and polymer. Similarly to my work, through the use of MSD analysis, the mobility of the matrix is shown to decrease with increasing POSS concentration. The mobility of the matrix tangential to the POSS surface is demonstrated to be greater than that of the remaining bulk. This study emphasises the critical nature of polymer and POSS selection for nanocomposite production, as the degree of agglomeration affects the volume fraction of interfacial matrix and, therefore, fundamentally changes the POSS polymer interaction. Within my work, I have described the observed differences in T_g between HTPB and octetraene blended systems through molecular level analyses. Here, I have observed and

characterised the formation of microcrystallites of rigid POSS species in both HTPB and octatetrane blends. For these systems, agglomeration is limited by the POSS concentration and temperature of the system. The entangled nature of HTPB does not prevent the agglomeration of rigid POSS during simulation as crystallisation is observed in both HTPB and octatetraene blends at high POSS loadings.

In a more recent study, Jia Xiang-Meng *et al* have investigated T_8aminophenyl$_8$ blended with poly(2-vinylpyridine) (P2VP).[152] Previous experimental work of this system has described a significant increase in T_g with POSS loading due to favourable POSS-polymer interaction. The effects of the hydrogen-bonds formed between the POSS and polymer are observed by running simulations with and without partial charges in parallel. The inclusion of partial charges leads to a lower degree of penetration into the inner-most region of the POSS-polymer interface due to the formation of H-bonds further from the POSS center of mass. When partial charges are included, the mobility of P2VP monomers is reduced up to 20 $\mathring{A}$ from the POSS center of mass. These simulations only contain a single T_8aminophenyl$_8$ molecule at the center of the simulation cell with 120 surrounding P2VP chains. Thus, this study provides an excellent analysis of the fine interactions occurring at the POSS-polymer interface. However, due to the inclusion of only a single POSS molecule, this study is limited to consideration of a single concentration. Further aspects such as aggregation cannot be considered. Within my work, I have characterised the impact of several different blended POSS species on the identified mode of glass transition in HTPB, the dihedral crankshaft motion. As I have demonstrated, the T_8propyl-methacrylate$_8$ blended system at 50% loading increases the frequency of dihedral rotation along the HTPB backbone compared to the pure HTPB 311 system. In contrast to the POSS-HTPB grafted systems, I do not observe significant local or global reduction of this mechanism for all blended systems on my work.

Throughout this chapter, I have demonstrated the formation of microcrystallites for T_8H_8

blends which contribute to the observed low mobility. In HTPB and octatetraene blends, the lack of interaction between POSS and matrix results in a great deal of phase separation. Radial distribution function analysis has been utilised and demonstrates the long range order within these blends at 30% and 50% POSS concentration. Similar trends have been observed in the T_8t-butyl$_8$ blended systems, although not to the same degree of agglomeration. T_8propyl-methacrylate$_8$ blends, in contrast, demonstrate a more amorphous arangement, presenting a greater propensity to interact with both the HTPB and octatetraene matrices. Despite this increased interaction, the dihedral freedom of the HTPB backbone remains unhindered by their presence. In fact, at the highest concentration as shown in figure 6.2.34, I see that the dihedral rotational freedom is actually increased on average for the 50% blend system. Despite this, I predict that this system has the highest T_g of all concentrations.

Within this section I have conducted a systematic study a variety of POSS-polymer blended species. I have utilised a number of different analysis protocols to probe the molecular and macroscale behaviour. The impact per POSS molecule on the glass transition behaviour is reduced for blended systems compared with grafted ones. However, blended nanocomposite systems are able to exhibit structures and, thus, material properties that are not accessible to pure POSS or pure polymer systems.

Chapter 7

Summary, Conclusions and Future Work

As stated in chapter 1, the aim of this project has been to utilise atomistic MD techniques to better understand the molecular behaviour of POSS species and elucidate the mechanisms that give rise to the change in the macroscopic properties of POSS containing materials. This work has covered a variety of POSS species modelled as pure entities and as part of a nanocomposite.

Within chapter 4, a number of developments have been undertaken in the context of pure POSS systems. The systematic study of flexible pure POSS systems has elucidated that a molecular level feature, namely, the breathing mode, can be used to control the T_g. As discussed in chapter 1, controlling T_g in materials can be crucial during development. By increasing the linker length of octa-methacrylate functionalised POSS species, and thus percentage organic character, the T_g decreases. Based on the analyses carried out in this chapter, this trend can be attributed to the increased capacity of the organic halo surrounding the silica core to express micro-movements in atomic position. The identification of the breathing mode has not been previously mentioned within the literature pertaining to POSS systems.

G(r) and MSD analysis has shown that, even at high temperatures, these systems are amorphous, highly entangled and the centre of mass for each molecule is locked-in. In simulation studies, this may result from insufficiently equilibrated systems. However, through the examination of repeat simulations, this isotropic structure arises from the nature of the molecular structure. Thus, molecular entanglement is a crucial factor when considering the macroscopic properties of POSS species containing flexible R groups. Voronoi analysis has demonstrated that that the degree of entanglement and intermolecular penetration scales with increasing number of linker length. This work denotes a step forward in the understanding of the molecular behaviour of amorphous POSS systems.

Morphological contributions have also been studied in the context of molecular behaviour and macroscopic properties through the analysis of tetra and shuttlecock POSS morphologies with flexible linkers. For these structural isomers, Similarly to the octa-methacrylate functionalised counter-parts, the breathing mode plays a critical role in the glass transition process. As these configurations have been observed within the experimental literature, the ubiquity of the breathing mode in flexible POSS systems offers experimentalists new perspectives on a variety of POSS structures. This is a novel discovery that can be utilised to access and understand a range of POSS materials with different glass transition temperatures.

By increasing the linker length of tetra-functionalised POSS, diverging trends have been identified in the predicted T_g. For both morphology types, molecular entanglement is observed. However, shuttlecock POSS morphologies undergo preferential stacking at none functionalised facets. This observation coincides with significantly higher T_g for butyl and pentyl linker length shuttlecock tetra-functionalised POSS. Thus, I can conclude that for a variety of flexible R group POSS species, the entangled interstitial organic zone between POSS cores is pivotal for flexible POSS systems to exhibit a glass transition. In addition,

increasing the consistency of this region throughout the sample results in a lower T_g compared to confined regions observed for shuttlecock morphologies.

In addition, from studies on rigid POSS structures at high temperatures, highly ordered crystalline structures from disordered starting configurations have been observed. Through the analysis of molecular mobility and rotation, I have characterised the crystallisation temperature for these systems. However, as shown in section 4.3, a small change, such as the conformation of butyl funtionalising group, can change the fundamental behaviour of rigid POSS systems. Thus, within this section, the functionalising group isomerism has also been investigated. These sections have further elucidated the causal link between the molecular structure, for a range of POSS species, and their macroscopic properties. In accordance with the aims defined in section 1, a this work contains a comprehensive study of pure POSS systems in a variety of structural and chemical conformations. This work has identified a measurable and tunable molecular level feature that can be utilised to control the T_g of a system. Such diverse analyses of of pure POSS structures has not been previously reported in the literature.

Of course, there are an extremely large number of possible POSS structures and nanocomposite combinations. However, as this work demonstrates, the principle that T_g can be controlled via the breathing mode of the POSS molecules can be applied to a number of different structures and morphologies. For researchers in the field, this may prove to be a useful metric for predicting the outcome of new formulations containing POSS. The ability to control the thermomechanical properties of a POSS nanocomposite system depend on understanding the nature of the utilised POSS species.

In order to fulfil the aims given in chapter 1, The study of POSS as part of a nanocomposite systems has also been developed within this body of work. I have demonstrated that

when integrated as pendant groups, POSS species behave as anchoring sites for the polymer matrix. Similar results have been reported by Bizet *et al*, who investigated the addition of cubic POSS pendant groups to polymethyl methacrylate via a methacrylate bridge.[87] This study concludes that POSS species behave as 'anchoring points', however only in context of POSS mobility. From the current study, the scope of this anchoring effect into the polymer backbone has been determined via the analysis of the dihedral rotational freedom. For these grafted systems of HTPB and POSS, this results in a significant reduction in the local dihedral freedom about the grafting site. Thus, as a result of including POSS species, I have observed 20-30 K increase in predicted T_g from the pure HTPB systems.

In the wider context, this work is important as identification of routes to alter the properties of polymers, such as HTPB, are necessary to produce superior materials. This may not only be in the context of material service and properties, but also ease of manufacture and longevity. This work has shown how a range of POSS molecules impact HTPB molecular behaviour when incorporated as a grafted component.

Additionally, when incorporated as blended discrete molecules, different regimes of interactions are observed. Here, the dihedral freedom of the HTPB backbone is affected to a lesser degree by the presence of POSS. In-fact, there is some suggestion that the presence of POSS may facillitate slightly higher degrees of rotational freedom across certain bonds. From this work, I have identified that the molecular mobility of the HTPB chains decreases with increasing concentration of POSS. This is in agreement with the observations of Capaldi *et al*, who studied POSS-polyethylene blends.[71] As shown within this work, The impact of different POSS species and their concentrations can dramatically change the morphology and properties. For rigid species, at higher concentrations, phase separation often occurs to produce microcrystallite regions. The formation of these regions is associated an increase in the predicted T_g.

Further, The same tendency for agglomeration has also been observed in octatetraene blended systems, a medium with a much lower capacity for entanglement. These systems exhibit a rich set of behaviour due to the range of mixing and entanglement. These systems have displayed phase separated co-crystalline compositions of T_8H_8 and octatetraene, and randomised amorphous structures when blended with T_8propyl-methacrylate$_8$. The observed diversity in behaviours exhibited in these systems speaks to the range of possible arrangements, conformations and applications of these systems. Collectively, this section of work has elucidated the molecular behaviour of POSS in contrasting matrices. From this section, it can be concluded that strong effective potentials between rigid POSS species leads to the formation of microcrystallites at high temperature in polymer matrices. In addition, the interpenetration, within the matrix, of flexible POSS species promotes randomised distributions. Also, in matrices containing smaller molecules, the flexible POSS R groups can disrupt the long range ordered packing of molecules. The glass transition behaviour of blended systems has been observed as highly sensitive to the nature of the functionalising ligands.

7.0.1   Future Work

This work has demonstrated a range of behaviours that POSS speices are capable of exhibiting. However, there are a few areas that have not been covered in this section that I would consider for future work:

- Consider the inclusion of dynamic charges. Given more time and computational resource, I would have investigated the efficacy of improving the model with dynamic partial charges. This may result is somewhat better predictions but add significant computational cost.

- Investigate cross-linked methacrylate systems. This is one of the feasible states that POSS can exist in that is not covered within this work. Particularly for HTPB systems, the change in T_g due to cross-linking POSS and associated molecular mechanism would be interesting to investigate. In addition, varying the number of cross-linking ligands would be interesting to observe. This would provide a powerful contrast between blended, grafted and cross-linked species.

- As mentioned in chapter 2, obtaining experimental samples of POSS that only contain T_8 conformations is difficult. Therefore, being able to quantify the difference in structure-property relationship between T_8, T_{10}, T_{12} etc may lead to the capacity to predict the sensitivity of system properties to the mixing ratios.

- Testing the limitations of the breathing mode. Investigating flexible systems with different groups, such as aromatic or aliphatic rings, could be used to examine the limiting factor for this molecular level feature in predicting T_g.

- Investigate methods of plasticizing rigid POSS systems. These systems have proved to have the strongest tendency to agglomerate. The sensitivity for these rigid POSS to small molecule plasticizer would be an interesting area for future study.

- Investigate unique variants of functionalising R groups. For example, POSS systems functionalised with liquid crystalline ligands have already been achieved experimentally,[153]. However, hybrid and nano composite behaviours have not been widely studied. This presents an interesting opportunity to investigate the behaviour of POSS species at the phase boundaries of liquid crystals.

Appendix A

atom type	description
c	sp3 carbon - connect to four C
c1	sp3 carbon -CH - connect to three C
c2	sp3 carbon -CH2 - connect to two C
c3	sp3 carbon -CH3 - connect to one C
c=	end double bond carbon
c=1	next to end double bond carbon
c_1	carbon of carbonyl (C=O)
cp	aromatic carbon atom
o_2	ester group (C-O-C) oxygen
oh	alcohol (-O-H) oxygen
o_1	oxygen of carbonyl (C=O)
sio	silicon atom with adjacent oxygen atom
hc	hydrogen atom bonded to carbon
ho	hydrogen atom bonded to oxygen
hsi	hydrogen atom bonded to silicon
osi	oxygen atom bonded to silicon

Table A.1: Key to describe all atom types in PCFF

atom type 1	atom type 2	K_2^b	K_3^b	K_4^b	R_0
c	c3	599.34	-1505.31	2719.24	1.53
c1	c1	599.34	-1505.31	2719.24	1.53
c1	c2	599.34	-1505.31	2719.24	1.53
c1	c3	599.34	-1505.31	2719.24	1.53
c1	c=	624.7034	-1746.5583	1359.5884	1.506
c1	hc	690	-2075.67	3378.4	1.101
c2	c1	599.34	-1505.31	2719.24	1.53
c2	c2	599.34	-1505.31	2719.24	1.53
c2	c=	624.7034	-1746.5583	1359.5884	1.506
c2	cp	643.8042	-1565.4624	2288.6512	1.501
c2	hc	690	-2075.67	3378.4	1.101
c2	o_2	653.4546	-1825.5918	2756.1332	1.43
c2	oh	800.7908	-2505.5853	5252.0568	1.42
c3	hc	690	-2075.67	3378.4	1.101
c=	c1	624.7034	-1746.5583	1359.5884	1.506
c=	c2	624.7034	-1746.5583	1359.5884	1.506
c=	c3	624.7034	-1746.5583	1359.5884	1.506
c=	c=	1090.5326	-3016.899	4902.966	1.3521
c=	c=1	1087.98	-3714.6075	6576.1128	1.34
c=	hc	731.5358	-2176.6212	3126.6484	1.0883
c=1	c=	1087.98	-3714.6075	6576.1128	1.34
c=1	c=1	640	0	0	1.48
c=1	hc	731.5358	-2176.6212	3126.6484	1.0883
c_1	c1	507.4134	-1269.111	1587.6	1.5202
c_1	c=	540.24	-1299.7557	1621.4404	1.46
c_1	o_1	1702.2806	-5755.4646	8643.0636	1.202
c_1	o_2	734.2962	-2384.3724	4220.9276	1.3683
cp	cp	941.6722	-1882.8537	5310.538	1.417
cp	hc	745.6502	-2410.3578	3577.2692	1.0982
o_2	c2	653.4546	-1825.5918	2756.1332	1.43
o_2	c_1	734.2962	-2384.3724	4220.9276	1.3683
oh	ho	1065.0124	-3848.715	8019.0632	0.965
sio	c	314.0098	-713.1069	1424.1312	1.9073
sio	c2	314.0098	-713.1069	1424.1312	1.9073
sio	c3	314.0098	-713.1069	1424.1312	1.9073
sio	hsi	576.6336	0	0	1.463
sio	osi	612.2464	-1552.0272	2694.8268	1.6562

Table A.2: The force constants for the bond potential within PCFF throughout this thesis.

atom type 1	atom type 2	atom type 3	K_2^a	K_3^a	K_4^B	θ_0
c	c3	hc	82.906	-31.812	20.516	110.77
c1	c1	c1	79.032	-22.329	-38.2332	112.67
c1	c1	c2	79.032	-22.329	-38.2332	112.67
c1	c1	hc	82.906	-31.812	20.516	110.77
c1	c2	c1	79.032	-22.329	-38.2332	112.67
c1	c2	c2	79.032	-22.329	-38.2332	112.67
c1	c2	c=	91.4052	-31.9188	-39.6484	111.76
c1	c2	hc	82.906	-31.812	20.516	110.77
c1	c3	hc	82.906	-31.812	20.516	110.77
c1	c=	c=	87.65	-83.1798	4.0224	126.26
c1	c=	hc	60.1888	-24.2478	-34.7124	117.27
c2	c1	c1	79.032	-22.329	-38.2332	112.67
c2	c1	c2	79.032	-22.329	-38.2332	112.67
c2	c1	c3	79.032	-22.329	-38.2332	112.67
c2	c1	c=	91.4052	-31.9188	-39.6484	111.76
c2	c1	c_1	103.9494	-28.4553	-43.994	108.5295
c2	c1	hc	82.906	-31.812	20.516	110.77
c2	c2	c1	79.032	-22.329	-38.2332	112.67
c2	c2	c2	79.032	-22.329	-38.2332	112.67
c2	c2	c=	91.4052	-31.9188	-39.6484	111.76
c2	c2	cp	87.9188	-25.1772	-37.3516	108.4
c2	c2	hc	82.906	-31.812	20.516	110.77
c2	c2	o_2	126.7814	-40.3539	6.66	107.41
c2	c=	c=	87.65	-83.1798	4.0224	126.26
c2	c=	hc	60.1888	-24.2478	-34.7124	117.27
c2	cp	cp	89.4296	-68.2056	0	120.05
c2	o_2	c_1	122.5736	-86.9358	31.9716	113.288
c2	oh	ho	105.4122	-36.327	-39.4724	105.8
c3	c	c3	79.032	-22.329	-38.2332	112.67
c3	c1	hc	82.906	-31.812	20.516	110.77
c3	c=	c=	87.65	-83.1798	4.0224	126.26
c=	c1	c2	91.4052	-31.9188	-39.6484	111.76
c=	c1	hc	82.5568	-42.8889	20.8916	110.06
c=	c2	c1	91.4052	-31.9188	-39.6484	111.76
c=	c2	c2	91.4052	-31.9188	-39.6484	111.76
c=	c2	hc	82.5568	-42.8889	20.8916	110.06
c=	c2	oh	92	0	0	110.5
c=	c3	hc	82.5568	-42.8889	20.8916	110.06
c=	c=	c1	87.65	-83.1798	4.0224	126.26

Table A.3: The force constants for the angles potential within PCFF throughout this thesis (part 1).

atom type 1	atom type 2	atom type 3	K_2^a	K_3^a	K_4^B	θ_0
c=	c=	c2	87.65	-83.1798	4.0224	126.26
c=	c=	c3	87.65	-83.1798	4.0224	126.26
c=	c=	hc	70.5532	-53.322	-6.486	124.88
c=	c=1	c=1	112.96	-48.6849	-50.5332	117.6
c=	c=1	hc	70.5532	-53.322	-6.486	124.88
c=	c_1	o_1	92.12	-55.6389	-44.3992	125.9
c=	c_1	o_2	136	0	0	120
c=1	c=	hc	70.5532	-53.322	-6.486	124.88
c=1	c=1	c=	112.96	-48.6849	-50.5332	117.6
c=1	c=1	c=1	112.96	-48.6849	-50.5332	117.6
c=1	c=1	hc	70.5532	-53.322	-6.486	124.88
c_1	c1	c3	103.9494	-28.4553	-43.994	108.5295
c_1	c1	hc	81.2198	-86.4363	0	107.7336
c_1	c=	c3	72.4	0	0	120
c_1	c=	c=	132.22	-66.0618	-60.8532	121.1
c_1	o_2	c2	122.5736	-86.9358	31.9716	113.288
cp	cp	cp	122.0452	-104.9793	0	118.9
cp	cp	hc	70.3116	-37.4046	0	117.94
hc	c1	c1	82.906	-31.812	20.516	110.77
hc	c1	c2	82.906	-31.812	20.516	110.77
hc	c2	c1	82.906	-31.812	20.516	110.77
hc	c2	c2	82.906	-31.812	20.516	110.77
hc	c2	cp	88.6468	-28.3362	0	111
hc	c2	hc	79.282	-38.763	-9.7272	107.66
hc	c2	o_2	130.9602	-31.0494	23.5464	107.688
hc	c3	hc	79.282	-38.763	-9.7272	107.66
hc	c=	hc	59.2726	-37.4559	-24.8872	115.49
hc	cp	cp	70.3116	-37.4046	0	117.94
o_1	c_1	c1	111.0862	-51.6369	0.5392	123.1451
o_1	c_1	c=	92.12	-55.6389	-44.3992	125.9
o_1	c_1	o_2	190.6892	-96.8607	25.5112	120.797
o_2	c2	c2	126.7814	-40.3539	6.66	107.41
o_2	c2	hc	130.9602	-31.0494	23.5464	107.688
o_2	c_1	c1	77.7262	-11.4969	-31.9208	100.3182
o_2	c_1	c=	136	0	0	120
o_2	c_1	o_1	190.6892	-96.8607	25.5112	120.797
oh	c2	hc	117.0892	-32.4264	-49.6024	108.728
osi	sio	c	46.0436	-94.1979	99.9256	114.906
osi	sio	c2	46.0436	-94.1979	99.9256	114.906
osi	sio	c3	46.0436	-94.1979	99.9256	114.906

Table A.4: The force constants for the angles potential within PCFF throughout this thesis (part 2).

atom type 1	atom type 2	atom type 3	K_2^a	K_3^a	K_4^B	θ_0
osi	sio	hsi	115.3286	-31.9518	18.5096	107.355
osi	sio	osi	140.6138	-20.8125	0	110.693
sio	c	c3	69.2	0	0	112.3
sio	c2	c2	69.2	0	0	112.3
sio	c2	hc	60.4962	-46.5765	0	111.536
sio	c3	hc	60.4962	-46.5765	0	111.536
sio	osi	sio	18.148	-58.6728	34	157.026

Table A.5: The force constants for the angles potential within PCFF throughout this thesis (part 3).

atom type 1	atom type 2	atom type 3	atom type 4	K_1^d	K_2^d	K_3^d
c3	c	c3	hc	0	0.0316	-0.1681
sio	c	c3	hc	0.158	0.158	0.158
c2	c1	c1	c1	0	0.0514	-0.143
hc	c1	c1	c1	0	0.0316	-0.1681
c1	c1	c1	c2	0	0.0514	-0.143
c2	c1	c1	c2	0	0.0514	-0.143
hc	c1	c1	c2	0	0.0316	-0.1681
hc	c1	c1	hc	-0.1432	0.0617	-0.1083
c1	c1	c1	hc	0	0.0316	-0.1681
c2	c1	c1	hc	0	0.0316	-0.1681
c2	c1	c2	c1	0	0.0514	-0.143
hc	c1	c2	c1	0	0.0316	-0.1681
c1	c1	c2	c1	0	0.0514	-0.143
c=	c1	c2	c1	0.0883	0	-0.0198
hc	c1	c2	c2	0	0.0316	-0.1681
c1	c1	c2	c2	0	0.0514	-0.143
c=	c1	c2	c=	0	0	-0.316
hc	c1	c2	c=	0	0	-0.1166
c2	c1	c2	c=	0.0883	0	-0.0198
hc	c1	c2	hc	-0.1432	0.0617	-0.1083
c2	c1	c2	hc	0	0.0316	-0.1681
c=	c1	c2	hc	0	0	-0.1166
c1	c1	c2	hc	0	0.0316	-0.1681
c_1	c1	c3	hc	-0.0228	0.028	-0.1863
hc	c1	c3	hc	-0.1432	0.0617	-0.1083
c2	c1	c3	hc	0	0.0316	-0.1681
hc	c1	c=	c=	0.1143	0	0.1854
c2	c1	c=	c=	0.2433	0	0.104
hc	c1	c=	hc	-0.1143	0	-0.1349
c2	c1	c=	hc	-0.2433	0	-0.3281
hc	c2	c1	c1	0	0.0316	-0.1681
c1	c2	c1	c1	0	0.0514	-0.143
c1	c2	c1	c2	0	0.0514	-0.143
hc	c2	c1	c2	0	0.0316	-0.1681
c2	c2	c1	c2	0	0.0514	-0.143
c=	c2	c1	c2	0.0883	0	-0.0198
c1	c2	c1	c3	0	0.0514	-0.143
hc	c2	c1	c3	0	0.0316	-0.1681
hc	c2	c1	c=	0	0	-0.1166

Table A.6: The force constants for the dihedral potential within PCFF throughout this thesis (Part 1).

atom type 1	atom type 2	atom type 3	atom type 4	K_1^d	K_2^d	K_3^d
c=	c2	c1	c=	0	0	-0.316
c2	c2	c1	c=	0.0883	0	-0.0198
hc	c2	c1	c_1	-0.0228	0.028	-0.1863
c1	c2	c1	c_1	0.0972	0.0722	-0.2581
hc	c2	c1	hc	-0.1432	0.0617	-0.1083
c=	c2	c1	hc	0	0	-0.1166
c1	c2	c1	hc	0	0.0316	-0.1681
c2	c2	c1	hc	0	0.0316	-0.1681
hc	c2	c2	c1	0	0.0316	-0.1681
c=	c2	c2	c1	0.0883	0	-0.0198
c1	c2	c2	c2	0	0.0514	-0.143
c2	c2	c2	c2	0	0.0514	-0.143
o_2	c2	c2	c2	0	0	-0.25
hc	c2	c2	c2	0	0.0316	-0.1681
sio	c2	c2	c2	0.158	0.158	0.158
c=	c2	c2	c=	0	0	-0.316
hc	c2	c2	c=	0	0	-0.1166
hc	c2	c2	cp	-0.0228	0.028	-0.1863
hc	c2	c2	cp	-0.1863	0	0.0316
hc	c2	c2	cp	-0.1863	-0.1432	0.0617
hc	c2	c2	cp	0.028	-0.1863	-0.2802
hc	c2	c2	cp	0.028	-0.1863	0
hc	c2	c2	cp	0.028	-0.1863	-0.1432
c2	c2	c2	cp	0.158	-0.1432	0.0617
hc	c2	c2	hc	-0.1083	-0.1432	0.0617
hc	c2	c2	hc	-0.1083	-0.0228	0.028
hc	c2	c2	hc	-0.1432	0.0617	-0.1083
c2	c2	c2	hc	-0.1681	0	0.0316
c2	c2	c2	hc	-0.1681	0.158	-0.1432
c=	c2	c2	hc	0	0	-0.1166
c1	c2	c2	hc	0	0.0316	-0.1681
o_2	c2	c2	hc	0	0	-0.25
c2	c2	c2	hc	0	0.0316	-0.1681
c2	c2	c2	hc	0.0316	-0.1681	0
c2	c2	c2	hc	0.0316	-0.1681	0.158
hc	c2	c2	hc	0.0617	-0.1083	-0.1432
hc	c2	c2	hc	0.0617	-0.1083	-0.0228
sio	c2	c2	hc	0.158	0.158	0.158
c2	c2	c2	o_2	0	0	-0.25
hc	c2	c2	o_2	0	0	-0.25

Table A.7: The force constants for the dihedral potential within PCFF throughout this thesis (Part 2).

atom type 1	atom type 2	atom type 3	atom type 4	K_1^d	K_2^d	K_3^d
sio	c2	c2	o_2	0.158	0.158	0.158
hc	c2	c=	c=	0	0.1854	-0.1143
hc	c2	c=	c=	0.1143	0	0.1854
oh	c2	c=	c=	0.211	0.211	0.1143
c2	c2	c=	c=	0.2433	0	0.104
c1	c2	c=	c=	0.2433	0	0.104
hc	c2	c=	hc	-0.1143	0	-0.1349
c1	c2	c=	hc	-0.2433	0	-0.3281
c2	c2	c=	hc	-0.2433	0	-0.3281
hc	c2	c=	hc	0	-0.1349	0.13
hc	c2	c=	hc	0	-0.1349	0.1143
hc	c2	cp	cp	-0.0678	-0.0122	-0.2801
hc	c2	cp	cp	-0.0678	-0.0122	-0.2802
c2	c2	cp	cp	-0.0678	-0.0122	-0.2801
c2	c2	cp	cp	-0.0678	-0.0122	-0.2802
hc	c2	cp	cp	-0.0678	-0.0122	0
hc	c2	cp	cp	-0.2801	-0.0678	-0.0122
c2	c2	cp	cp	-0.2802	-0.0678	-0.0122
c2	c2	o_2	c_1	0	0	-0.1932
hc	c2	o_2	c_1	0	0	-0.1932
hc	c2	oh	ho	0.1863	-0.4338	-0.2121
hc	c=	c1	c2	-0.2433	0	-0.3281
c=	c=	c1	c2	0.2433	0	0.104
hc	c=	c1	hc	-0.1143	0	-0.1349
c=	c=	c1	hc	0.1143	0	0.1854
hc	c=	c2	c1	-0.2433	0	-0.3281
c=	c=	c2	c1	0.2433	0	0.104
hc	c=	c2	c2	-0.2433	0	-0.3281
c=	c=	c2	c2	0.2433	0	0.104
hc	c=	c2	hc	-0.1143	0	-0.1349
hc	c=	c2	hc	0	-0.1349	0.13
hc	c=	c2	hc	0	-0.1349	-0.1143
c=	c=	c2	hc	0.1143	0	0.1854
c=	c=	c2	hc	0.1854	0.211	-0.1143
c=	c=	c2	hc	0.1854	0.1143	0
c=	c=	c2	oh	0.211	0.1143	0
c=	c=	c3	hc	0.1143	0	0.1854
c=	c=	c3	hc	0.1854	4.075	4.075
c=	c=	c3	hc	0.1854	0.1143	0
c_1	c=	c3	hc	0.211	0.1143	0

Table A.8: The force constants for the dihedral potential within PCFF throughout this thesis (Part 3).

atom type 1	atom type 2	atom type 3	atom type 4	K_1^d	K_2^d	K_3^d
c_1	c=	c3	hc	0.211	0.211	0.211
hc	c=	c=	c1	0	5.2097	0
c2	c=	c=	c1	0.086	5.1995	0
hc	c=	c=	c2	0	5.2097	0
c2	c=	c=	c2	0.086	5.1995	0
c1	c=	c=	c2	0.086	5.1995	0
c3	c=	c=	hc	0	5.2097	0
c1	c=	c=	hc	0	5.2097	0
c2	c=	c=	hc	0	5.2097	0
hc	c=	c=	hc	0	4.8974	0
hc	c=	c=1	c=1	4.075	0	4.8974
hc	c=	c=1	hc	0	4.075	0
hc	c=	c=1	hc	4.8974	0	0.625
hc	c=1	c=	hc	0	4.8974	0
c=1	c=1	c=1	c=	0.625	0.625	0.625
hc	c=1	c=1	c=1	0.625	0.625	0.625
c=1	c=1	c=1	c=1	0.625	0.625	0.625
hc	c=1	c=1	hc	0.625	0.625	0.625
hc	c=1	c=1	hc	0.625	4.075	4.075
c=	c=1	c=1	hc	0.625	0.625	0.625
c=1	c=1	c=1	hc	0.625	0.625	0.625
o_1	c_1	c1	c2	0.0442	0.0292	0.0562
o_2	c_1	c1	c2	1.8341	2.0603	-0.0195
o_1	c_1	c1	c3	0.0442	0.0292	0.0562
o_2	c_1	c1	c3	1.8341	2.0603	-0.0195
o_1	c_1	c1	hc	-0.1804	0.0012	0.0371
o_2	c_1	c1	hc	-0.6359	1.4807	-0.0438
o_1	c_1	c=	c3	0.45	4.075	4.075
o_2	c_1	c=	c3	0.45	0	2.2089
o_2	c_1	c=	c3	0.45	0.45	0.45
o_1	c_1	c=	c=	0.45	0.211	0.211
o_1	c_1	c=	c=	0.45	0.45	0.45
o_2	c_1	c=	c=	0.45	0.45	0.45
o_1	c_1	o_2	c2	0	-2.5594	2.2013
c=	c_1	o_2	c2	0.0325	4.075	4.075
c2	cp	cp	cp	0	4.4072	0
hc	cp	cp	cp	0	3.9661	0
cp	cp	cp	cp	1.1932	0	0
hc	cp	cp	cp	3.9661	0	0
c2	cp	cp	cp	4.4072	0	0

Table A.9: The force constants for the dihedral potential within PCFF throughout this thesis (Part 4).

atom type 1	atom type 2	atom type 3	atom type 4	K_1^d	K_2^d	K_3^d
cp	cp	cp	cp	8.3667	1.1932	0
cp	cp	cp	hc	0	3.9661	0
hc	cp	cp	hc	0	1.8769	0
c2	cp	cp	hc	0	1.559	0
c2	cp	cp	hc	1.559	0	0
hc	cp	cp	hc	1.8769	0	0
hc	cp	cp	hc	1.8769	0	0
cp	cp	cp	hc	3.9661	0	0
c_1	o_2	c2	c2	0	0	-0.1932
c_1	o_2	c2	hc	0	0	-0.1932
c2	o_2	c_1	c1	-2.5594	2.2013	0.0325
c2	o_2	c_1	c=	-2.5594	2.2013	0.0325
c2	o_2	c_1	o_1	0	2.2089	0
osi	sio	c	c3	0.1111	0.1111	0.1111
osi	sio	c2	c2	0.1111	-1.3513	0
osi	sio	c2	hc	-0.058	-1.3513	0
osi	sio	c2	hc	-0.058	0.1111	-1.3513
osi	sio	c2	hc	-1.3513	0	-0.058
osi	sio	c2	hc	0	-0.058	-1.3513
osi	sio	c2	hc	0	-0.058	0.1111
osi	sio	c3	hc	-1.3513	0	-0.058
hsi	sio	osi	sio	0	0	-0.13
c2	sio	osi	sio	0	0	-0.13
c	sio	osi	sio	0	0	-0.13
c3	sio	osi	sio	0	0	-0.13
osi	sio	osi	sio	0.3	0.3658	0

Table A.10: The force constants for the dihedral potential within PCFF throughout this thesis (Part 5).

atom type 1	atom type 2	atom type 3	atom type 4	K^i	ω_0
c=	c1	c=	hc	4.153	0
c=	c2	c=	hc	4.153	0
cp	c2	cp	cp	15.6306	0
c=	c=	c2	hc	4.153	0
c=1	c=	c=1	hc	4.1136	0
c=	c=	hc	hc	5.7122	0
c=1	c=1	c=	hc	4.1136	0
c=1	c=1	c=	hc	4.1136	0
c=1	c=1	c=	hc	4.1136	0
c=1	c=1	c=1	hc	4.1136	0
c=1	c=1	c=1	hc	4.1136	0
c=	c=1	hc	hc	5.7122	0
c=	c_1	c3	c=	4.1136	0
c=	c_1	c=	c3	4.1136	0
c=	c_1	c=	c3	4.1136	0
cp	cp	hc	cp	9.7824	0
c_1	o_1	c=	o_2	72	0
c_1	o_2	c=	o_1	72	0
c_1	o_2	o_1	c1	93.8528	0
c_1	o_2	o_1	c=	72	0
c_1	o_2	o_1	c=	72	0

Table A.11: The force constants for the inversions potential within PCFF throughout this thesis (Part 5).

atom type 1	atom type 2	ϵ	σ
ho	c	0.001087	3.572755
hc	c	0.023334	3.669091
c	c	0.054	4.01
c3	c	0.054	4.01
c2	c	0.054	4.01
c1	c	0.054	4.01
c=	c	0.058584	3.95691
c_1	c	0.079559	3.916372
o_2	c	0.101994	3.771723
o_1	c	0.102122	3.737246
oh	c	0.106158	3.809127
ho	c1	0.001087	3.572755
hc	c1	0.023334	3.669091
c2	c1	0.054	4.01
c3	c1	0.054	4.01
c1	c1	0.054	4.01
c=	c1	0.058584	3.95691
sio	c1	0.060293	4.158251
c_1	c1	0.079559	3.916372
osi	c1	0.099071	3.751057
o_2	c1	0.101994	3.771723
o_1	c1	0.102122	3.737246
oh	c1	0.106158	3.809127
ho	c2	0.001087	3.572755
hc	c2	0.023334	3.669091
hsi	c2	0.024044	3.659509
c3	c2	0.054	4.01
c	c2	0.054	4.01
c2	c2	0.054	4.01
c1	c2	0.054	4.01
c=	c2	0.058584	3.95691
cp	c2	0.058788	4.01
sio	c2	0.060293	4.158251
c_1	c2	0.079559	3.916372
osi	c2	0.099071	3.751057
o_2	c2	0.101994	3.771723
o_1	c2	0.102122	3.737246
oh	c2	0.106158	3.809127
ho	c3	0.001087	3.572755

Table A.12: The force constants for the VDW potential within PCFF throughout this thesis (Part 1).

atom type 1	atom type 2	ϵ	σ
hc	c3	0.023334	3.669091
c2	c3	0.054	4.01
c1	c3	0.054	4.01
c3	c3	0.054	4.01
c=	c3	0.058584	3.95691
sio	c3	0.060293	4.158251
c_1	c3	0.079559	3.916372
osi	c3	0.099071	3.751057
o_2	c3	0.101994	3.771723
o_1	c3	0.102122	3.737246
oh	c3	0.106158	3.809127
ho	c=	0.001287	3.474793
hc	c=	0.026891	3.584244
hsi	c=	0.027775	3.573462
c	c=	0.058584	3.95691
c2	c=	0.058584	3.95691
c3	c=	0.058584	3.95691
c1	c=	0.058584	3.95691
c=1	c=	0.064	3.9
c=	c=	0.064	3.9
sio	c=	0.064362	4.114266
c_1	c=	0.087421	3.856312
osi	c=	0.112077	3.675653
o_2	c=	0.114901	3.698487
o_1	c=	0.115864	3.660348
oh	c=	0.118739	3.739621
hc	c=1	0.026891	3.584244
hsi	c=1	0.027775	3.573462
c3	c=1	0.058584	3.95691
c	c=1	0.058584	3.95691
c2	c=1	0.058584	3.95691
c=1	c=1	0.064	3.9
sio	c=1	0.064362	4.114266
c_1	c=1	0.087421	3.856312
osi	c=1	0.112077	3.675653
o_2	c=1	0.114901	3.698487
o_1	c=1	0.115864	3.660348
hc	c_1	0.038508	3.51631
c2	c_1	0.079559	3.916372
c3	c_1	0.079559	3.916372

Table A.13: The force constants for the VDW potential within PCFF throughout this thesis (Part 2).

atom type 1	atom type 2	ϵ	σ
sio	c_1	0.086259	4.081091
c=	c_1	0.087421	3.856312
c_1	c_1	0.12	3.81
osi	c_1	0.157803	3.616168
o_2	c_1	0.161173	3.640905
o_1	c_1	0.16356	3.599544
cp	cp	0.064	4.01
ho	hc	0.001585	2.66932
hc	hc	0.02	2.995
hsi	hc	0.021414	2.968137
sio	hc	0.022897	3.887505
c1	hc	0.023334	3.669091
c	hc	0.023334	3.669091
c2	hc	0.023334	3.669091
c3	hc	0.023334	3.669091
cp	hc	0.025403	3.669091
c=	hc	0.026891	3.584244
c_1	hc	0.038508	3.51631
oh	hc	0.061517	3.318925
o_2	hc	0.064133	3.241914
osi	hc	0.065546	3.19693
o_1	hc	0.070088	3.165749
sio	ho	0.001016	3.81679
c3	ho	0.001087	3.572755
c_1	ho	0.00189	3.394648
o_2	ho	0.003693	3.047429
osi	ho	0.003929	2.985127
o_1	ho	0.004334	2.94063
ho	ho	0.013	1.098
ho	hsi	0.001797	2.620425
hc	hsi	0.021414	2.968137
hsi	hsi	0.023	2.94
c3	hsi	0.024044	3.659509
c1	hsi	0.024044	3.659509
c2	hsi	0.024044	3.659509
c=	hsi	0.027775	3.573462
c_1	hsi	0.039862	3.504435
oh	hsi	0.064227	3.303017
o_2	hsi	0.067255	3.223991
o_1	hsi	0.073884	3.14552

Table A.14: The force constants for the VDW potential within PCFF throughout this thesis (Part 3).

atom type 1	atom type 2	ϵ	σ
hc	o_1	0.070088	3.165749
c3	o_1	0.102122	3.737246
c2	o_1	0.102122	3.737246
sio	o_1	0.103378	3.939226
c=	o_1	0.115864	3.660348
o_2	o_1	0.251694	3.362674
osi	o_1	0.252883	3.32547
o_1	o_1	0.267	3.3
hc	o_2	0.064133	3.241914
c3	o_2	0.101994	3.771723
c2	o_2	0.101994	3.771723
sio	o_2	0.10477	3.965889
c=	o_2	0.114901	3.698487
c_1	o_2	0.161173	3.640905
osi	o_2	0.239539	3.385904
o_2	o_2	0.24	3.42
o_1	o_2	0.251694	3.362674
ho	oh	0.003345	3.149798
hc	oh	0.061517	3.318925
c3	oh	0.106158	3.809127
sio	oh	0.110702	3.995176
c_1	oh	0.165508	3.685277
osi	oh	0.236913	3.44869
o_2	oh	0.238824	3.479873
oh	oh	0.24	3.535
o_1	oh	0.247844	3.427538
ho	osi	0.003929	2.985127
hc	osi	0.065546	3.19693
hsi	osi	0.068941	3.177687
c	osi	0.099071	3.751057
c1	osi	0.099071	3.751057
c2	osi	0.099071	3.751057
c3	osi	0.099071	3.751057
cp	osi	0.107855	3.751057
c=	osi	0.112077	3.675653
c_1	osi	0.157803	3.616168
oh	osi	0.236913	3.44869
o_2	osi	0.239539	3.385904
osi	osi	0.24	3.35
o_1	osi	0.252883	3.32547

Table A.15: The force constants for the VDW potential within PCFF throughout this thesis (Part 4).

atom type 1	atom type 2	ϵ	σ
ho	sio	0.001016	3.81679
hc	sio	0.022897	3.887505
hsi	sio	0.023485	3.880342
c1	sio	0.060293	4.158251
c	sio	0.060293	4.158251
c2	sio	0.060293	4.158251
c3	sio	0.060293	4.158251
c=	sio	0.064362	4.114266
cp	sio	0.065638	4.158251
sio	sio	0.07	4.284
c_1	sio	0.086259	4.081091
osi	sio	0.100889	3.949867
o_1	sio	0.103378	3.939226
o_2	sio	0.10477	3.965889
oh	sio	0.110702	3.995176

Table A.16: The force constants for the VDW potential within PCFF throughout this thesis (Part 5).

Bibliography

1. Kuo, S.-W. & Chang, F.-C. POSS related polymer nanocomposites. eng. *Progress in polymer science* **36,** 1649–1696. ISSN: 0079-6700 (2011).

2. Kumar, S. K., Benicewicz, B. C., Vaia, R. A. & Winey, K. I. 50th Anniversary Perspective: Are Polymer Nanocomposites Practical for Applications? eng. *Macromolecules* **50,** 714–731. ISSN: 0024-9297 (2017).

3. Raftopoulos, K. N. & Pielichowski, K. Segmental dynamics in hybrid polymer/POSS nanomaterials. eng. *Progress in polymer science* **52,** 136–187. ISSN: 0079-6700 (2016).

4. Zhou, Z., Cui, L., Zhang, Y., Zhang, Y. & Yin, N. Preparation and properties of POSS grafted polypropylene by reactive blending. eng. *European polymer journal* **44,** 3057–3066. ISSN: 0014-3057 (2008).

5. *Applied plastics engineering handbook : processing, materials, and applications* eng, 455–468. ISBN: 0-323-39041-2 (Elsevier, Boston, MA, 2017).

6. Fukahori, Y. Carbon Black Reinforcement of Rubber (1): General Rules of Reinforcement. eng. *International Polymer Science and Technology* **31,** 11, 17. ISSN: 0307-174X (2004).

7. Donate-Robles, J. & Martín-Martínez, J. M. Addition of precipitated calcium carbonate filler to thermoplastic polyurethane adhesives. eng. *International Journal of Adhesion and Adhesives* **31,** 795, 804. ISSN: 0143-7496 (2011).

8. Umar, A. & Hahn, Y. B. ZnO nanosheet networks and hexagonal nanodiscs grown on silicon substrate: growth mechanism and structural and optical properties. eng. *Nanotechnology* **17,** 2174–2180. ISSN: 0957-4484 (2006).

9. Kim, Y. S. *et al.* Building a hybrid nanocomposite assembly of gold nanowires and thienyl-derivative fullerenes to enhance electron transfer in photovoltaics. *J. Mater. Chem. A* **1,** 5015–5020. `http://dx.doi.org/10.1039/C3TA01416A` (16 2013).

10. Kumar, A. P., Depan, D., Singh Tomer, N. & Singh, R. P. Nanoscale particles for polymer degradation and stabilization—Trends and future perspectives. eng. *Progress in polymer science* **34,** 479–515. ISSN: 0079-6700 (2009).

11. Mishra, R. *Nanotechnology in textiles : theory and application* eng, 263–310. ISBN: 0-08-102627-7 (Woodhead Publishing, Duxford, 2019).

12. Sarkar, B. & Alexandridis, P. Block copolymer–nanoparticle composites: Structure, functional properties, and processing. eng. *Progress in Polymer Science* **40,** 33, 62. ISSN: 0079-6700 (2015).

13. Tjong, S. Structural and mechanical properties of polymer nanocomposites. eng. *Materials Science and Engineering R* **53,** 73, 197. ISSN: 0927-796X (2006).

14. Lopez-Cuesta, J. in *Advances in Polymer Nanocomposites: Types and Applications* 540, 566 (Elsevier Inc., 2012). ISBN: 9781845699406.

15. Fukushima, Y., Okada, A., Kawasumi, M., Kurauchi, T. & Kamigaito, O. Swelling behaviour of montmorillonite by poly-6-amide. *Clay Minerals* **23,** 27–34 (1988).

16. Okada, A. & Usuki, A. Twenty Years of Polymer-Clay Nanocomposites. eng. *Macromolecular Materials and Engineering* **291,** 1449, 1476. ISSN: 1438-7492 (2006).

17. Yano, K., Usuki, A., Okada, A., Kurauchi, T. & Kamigaito, O. *Synthesis and properties of polyimide-clay hybrid* in. **32** (Publ by ACS, 1991), 65, 66.

18. Haraguchi, K. & Takehisa, T. Nanocomposite Hydrogels: A Unique Organic–Inorganic Network Structure with Extraordinary Mechanical, Optical, and Swelling/De-swelling Properties. eng. *Advanced Materials* **14,** 1120, 1124. ISSN: 0935-9648 (2002).

19. Wang, Z. & Xiao, H. Nanocomposites: Recent Development and Potential Automotive Applications. eng. *SAE International Journal of Materials and Manufacturing* **1,** 631–640. ISSN: 1946-3979 (2009).

20. Ray, S. S. *Clay-containing polymer nanocomposites from fundamentals to real applications* eng. ISBN: 9780444594600 (Elsevier, Amsterdam ; 2013).

21. Das, P. *et al.* Current synthesis and characterization techniques for clay-based polymer nano-composites and its biomedical applications: A review. eng. *Environmental research* **212,** 113534–113534. ISSN: 0013-9351 (2022).

22. Bhat, H., Rangreez, A., Inamuddin & Hamida-Tun-Nisa, C. Wastewater Treatment and Biomedical Applications of Montmorillonite Based Nanocomposites: A Review. *Current Analytical Chemistry* **18,** 269–287. ISSN: 1573-4110/1875-6727. http://www.eurekaselect.com/article/108636 (2022).

23. Karnik, S., Jammalamadaka, U. M., Tappa, K. K., Giorno, R. & Mills, D. K. Performance evaluation of nanoclay enriched anti-microbial hydrogels for biomedical applications. eng. *Heliyon* **2,** e00072–e00072. ISSN: 2405-8440 (2016).

24. Wypych, G. *Handbook of fillers* Fourth edition. eng. Chap. 1. ISBN: 1-927885-10-8 (ChemTec Publishing, Toronto, 2016).

25. *Polymer Composites with Functionalized Nanoparticles: Synthesis, Properties, and Applications* eng. ISBN: 9780128140642 (Elsevier Science, 2018).

26. *Nanomaterials and polymer nanocomposites : raw materials to applications* eng. Chap. 1. ISBN: 0-12-814616-8 (Elsevier, Amsterdam, Netherlands, 2019).

27. Li, G., Wang, L., Ni, H. & Pittman, C. U. Polyhedral Oligomeric Silsesquioxane
     (POSS) Polymers and Copolymers: A Review. eng. *Journal of Inorganic and Organometal-
     lic Polymers* **11,** 123, 154. ISSN: 1053-0495 (2001).

28. Müller, R., Köhne, R. & Sliwinski, S. Über Silikone. XLVII. Ein definiertes Siloxan
     aus Siliciumchloroform. *Journal für Praktische Chemie* **9,** 71–74. eprint: `https://`
     `onlinelibrary.wiley.com/doi/pdf/10.1002/prac.19590090113` (1959).

29. Nie, W. Y., Li, G., Li, Y. & Xu, H. Y. Preparation and properties of a POSS-containing
     organic–inorganic hybrid crosslinked polymer. eng. *Chinese chemical letters* **20,** 738–
     742. ISSN: 1001-8417 (2009).

30. Li, Q. *et al.* Synthesis and characterization of a novel arylacetylene oligomer containing
     POSS units in main chains. eng. *European polymer journal* **44,** 2538–2544. ISSN: 0014-
     3057 (2008).

31. Lickiss, P. D. & Rataboul, F. *Chapter 1 Fully Condensed Polyhedral Oligosilsesquiox-
     anes (POSS): From Synthesis to Application* eng. in *Advances in Organometallic
     Chemistry* **57** (2008), 1–116. ISBN: 0123744652.

32. Auf der Heyde, T. P., Burgi, H.-B., Burgy, H. & Tornroos, K. W. The Crystal and
     Molecular Structure of the Symmetrical Silasesquioxane H8Si8O12 at 100 K, a Molec-
     ular Building tslock of Some Zeolites. eng. *Chimia* **45,** 38–40. ISSN: 0009-4293 (1991).

33. Kopesky, E. T., Haddad, T. S., McKinley, G. H. & Cohen, R. E. Miscibility and vis-
     coelastic properties of acrylic polyhedral oligomeric silsesquioxane–poly(methyl methacry-
     late) blends. eng. *Polymer (Guilford)* **46,** 4743–4752. ISSN: 0032-3861 (2005).

34. Baertsch, M., Bornhauser, P., Calzaferri, G. & Imhof, R. H8Si8O12: A model for the
     vibrational structure of zeolite A. *The Journal of Physical Chemistry* **98,** 2817–2831
     (1994).

35.   Wann, D. A. *et al.* Accurate Gas-Phase Experimental Structures of Octasilsesquiox-
      anes (Si8O12X8; X = H, Me). eng. *Organometallics* **27,** 4183–4187. ISSN: 0276-7333
      (2008).

36.   Jung, C. Y., Kim, H. S., Hah, H. J. & Koo, S. M. Self-assembly growth process for
      polyhedral oligomeric silsesquioxane cubic crystals. eng. *Chemical communications
      (Cambridge, England),* 1219–1221. ISSN: 1359-7345 (2009).

37.   Fina, A., Abbenhuis, H., Tabuani, D., Frache, A. & Camino, G. Polypropylene metal
      functionalised POSS nanocomposites: A study by thermogravimetric analysis. eng.
      Polymer degradation and stability **91,** 1064–1070. ISSN: 0141-3910 (2006).

38.   Sánchez-Soto, M., Schiraldi, D. A. & Illescas, S. Study of the morphology and prop-
      erties of melt-mixed polycarbonate–POSS nanocomposites. eng. *European polymer
      journal* **45,** 341–352. ISSN: 0014-3057 (2009).

39.   Cordes, D., Lickiss, P. & Rataboul, F. Recent Developments in the Chemistry of
      Cubic Polyhedral Oligosilsesquioxanes. English. *Chemical Reviews* **110,** 2081, 2173.
      ISSN: 0009-2665 (2010).

40.   Agaskar, P. NEW SYNTHETIC ROUTE TO THE HYDRIDOSPHEROSILOXANES
      OH-H8SI8O12 AND D5H-H10SI10O15. English. *Inorganic Chemistry* **30,** 2707, 2708.
      ISSN: 0020-1669 (1991).

41.   Drazkowski, D. B., Lee, A., Haddad, T. S. & Cookson, D. J. Chemical Substituent Ef-
      fects on Morphological Transitions in Styrene-Butadiene-Styrene Triblock Copolymer
      Grafted with Polyhedral Oligomeric Silsesquioxanes. *Macromolecules* **39,** 1854–1863
      (2006).

42.   Feher, F. J. Polyhedral oligometallasilsesquioxanes (POMSS) as models for silica-
      supported transition-metal catalysts. Synthesis and characterization of (C5Me5)Zr[(Si7O12)(c-
      C6H11)7]. *Journal of the American Chemical Society* **108,** 3850–3852 (1986).

43. *Advances in organometallic chemistry. Volume 57* eng. ISBN: 1-281-79551-8 (Academic Press, Amsterdam, 2008).

44. Mccabe, C., Glotzer, S., Kieffer, J., Neurock, M. & Cummings, P. Multiscale Simulation of the Synthesis, Assembly and Properties of Nanostructured Organic/Inorganic Hybrid Materials. *Journal of Computational and Theoretical Nanoscience* **1,** 265–279 (Oct. 2004).

45. Ionescu, T. C. *et al.* Evaluation of Force Fields for Molecular Simulation of Polyhedral Oligomeric Silsesquioxanes. eng. *The journal of physical chemistry. B* **110,** 2502–2510. ISSN: 1520-6106 (2006).

46. Peng, Y. & McCabe, C. Molecular simulation and theoretical modeling of polyhedral oligomeric silsesquioxanes. eng. *Molecular physics* **105,** 261–272. ISSN: 0026-8976 (2007).

47. Kudo, T., Machida, K. & Gordon, M. S. Exploring the Mechanism for the Synthesis of Silsesquioxanes. 4. The Synthesis of T8. *The journal of physical chemistry. A, Molecules, spectroscopy, kinetics, environment, and general theory* **109,** 5424–5429. ISSN: 1089-5639 (2005).

48. Zhou, J. & Kieffer, J. Molecular Dynamics Simulations of Monofunctionalized Polyhedral Oligomeric Silsesquioxane C6H13(H7Si8O12). eng. *Journal of physical chemistry. C* **112,** 3473–3481. ISSN: 1932-7447 (2008).

49. Neyertz, S., Brachet, P., Brown, D. & Männle, F. The structure of amino-functionalized polyhedral oligomeric silsesquioxanes (POSS) studied by molecular dynamics simulations. eng. *Computational materials science* **62,** 258–265. ISSN: 0927-0256 (2012).

50. Neyertz, S. *et al.* Oxygen Transport in Amino-Functionalized Polyhedral Oligomeric Silsesquioxanes (POSS). eng. *Soft materials* **12,** 113–123. ISSN: 1539-445X (2014).

51. Abe, H. *et al.* Thermal Behavior of Caged Silsesquioxane (POSS) Studied by Molecular Dynamics Simulations. eng. *Journal of inorganic and organometallic polymers and materials* **22,** 845–851. ISSN: 1574-1443 (2011).

52. Knight, P. T., Lee, K. M., Qin, H. & Mather, P. T. Biodegradable Thermoplastic Polyurethanes Incorporating Polyhedral Oligosilsesquioxane. *Biomacromolecules* **9,** 2458–2467 (2008).

53. Yen, Y.-C., Kuo, S.-W., Huang, C.-F., Chen, J.-K. & Chang, F.-C. Miscibility and Hydrogen-Bonding Behavior in Organic/Inorganic Polymer Hybrids Containing Octaphenol Polyhedral Oligomeric Silsesquioxane. *The Journal of Physical Chemistry B* **112.** PMID: 18698814, 10821–10829 (2008).

54. Xu, H., Yang, B., Wang, J., Guang, S. & Li, C. Preparation, Thermal Properties, and Tg Increase Mechanism of Poly(acetoxystyrene-co-octavinyl-polyhedral oligomeric silsesquioxane) Hybrid Nanocomposites. *Macromolecules* **38,** 10455–10460 (2005).

55. Harreld, J. H., Esaki, A. & Stucky, G. D. Low-Shrinkage, High-Hardness, and Transparent Hybrid Coatings: Poly(methyl methacrylate) Cross-Linked with Silsesquioxane. eng. *Chemistry of materials* **15,** 3481–3489. ISSN: 0897-4756 (2003).

56. Chen, Y., Chen, L., Nie, H. & Kang, E. T. Low-k nanocomposite films based on polyimides with grafted polyhedral oligomeric silsesquioxane. eng. *Journal of applied polymer science* **99,** 2226–2232. ISSN: 0021-8995 (2006).

57. Devaux, E., Rochery, M. & Bourbigot, S. Polyurethane/clay and polyurethane/POSS nanocomposites as flame retarded coating for polyester and cotton fabrics. eng. *Fire and materials* **26,** 149–154. ISSN: 0308-0501 (2002).

58. Pyun, J. *et al.* ABA triblock copolymers containing polyhedral oligomeric silsesquioxane pendant groups: synthesis and unique properties. eng. *Polymer* **44,** 2739, 2750. ISSN: 0032-3861 (2003).

59. Glodek, T. E., Boyd, S. E., McAninch, I. M. & LaScala, J. J. Properties and performance of fire resistant eco-composites using polyhedral oligomeric silsesquioxane (POSS) fire retardants. eng. *Composites science and technology* **68,** 2994–3001. ISSN: 0266-3538 (2008).

60. Martin, A. W. THERMALLY STABLE AND ELECTRICALLY ISOLATING BARRIER FILM. *US patent application No: 20190106570* (2019).

61. Fong, H., Dickens, S. H. & Flaim, G. M. Evaluation of dental restorative composites containing polyhedral oligomeric silsesquioxane methacrylate. eng. *Dental Materials* **21,** 520, 529. ISSN: 0109-5641 (2005).

62. Liu, Y., Wu, X., Sun, Y. & Xie, W. POSS Dental Nanocomposite Resin: Synthesis, Shrinkage, Double Bond Conversion, Hardness, and Resistance Properties. eng. *Polymers* **10.** ISSN: 2073-4360 (2018).

63. Fu, B. X. *et al.* Crystallization studies of isotactic polypropylene containing nanostructured polyhedral oligomeric silsesquioxane molecules under quiescent and shear conditions. eng. *Journal of polymer science. Part B, Polymer physics* **39,** 2727–2739. ISSN: 0887-6266 (2001).

64. Fu, B. X. *et al.* Physical gelation in ethylene–propylene copolymer melts induced by polyhedral oligomeric silsesquioxane (POSS) molecules. eng. *Polymer (Guilford)* **44,** 1499–1506. ISSN: 0032-3861 (2003).

65. Fina, A., Tabuani, D., Frache, A. & Camino, G. Polypropylene–polyhedral oligomeric silsesquioxanes (POSS) nanocomposites. eng. *Polymer (Guilford)* **46,** 7855–7866. ISSN: 0032-3861 (2005).

66. Bharadwaj, R., Berry, R. & Farmer, B. Molecular dynamics simulation study of norbornene–POSS polymers. eng. *Polymer* **41,** 7209, 7221. ISSN: 0032-3861 (2000).

67. Choi, J., Yee, A. F. & Laine, R. M. Organic/Inorganic Hybrid Composites from Cubic Silsesquioxanes. Epoxy Resins of Octa(dimethylsiloxyethylcyclohexylepoxide) Silsesquioxane. eng. *Macromolecules* **36,** 5666–5682. ISSN: 0024-9297 (2003).

68. Patel, R. R., Mohanraj, R. & Pittman Jr, C. U. Properties of polystyrene and poly-methyl methacrylate copolymers of polyhedral oligomeric silsesquioxanes: A molecular dynamics study. eng. **44,** 234–248. ISSN: 0887-6266 (2006).

69. Striolo, A., Mccabe, C. & Cummings, P. T. Thermodynamic and transport properties of polyhedral oligomeric sislesquioxanes in poly(dimethylsiloxane). eng. *The journal of physical chemistry. B* **109,** 14300–14307. ISSN: 1520-6106 (2005).

70. Striolo, A., McCabe, C. & Cummings, P. T. Effective Interactions between Polyhedral Oligomeric Sislesquioxanes Dissolved in Normal Hexadecane from Molecular Simulation. eng. *Macromolecules* **38,** 8950–8959. ISSN: 0024-9297 (2005).

71. Capaldi, F. M., Rutledge, G. C. & Boyce, M. C. Structure and Dynamics of Blends of Polyhedral Oligomeric Silsesquioxanes and Polyethylene by Atomistic Simulation. eng. *Macromolecules* **38,** 6700–6709. ISSN: 0024-9297 (2005).

72. Yani, Y. & Lamm, M. H. Molecular dynamics simulation of mixed matrix nanocomposites containing polyimide and polyhedral oligomeric silsesquioxane (POSS). eng. *Polymer* **50,** 1324, 1332. ISSN: 0032-3861 (2009).

73. Zhu, Y., Cao, S. & Huo, F. Molecular dynamics simulation study of the solid polymer electrolyte that PEO grafted POSS. eng. *Chemical physics letters* **756,** 137834–. ISSN: 0009-2614 (2020).

74. Zhang, J. *et al.* Cross-Linked Nanohybrid Polymer Electrolytes With POSS Cross-Linker for Solid-State Lithium Ion Batteries. eng. *Frontiers in chemistry* **6,** 186–186. ISSN: 2296-2646 (2018).

75. Xie, J. *et al.* Molecular simulation of nano polyhedral oligomeric silsesquioxane doping effect on the properties of two-component crosslinked epoxy resin. *Journal of molecular graphics and modelling* **107,** 107961–107961. ISSN: 1093-3263 (2021).

76. Sun, Y., Chen, L., Cui, L., Zhang, Y. & Du, X. Molecular dynamics simulation of cross-linked epoxy resin and its interaction energy with graphene under two typical force fields. eng. *Computational materials science* **143,** 240–247. ISSN: 0927-0256 (2018).

77. KOPESKY, E. T., HADDAD, T. S., COHEN, R. E. & MCKINLEY, G. H. Thermo-mechanical properties of Poly(methyl methacrylate)s containing tethered and untethered polyhedral oligomeric silsesquioxanes. eng. *Macromolecules* **37,** 8992–9004. ISSN: 0024-9297 (2004).

78. Kopesky, E. T., Haddad, T. S., McKinley, G. H. & Cohen, R. E. Miscibility and viscoelastic properties of acrylic polyhedral oligomeric silsesquioxane–poly(methyl methacrylate) blends. eng. *Polymer (Guilford)* **46,** 4743–4752. ISSN: 0032-3861 (2005).

79. KOPESKY, E. T., BOYES, S. G., TREAT, N., COHEN, R. E. & MCKINLEY, G. H. Thermorheological properties near the glass transition of oligomeric poly(methyl methacrylate) blended with acrylic polyhedral oligomeric silsesquioxane nanocages. *Rheologica acta* **45,** 971–981. ISSN: 0035-4511 (2006).

80. Li, S., Simon, G. P. & Matisons, J. G. Morphology of blends containing high concentrations of POSS nanoparticles in different polymer matrices. *Polymer engineering and science* **50,** 991–999. ISSN: 0032-3888 (2010).

81. Heeley, E. L., Hughes, D. J., Taylor, P. G. & Bassindale, A. R. Crystallization and morphology development in polyethylene-octakis(n-octadecyldimethylsiloxy)octasilsesquioxane nanocomposite blends. eng. *RSC advances* **5,** 3479–34719. ISSN: 2046-2069 (2015).

82. Li, S., Simon, G. P. & Matisons, J. G. effect of incorporation of POSS units on polymer blend compatibility. eng. *Journal of applied polymer science* **115,** 1153–1159. ISSN: 0021-8995 (2010).

83. Raftopoulos, K. N. & Pielichowski, K. Segmental dynamics in hybrid polymer/POSS nanomaterials. eng. *Progress in polymer science* **52,** 136–187. ISSN: 0079-6700 (2016).

84. Striolo, A., Mccabe, C. & Cummings, P. T. Effective Interactions between Polyhedral Oligomeric Sislesquioxanes Dissolved in Normal Hexadecane from Molecular Simulation. eng. *Macromolecules* **38,** 8950, 8959. ISSN: 0024-9297 (2005).

85. Striolo, A., McCabe, C., Cummings, P. T., Chan, E. R. & Glotzer, S. C. Aggregation of POSS Monomers in Liquid Hexane: A Molecular-Simulation Study. eng. *The journal of physical chemistry. B* **111,** 12248–12256. ISSN: 1520-6106 (2007).

86. Zhang, Q. G., Liu, Q. L., Wu, J. Y., Chen, Y. & Zhu, A. M. Structure-related diffusion in poly(methyl methacrylate)/polyhedral oligomeric silsesquioxanes composites: A molecular dynamics simulation study. eng. *Journal of membrane science* **342,** 105–112. ISSN: 0376-7388 (2009).

87. Bizet, S., Galy, J. & Gérard, J.-F. Molecular dynamics simulation of organic–inorganic copolymers based on methacryl-POSS and methyl methacrylate. *Polymer* **47,** 8219–8227. ISSN: 0032-3861. http://www.sciencedirect.com/science/article/pii/S0032386106011001 (2006).

88. Liu, Y.-L., Tseng, M.-C. & Fangchiang, M.-H. Polymerization and nanocomposites properties of multifunctional methylmethacrylate POSS. eng. *Journal of polymer science. Part A, Polymer chemistry* **46,** 5157–5166. ISSN: 0887-624X (2008).

89. Amir, N., Levina, A. & Silverstein, M. S. Nanocomposites through copolymerization of a polyhedral oligomeric silsesquioxane and methyl methacrylate. eng. *Journal of polymer science. Part A, Polymer chemistry* **45,** 4264–4275. ISSN: 0887-624X (2007).

90. Martínez, L., Andrade, R., Birgin, E. G. & Martínez, J. M. PACKMOL: A package for building initial configurations for molecular dynamics simulations. *Journal of Computational Chemistry* **30,** 2157–2164. eprint: https://onlinelibrary.wiley.com/

`doi/pdf/10.1002/jcc.21224.` `https://onlinelibrary.wiley.com/doi/abs/10.` `1002/jcc.21224` (2009).

91. Yong, C. W. Descriptions and Implementations of DL_F Notation: A Natural Chemical Expression System of Atom Types for Molecular Simulations. *Journal of Chemical Information and Modeling* **56.** PMID: 27455451, 1405–1409. eprint: `https://doi.` `org/10.1021/acs.jcim.6b00323.` `https://doi.org/10.1021/acs.jcim.6b00323` (2016).

92. Brooks, B., Brooks III, C. & et al., A. M. J. CHARMM: The Biomolecular Simulation Program. *J. Comput. Chem.* **30.** PMC2810661, 1545–1614 (2009).

93. London, F. The general theory of molecular forces. *Trans. Faraday Soc.* **33,** 8b–26. `http://dx.doi.org/10.1039/TF937330008B` (0 1937).

94. Israelachvili, J. N. *Intermolecular and surface forces* 3rd ed. eng. Chap. 6. ISBN: 0123751829 (Academic Press, Burlington, MA, 2011).

95. Sun, H., Mumby, S. J., Maple, J. R. & Hagler, A. T. An ab Initio CFF93 All-Atom Force Field for Polycarbonates. *Journal of the American Chemical Society* **116,** 2978–2987. eprint: `https://doi.org/10.1021/ja00086a030.` `https://doi.org/10.1021/` `ja00086a030` (1994).

96. Verlet, L. Computer "Experiments" on Classical Fluids. I. Thermodynamical Properties of Lennard-Jones Molecules. *Phys. Rev.* **159,** 98–103. `https://link.aps.org/` `doi/10.1103/PhysRev.159.98` (1 July 1967).

97. Hockney, R. W. POTENTIAL CALCULATION AND SOME APPLICATIONS. *Methods Comput. Phys. 9: 135-211(1970).* `https://www.osti.gov/biblio/4079632` (Jan. 1970).

98. Swope, W. C., Andersen, H. C., Berens, P. H. & Wilson, K. R. A computer simulation method for the calculation of equilibrium constants for the formation of physical clusters of molecules: Application to small water clusters. *The Journal of Chemi-*

cal Physics **76,** 637–649. eprint: `https://doi.org/10.1063/1.442716`. `https://doi.org/10.1063/1.442716` (1982).

99.   Allen, M., Allen, M., Tildesley, D., Tildesley, D. & ALLEN, T. *Computer Simulation of Liquids* ISBN: 9780198556459. `https://books.google.co.uk/books?id=O32VXB9e5P4C` (Clarendon Press, 1989).

100. Todorov, I. T., Smith, W., Trachenko, K. & Dove, M. T. DL_POLY_3: new dimensions in molecular dynamics simulations via massive parallelism. *J. Mater. Chem.* **16,** 1911–1918. `http://dx.doi.org/10.1039/B517931A` (20 2006).

101. BEKKER, H. *et al.* GROMACS - A PARALLEL COMPUTER FOR MOLECULAR-DYNAMICS SIMULATIONS. English (eds DeGroot, R. & Nadrchal, J.) 4th International Conference on Computational Physics (PC 92) ; Conference date: 24-08-1992 Through 28-08-1992, 252–256 (1993).

102. Mayo, S. L., Olafson, B. D. & Goddard, W. A. DREIDING: a generic force field for molecular simulations. *The Journal of Physical Chemistry* **94,** 8897–8909 (1990).

103. Smith, W. & Forester, T. DL_POLY_2.0: A general-purpose parallel molecular dynamics simulation package. *Journal of molecular graphics* **14,** 136–141 (1996).

104. Neese, F. The ORCA program system. *WIREs Computational Molecular Science* **2,** 73–78. eprint: `https://wires.onlinelibrary.wiley.com/doi/pdf/10.1002/wcms.81`. `https://wires.onlinelibrary.wiley.com/doi/abs/10.1002/wcms.81` (2012).

105. Lu, T. & Chen, F. Multiwfn: A multifunctional wavefunction analyzer. *Journal of Computational Chemistry* **33,** 580–592 (2012).

106. Breneman, C. M. & Wiberg, K. B. Determining atom-centered monopoles from molecular electrostatic potentials. The need for high sampling density in formamide conformational analysis. *Journal of Computational Chemistry* **11,** 361–373. eprint: `https://onlinelibrary.wiley.com/doi/pdf/10.1002/jcc.540110311`. `https://onlinelibrary.wiley.com/doi/abs/10.1002/jcc.540110311` (1990).

107. Bayly, C. I., Cieplak, P., Cornell, W. & Kollman, P. A. A well-behaved electrostatic potential based method using charge restraints for deriving atomic charges: the RESP model. *The Journal of Physical Chemistry* **97,** 10269–10280. eprint: `https://doi.org/10.1021/j100142a004`. `https://doi.org/10.1021/j100142a004` (1993).

108. Berendsen, H. J. C., Postma, J. P. M., van Gunsteren, W. F., DiNola, A. & Haak, J. R. Molecular dynamics with coupling to an external bath. *The Journal of Chemical Physics* **81,** 3684–3690. eprint: `https://doi.org/10.1063/1.448118`. `https://doi.org/10.1063/1.448118` (1984).

109. Hoover, W. G. *Computational statistical mechanics* (Elsevier, 2012).

110. Dossi, E. *et al.* Understanding and controlling the glass transition of HTPB oligomers. *Polym. Chem.* **12,** 2606–2617. `http://dx.doi.org/10.1039/D1PY00233C` (17 2021).

111. Dyre, J. C. Colloquium : The glass transition and elastic models of glass-forming liquids. eng. *Reviews of modern physics* **78,** 953–972. ISSN: 0034-6861 (2006).

112. Glass transition of polymers in bulk, confined geometries, and near interfaces. eng. *Reports on progress in physics* **80,** 036602–036602. ISSN: 0034-4885 (2017).

113. Bejagam, K. K., Iverson, C. N., Marrone, B. L. & Pilania, G. Molecular dynamics simulations for glass transition temperature predictions of polyhydroxyalkanoate biopolymers. eng. *Physical chemistry chemical physics : PCCP* **22,** 17880–17889. ISSN: 1463-9076 (2020).

114. Han, J., Gee, R. H. & Boyd, R. H. Glass Transition Temperatures of Polymers from Molecular Dynamics Simulations. *Macromolecules* **27,** 7781–7784. eprint: `https://doi.org/10.1021/ma00104a036`. `https://doi.org/10.1021/ma00104a036` (1994).

115. Free Volume in a PVME Polymer–Water Solution. eng. *Macromolecules* **53,** 4770–4782. ISSN: 0024-9297 (2020).

116. Fox, T. G. & Flory, P. J. The glass temperature and related properties of polystyrene. Influence of molecular weight. *Journal of Polymer Science* **14,** 315–319. eprint: `https://onlinelibrary.wiley.com/doi/pdf/10.1002/pol.1954.120147514`. `https://onlinelibrary.wiley.com/doi/abs/10.1002/pol.1954.120147514` (1954).

117. Fox Thomas G., J. & Flory, P. J. Second-Order Transition Temperatures and Related Properties of Polystyrene. I. Influence of Molecular Weight. *Journal of Applied Physics* **21,** 581–591. ISSN: 0021-8979. eprint: `https://pubs.aip.org/aip/jap/article-pdf/21/6/581/7917644/581\_1\_online.pdf`. `https://doi.org/10.1063/1.1699711` (Apr. 2004).

118. Novikov, V. & Rössler, E. Correlation between glass transition temperature and molecular mass in non-polymeric and polymer glass formers. *Polymer* **54,** 6987–6991. ISSN: 0032-3861. `https://www.sciencedirect.com/science/article/pii/S0032386113010288` (2013).

119. Ogawa, T. Effects of molecular weight on mechanical properties of polypropylene. *Journal of Applied Polymer Science* **44,** 1869–1871. eprint: `https://onlinelibrary.wiley.com/doi/pdf/10.1002/app.1992.070441022`. `https://onlinelibrary.wiley.com/doi/abs/10.1002/app.1992.070441022` (1992).

120. Wei, H., Wang, D. & Li, S. A Predictive Method of Thermal Expansion Coefficient of POSS Reinforced Silicone Materials. eng. *Journal of physics. Conference series* **1965,** 12061–. ISSN: 1742-6588 (2021).

121. Wei, G. *et al.* Mechanism of two-dimensional crystal formation from soft microgel particles. eng. *Soft matter* **9,** 9924–9930. ISSN: 1744-683X (2013).

122. Aste, T. *et al.* An invariant distribution in static granular media. eng. *Europhysics letters* **79,** 24003–. ISSN: 0295-5075 (2007).

123. Weis, S., Schönhöfer, P. W. A., Schaller, F. M., Schröter, M. & Schröder-Turk, G. E. Pomelo, a tool for computing Generic Set Voronoi Diagrams of Aspherical Particles of Arbitrary Shape. eng. *EPJ Web of Conferences* **140,** 6007–. ISSN: 2101-6275 (2017).

124. Wang, J., Wolf, R. M., Caldwell, J. W., Kollman, P. A. & Case, D. A. Development and testing of a general amber force field. eng. *Journal of computational chemistry* **25,** 1157–1174. ISSN: 0192-8651 (2004).

125. Ewig, C. S. *et al.* Derivation of class II force fields. VIII. Derivation of a general quantum mechanical force field for organic compounds. eng. *Journal of computational chemistry* **22,** 1782–1800. ISSN: 0192-8651 (2001).

126. MAPLE, J. R., DINUR, U. & HAGLER, A. T. Derivation of Force Fields for Molecular Mechanics and Dynamics from ab initio Energy Surfaces. eng. *Proceedings of the National Academy of Sciences - PNAS* **85,** 5350–5354. ISSN: 0027-8424 (1988).

127. Sun, H. COMPASS: An ab Initio Force-Field Optimized for Condensed-Phase Applications Overview with Details on Alkane and Benzene Compounds. eng. *The journal of physical chemistry. B* **102,** 7338–7364. ISSN: 1520-6106 (1998).

128. Sun, H., Mumby, S. J., Maple, J. R. & Hagler, A. T. An ab Initio CFF93 All-Atom Force Field for Polycarbonates. eng. *Journal of the American Chemical Society* **116,** 2978–2987. ISSN: 0002-7863 (1994).

129. Dauber-Osguthorpe, P. *et al.* Structure and energetics of ligand binding to proteins: Escherichia coli dihydrofolate reductase-trimethoprim, a drug-receptor system. *Proteins: Structure, Function, and Bioinformatics* **4,** 31–47. eprint: `https://onlinelibrary.wiley.com/doi/pdf/10.1002/prot.340040106`. `https://onlinelibrary.wiley.com/doi/abs/10.1002/prot.340040106` (1988).

130. Yang, X. H., Giovenzana, T., Feild, B., Jabbour, G. E. & Sellinger, A. Solution processeable organic-inorganic hybrids based on pyrene functionalized mixed cubic

silsesquioxanes as emitters in OLEDs. eng. *Journal of materials chemistry* **22,** 12689–12694. ISSN: 0959-9428 (2012).

131.   Böhning, M., Hao, N. & Schönhals, A. Gas transport and molecular mobility in polymer/POSS nanocomposites. eng. *Desalination* **200,** 142–143. ISSN: 0011-9164 (2006).

132.   Hao, N., Böhning, M. & Schönhals, A. Dielectric Properties of Nanocomposites Based on Polystyrene and Polyhedral Oligomeric Phenethyl-Silsesquioxanes. eng. *Macromolecules* **40,** 9672–9679. ISSN: 0024-9297 (2007).

133.   Lin, X., Siew, W. H., Liggat, J., Given, M. & He, J. Octavinyl polyhedral oligomeric silsesquioxane on tailoring the DC electrical characteristics of polypropylene. eng. *High voltage* **7,** 137–146. ISSN: 2397-7264 (2022).

134.   Humphrey, W., Dalke, A. & Schulten, K. VMD: Visual molecular dynamics. eng. *Journal of molecular graphics* **14,** 33–38. ISSN: 0263-7855 (1996).

135.   Soong, S. Y., Cohen, R. E. & Boyce, M. C. Polyhedral oligomeric silsesquioxane as a novel plasticizer for poly(vinyl chloride). eng. *Polymer (Guilford)* **48,** 1410–1418. ISSN: 0032-3861 (2007).

136.   Kumar, V. S. & Kumaran, V. Voronoi neighbor statistics of hard-disks and hard-spheres. eng. *The Journal of chemical physics* **123,** 074502-074502–10. ISSN: 0021-9606 (2005).

137.   Neyertz, S., Brown, D., Raaijmakers, M. & Benes, N. E. The influence of the dianhydride precursor in hyper-cross-linked hybrid polyPOSS-imide networks. eng. *Physical chemistry chemical physics : PCCP* **18,** 28688–28703. ISSN: 1463-9076 (2016).

138.   Brown, D., Neyertz, S., Raaijmakers, M. J. & Benes, N. E. Sorption and permeation of gases in hyper-cross-linked hybrid poly(POSS-imide) networks: An in silico study. eng. *Journal of membrane science* **577,** 113–128 (2019).

139.   Neyertz, S., Salimi, S., Radmanesh, F., Benes, N. E. & Brown, D. High-temperature molecular screening of hybrid polyOAPS-imide networks based on octa(aminophenyl)silsesquioxane for increased thermomechanical resistance. eng. *Physical chemistry chemical physics : PCCP* **23,** 11438–11454. ISSN: 1463-9076 (2021).

140.   Marcinkowska, A., Przadka, D. & Andrzejewska, E. POSS functionalized with mixed fluoroalkyl and methacryloxy substituents as modifiers for UV-curable coatings. eng. *Journal of Coatings Technology and Research* **16,** 167–178. ISSN: 1547-0091 (2019).

141.   Zhang, C., Bunning, T. J. & Laine, R. M. Synthesis and Characterization of Liquid Crystalline Silsesquioxanes. eng. *Chemistry of materials* **13,** 3653–3662. ISSN: 0897-4756 (2001).

142.   Chan, E. R., Zhang, X., Lee, C.-Y., Neurock, M. & Glotzer, S. C. Simulations of Tetra-Tethered Organic/Inorganic Nanocube Polymer Assemblies. eng. *Macromolecules* **38,** 6168–6180. ISSN: 0024-9297 (2005).

143.   Zhou, Q., Jie, S. & Li, B.-G. Preparation of Hydroxyl-Terminated Polybutadiene with High Cis-1,4 Content. eng. *Industrial and engineering chemistry research* **53,** 17884–17893. ISSN: 0888-5885 (2014).

144.   Sekkar, V., Alex, A. S., Kumar, V. & Bandyopadhyay, G. G. Pot life extension of hydroxyl terminated polybutadiene based solid propellant binder system by tailoring the binder polymer microstructure. eng. *Journal of macromolecular science. Part A, Pure and applied chemistry* **54,** 171–175. ISSN: 1060-1325 (2017).

145.   Cao, Z., Zhou, Q., Jie, S. & Li, B.-G. High cis-1,4 Hydroxyl-Terminated Polybutadiene-Based Polyurethanes with Extremely Low Glass Transition Temperature and Excellent Mechanical Properties. eng. *Industrial and engineering chemistry research* **55,** 1582–1589. ISSN: 0888-5885 (2016).

146.   Ajaz, A. Hydroxyl-terminated polybutadiene telechelic polymer (htpb): binder for solid rocket propellants. *Rubber chemistry and technology* **68,** 481–506 (1995).

147.   Short, J., Kraus, G., Zelinski, R. & Naylor, F. Polybutadienes of controlled cis, trans and vinyl structures. *Rubber Chemistry and Technology* **32,** 614–627 (1959).

148.   Mayo, S. L., Olafson, B. D. & Goddard, W. A. DREIDING: a generic force field for molecular simulations. *The Journal of Physical Chemistry* **94,** 8897–8909 (1990).

149.   Lin, C.-T. & Liu, M.-C. Studies on the graft polymerizations of styrene and methyl methacrylate to hydroxyl terminated polybutadiene. eng. *Journal of polymer research* **2,** 127–132. ISSN: 1022-9760 (1995).

150.   Pan, R., Wang, L. L., Shanks, R. & Liu, Y. The Influence of Trisilanolisobutyl POSS on Domain Microstructure of a Polyurethane Hybrid Composite: A Molecular Simulation Approach. eng. *SILICON* **11,** 2253–2260. ISSN: 1876-990X (2019).

151.   Yamamoto, K., Suzuki, S. & Tsuji, J. Preparation of (E)-1,3,5-Hexatriene and (3E, 5E)-1,3,5,7-Octatetraene by the Palladium Catalyzed Elimination of Acetic Acid from Allylic Acetates. *Bulletin of the Chemical Society of Japan* **54,** 2541–2542. eprint: `https://doi.org/10.1246/bcsj.54.2541`. `https://doi.org/10.1246/bcsj.54.2541` (1981).

152.   Jia, X.-M., Qian, H.-J. & Lu, Z.-Y. The interfacial structure and dynamics in a polymer nanocomposite containing small attractive nanoparticles: a full atomistic molecular dynamics simulation study. eng. *Physical chemistry chemical physics : PCCP* **22,** 114–1148. ISSN: 1463-9076 (2020).

153.   Jin, J. *et al.* Synthesis of POSS-functionalized liquid crystalline block copolymers via RAFT polymerization for stabilizing blue phase helical soft superstructures. eng. *Polymer chemistry* **9,** 2101–2108. ISSN: 1759-9954 (2018).